SAN-1735-4
Distribution Category UC-94cb

FUEL CELL RESEARCH ON SECOND-GENERATION MOLTEN-CARBONATE SYSTEMS

Project 9105 Final Technical Report

For the Period October 1, 1977, Through September 30, 1978

Prepared by

Institute of Gas Technology
IIT Center, 3424 S. State Street
Chicago, Illinois 60616

Date Published — April 1979

Prepared for the

UNITED STATES DEPARTMENT OF ENERGY

Under Contract No. EC-78-C-03-1735

EXECUTIVE SUMMARY

The objectives of the FY 1978 molten-carbonate fuel cell program were to a) develop fuel cell components with improved performance and endurance and to b) investigate, develop, and test cost-effective processes for electrolyte powder preparation and electrolyte tile fabrication. The effort was subdivided into three tasks:

- Task 1. Cell and Component Development

  Improved components and cost-effective fabrication processes were developed. This included developing stable anode structures and improved electrolyte structures that can be fabricated by cost-effective processes.

- Task 2. Fuel Cell Electrolyte Optimization

  New melt compositions were tested in laboratory-scale cells. Supporting information necessary for electrolyte selection and for understanding the processes occurring in these systems was obtained by developing models to describe cell performance and by electrode kinetic measurements.

- Task 3. Cell Operation at High Pressure

  The system was operated at high pressure to identify and provide solutions to cell-decay mechanisms and to identify problems associated with operating these cells at high pressures.

The anode developmental work focused on using nickel- and cobalt-based structures containing additives to inhibit sintering. Electrodes fabricated from cobalt with the addition of 10% chromium showed the best cell performance and physical stability after 3000 hours of testing with high- and low-Btu fuels. This same electrode also demonstrated the best tolerance to low-Btu fuels containing approximately 10 ppm H_2S.

A significant experimental effort was devoted to defining the processing parameters necessary for producing acceptable electrolyte powders by an aqueous slurry technique. Both physical (thermal expansion, yield, etc.) measurements and fuel cell tests were used to qualify the batches produced. Promising results were obtained as demonstrated by operating cells using developmental tiles with Co-10% Cr anodes for 3000 hours, during which time the performance exceeded that of standard state-of-the-art components.

Potentially cost-effective tile manufacturing processes using the powders produced by the aqueous slurry process were identified in a cooperative effort with Coors Porcelain Co. Cell performance using such tiles was comparable with cells using conventionally hot-pressed tiles. These promising results indicate that scale-up and mass-producibility are feasible and should be investigated further.

Efforts to optimize the electrolyte composition focused on identifying the rates of fuel oxidation as a function of anode material, temperature, carbonate composition, and gas composition and the development of mathematical models for the prediction of fuel cell performance as a function of various system operating parameters. In general, it was found that the kinetics of fuel oxidation were high. Measured exchange current densities, i_o, ranged from approximately 8 to approximately 80 mA/cm^2 at 650°C for the combinations tested. The highest exchange currents were obtained with a ternary carbonate eutectic. Subsequent laboratory-scale cell testing in the 550 to 650°C temperature range using an off-eutectic ternary composition showed the highest cell performance of all the compositions tested. This ternary off-eutectic composition performed approximately 30 mV better at 160 mA/cm^2 and 650°C than the usual 62% Li/38% K carbonate composition.

The mathematical model developed predicts the performance of a scaled-up molten-carbonate fuel cell with crossflow of fuel and oxidant for various inlet gas compositions, gas flow rates, and operating pressures. The model takes into account the water-gas equilibrium of CO and, in pressurized operation, the methane steam-reforming equilibrium. It contains only a single adjustable parameter, the effective impedance, which may be adjusted locally or given an average value. For all inlet gas compositions, the performance at 75% conversion predicted by the model agrees to within 4% of the experimental data.

Several system control and component problems that prevented long-term endurance operation in the 5 to 10-atm pressure range were identified. The system problems were corrected, and high-pressure operation will be resumed during the FY 1979 program.

TABLE OF CONTENTS

Page

TABLE OF CONTENTS, Cont.

TABLE OF CONTENTS, Cont.

TABLE OF CONTENTS, Cont.

LIST OF FIGURES

LIST OF FIGURES, Cont.

LIST OF FIGURES, Cont.

LIST OF FIGURES, Cont.

LIST OF FIGURES, Cont.

LIST OF FIGURES, Cont.

LIST OF FIGURES, Cont.

LIST OF TABLES

LIST OF TABLES, Cont.

LIST OF TABLES, Cont.

TASK 1. CELL AND COMPONENT DEVELOPMENT

1. Summary

The objective of Task 1 was to develop an improved and cost-effective anode/electrolyte tile/cathode fuel cell package with demonstrated performance equal to or better than state-of-the-art cells. Nickel- and cobalt-based anodes containing additives to inhibit sintering were commercially fabricated and evaluated in screening tests and operating cells. Unstabilized porous nickel compacts, which oxidize in situ to form NiO, were utilized as the cathode material. Improved and more cost-effective fabrication techniques were emphasized in the development of the lithium aluminate/alkali carbonate electrolyte powder and tile materials. A significant experimental effort was devoted to defining the processing parameters necessary for producing acceptable electrolyte powders by an aqueous slurry technique.

The materials and components developed in the program were subjected to detailed physical and chemical characterizations to determine their as-fabricated properties as well as their physicochemical stabilities during cell operation. The most promising electrode and tile materials and structures were tested in laboratory-scale (3 cm^2) and bench-scale (94 cm^2) fuel cells with sulfur-free fuel gases and with fuels containing low levels of sulfur (10 ppm H_2S + COS).

Achievements realized during the course of the program included —

- The development of a modified aqueous slurry process for producing acceptable fuel cell grade $LiAlO_2$.
- Fuel cells operated with developmental tile from an aqueous slurry process and with Co-10% Cr anode/NiO equalled or exceeded performance with standard state-of-the-art components.
- Co-10% Cr porous anodes showed very good cell performance and physical stability after as long as 3000 hours of testing with high- and low-Btu fuels.
- The Co-10% Cr anode also demonstrated good resistance to ~10 ppm H_2S contaminant in low-Btu fuel (~40 mV loss at 160 mA/cm^2).
- Promising cell performance results were obtained at 650°C with several carbonate electrolyte compositions different from the standard 62 mole percent Li_2CO_3/38 mole percent K_2CO_3 eutectic. An off-eutectic ternary $Li_2CO_3/Na_2CO_3/K_2CO_3$ composition showed lower, but still encouraging, performance at 550° to 600°C. Cathode performance improvements are necessary to obtain acceptable performance levels at these lower temperatures.

- A potentially cost-effective tile manufacturing process was identified and investigated in a cooperative effort with Coors Porcelain Co. Cell performance of tiles made by this process was comparable with that of conventionally hot-pressed tiles. The results indicate that scale-up of the process should be investigated.

1.1. Anode and Tile Development

1.1.1. Anode Development

A literature survey was conducted to identify anode materials that were potentially more stable in sulfur-containing fuels than the nickel-based anodes currently used. Based on available thermodynamic data, cobalt is expected to be more sulfidation-resistant than nickel in fuel gases that contain H_2S. At the cell operating temperature of 650°C (923 K), the Ni/NiS_y equilibrium occurs[1] at $\log (p_{H_2S}/p_{H_2}) = -2.74$ while the Co/Co_9S_8 equilibrium occurs[1] at $\log (p_{H_2S}/p_{H_2}) = -2.30$. Thus, for a low-Btu fuel gas containing 18.6 volume percent H_2, nickel would be sulfidized at H_2S levels above 338 ppm (by volume), while cobalt would remain metallic until the H_2S level reached 932 ppm (by volume). Sulfidation of nickel is particularly detrimental because a Ni/Ni_3S_2 liquid eutectic occurs at 645°C. However, poisoning of catalytic activity of metals by chemisorption of sulfur can occur at sulfur activities far below those required for the formation of a metal sulfide corrosion product.[2,3] For example, Rostrup-Neilsen observed poisoning of a nickel catalyst at p_{H_2S}/p_{H_2} ratios 10^2 to 10^3 times lower than that required to form the sulfide.

Nickel- and cobalt-based anode materials 0.75-mm (0.030 in.) thick, with nominal porosities of 65% to 80% and mean pore sizes of 5μ, 10μ, and 15μ, were selected for the anode development studies. Nichrome, chromium, and tungsten carbide anode sintering inhibitors were investigated. Porous nickel cathodes were selected for the cell-testing phase of this work. These candidate electrode materials were fabricated by Gould Laboratories, Gould, Inc., Cleveland, Ohio, a company with a good reputation for delivery of high-quality electrodes.

1.1.1.1. Characterization of As-Fabricated Electrodes

Table 1.1 lists the anode and cathode plaques fabricated by Gould Laboratories and presents the characterization results obtained on the as-fabricated plaques. The electrodes were characterized by krypton

Table 1. CHARACTERIZATION RESULTS OBTAINED ON DEVELOPMENTAL ANODE AND CATHODE MATERIALS

			Mercury Porosimetry			B.E.T.	Quantitative Microscopy			
Material	Plaque No.	Thickness, mm	Porosity, %	mps, μ	80% Pore Size Range, μ	Surface Area m^2/g	Porosity, %	S_v, cm^{-1}	ℓ_p, μ	ℓ_s, μ
ANODES										
Ni	480-31-36	0.76	83.3	7.9	4.1 to 14.8	0.24	79.8	2345	13.6	3.4
Ni	480-31-37	0.74	83.5	8.5	4.3 to 14.6	0.22	81.7	2050	16.0	3.6
Ni	480-31-42	0.79	75.4	5.7	3.2 to 7.9	0.23	65.2	3530	7.4	4.0
Ni	480-31-44	0.79	76.2	6.1	3.3 to 10.2	0.23	72.2	2990	9.7	3.7
Ni	480-31-51	0.76	80.5	15.1	7.6 to 22.6	0.23	83.6	1520	22.0	4.3
Ni	480-31-53	0.76	80.4	14.8	7.7 to 17.5	0.21	73.8	1540	19.1	6.8
Ni + 10% NiCr	416-71-4	--	76.3	7.0	3.7 to 14.9	0.20	69.8	2760	10.1	4.4
Ni + 10% NiCr	416-71-5	--	--	--	--	0.19	60.3	3250	7.4	4.9
Co	480-31-62	0.76	78.7	4.1	2.4 to 6.1	0.31	71.2	5120	5.6	2.2
Co	480-31-65	0.76	77.1	3.5	2.1 to 6.1	0.34	71.2	5340	5.3	2.2
Co	480-31-66	0.76	83.9	9.3	2.9 to 18.6	0.28	79.4	3820	8.3	2.2
Co	480-31-67	0.79	83.6	7.2	2.7 to 15.7	0.33	75.0	3450	8.7	2.9
Co	480-31-70	0.81	63.6	21.7	15.3 to 40.7	0.03	55.5	1000	22.2	17.8
Co	480-31-71	0.74	60.7	16.3	11.0 to 33.2	0.04	59.2	1020	23.2	16.0
Co + 10% WC	416-66-1	0.74	80.1	4.6	2.5 to 7.8	0.34	70.0	4610	6.1	2.6
Co + 10% WC	416-66-2	0.81	81.2	3.7	2.0 to 5.5	0.54	71.6	4990	5.7	2.3
Co + 10% NiCr	416-66-3	0.84	80.7	3.7	2.1 to 5.5	0.48	74.8	5880	5.1	1.7
Co + 10% NiCr	416-66-4	0.79	70.3	3.0	1.9 to 5.2	0.23	61.9	6090	4.1	2.5
Co + 10% Cr	416-66-5	0.79	80.1	3.2	1.7 to 5.2	0.46	70.0	5340	5.2	2.2
Co + 10% Cr	416-66-6	0.79	76.5	3.0	1.7 to 7.6	0.46	67.8	5360	5.1	2.4
CATHODES										
Ni	480-31-27	0.53	80.3	9.6	4.7 to 15.5	0.21	73.1	2700	10.8	4.0
Ni	480-31-29	0.53	79.6	8.9	4.5 to 16.5	0.16	70.6	2620	10.8	4.5
Ni	480-31-50	0.53	81.3	13.3	7.2 to 35.1	0.28	77.7	1760	17.7	5.1
Ni	480-31-54	0.51	81.7	14.7	7.4 to 27.8	0.22	82.5	1570	21.0	4.4
Ni	480-31-68	0.51	49.4	18.9	15.0 to 60.3	0.02	40.6	753	21.6	31.5
Ni	480-31-69	0.46	41.5	18.6	18.6 to 46.0	0.03	44.7	772	23.2	28.7

adsorption B.E.T. (Brunauer, Emmett, and Teller) measurements, mercury porosimetry, and quantitative optical microscopy (QM). Selected anodes were also evaluated by QM after cell testing. These results will be discussed below. Scanning electron microscopy was also performed on fractured surfaces of selected anodes.

The surface areas determined for the pure, unstabilized cobalt anodes were significantly higher than those of the unstabilized nickel anodes. These results are consistent with observations made during scanning electron microscopy (SEM) analysis of fractured anode surfaces. As shown in the typical SEM micrographs of nickel and cobalt materials in Figures 1.1 and 1.2, the cobalt anode microstructure consists of significantly finer particulate chains than does that of nickel. The addition of fine nichrome, chromium, or tungsten carbide stabilizing particles to the cobalt structure increased the measured surface areas even further.

Specimens from selected areas of each 15.2 x 15.2 cm (6 x 6 in.) anode and cathode plaque were also prepared for characterization by quantitative microscopy. After impregnation of the porous structures with epoxy, electrode cross sections were ground with 240, 320, 400, and 600-grit SiC abrasive paper and polished with 1μ diamond paste. Care was taken during this metallographic preparation to minimize rounding of particle edges and loss of material through pulling out. The polished surfaces were then viewed at 1600X magnification using an oil immersion objective lens. From a statistical analysis of the number of particle intersections with a circular probe, it was possible to determine particle surface area per unit volume, porosity, mean intercept length in the solid, and mean intercept in the porosity, as well as the standard deviation in each of these quantities. The use of this technique for the evaluation of porous electrodes has been discussed by Johnson.[4] The results of these QM analyses also appear in Table 1.1. Figures 1.3 and 1.4 show the comparisons between the electrode porosity and mean pore size as determined by mercury porosimetry versus quantitative microscopy. There are obvious systematic differences between these two measurement techniques. The porosity values determined by mercury porosimetry were generally larger than those found by QM, while the mean pore sizes measured by porosimetry were smaller than the QM values. As shown in Figure 1.5, QM surface areas were consistently and systematically smaller than those determined by the B.E.T. method.

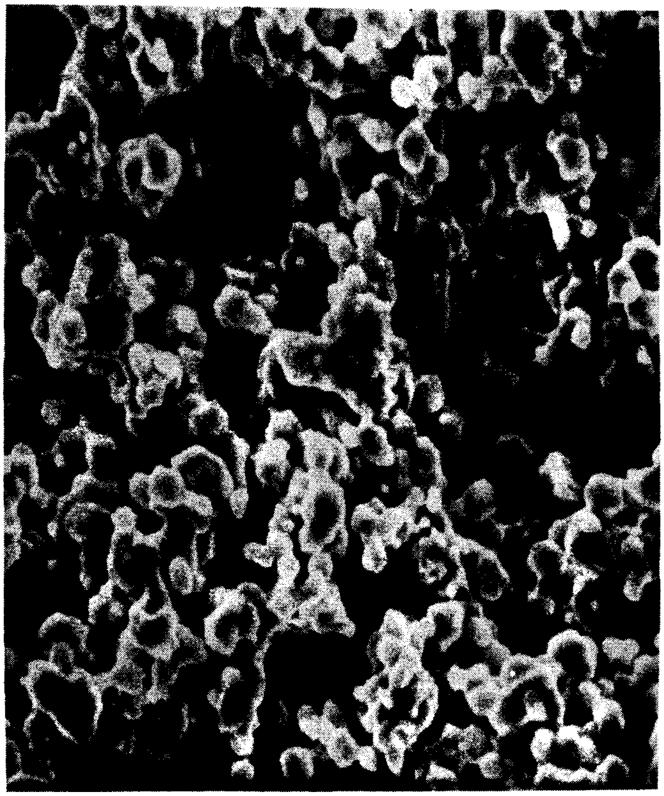

Figure 1.1. TYPICAL MICROSTRUCTURE OF UNSTABILIZED NICKEL ANODE AS SHOWN BY SEM (2000X) (Electrode Plaque 480-31-42, 5.7μ Mean Pore Size)

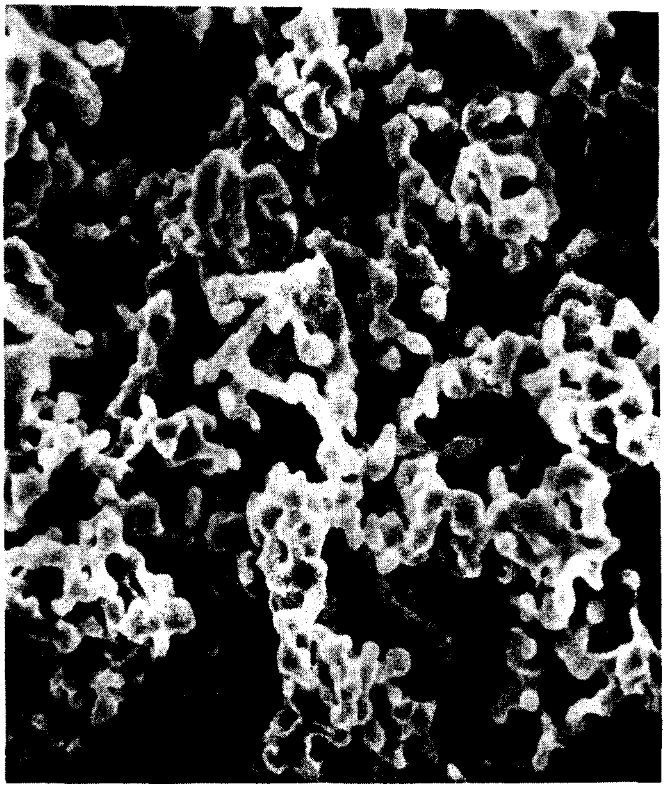

Figure 1.2. TYPICAL MICROSTRUCTURE OF UNSTABILIZED COBALT ANODE AS SHOWN BY SEM (2000X)
(Electrode Plaque 480-31-62, 4.1μ Mean Pore Size)

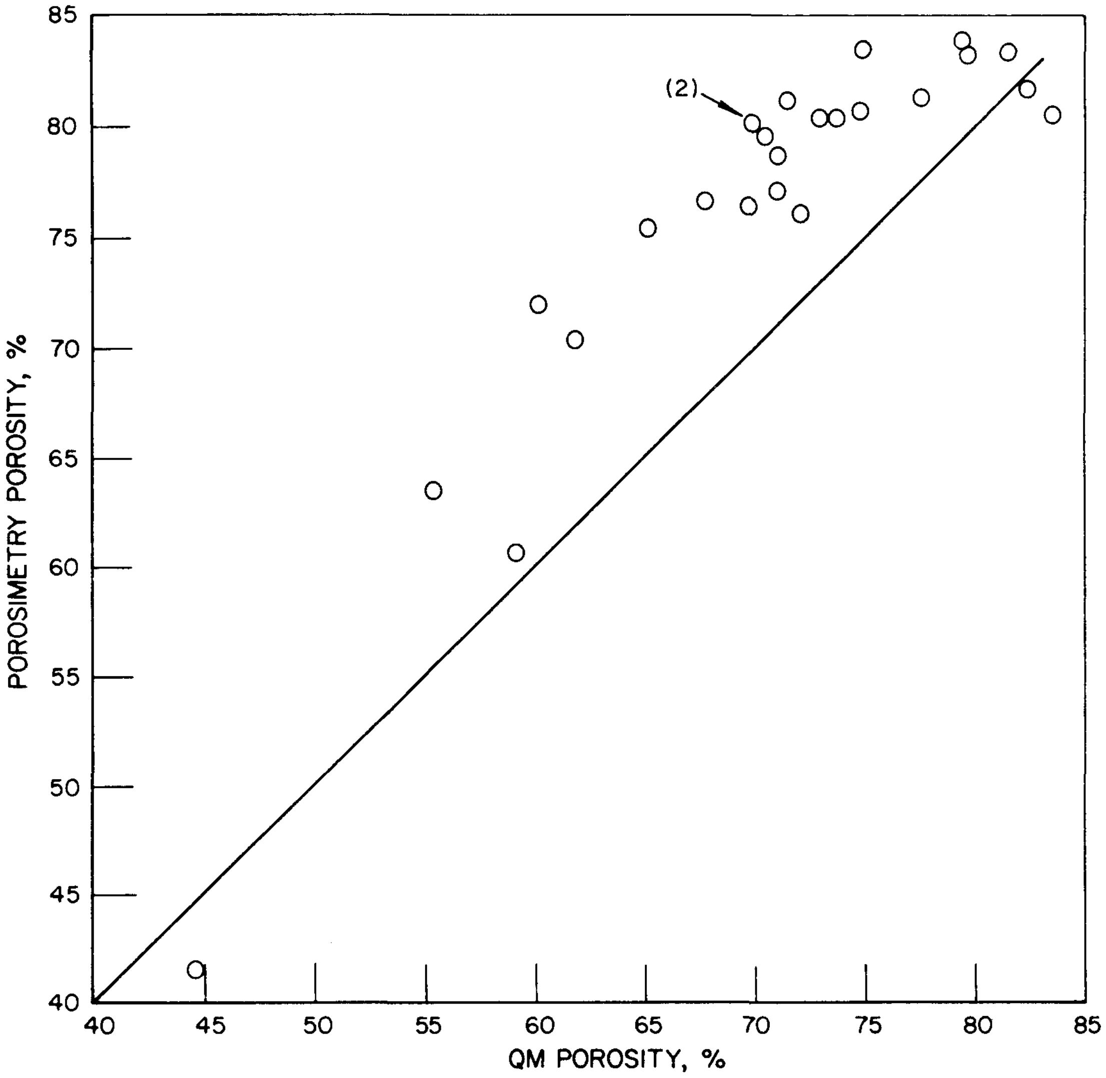

A79020454

Figure 1.3. COMPARISON OF ELECTRODE POROSITIES MEASURED BY MERCURY POROSIMETRY AND QUANTITATIVE MICROSCOPY

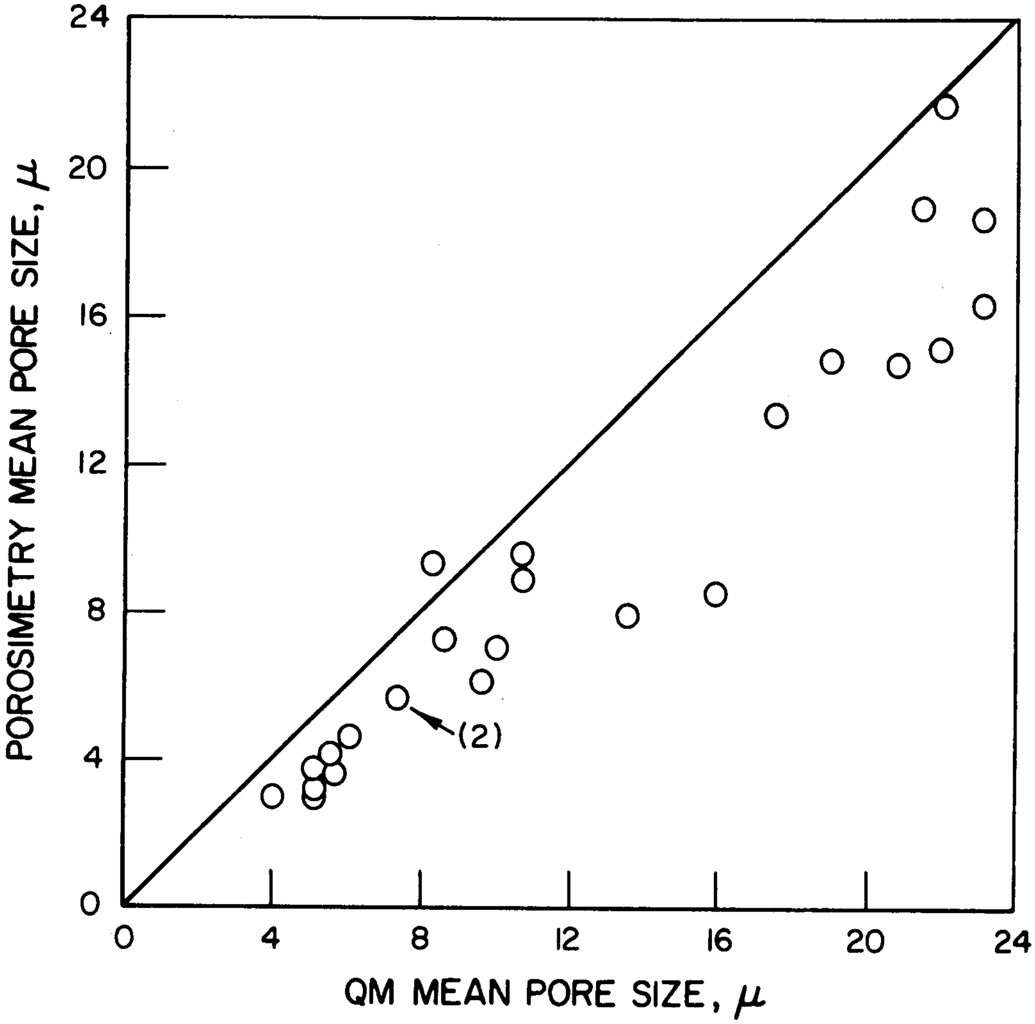

A79020480

Figure 1.4. COMPARISON OF ELECTRODE MEAN PORE SIZES MEASURED BY MERCURY POROSIMETRY AND QUANTITATIVE MICROSCOPY

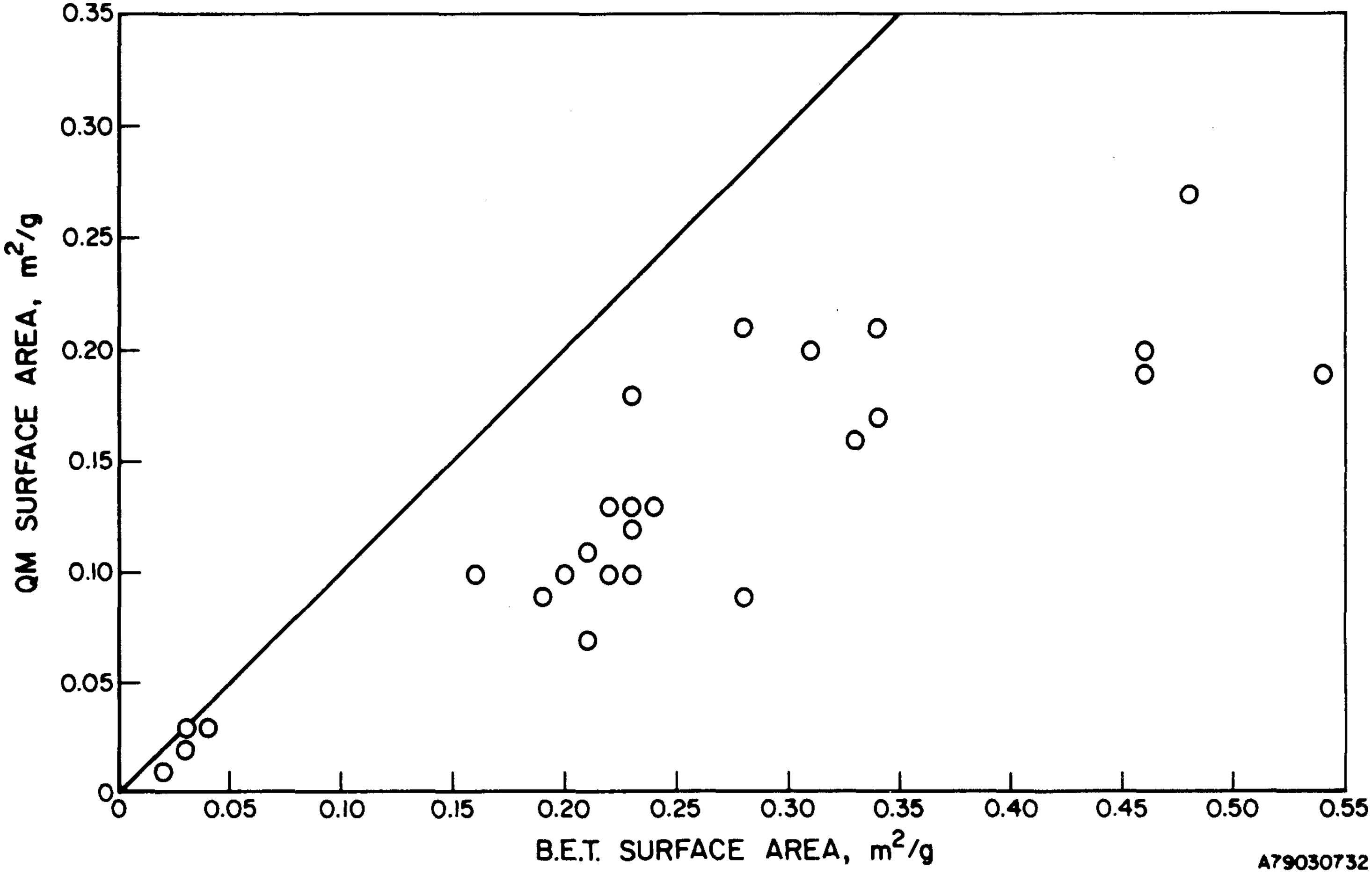

Figure 1.5. COMPARISON OF ELECTRODE SURFACE AREAS MEASURED BY B.E.T. GAS ADSORPTION AND QUANTITATIVE MICROSCOPY

Pore size distributions measured on samples of the as-received Co-10% Cr anode plaques are shown in Figure 1.6. Plaque-to-plaque structural variations were within acceptable limits, and a reasonably uniform chromium distribution was achieved during fabrication. This anode material demonstrated the best cell performance and stability of those tested and was thus used in most of the electrolyte tile performance tests to be discussed under Task 2.

1.1.1.2. Characterization of Anodes After Cell Testing

Quantitative microscopy analyses were performed on anode electrodes from laboratory-scale cells operated for the purpose of testing both these developmental electrodes as well as tile materials. (Cell performance results are discussed under Task 2.) Anodes of cobalt and nickel — pure or with a 10 wt % addition of sintering inhibitor — were analyzed by QM to observe the structural changes occurring in the various materials under actual cell testing conditions. The types of anode materials evaluated included Ni, Co, Co-10% Cr, and Co-10% WC. The structural stabilities of these anodes were then correlated with cell performance level and stability.

The results of QM analyses on anodes from terminated cells are presented in Table 1.2. The surface area, porosity, mean intercept length in pores ($\bar{\ell}_p$), and the mean intercept length in the solids or particle size ($\bar{\ell}_s$) of the as-received and of the cell electrodes are shown on this table. The last two columns, the percent surface area loss and the ratio of final-to-initial particle size, refer to changes of the electrode during cell operation and indicate the relative structural stability. The results for the solid area refer to the changes occurring under the solid portion of the perforated-plate anode current collector and those for the open area refer to the changes occurring under the holes of this type of anode current collector. The anode structure under both the solid and open portions of the current collector was studied because the compressive stresses applied to the anode in the hole regions (as a result of the cell holding force) are significantly less than those under the solid regions. The higher stresses under the solid regions often manifest themselves by enhanced anode densification and sintering.

As seen in Table 1.2, the pure nickel and cobalt anodes showed relatively poor structural stability. Under the open area the nickel showed a 24% reduction in surface area as a result of particle growth by sintering. The

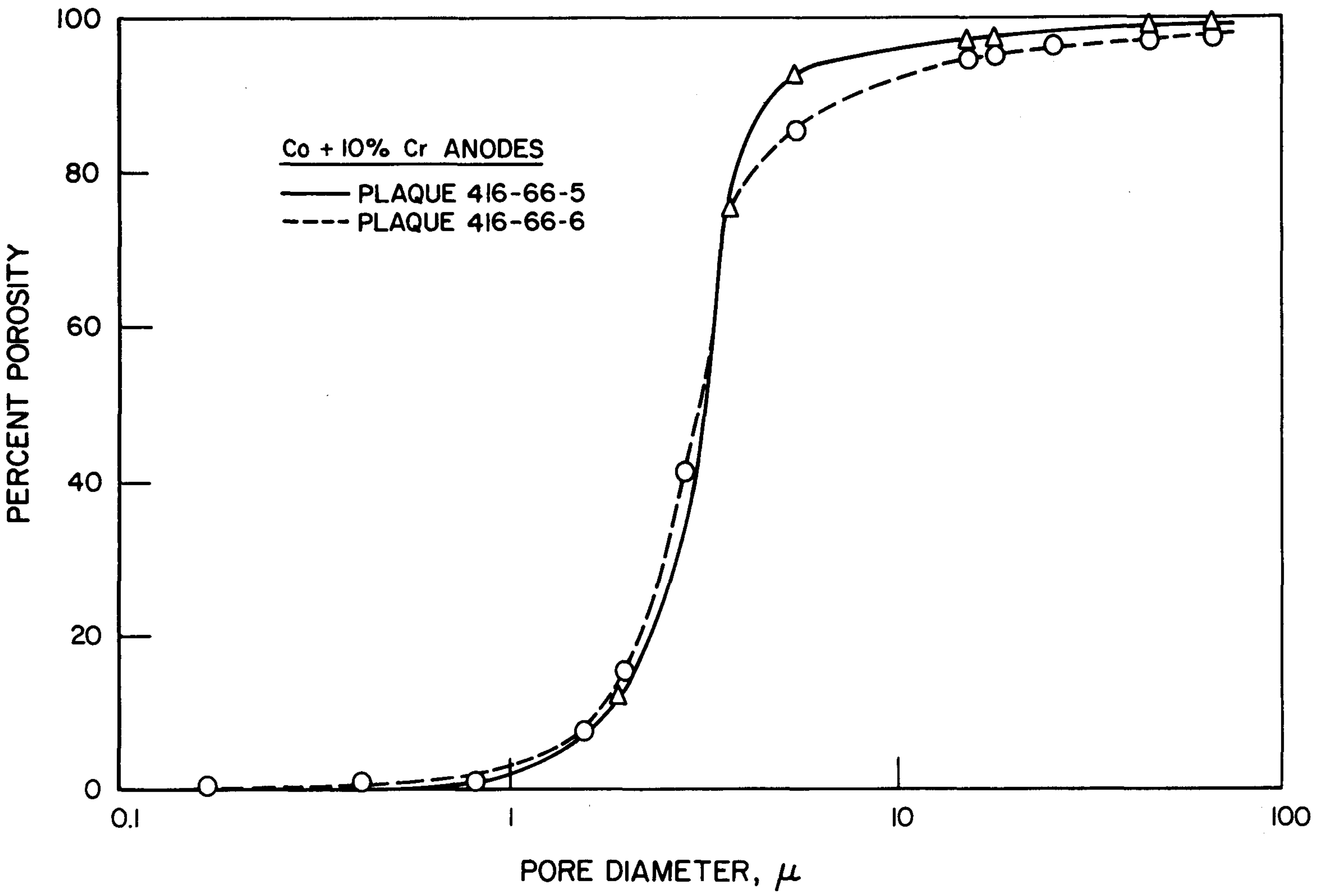

A79020469

Figure 1.6. PORE SIZE DISTRIBUTIONS OF Co-10% Cr ANODES MEASURED BY MERCURY POROSIMETRY

Table 1.2. QUANTITATIVE MACROSCOPY ANALYSES OF ANODES AFTER CELL TESTING

Material and Test Duration†	Surface Area m^2/g	Porosity, %	Mean Intercept Length μ Pores(ℓ_p)	Mean Intercept Length μ Solids(ℓ_s)	Surface Area Loss, %	Relative Final Particle Size $\bar{\ell}_s$ Final / $\bar{\ell}_s$ AR*
Ni (480-31-36)						
624 Hrs (DOE-2)						
As-Received (AR)	0.131	79.8	13.6	3.4	-	-
Solid Area	0.076	44.1	4.7	6.0	42.0	1.75
Open Area	0.099	67.8	9.6	4.6	24.0	1.34
Co (48-31-62)						
1320 Hrs (DOE-10)						
As-Received	0.200	71.2	5.6	2.2	-	-
Solid Area	0.066	35.8	3.8	6.8	67.0	3.1
Open Area	0.096	71.4	1.8	4.7	52.0	2.1
Co - 10% NiCr (416-66-3)						
2040 Hrs (DOE-3)						
As-Received	0.265	74.8	5.10	1.7	-	-
Solid Area	0.074	29.5	2.6	6.1	72.1	3.60
Open Area	0.211	77.8	7.6	2.1	20.4	1.26
1824 Hrs (DOE-8)						
Solid Area	0.122	35.0	2.0	3.7	54.0	2.19
Open Area	0.124	57.5	5.0	3.7	53.2	2.18
Co - 10% Cr						
3024 Hrs (DOE-5)						
As-Received (416-66-6)	0.192	67.8	5.1	2.4	-	-
Solid Area	0.159	49.1	3.6	3.1	17.2	1.29
Open Area	0.195	68.6	5.5	2.5	- 1.6	0.74
1992 Hrs (DOE-4)						
As-Received (416-66-5)	0.205	70.0	5.2	2.2	-	-
Solid Area	0.201	62.6	4.1	2.5	2.0	1.16
Open Area	0.207	70.6	5.7	2.4	- 1.0	1.09
Li/Na/K Off-Eutectic						
672 Hrs (DOE-12)						
Solid Area	0.389	67.8	2.7	1.3	- 89.8	0.59
Open Area	0.459	78.0	3.8	1.1	-139.9	0.50
75% Li/25% K Electrolyte						
648 Hrs (DOE-13)						
Solid Area	0.247	62.7	3.4	2.0	- 20.5	0.91
Open Area	0.481	83.4	5.2	1.0	-134.6	0.47
Li/Na Electrolyte						
504 Hrs (DOE-15)						
Solid Area	0.308	72.8	4.3	1.6	- 50.2	0.73
Open Area	-	-	-	-	-	-
Co - 10% WC (416-66-1)						
1272 Hrs (DOE-11)						
As-Received	0.166	70.0	6.1	2.6	-	-
Solid Area	0.033	13.3	2.0	13.6	80.1	5.1
Open Area	-	-	-	-	-	-

---

* As-Received

† Electrolyte composition = 62 Li/38 K unless otherwise indicated.

smaller mean intercept in the pores after cell testing was associated with a lower porosity. The results for the solid area indicate that the holding force applied to the cell greatly accelerated the sintering process — a 42% surface area reduction was observed after only 624 hours of operation. The particles under the solid area were almost double their original size, the mean pore size was substantially smaller, and porosity had decreased from 79.8% to 44.1%. The relative losses of surface area and porosity in the pure cobalt anode were as high as, or higher than, those of pure nickel, in that the initial surface area was higher (0.20 m^2/g for Co versus 0.13 m^2/g for Ni) and the particles were smaller (2.2μ for Co versus 3.4μ for Ni). These results indicate poor structural stability and explain the low performance and poor stability observed in cells DOE-2 (nickel anode) and DOE-10 (cobalt anode).

Of the sintering inhibitors used, (nichrome, tungsten carbide, and chromium) only chromium proved to be effective. Cobalt-10% chromium anodes were used in cells DOE-5 (operated 3024 hours) and DOE-4 (operated 1992 hours) and yielded good cell performance and stability. Comparison of the changes of the pure cobalt electrode (Cell DOE-10) with those of the Co-10% Cr showed that the addition of 10% Cr provided good structural stability, even under the solid areas of the current collector where the holding force applied to the cell creates the highest stress levels.

The structural stability of this anode material correlates with the good and stable performance observed in cells assembled with Co-10% Cr anodes. In fact, while the pure cobalt anode under the open area showed a 52.0% surface area reduction and a doubling of the mean particle size, the Co-10% Cr of Cells DOE-4 and DOE-5 showed 1.0% and 1.6% surface area increases, respectively, and the particle size either did not change or had a tendency to decrease (relative final-to-initial particle size of 0.74 in DOE-5). The changes of the Co-10% Cr observed under the solid area were small (2% to 17% surface area loss and 1.16 to 1.29 relative particle size increase). The very good structural stability of the Co-10% Cr anode observed after 3024 hours of operation in Cell DOE-5 is illustrated in the optical micrographs of polished cross sections in Figure 1.7. The appearance of the cell-tested anode under the solid and open areas of the current collector are compared with the as-fabricated microstructure in this series of micrographs.

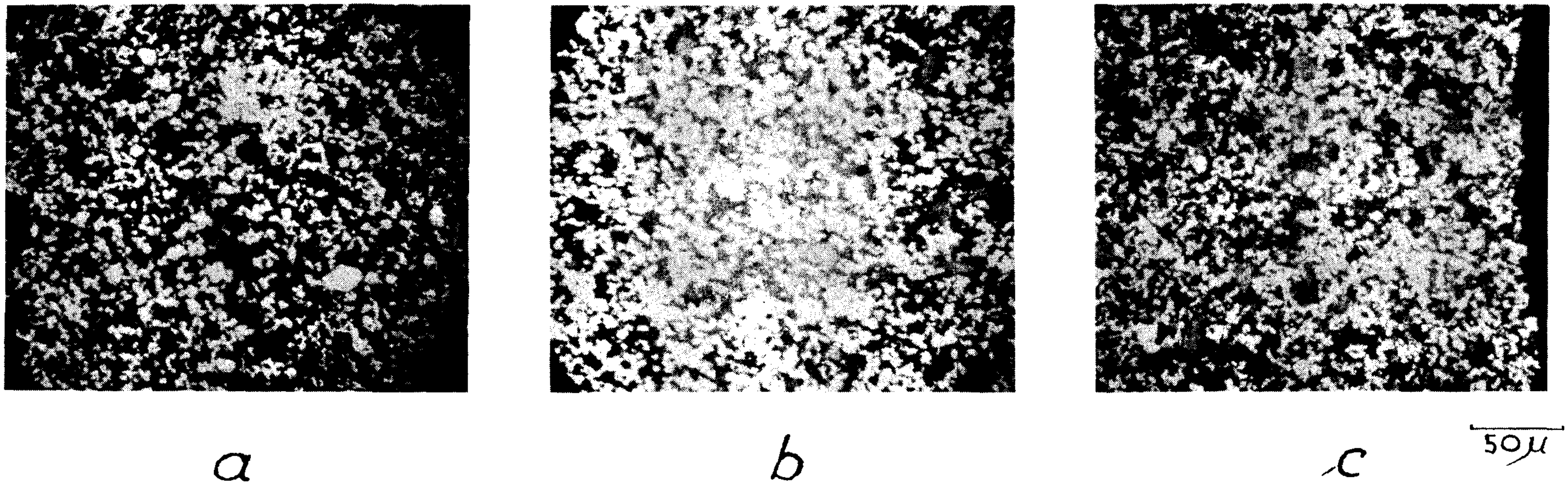

Figure 1.7. STRUCTURAL STABILITY OF THE Co-10% Cr ANODE OF CELL DOE-5, OPERATED FOR 3024 HOURS. a) AS-RECEIVED STRUCTURE. b) CENTRAL PORTION UNDER A CURRENT COLLECTOR HOLE. c) ELECTROLYTE SIDE UNDER THE SOLID AREA OF THE CURRENT COLLECTOR

A Co-10% Cr anode was also used in cells assembled with electrolytes different from the standard 62 mole percent $LiCO_3$/38 mole percent K_2CO_3 composition. The structural changes observed in the anodes of these cells also indicated that a surface area increase and a breaking-up of the particles may be occurring in the Co-10% Cr electrode. As seen in Table 1.2, the anode of Cell DOE-12, assembled with a ternary off-eutectic electrolyte and operated for 672 hours, showed a very large increase in surface area (124% in the open area, 90% in the solid area) and the particles decreased to half the original size. Similar increases in surface area and breaking-up of particles were observed in cell DOE-13, assembled with a 75 mole percent Li_2CO_3/25 mole percent K_2CO_3 electrolyte and operated for 648 hours, and in cell DOE-15, assembled with a Li_2CO_3/Na_2CO_3 electrolyte and operated for 504 hours. Cells DOE-12, DOE-13, and DOE-15 showed better performance than the average shown by cells assembled with the standard electrolyte.

As stated above, chromium was the only sintering inhibitor that proved effective. Both nichrome and tungsten carbide additives were ineffective against anode sintering. The surface area loss and particle growth observed in Cells DOE-3 and DOE-8, assembled with a Co-10% NiCr anode, were approximately the same as those for pure Co (20% to 53% surface area loss and 1.26 to 2.15 relative particle size versus 52% and 2.1 for pure cobalt). The surface area loss and particle growth of the Co-10% WC anode were even greater than those of the pure cobalt anode. Cells assembled with Co-10% NiCr anode showed low performance but were more stable than those assembled with pure Co anodes.

Cells assembled with Co-10% WC anode material showed extremely poor and erratic performance. Examination of the as-received Co-10% WC anode structure by SEM and energy-dispersive X-ray analysis revealed significant inhomogeneities in the distribution of the WC additive. Discussions with the electrode fabrication group at Gould Laboratories indicated that experimental difficulties were encountered in manufacturing these plaques because of agglomeration of the WC particles. Because of the resultant inferior anode structures and associated poor cell performance, the Co-10% WC material was not studied extensively.

The results observed with the Co-10% Cr anode indicate that chromium is effective in preventing structural changes during cell operation and that long-term stable performance may be obtained. The mechanism of sintering retardation by chromium is not fully understood. It is recognized that chromium is not stable as the metal in the anode environment, but is likely converted into Cr_2O_3 or $LiCrO_2$. The distribution of these second-phase chromium-containing oxide particles throughout the porous metal matrix apparently acts to retard the sintering of the cobalt by reducing diffusion. However, more detailed surface characterizations of as-fabricated and cell-tested anodes are needed to more clearly elucidate the mechanisms involved and to explain the increases in surface area and cobalt particle breakup observed for the Co-10% Cr materials.

1.1.1.3. Compressive Deformation of Porous Anodes

It is generally observed in metallographic cross sections from terminated cells that a noticeable amount of anode deformation has occurred under the solid portions of the perforated plate current collector as a result of the compressive cell-holding forces. The resulting compressive stresses can cause both gross compressive deformation of the anode plaque and accelerate particle growth by sintering. Because of the importance of this problem to long-term anode stability in an operating cell stack, some scoping experiments were performed to investigate anode compressive deformation behavior.

Anode specimens 0.75 inch in diameter x 0.03 inch thick were punched from the 6 x 6-inch plaques and tested under compressive loading in an Instron Universal testing machine.* The specimens were held between two cylindrical stainless steel platens situated in the cavity of a resistance-heated tube furnace. The temperature of the specimen was maintained at 650°C and continuously monitored by a thermocouple. A rapid purge of high-purity argon was continually passed through the furnace cavity in an effort to avoid oxidation of the anode samples. The Arinert gas blanket provided oxidation protection for the nickel-based samples but not for the cobalt-based materials. All of the cobalt-containing samples (Co, Co-10% Cr, Co-10% NiCr, and Co-10% WC) were severely oxidized because of the greater tendency of cobalt to oxidize in trace amounts of moisture or oxygen.

---

* Experimental work performed in the Metallurgical and Materials Engineering Department of the Illinois Institute of Technology, Chicago, Illinois.

Therefore, meaningful measurements were obtained only on the Ni and Ni-10% NiCr anode materials.

The compressive behaviors of Ni (5μ and 10μ nominal mean pore sizes from plaques 480-31-42 and 480-31-36, respectively) and of Ni-10% NiCr (5μ nominal mean pore size from plaque 416-71-4) were measured at a deformation rate of 0.02 inch/minute. This was the minimum crosshead speed for the Instron machine and corresponded to a strain rate of approximately 0.01 inch/inch-second. The compressive stress-strain behavior observed at 650°C for these materials is shown in Figure 1.8. The compressive strength at 650°C was found to decrease with increasing pore size of the electrode materials tested. Three samples were tested from 2 of the 3 plaques under evaluation, and reproducibility of the σ-ε curves was very good. For compressive stresses generated under typical cell-holding forces (<25 psi), strains at 650°C were in the 2% to 4% range. At higher stresses, the porous electrodes exhibited noticeable nonlinear deformation behavior, which may be suggestive of a "hardening" mechanism. However, detailed microstructural characterizations of these porous, sintered materials before and after testing are needed before the operating deformation mechanisms are identified and understood in detail.

An effort was made to study the compressive creep behavior of a nickel-based anode at 650°C under a constant, low stress. A sample of Ni from plaque 480-31-42 (5.7μ mps) was held under a constant stress of 20 psi for approximately 4 hours at 650°C under the Ar purge. After testing, however, the specimen was found to be partially oxidized and warped so that no meaningful information was obtained. Thus, it is evident that in order to adequately test Co and Ni anode materials at elevated temperatures, it is necessary to provide a better control of the gas environment than is possible with the present furnace design. We are investigating the possibility of obtaining a controlled-environment furnace chamber attachment for the Instron testing machine to provide this capability.

1.1.2. Tile Development

Introduction

The objective of this subtask was to develop an electrolyte tile having the characteristics ($LiAlO_2$ particle size distribution, surface area, thermal

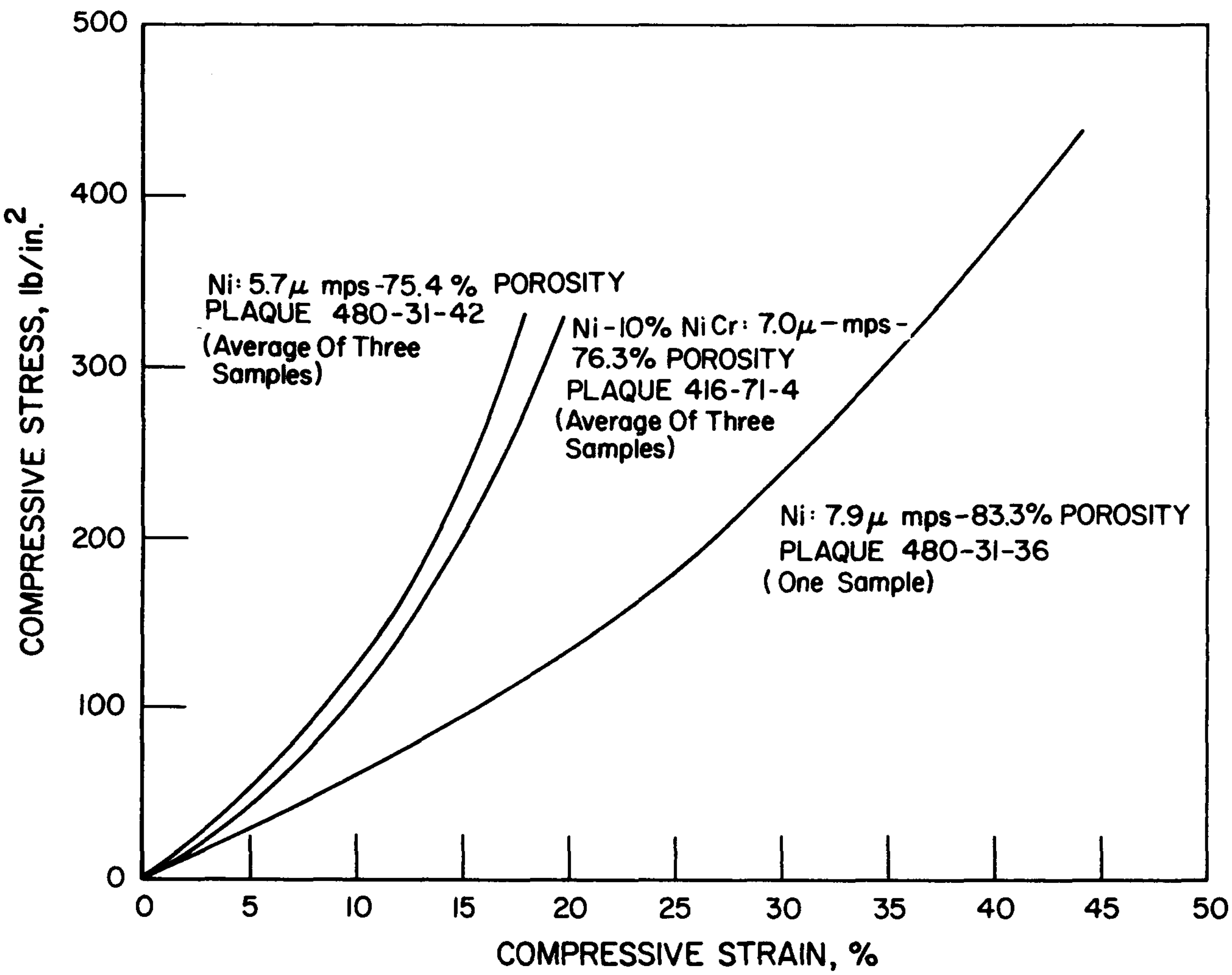

A79030492

Figure 1.8. COMPRESSIVE STRESS-STRAIN BEHAVIOR OF POROUS NICKEL-BASED ANODES AT 650°C IN HIGH-PURITY ARGON

expansion behavior, yield upon melting, etc.) required for high and stable cell performance when coupled with the electrodes developed under Subtask 1.1.1. The electrolyte tile is a composite material containing 45 weight percent $LiAlO_2$ and 55 weight percent lithium-rich carbonate eutectic composed of 62 mole percent Li_2CO_3/38 mole percent K_2CO_3. At a cell operating temperature of 650°C, this composition corresponds to approximately 62 volume percent molten carbonate and 38 volume percent $LiAlO_2$ (assuming a $LiAlO_2$ density of 2.6 g/cm^3).

Efforts were focused upon four areas of tile development: 1) electrolyte powder processing, 2) tile fabrication, 3) characterization of tiles and their aluminate and carbonate constituents, and 4) cell testing of developmental tiles coupled with both state-of-the-art and developmental electrodes.

The objectives of this task were met by developing an electrolyte processing procedure based on modification of the original aqueous slurry process studied at Argonne National Laboratory. The modified procedure was derived after a careful investigation of the various factors affecting the $LiAlO_2$ properties, tile thermomechanical behavior, and the ultimate performance in cells. Batches as large as 2500 grams have been prepared, and scale-up of the process for mass production of electrolyte powder appears to be feasible. Preliminary tests indicate a good potential for using the less expensive hydrated aluminas in place of Degussa "C" γ-Al_2O_3 that is presently used as starting material.

In this report, the effect of various processing parameters on the final electrolyte properties will be reviewed and the optimized process will be summarized. The physical and chemical stabilities of various $LiAlO_2$ products during out-of-cell tests will also be discussed.

1.1.2.1. Electrolyte Preparation and Characterization

The original aqueous slurry process, developed at Argonne National Laboratory,[5,6] involves suspension into an aqueous slurry of all the Li, K, and Al needed in the final electrolyte in the forms of $LiOH \cdot H_2O$, KOH, and Degussa "C" γ-Al_2O_3, respectively. The slurry is stirred at 80°C to obtain an intimate mixture and dried at 110°C in air. The dried slurry is then pulverized and reacted with CO_2 gas to convert the hydroxides to carbonate.

Finally, the powder is fired for 22 hours at 600°C to convert any unreacted Al_2O_3 to $LiAlO_2$ and to homogenize the mixture. (Details of the experimental procedure used during this program to evaluate this original slurry process are outlined in Appendix A, along with characterization data of the $LiAlO_2$ products obtained.) The product obtained by this procedure is β-$LiAlO_2$ (45% by weight) in a eutectic mixture of Li_2CO_3 and K_2CO_3 (Li:K = 62:38 on a molar basis). Although the $LiAlO_2$ particles have the rod-like morphology desired for good tile support, the particle sizes are too large and the surface area too low (less than 10 m^2/g) to be acceptable for good carbonate retention. Tiles pressed from such electrolytes slumped or deformed badly when subjected to our dilatometer thermal cycling test. Therefore, a study of the effects of different processing variables on $LiAlO_2$ particle characteristics was undertaken to improve electrolyte tile properties. Descriptions of the various electrolyte and tile characterization test methods used to evaluate these materials are presented in Appendix B.

1.1.2.2. Effects of Aqueous Slurry Processing Variables

The aqueous slurry method of electrolyte processing consists of four basic stages (Figure 1.9). There are a number of processing variables associated with each stage —

1. Mixing Stage
    a. Starting materials
    b. Chemical composition of the slurry
    c. Dispersing liquid
    d. Consistency of the slurry
    e. Mixing temperature
    f. Mixing time.
2. Drying Stage
    a. Temperature
    b. Time
    c. Extent of dryness.
3. Carbonation Stage
    a. Time and temperature
    b. Carbonation during slurry stage versus carbonation after drying.
4. High-Temperature Firing
    a. Time and temperature
    b. Electrolyte composition.

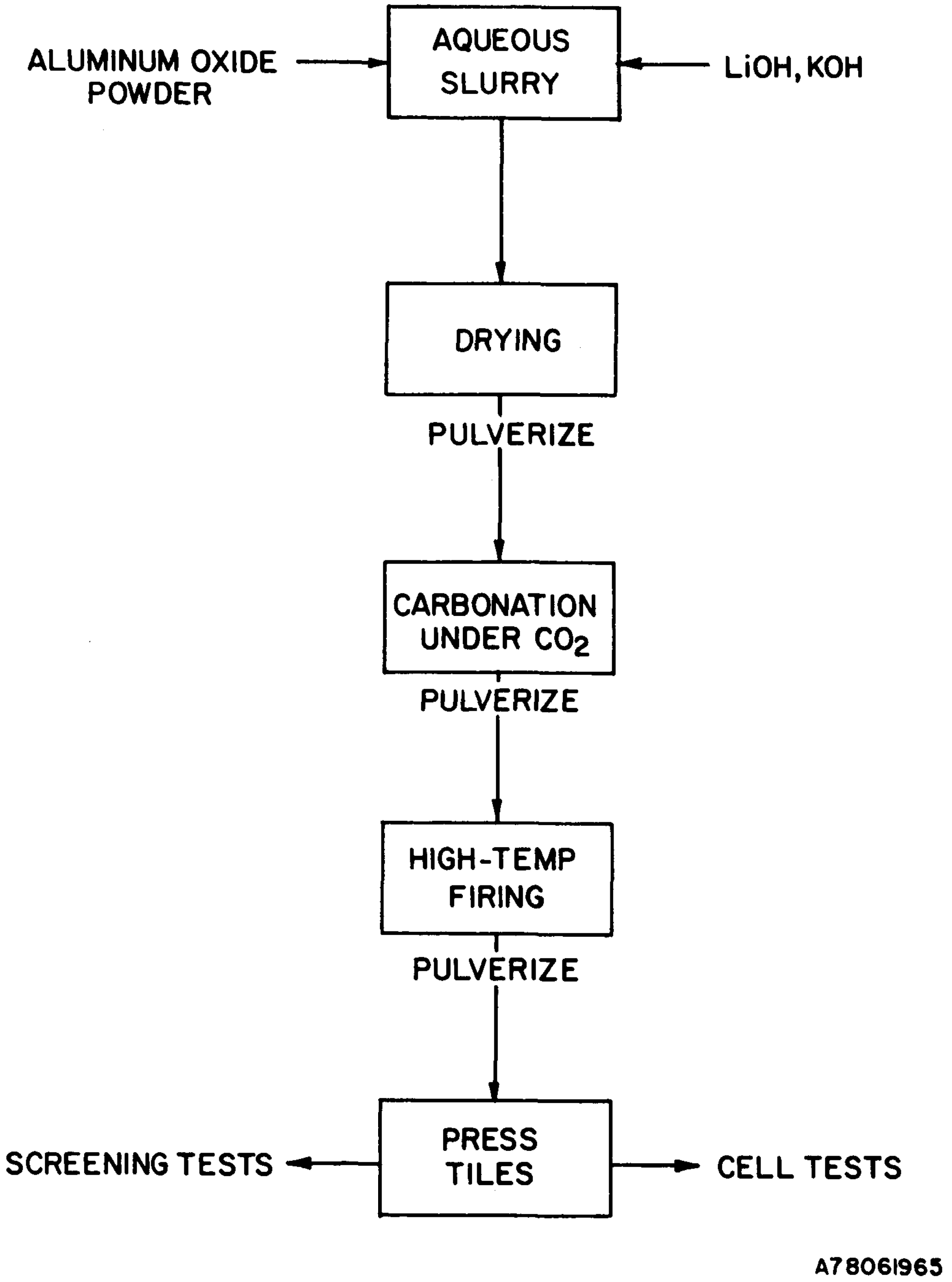

Figure 1.9. ELECTROLYTE POWDER PREPARATION BY THE AQUEOUS SLURRY PROCESS

To study the effect of each variable, our approach has been to vary the conditions related to that variable and then characterize the resulting electrolyte powder product. In the discussion that follows, results of these studies on each variable will be discussed in order with reference to Table 1.3, which summarizes the final properties of $Li_2CO_3/K_2CO_3/LiAlO_2$ electrolytes prepared by the slurry process.

1.1.2.3. Starting Materials

Cost is a significant factor in the choice of starting materials in any fuel cell scale-up effort. It would be desirable to use the low-cost hydrated aluminas* in place of the expensive Degussa gamma alumina (approximately \$3.00/lb) and the technical-grade alkali compounds in place of the purified reagent-grade hydroxides. With technical-grade alkali compounds, the effects of impurities and anionic constituents should be taken into consideration, although this was not within the scope of the current program. Since the cost of Degussa alumina used in the conventional process has a striking effect on the cost of the final electrolyte, preliminary experiments were performed to investigate the possible use of lower-cost aluminas in the process.

Three electrolyte batches, namely, AD55-1A, AC55-1A, and AR55-1A were prepared from Degussa "C" Al_2O_3 (γ-Al_2O_3), Conoco Catapal SB hydrated alumina (Boehmite, or α-$Al_2O_3 \cdot H_2O$), and Reynolds RH-33 hydrated alumina ($Al_2O_3 \cdot 3H_2O$ or $Al(OH)_3$), respectively, following the original method. Analytical results of these electrolytes (presented in Appendix A) indicated that the formation mechanism of β-$LiAlO_2$ is the same for all three Al_2O_3 materials studied. Therefore, it appears likely that lower cost aluminas can be used in the slurry process for producing electrolytes. However, since all three electrolytes failed our dilatometer screening test because of significant yielding behavior, it was decided to modify the original process in order to produce a more acceptable carbonate-retaining electrolyte, capable of producing good cell performance. Because of our extensive electrolyte processing experience with Degussa alumina, we used it as the starting material in all subsequent

---

* Cost of Alcoa Grade C-33 hydrated alumina $Al(OH)_3$ is \$0.085/lb based on a quantity of at least 45,000 lbs, effective January 1979.

Table 1.3. PROPERTIES OF Li_2CO_3-K_2CO_3-$LiAlO_2$ ELECTROLYTE BATCHES PREPARED BY AQUEOUS SLURRY PROCESS

	Electrolyte Composition				LiAlO Properties		
Electrolyte	$LiAlO_2$	Li_2CO_3	K_2CO_3	Carbonate Molar Ratios, Li:K	Phase Composition $\alpha - \beta - \gamma$, %	Surface Area m^2/g	Purpose of Preparation
AD55-1A	40.8	28.9	30.2	1.792	0/100/0	7.5	To study $LiAlO_2$ formation mechanism in original aqueous slurry process.
AD55-2A	45.0	26.2	28.8	1.701	53/47/0	20.2	To study effect of eliminating K from slurry step.
AD55-2B	----	not available		----	71/29/0	23.1	To determine if carbonate composition affects $LiAlO_2$ development during the 600°C firing.
AD55-2C	49.9	35.2	14.9	4.441	22/78/0	17.4	Scale-up K-free slurry process to 900 g batch.
AD55-2D	44.1	26.7	29.2	1.711	29/71/0	19.6	Scale-up K-free process to 2500 g batch for use in cost effective tile development.
AD55-2E	44.9	25.2	29.9	-1.573	30/70/0	25.2	2500 g of electrolyte by K-free process for use in lab- and bench-scale cell testing.
AD55-3A	47.6	24.4	28.0	1.634	1/99/0	7.4	To determine effect of Li concentration in slurry on $LiAlO_2$ formation.
AD55-3B	----	not available		----	1/99/0	7.7	
AD55-5A	46.4	25.0	28.6	1.637	85% α 15% $(\beta+\gamma)$	111	To investigate acetic acid as an alternate slurry dispersing liquid.
AD55-6A	45.7	25.5	28.8	1.664	0/100/0	13.5	To determine effect of slurry drying rate on $LiAlO_2$ particle size and morphology.
AD55-8A	45.8	23.6	30.6	1.442	24/76/0	15.9	To determine effect of Li_2Co_3:K_2CO_3 ratio on $LiAlO_2$ development during 600°C firing.
AD55-9A	45.5	24.6	33.4	1.38	34/66/0	22.1	To reproduce AD55-2A.
AD55-10A	38.1	28.4	33.5	1.573	15/85/0	25.0	To determine effect of Li_2CO_3:K_2CO_3 on $LiAlO_2$ development during the 600°C firing.
AD55-12A	48.9	19.0	32.0	1.113	27/59/14	13.4	To determine feasibility of controlling $LiAlO_2$ particle size by freeze drying of slurry.
AC55-1A	----	not available		----	0/100/0	11.1	To investigate feasibility of using low-cost hydrated alumina (Boehmite) as starting material.
AR55-1A	----	not available		----	0/100/0	Not available	To investigate feasibility of using low-cost $Al(OH)_3$ as starting material.

electrolyte development studies. Further development with more cost-effective aluminas was deferred pending successful development of Degussa-derived electrolytes.

1.1.2.4. Chemical Composition of the Slurry

It was demonstrated in our initial experiments that β-$LiAlO_2$ was formed during the slurry reaction stage, most likely by a dissolution-precipitation process. Therefore, the composition of the starting mixture was expected to be a very important factor in the process. The slurry conditions may, in principle, affect both the crystal morphology and phase composition of the final $LiAlO_2$ particles. Thus, the effect of the Li/K ratio in the starting slurry mixture on the final $LiAlO_2$ properties was determined. For this purpose, Electrolytes AD55-2A and AD55-7A were prepared, starting with mixtures having Li/K ratios different from the conventional starting composition used in Electrolyte AD55-1A. In these electrolytes, all the required Li and Al were added to the slurry as $LiOH \cdot H_2O$ and Degussa alumina, respectively. Only the amount of K as KOH in the slurry was varied. The necessary makeup potassium was added as K_2CO_3 after the slurry had been dried and carbonated, but before the 600°C firing. The starting composition and characterization of Electrolytes AD55-1A, AD55-2A, and AD55-7A at different stages of electrolyte processing are presented in Table 1.4. It shows that the intermediate reaction products in the slurry and the $LiAlO_2$ in the final electrolyte were significantly different between batches AD55-1A and AD55-2A. When all the K required in the electrolyte was added to the slurry as KOH (Electrolyte AD55-1A), rod-like β-$LiAlO_2$ formed readily in the slurry stage (Figure 1.10), and the $LiAlO_2$ particles remained essentially unchanged in morphology after the 600°C firing (Figure 1.11), although some particle growth did occur. Its surface area of 7.5 m^2/g, however, is considered too low to sufficiently hold the molten carbonate in the tile structure and to prevent the electrolyte tile from deforming when subjected to nominally low compressive loading (3 psi) in the dilatometric test. On the other hand, when the slurry is potassium free (Electrolyte AD55-2A), the reaction products formed in the slurry consisted of β-$LiAlO_2$ and a hydrated lithium-aluminum oxide compound. On the basis of chemical and gravimetric analyses, this hydrate was found to correspond to the chemical formula $Li_2O \cdot 2Al_2O_3 \cdot 11H_2O$ cited by Lileev <u>et.al.</u>[7], although the X-ray diffraction pattern matched that of $Li_2O \cdot Al_2O_3 \cdot yH_2O$ given

Table 1.4. PROPERTIES OF ELECTROLYTES PREPARED FROM STARTING MATERIALS OF DIFFERENT COMPOSITIONS

Electrolyte	Starting Materials*	Aℓ Containing Compound Dried Slurry	Material Added Before 600°C Firing	Final $LiAlO_2$ Analysis: Surface Area, m^2/g	Final $LiAlO_2$ Analysis: $\alpha/\beta/\gamma$	Behavior During Dilatometer Test
AD55-1A	100% Li and Aℓ for $LiAlO_2$ 100% Li for Li_2CO_3 100% K for K_2CO_3	Rod-like β-$LialO_2$	None	7.5	0/100/0 (rod-like structure)	Slumped upon melting
AD55-2A	100% Li and Aℓ for $LiAlO_2$ 100% Li for Li_2CO_3 0% K for K_2CO_3	β-$LialO_2$ + Hydrated Li & Aℓ compound	Makeup K_2CO_3	20.7	53/47/0 (porous aggregate of polyhedral structure)	Slumped slightly upon melting
AD55-7A	100% Li and Aℓ for $LiAlO_2$ 100% Li for Li_2CO_3 50% K for K_2CO_3	Not analyzed	Makeup K_2CO_3	10.8	4/96/0 (structure not determined)	Slumped upon melting

*Numbers indicate percentage of materials required in final electrlytes' Li as $LiOH \cdot H_2O$, K as KOH, and Aℓ as γ-Al_2O_3.

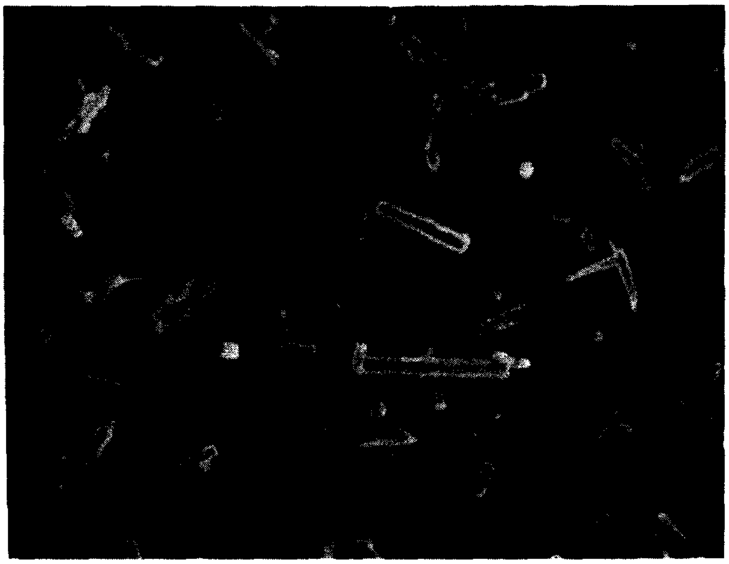

Figure 1.10. SEM MICROGRAPH OF $LiAlO_2$ PARTICLES WASHED FROM DRIED SLURRY OF ELECTROLYTE AD55-1A (5000X)

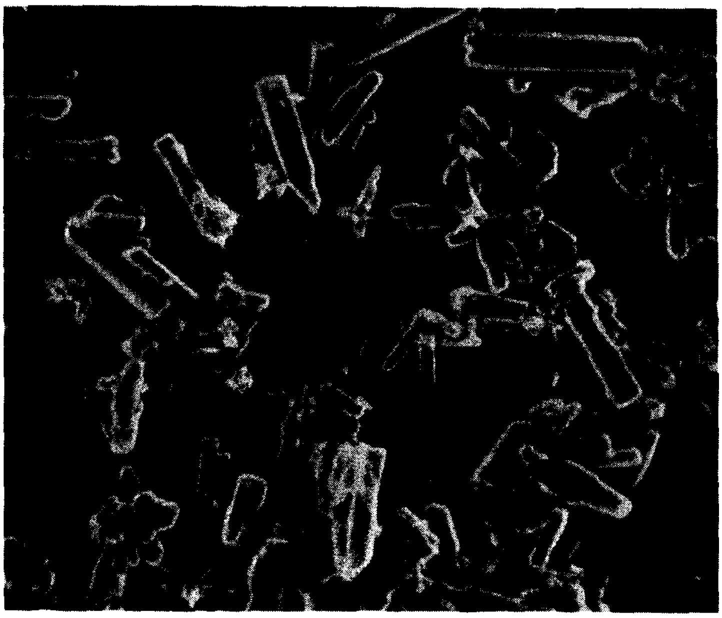

Figure 1.11. SEM MICROGRAPH OF $LiAlO_2$ PARTICLES WASHED FROM FINAL ELECTROLYTE AD55-1A (5000X)

in the X-ray diffraction File Card No. 20-618. It is believed that a significant fraction of this hydrate is transformed to α-$LiAlO_2$ in the subsequent firing. Thus, the final $LiAlO_2$ formed from the K-free slurry is a mixture of the α and β phases. The microstructure (Figure 1.12) consists of aggregates of polyhedral particles with relatively high surface area (20.7 m^2/g). No other type of morphology is distinguishable from the micrograph, although two $LiAlO_2$ phases, the α and the β, were identified by X-ray diffraction.

Electrolyte AD55-7A was prepared by adding to the slurry only half of the K (as KOH) required for the K_2CO_3 in the final electrolyte product. Analysis of the final $LiAlO_2$ from this electrolyte batch (Table 1.4) indicated minor formation of α-$LiAlO_2$ and increased surface area over the $LiAlO_2$ in Electrolyte AD55-1A prepared by the original aqueous slurry method. The increased surface area, however, still was not sufficient to hold the carbonate and the tile slumped during the thermal cycling test. However, it appeared that $LiAlO_2$, with properties intermediate between those exhibited by the $LiAlO_2$ from Electrolytes AD55-1A and AD55-2A and possessing acceptable carbonate retention behavior, could be obtained by adding less than half of the required K as KOH to the slurry.

1.1.2.5. Non-Aqueous Dispersing Liquid

Use of a non-aqueous dispersing liquid in the initial stage of preparation may result in a different type of $LiAlO_2$ formation reaction, and hence, different $LiAlO_2$ properties. Unfortunately, there are very few organic solvents (such as, methanol and acetic acid) that dissolve alkali hydroxides. One can, however, consider carbonates and perhaps nitrates in addition to the hydroxides as alkali sources.

Electrolyte AD55-5A was prepared using glacial acetic acid as the dispersing liquid instead of water. The detailed processing of this electrolyte has been discussed in the Project 9105 Second Quarterly Report. Analysis of the $LiAlO_2$ after the 600°C firing indicated 85% as α-phase and the remainder as β-phase. The surface area measured was 111 m^2/g and was consistent with significant α-$LiAlO_2$ diffraction peak broadening observed from the X-ray diffraction pattern, each of which indicated very fine α-$LiAlO_2$ crystallites. The thermal cycling behavior of a tile pressed from this electrolyte powder

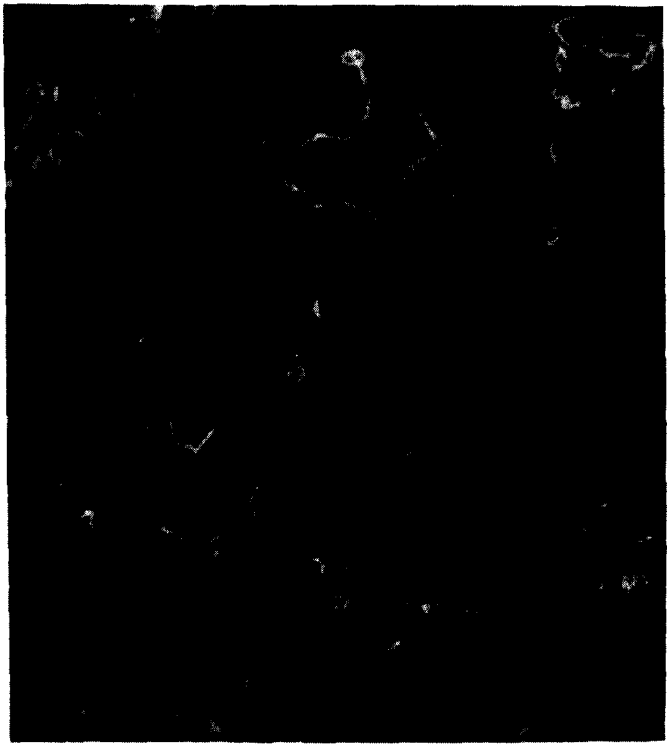

Figure 1.12. SEM MICROGRAPH OF $LiAlO_2$ WASHED FROM ELECTROLYTE AD55-2A (20,000X)

was unusual in that the tile expanded significantly, rather than yielding, after the carbonate became molten. Analysis of the thermal cycling test tile showed insignificant changes in $LiAlO_2$ composition, but the surface area was drastically reduced to 17.8 m^2/g. Similar changes were also observed when the electrolyte powder was subjected to additional heat treatments of 50 hours at 685°C and 48 hours at 650°C. The $LiAlO_2$ composition remained essentially unchanged but the surface area was reduced to 16.4 m^2/g. Thus, the tile expansion behavior observed when the carbonate melted was apparently related to a $LiAlO_2$ crystal growth process and associated surface area reduction.

1.1.2.6. Slurry Mixing Temperature

Several electrolyte powders with the standard carbonate composition (62 mole percent Li_2CO_3/38 mole percent K_2CO_3) were prepared to study the effect of slurry reaction temperature on resulting $LiAlO_2$ properties. Batch AD55-14 was processed according to the standard procedure of dissolving $LiOH \cdot H_2O$ in distilled water and reaction with Degussa γ-Al_2O_3 at a temperature of between 75° and 80°C for 1 hour. During the preparation of batch AD55-15 with the same starting slurry composition for AD55-14, the slurry temperature was maintained at 25°C. This modified procedure was employed to determine the feasibility of simplifying the preparation of large electrolyte batches by elimination of the slurry heating. Electrolyte AD55-15 and half of AD55-14 (designated AD55-14A) were then oven dried under the same conditions of 110°C for 20 hours. X-ray diffraction analyses of the two dried slurries (Table 1.4a) indicated nearly identical product phase assemblages. Thus, it appears that the slurry mixing temperature can be lowered from 80°C to room temperature without affecting the resulting dried slurry product. (More details on the preparation of batches AD55-15 and AD55-14 are given in Table 1.4b.)

The diffraction lines of the major reaction products in the dried slurries corresponded to those of LiOH and $Li_2Al_2O_4 \cdot yH_2O$ (ASTM Card 20-618). Although this latter lithium aluminum oxide hydrate phase was reported by Lejus[8] to have a Li/Al molar ratio of 1, our analyses indicated that the composition corresponds to $Li_2O \cdot 2Al_2O_3 \cdot 11H_2O$.

Table 1.4a. EFFECT OF SLURRY MIXING TEMPERATURE ON THE DRIED SLURRY PRODUCT

Electrolyte	Slurry Mixing Temp, °C	Oven Drying Conditions	Relative X-Ray Intensity at Indicated d-Spacing*							
			$Li_2Al_2O_4 \cdot yH_2O$		β-$LiAlO_2$		LiOH		$LiOH \cdot H_2O$	
			3.81A	2.492A	4.05A	3.87A	2.73A	4.37A	2.67A	2.97A
AD55-14A	75	20 hrs at 110°C	50	27	10	11	42	37	10	4
AD55-15	25	21 hrs at 110°C	60	18	9	11	43	25	7	3

* Peak heights of two selected reflections used to compare relative amount of the same crystalline phase.

1.1.2.7. Consistency of the Slurry

The consistency of the slurry did not appear to have a significant effect on the rate of $LiAlO_2$ formation. Larger volumes of liquid, however, increase the time necessary to dry the slurry and may consequently affect the final $LiAlO_2$ properties because, as will be discussed in a later section, slurry drying-time and temperature are important factors in the control of $LiAlO_2$ production by the slurry process.

1.1.2.8. Drying Conditions

The most probable cause of excessive deformation of tiles pressed from Electrolyte AD55-1A, the electrolyte batch processed by the original slurry process, was the unacceptable large β-$LiAlO_2$ particle size in the electrolyte. Some efforts were thus taken to control the particle growth of these rod-like β-$LiAlO_2$ structures during the slurry stage by varying the rate of slurry drying. Electrolyte AD55-6A was prepared exactly as AD55-1A, except that the amount of water used to make the slurry was reduced by 37.5% and the hot slurry was dried by spreading it thinly in a dish and blowing air over it. The $LiAlO_2$ in the final electrolyte had smaller particle sizes, yet maintained the same phase and morphology as that in Electrolyte AD55-1A. (See Figure 1.12a.) Nevertheless, a tile pressed from AD55-6A, although it showed acceptable behavior during the first cycle of the thermal deformation test, failed by cracking during the second cycle, indicating that further reduction in particle size or modification of morphology and phase assemblage may be necessary. The result, however, confirmed that rod-like β-$LiAlO_2$ particle size can be controlled by varying the drying conditions.

Table 1.4b. PREPARATION AND CHARACTERIZATION DATA FOR ELECTROLYTES AD55-14 AND AD55-15

	AD55-14A	AD55-14B	AD55-15
Starting Material, wt %			
Al_2O_3	49.6	49.6	49.6
LiOH	50.4	50.4	50.4
Slurry Mixing	1 hr at 75°C	1 hr at 75°C	1 hr at 25°C
Carbonation			
Material	powder	slurry	powder
pH Change	--	12.4 to 8.7	--
Slurry Drying	20 hrs at 110°C	24 hrs at 110°C	21 hrs at 110°C + 3 hrs at 130°C
Weight Ratio*	1.21	--	1.23
Dry Slurry + Co_2	17 hrs at 25°C	16 hrs at 25°C	23 hrs at 25°C
Weight Ratio*	1.44	1.40	1.31
Firing	22 hrs at 600°C	22 hrs at 600°C	22 hrs at 600°C
% Yield	93.5	95.1	94.9
Composition, Mole %			
Li_2CO_3	62	62	62
K_2CO_3	38	38	38
Washed $LiAlO_2$			
Surface Area, m^2/g	16.7	13.9	12.2
Density, g/cm^3	2.86	3.18	2.74
$\alpha/\beta/\gamma$	32/62/6	72/18/10	17/81/2

---

*Ratio of product to initial Al_2O_3 and LiOH materials

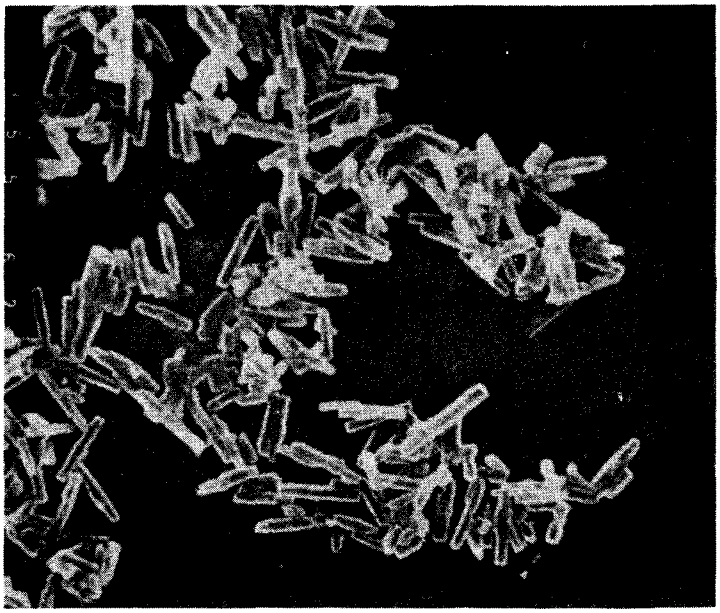

Figure 1.12a. SEM MICROGRAPHS OF $LiAlO_2$ WASHED FROM ELECTROLYTE AD55-6A (6000X)

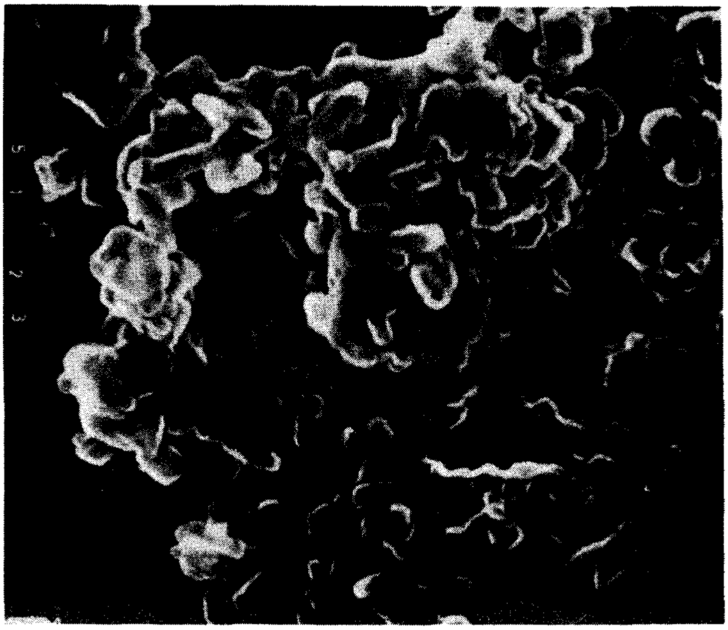

Figure 1.12b. SEM MICROGRAPHS OF $LiAlO_2$ WASHED FROM ELECTROLYTE AD55-12A (20,000 X)

Based on the encouraging results from AD55-6A, Electrolyte AD55-12A was prepared by freeze drying a slurry similar in composition to that of AD55-1A. The slurry was stirred for only 15 minutes at room temperature instead of the usual 60 minutes, immediately frozen, and then dried in a vacuum. The $LiAlO_2$ phase composition in the final electrolyte was a mixture of the three $LiAlO_2$ phases (26%α - 60%β - 14%γ), and the crystal morphology was polyhedral instead of rod-like. (See Figure 1.12b.) This change of $LiAlO_2$ morphology may have been a result of the shorter slurry reaction time. The $LiAlO_2$ surface area was 13.4 m^2/g, and, although it was lower than the $LiAlO_2$ from AD55-2 type electrolytes, a tile pressed from Electrolyte AD55-12A did not slump upon melting. However, due to malfunctioning of the thermal expansion apparatus, we were unable to trace its thermal expansion curve. The results of this experiment also indicate that the rate of drying of the slurry has an important effect on the properties of the electrolyte. Furthermore, non-slumping tiles can be pressed from an electrolyte containing a mixture of the α-, β-, and γ-$LiAlO_2$ phases produced by the aqueous slurry process. Based on the results observed from Electrolytes AD55-6A and AD55-12A, it appears that slurry reaction and drying times in between those of these two electrolytes should produce more desirable $LiAlO_2$ particle characteristics.

In potassium-free aqueous slurries typical of the Electrolyte Batch AD55-2A, a lithium aluminate hydrate phase was identified that appeared to ultimately determine the phase composition and morphology of the final $LiAlO_2$. Therefore, the effects of drying conditions on the hydrate formation and the final $LiAlO_2$ properties were investigated. Five electrolyte batches were prepared from potassium-free slurries following essentially the same procedure as that used for Electrolyte AD55-2A, except that the drying conditions were varied. The different slurry drying conditions and the characterization data are presented in Table 1.5. Electrolyte AD55-2-1 was dried for 1 day at 110°C. Electrolytes AD55-2-2 through AD55-2-5 were dried to constant weight during a 4-day period at temperatures ranging from 90° to 270°C. The weight of the dried slurries ranged from 110 to 210 grams, compared with a theoretical weight of 95 grams had the slurries undergone complete reaction and dehydration to $LiAlO_2$ and LiOH. A lithium aluminate hydrate phase with an X-ray diffraction pattern matching lines for the compound $Li_2O{\cdot}Al_2O_3{\cdot}yH_2O$, as given in Card No. 20-618 of the Inorganic Powder Diffraction File, was identified from the X-ray

Table 1.5. EFFECT OF DRYING CONDITIONS ON SLURRY AND FINAL $LiAlO_2$ PROPERTIES

				Final $LiAlO_2$	
Electrolyte	Slurry Drying Conditions*	Dried Slurry Weight,** g	H:B†	$\alpha:\beta:\gamma$	Surface Area, m^2/g
AD55-2-1	1 day at 110°C	~210	84:100	95:5:1	n.a.
AD55-2-2	4 days at 110°C	130	29:100	26:74:1	25.2
AD55-2-3	4 days at 90°C	170	--	67:27:6	26.9
AD55-2-4	4 days at 160°C	110	0:100	12:87:1	11.1
AD55-2-5	4 days at 270°C	114	0:100	10:90:1	7.8

* Except for Electrolyte AD55-2-1, all electrolytes were dried at the specified temperatures to constant weight.

** Theoretical weight of anhydrous $LiAlO_2$ + LiOH slurry is 95 g.

† From X-ray diffraction pattern of carbonated dry slurry, the peak height ratio of $Li_2O_2 \cdot 2Al_2O_3 \cdot yH_2O$ peak at d = 1.899 A to β-$LiAlO_2$ peak at d = 2.452 A.

diffraction patterns of the slurries dried at 110°C or lower. Chemical and gravimetric analyses of this hydrate produced by stirring $LiAlO_2$ (β or γ) in water showed its chemical formula to be $Li_2O \cdot 2Al_2O_3 \cdot 11H_2O$. No such hydrate phase was detected from the slurries dried at 160°C and 270°C. After carbonation, only Li_2CO_3 and β-$LiAlO_2$ were detected from the X-ray diffraction patterns of the dry slurry. The higher-than-theoretical dry slurry weight obtained from these electrolytes was perhaps due to $LiOH \cdot H_2O$ which subsequently transformed to Li_2CO_3 upon reaction with CO_2.

The data shown in Table 1.4 indicate that the more thoroughly the slurry is dried before further processing, the higher the β-phase $LiAlO_2$ content in both the dried slurry and in the final electrolyte powder after 600°C firing. However, higher slurry drying temperatures result in lower $LiAlO_2$ surface areas in the final electrolyte. It should be noted that some problems were encountered in processing batches AD55-2-3, AD55-2-4, and AD55-2-5. The composition of these electrolytes deviated from the nominal composition after adding K_2CO_3 to the carbonated slurry. The Li_2CO_3 to K_2CO_3 molar ratio was about 3.8 for all three electrolytes instead of the nominal value of 1.63.

This deviation, as will be discussed in a later section, could result in a higher percentage of α-$LiAlO_2$ in the final electrolyte, but the effect on the overall $LiAlO_2$ surface area should not be significant. The trend of decreasing α-phase content with increasing drying temperature shown by these three electrolytes is expected to also hold for electrolytes having the nominal Li_2CO_3 to K_2CO_3 molar ratio of 1.63.

The effect of drying conditions on properties unaffected by the electrolyte composition, such as the hydrate to β-$LiAlO_2$ ratio in the dried slurry and final $LiAlO_2$ surface area, are shown in Figure 1.13. Considering that $LiAlO_2$ surface areas below about 10 m^2/g do not retain carbonate adequately, as observed from thermal deformation behavior of tiles, the maximum allowable slurry drying temperature appears to be about 160°C.

The effect of slurry drying temperature was also studied on Electrolytes AD55-14A and AD55-15, which were prepared according to the same procedures, (Table 1.4a) except that AD55-15 had a lower slurry temperature (25°C versus 75°C) and higher drying temperatures (110° and 130°C versus 110°C) than AD55-14A. The powder products at various stages of preparation were characterized by X-ray diffraction, and the results are summarized in Table 1.4b.

At the low drying temperature of 110°C, the dried slurry was generally composed of the phase yielding the X-ray lines reported for $Li_2AL_2O_4 \cdot yH_2O$, excess LiOH and/or $LiOH \cdot H_2O$, and β-$LiAlO_2$. However, when this dried slurry was given an additional thermal treatment at 250°C for 16 hours, the phase assemblage changed to Li_2CO_3, β-$LiAlO_2$, and LiOH. All of the $Li_2AL_2O_4 \cdot yH_2O$ appeared to decompose to form a material that was undetected by X-ray diffraction. Most of the excess LiOH (about 85%) reacted with CO_2 in the air to form Li_2CO_3, and the β-$LiAlO_2$ content remained essentially unchanged.

After the addition of K_2CO_3 and final firing of the carbonated slurries for 22 hours at 600°C, AD55-14A had a $LiAlO_2$ α/β ratio of 0.47, while AD55-15 had a α/β ratio of 0.13. Because the slurry reaction temperature earlier was shown to have no significant influence on the dried slurry, it is suspected that the higher drying temperature was responsible for the lower α-$LiAlO_2$ phase content in the AD55-15 powder (11% α versus 30% α).

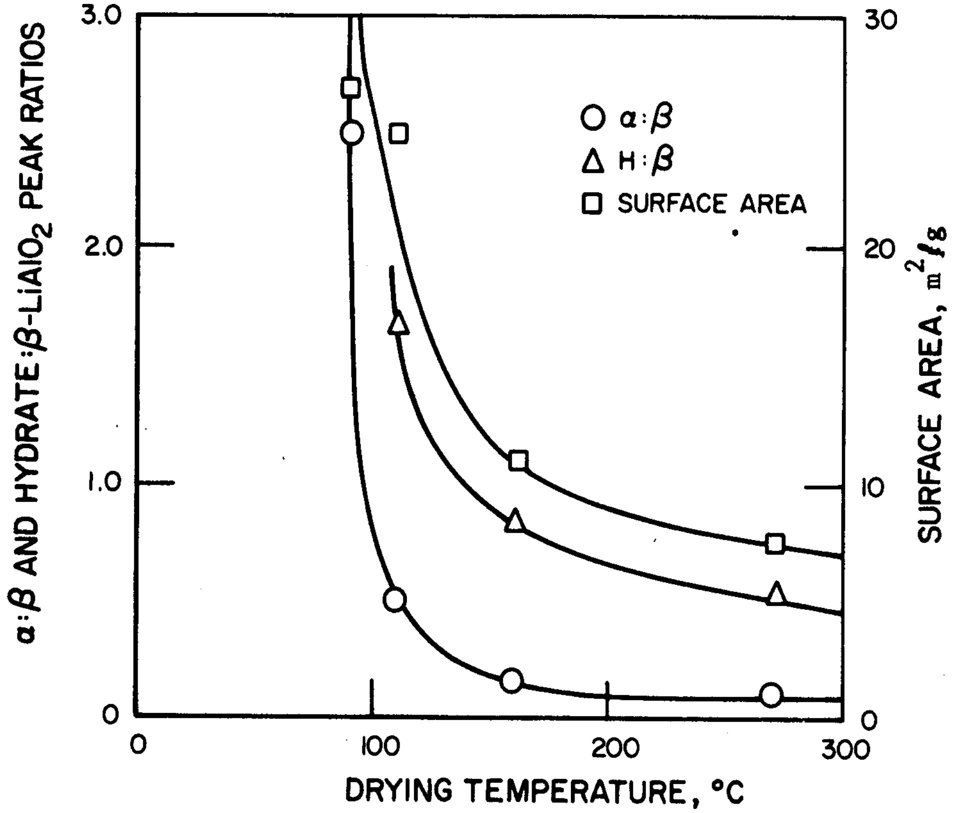

A79020482

Figure 1.13. HYDRATE TO β-$LiAlO_2$ PEAK RATIO IN DRIED SLURRY, AND γ:β RATIO AND SURFACE AREA OF FINAL $LiAlO_2$ PRODUCT AS FUNCTIONS OF DRYING TEMPERATURES FOR ELECTROLYTES WHOSE SLURRIES WERE DRIED TO CONSTANT WEIGHTS

1.1.2.9. Time and Temperature of Carbonation

Carbonation of the dried slurry powder was always performed without external heat for a sufficiently long period to ensure complete conversion of hydroxide to carbonate. The carbonation reaction itself is exothermic, and the heat liberated causes the powder to heat up. The temperature measured during carbonation was, typically, 50° to 60°C. No attempt was made to determine the effect of carbonation temperature on the final electrolyte properties.

Carbonation of Wet Slurry

The electrolyte processing could be simplified if carbonation could be performed on the wet slurry instead of the dry powder. In preparing Electrolyte AD55-14B, the potassium-free slurry was first stirred for 1 hour at 75°C and then CO_2 gas was bubbled through the slurry with continuous stirring at room temperature for 16 hours. The pH of the wet slurry before and after carbonation was measured to be 12.4 and 8.7, respectively, indicating the conversion of LiOH to Li_2CO_3 and, probably, the formation of carbonic acid. During the carbonation process, the formation of Li_2CO_3, rather than $LiHCO_3$, is thermodynamically favored because Li_2CO_3 has a lower free-energy of formation (−266.7 versus −210.5 kcal/mole).

After carbonation, the wet slurry was oven-dried at 110°C for 24 hours. The X-ray diffraction pattern of the dried powder was compared with that of Electrolyte AD55-14A, which was prepared in a way similar to AD55-14B, except that carbonation was performed on the dried slurry. AD55-14B (CO_2 through wet slurry) had more Li_2CO_3 but less $Li_2O \cdot 2Al_2O_3 \cdot yH_2O$ than AD-55-14A and no β-$LiAlO_2$. The ratio of the weight of the dry powder after carbonation to that of the dry slurry materials (Al_2O_3 and LiOH) was almost the same for both AD55-14B and AD55-14A (1.40 versus 1.44), which indicates that the degree of carbonation was about the same for both Electrolytes AD55-14B and AD55-14A. However, the $LiAlO_2$ from AD55-14B had a lower surface area (13.0 versus 16.7 m^2/g) and a significantly higher α/β ratio ($\alpha/\beta/\gamma$ composition being 74/17/9 versus 30/64/6). This phase difference in β-$LiAlO_2$ had been evident earlier by the lack of β-$LiAlO_2$ in the dried CO_2 slurry from AD55-14B. These data indicate that the pH value of the slurry is affecting the phase assemblage of the final product; a less basic wet slurry (e.g., 8.7 versus 12.4) favors the production of more α-$LiAlO_2$ (74% versus 30%).

1.1.2.10. Firing Schedule

As previously reported (Project 9105 Second Quarterly Report), some electrolyte powders have been given additional thermal treatment after the 600°C firing at a temperature equal to or greater than the normal cell operating temperature of 650°C. The purpose of this treatment is to "stabilize" the $LiAlO_2$ with its carbonate environment prior to cell operation and thus minimize the changes occurring during the cell lifetime. The results showed that the additional firing causes a significant reduction in measured $LiAlO_2$ surface area. Consequently, dilatometric yield upon melting is higher with tiles pressed from more severely heat-treated electrolytes. The $LiAlO_2$ composition, however, showed only insignificant β to α transformation during a 40 to 50-hour treatment at 685°C.

1.1.2.11. Carbonate Composition During Firing

The effect of carbonate composition in contact with the $LiAlO_2$ during the 600°C firing of electrolytes has been discussed in both the Project 9105 Second and Third Quarterly Reports. Four electrolyte batches, namely, AD55-2A, AD55-2B, AD55-8A, and AD55-10A were prepared from potassium-free slurries. For Electrolytes AD55-2A and AD55-2B, all the required lithium for the final electrolyte was added to the slurry as $LiOH \cdot H_2O$. For Electrolytes AD55-8A and AD55-10A, only 50% and 25%, respectively, of the required amount of lithium for the final Li_2CO_3 were added to the slurries as $LiOH \cdot H_2O$, in addition to the stoichiometric $LiOH \cdot H_2O$ required to form $LiAlO_2$ by reaction with Al_2O_3. After drying and carbonating the slurries, all the required amounts of K_2CO_3 for the electrolytes were added before firing at 600°C, except for Electrolyte AD55-2B which was fired without added K_2CO_3. Thus, the Li_2CO_3 to K_2CO_3 molar ratio during the 600°C firing was different for all these four electrolytes. (See Table 1.6.) The corresponding $LiAlO_2$ characteristics after the 600°C firing are also included in Table 1.6. The results indicate that the $LiAlO_2$ α/β phase ratio increases as the Li_2CO_3-to-K_2CO_3 ratio during firing is increased. The surface area, on the other hand, appears to be independent of the carbonate composition, with values ranging from 21 to 25 m^2/g for the four electrolytes.

Table 1.6. EFFECT OF CARBONATE COMPOSITION DURING 600°C FIRING STEP ON FINAL $LiAlO_2$ PROPERTIES

Electrolyte	K_2CO_3/Li_2CO_3 Molar Ratio During Firing	LiAlO $\alpha/\beta/\gamma$, %	$LiAlO_2$ Surface Area, m^2/g
AD55-2B	0	71/29/0	23.1
AD55-2A	0.61*	47/53/0	20.7
AD55-8A	1.22	24/76/0	24.0
AD55-10A	2.44	15/85/0	25.0

* Standard composition: 62 mole percent Li_2CO_3/38 mole percent K_2CO_3.

The morphology of the $LiAlO_2$ appears to be unaffected by the carbonate composition in which the $LiAlO_2$ was fired. SEM micrographs of lithium aluminates washed from Electrolytes AD55-2A and AD55-2B after both had undergone similar heat treatments are shown in Figures 1.14 and 1.15. They have similar structures. The particles are plate-like and have internal porosity. Although both lithium aluminates consisted of two different phases, α and β, as identified by X-ray diffraction, no two distinguishable particle structures can be identified from the SEM micrographs.

The electrolytes whose carbonate compositions differed from the nominal composition of the eutectic after the 600°C firing were adjusted by adding the makeup components after firing and then heat treating the electrolytes to homogenize the carbonate distribution. This additional heat treatment reduced the $LiAlO_2$ surface area, but had no significant effect on $LiAlO_2$ phase composition and morphology.

From the observed dependence of the α/β ratio on carbonate composition of electrolyte during the 600°C firing, it appears that pure β phase could be synthesized from a mixture containing minimum Li_2CO_3. Because, as discussed earlier, drying the slurry at higher temperatures also affects $LiAlO_2$ phase composition, varying the drying temperature and carbonate composition allowed production of a variety of $LiAlO_2$ phase compositions and morphologies.

1.1.2.12. Recommended Preparation Procedure

Based on characterizations and cell performance (reported in later sections) of electrolyte powders prepared under varying conditions, the

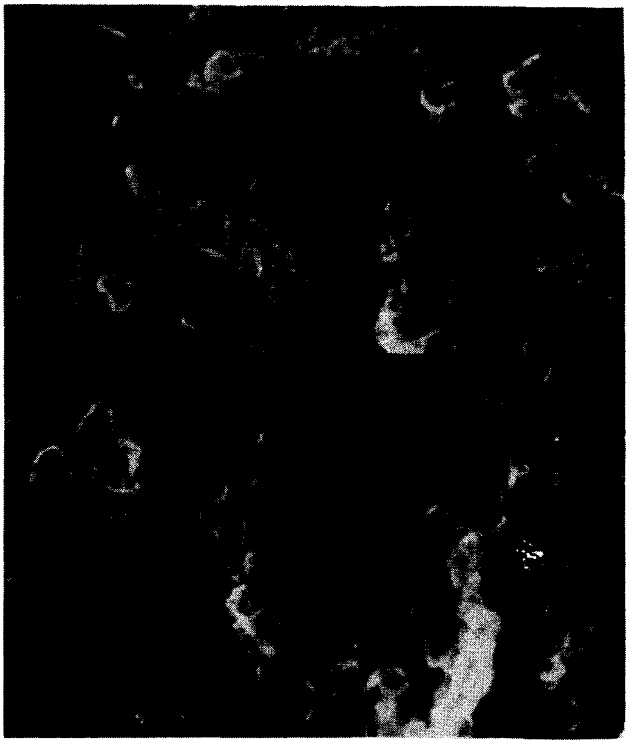

Figure 1.14. SEM MICROGRAPH OF $LiAlO_2$ WASHED FROM ELECTROLYTE AD55-2A, (50 hrs at 680°C) (20,000 X)

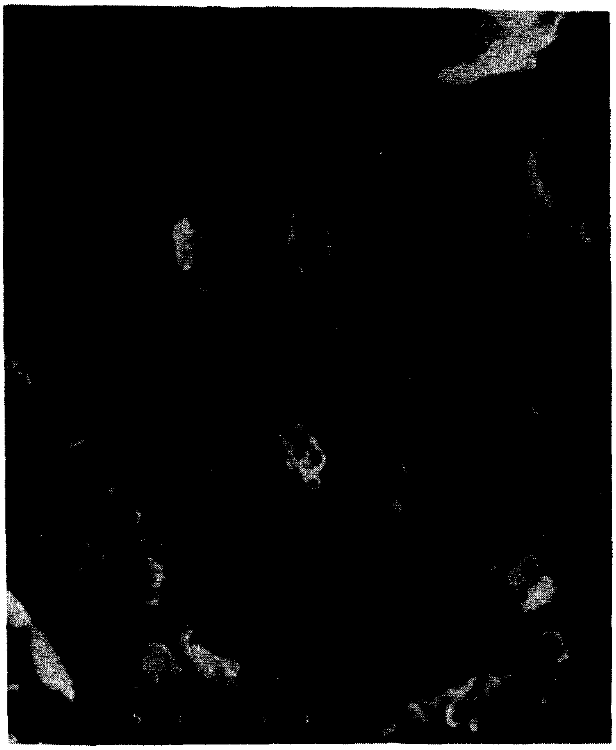

Figure 1.15. SEM MICROGRAPH OF $LIAlO_2$ WASHED FROM ELECTROLYTE AD55-2B, (40 hrs at 685°C) (20,000 X)

following processing procedure was adopted for preparation of the 55 weight percent Li_2CO_3-K_2CO_3/45 weight percent $LiAlO_2$ powder having a Li/K eutectic molar ratio of 1.63.

Characteristics of the electrolyte powder are —

a. Nominal Final Composition: 45 weight percent $LiAlO_2$, 25.6 weight percent Li_2CO_3, 29.4 weight percent K_2CO_3

b. Carbonate Electrolyte Composition: 62 mole percent Li_2CO_3/38 mole percent K_2CO_3 eutectic

c. Materials needed for 2500 gram batch of electrolyte powder: Gamma alumina (Degussa "C"): 941 grams with $\frac{1}{0.925}$ assay correction factor is (870 grams theoretical); $LiOH \cdot H_2O$ (Fisher Reagent Grade No. L-127): 1445 grams; and K_2CO_3 (Fisher Reagent Grade No. P-208): 754 grams with $\frac{1}{0.975}$ assay correction is factor (735 grams theoretical).

The processing steps are —

a. Step 1. Dissolve all the $LiOH \cdot H_2O$ in 7 liters of distilled water and all the Al_2O_3 in 6 liters of water (14.5 g Al_2O_3/100 ml) separately at room temperature.

b. Step 2. Add the Al_2O_3 solution slowly into the $LiOH \cdot H_2O$ solution and stir the mixture for 1 hour at room temperature.

c. Step 3. Pour the slurry into shallow containers to about 3 inches deep and dry in an oven at 110° to 160°C to constant weight (the weight ratio of dried slurry to starting dry Al_2O_3 and LiOH powders is approximately 1.0:1.25). After overnight drying of stagnant slurry, the lumps can be broken to speed final drying under vacuum.

d. Step 4. Carbonate the dried slurry by passing CO_2 gas through the powder for 6 hours, mixing occasionally.

e. Step 5. Pulverize carbonated cakes to —80 mesh.

f. Step 6. Pass CO_2 gas through pulverized powder for an additional 4 hours to ensure complete carbonation.

g. Step 7. Blend carbonated powder with —325 mesh K_2CO_3 and fire under flowing CO_2 at 600°C for 22 hours.

h. Step 8. Pulverize the electrolyte to —100 mesh and mix well in "V"-blender. The powder is now ready for characterization and pressing.

1.1.2.13. Alternative Electrolyte Composition Studies

In order to optimize the carbonate composition in the electrolyte, five additional electrolyte compositions other than the 62 mole percent Li_2CO_3/38% K_2CO_3 (62 Li/38 K) eutectic were prepared for cell testing purposes. The alternative compositions were selected based upon considerations of electrical conductivity, melting point, vapor pressure, gas solubility, and diffusion coefficients. The details of the five chosen compositions are outlined in Table 1.7. Two of them are eutectic compositions, namely Li-Na binary eutectic of 52 Li/48 Na and Li-K-Na ternary eutectic of 43.5 Li/25 K/31.5 Na. The three remaining compositions are non-eutectic, including the Li-K binary of 75 Li/25 K and 50 Li/50 K, and one Li-K-Na ternary of 56 Li/12.5 K/31.5 Na.

As shown in Table 1.8, the five alternative electrolytes (carbonates plus $LiAlO_2$) were prepared on the basis of maintaining the same volume fraction of molten carbonate (~0.62) at the cell operating temperature as that in the standard electrolyte composition of 45 weight percent $LiAlO_2$ plus 55% carbonate of composition 62 Li/38 K. The five alternative electrolytes were prepared by using the potassium- and sodium-free aqueous slurry process. A summary of the starting materials and the calculated final compositions for the five alternative electrolytes is presented in Table 1.9. The slurries were formed by slowly pouring the Degussa γ-Al_2O_3 aqueous dispersion (about 18 grams Al_2O_3 per 100 ml) into the $LiOH{\cdot}H_2O$ aqueous solution (about 23 grams per 100 ml) and mixing at room temperature for one hour. All the lithium required in the final electrolyte powder was added to the slurry in the form of $LiOH{\cdot}H_2O$. The various slurries were then dried at 130° to 155°C for 20 to 68 hours. The dried slurries were pulverized to −80 mesh and carbonated at room temperature for 20 to 40 hours. The carbonated powder was again pulverized to −80 mesh and mixed with −325 mesh carbonates of K_2CO_3 and/or Na_2CO_3 prior to firing at 600°C for 22 hours. The details of the various electrolyte preparations are summarized in Table 1.10. It was noted that under the same drying and carbonation conditions, the ratio of final powder weight to the weight of the Al_2O_3 and LiOH starting materials was proportional to the starting LiOH content. The carbonation step seemed to be completed in about 20 hours, and there was little change in weight during any further carbonation. Complete carbonation to Li_2CO_3 was confirmed by X-ray diffraction analysis.

The five alternative electrolytes were characterized by X-ray diffraction, B.E.T. surface area, SEM, chemical analysis, thermal cycling tests, and laboratory-scale cell tests. The test results are listed in Table 1.10 and discussed as follows. The five alternative electrolyte slurries were dried at higher temperatures of 130° to 155°C for 20 to 68 hours, compared with

Table 1.7. LIST OF CARBONATE COMPOSITIONS USED IN VARIOUS ELECTROLYTES

Electrolyte Type	Purpose of Test	Carbonate Composition	Composition, Mol. %			Composition, Wt. %			Molecular Wt.	Melting Point, °C
			Li_2CO_3	K_2CO_3	Na_2CO_3	Li_2CO_3	K_2CO_3	Na_2CO_3		
AD55-2D	Baseline eutectic for 650°C cell operation	62 Li/38 K	62.0	38.0	--	46.6	53.4	--	98.3	488
AD55-50-2	Investigate congruently melting $LiKCO_3$ composition between two eutectics. Increased gas solubility at 650°C	50 Li/50 K	50.0	50.0	--	34.8	65.2	--	106.1	505
AD55-50-1	Li_2CO_3-rich to compensate for preferential cell operation. Increased conductivity at 650°C	75 Li/25 K	75.0	25.0	--	61.6	38.4	--	90.0	590
AD55-LN	Li_2CO_3-Na_2CO_3 eutectic for 650°C cell operation. Lower vapor pressure	52 Li/48 Na	52.0	--	48.0	43.0	--	57.0	89.3	501
AD56-T-3	Study low-melting (397°C) ternary eutectic for 550°C cell operation	43.5 Li/ 25 K/ 31.5 Na	43.5	25.0	31.5	32.1	34.5	33.4	100.1	397
AD56-T-1	Off-eutectic ternary for 650°C cell operation. Increased conductivity	56 Li/ 12.5 K/ 31.5 Na	56.0	12.5	31.5	44.9	18.8	36.3	92.0	508

Table 1.8. ESTIMATION OF ELECTROLYTE COMPOSITIONS BASED ON 0.62 VOLUME FRACTION OF CARBONATE PHASE*

Electrolyte	Material Basis	Weight, g	Density, g/cm^3	Volume, %	Molar Ratio
	$LiAlO_2$	45	2.60	38.12	1.0
AD55-2D	62 Li_2CO_3	25.62	1.957	61.88	0.508
	38 K_2CO_3	29.38			0.311
		55.00			0.819
AD55-50-2	50 Li_2CO_3	19.20	1.963	61.88	0.381
	50 K_2CO_3	35.96			0.381
		55.16			0.762
AD55-50-1	75 Li_2CO_3	33.25	1.921	61.88	0.659
	25 K_2CO_3	20.73			0.220
		53.98			0.879
AD55-LN	52 Li_2CO_3	23.94	1.981	61.88	0.475
	48 Na_2CO_3	31.73			0.438
		55.67			0.913
AD56-T-3	43.5 Li_2CO_3	18.38	2.038	61.88	0.364
	25 K_2CO_3	19.76			0.209
	31.5 Na_2CO_3	19.13			0.264
		57.27			0.837
AD56-T-1	56 Li_2CO_3	24.78	1.964	61.88	0.491
	12.5 K_2CO_3	10.38			0.110
	31.5 Na_2CO_3	20.03			0.277
		55.19			0.878

---

*Assuming a $LiAlO_2$ density of 2.6 g/cm^3

Table 1.9. COMPOSITIONS OF STARTING MATERIAL AND CALCULATED FINAL PRODUCT COMPOSITION FOR VARIOUS ELECTROLYTES

	Composition, Wt. %						
Electrolyte	Al_2O_3	LiOH	Li_2CO_3	K_2CO_3	Na_2CO_3	$LiAlO_2$	Total
AD55-2D, 62 Li_2CO_3/38 K_2CO_3							
Starting Material (1)*	51.4	48.6	--	--	--	--	100.0
(2)*	35.8	33.9	--	30.3	--	--	100.0
Final Product	--	--	25.6	29.4	--	45.0	100.0
AD55-50-2, 50 Li_2Co_3/50 K_2CO_3							
Starting Material (1)*	54.7	45.3	--	--	--	--	100.0
(2)*	35.9	28.9	--	36.1	--	--	100.0
Final Product	--	--	19.2	35.9	--	44.9	100.0
AD55-50-1, 75 Li_2CO_3/25 K_2CO_3							
Starting Material (1)*	47.9	52.1	--	--	--	--	100.0
(2)*	37.2	40.6	--	22.2	--	--	100.0
Final Product	--	--	33.6	20.9	--	45.5	100.0
AD55-LN, 52 Li_2CO_3/48 Na_2CO_3							
Starting Material (1)*	52.2	47.8	--	--	--	--	100.0
(2)*	35.4	32.4	--	--	32.2	--	100.0
Final Product	--	--	23.8	--	31.5	44.7	100.0
AD56-T-3, 43.5 Li_2CO_3/25 K_2CO_3/31.5 Na_2CO_3							
Starting Material (1)*	55.2	44.8	--	--	--	--	100.0
(2)*	34.1	27.7	--	19.4	18.8	--	100.0
Final Product	--	--	18.0	19.3	18.7	44.0	100.0
AD56-T-1, 56 Li_2CO_3/12.5 K_2CO_3/31.5 Na_2CO_3							
Starting Material (1)*	51.8	48.2	--	--	--	--	100.0
(2)*	35.7	33.2	--	10.6	20.5	--	100.0
Final Product	--	--	24.7	10.4	20.0	44.9	100.0

---

*(1) = Slurry (2) = 600°C Firing

Table 1.10. PREPARATION AND CHARACTERIZATION DATA FOR VARIOUS ELECTROLYTES

Electrolyte	AD55-2D	AD55-50-2	AD55-50-1	AD55-LN	AD56T-3	AD56T-1
Starting Material, wt %						
Al_2O_3	49.6	54.7	47.9	52.2	55.2	51.8
LiOH	50.4	45.3	52.1	47.8	44.8	48.2
Slurry Mixing	1 hr at 25°C	1 hr at 25°C	1 hr at 25°C	1 hr at 25°C	1 hr at 25°C	1 hr at 25°C
Slurry Drying,	>120 hrs at 95°C	64 hrs at 135°C	66 hrs at 155°C	66 hrs at 155°C	68 hrs at 130°C	20 hrs at 155°C
Weight Ratio[**]	1.24	1.08	1.02	1.03	1.07	1.0
Dry Slurry + CO_2,	>12 hrs at 25°C	22 hrs at 25°C	16+24 hrs at 25°C	16+24 hrs at 25°C	22 hrs at 25°C	20 hrs at 25°C
Weight Ratio[**]	1.44	1.29	1.16	1.25	1.22	1.21
Firing	22 hrs at 600°C	16 hrs at 520°C+8 hrs at 600°C	22 hrs at 600°C	22 hrs at 600°C	16 hrs at 520°C+8 hrs 600°C	22 hrs at 600°C
% Yield	97.9	94.7	94.5	96.1	97.5	97.1
Composition, Wt % Mol %						
Li_2CO_3	26.7/63.1	18.6/49.2	32.8/76.6	25/52.2	18.2/43.4	26/56.8
K_2CO_3	29.2/36.9	35.8/50.8	18.7/23.4	--	18.7/23.9	10.2/12.0
Na_2CO_3	--	--	--	32.9/47.8	19.7/32.7	20.5/31.2
$LiAlO_2$	44.1/--	45.6/--	48.5/--	42.1/--	43.4/--	43.3/--
Washed LiAlO						
Surface Area, m^2/g	19.6	18.5	10.1	13.7	17.5	10.5
Density, g/cm^3	2.83	2.63	2.62	2.66	2.62	2.66
$\alpha/\beta/\gamma$	29/66/5	4/96/0	3/94/3	7/90/3	2/98/0	8.90/2
3 cm^2 Cell Testing[*]						
mV at 160 mA/cm^2	870	660	905	879	675	914

---

[*] Test with high-Btu fuel Co + 10% Cr anode and NiO cathode at 650°C.

[**] Ratio of product to initial Al_2O_3 and LiOH materials.

95° to 120°C used for drying the standard AD55-type electrolyte. The slurries dried at 155°C consisted of β-$LiAlO_2$, none or trace γ-$LiAlO_2$, no α-$LiAlO_2$, excess LiOH and $LiOH \cdot H_2O$, and small amounts of Li_2CO_3. The presence of Li_2CO_3 in the dry slurries indicates that at the drying temperature of 155°C, some small amount of LiOH and/or $LiOH \cdot H_2O$ starts to react with CO_2 in the air to form Li_2CO_3. During the subsequent carbonation, all LiOH and $LiOH \cdot H_2O$ remaining in the dried slurries were transformed into Li_2CO_3 in about 20 hours. Diffraction lines for the individual carbonates, Li_2CO_3 and K_2CO_3, were observed before firing (in separate experiments) and when each pure carbonate was fired individually at 600°C. No phase change was observed for Li_2CO_3 or Na_2CO_3 alone, but some change in X-ray lines was noted for K_2CO_3 during the firing. However, upon firing at 600°C, the carbonates in the electrolyte combine to form eutectic compounds. This was the case for both the eutectic and the non-eutectic electrolyte compositions, though the magnitude of the eutectic compound formation varied. This finding seems to agree with the DSC (Differential Scanning Calorimetry) measurements on AD56T-1 (an off-eutectic ternary), as shown below —

Temperature, °C	Melting, %
398	60
449	25
505	15
508	Melting point as estimated from phase diagram
397	Melting point of eutectic ternary

The carbonates in the off-eutectic ternary composition have a melting point of 508°C, based on the ternary phase diagram. However, the majority of the carbonates (60%) melt almost at the eutectic temperature of 397°C. Of the remaining carbonates, 25% melt at 449°C and 15% melt near the liquidus of 508°C. Finally, the α-$LiAlO_2$ produced in the final washed product of the five alternative electrolytes ranged from 2% to 8% and was much lower than that in the standard electrolyte compositions after drying at lower temperatures of 95° to 120°C (17% to 75%). Thus, higher drying temperatures tend to produce less α-$LiAlO_2$ phase. This confirms the same conclusion reached during the preparation of standard electrolyte compostions of 62 Li/38 K.

Because the drying of the wet slurry is critical in controlling the final $LiAlO_2$ phase assemblage and surface area, the drying step and its effects on $LiAlO_2$ were studied in detail. The drying conditions were found to be critical to the stability of the lithium aluminate hydrate phase, the so-called $LiAlO_2 \cdot yH_2O$ (ASTM 20-618). The exact composition of the hydrate was identified as $Li_2O \cdot 2Al_2O_3\ 11H_2O$. Such a hydrate always forms during the potassium-free slurry process, and all of the eleven hydration waters will be preserved when dried at 80°C or lower. As the drying temperature or time increases, the hydrate starts to lose hydration water. According to DSC measurements, the eleven hydration waters were lost at the following temperatures:

Temperature, °C	Molecules of Hydration Water Lost
218.5	5
270	4
280.5	1
304.3	1

Since the hydration water peaks are very broad, it was suspected, and later confirmed, that the hydration water may be driven off at a much lower drying temperature but at longer drying times. For example, when dried at 155°C for 20 hours, all the hydration water was driven off and the hydrate was decomposed to the extent that no "yH_2O" phase remained. The "yH_2O" phase was reported to be a hexagonal structure and was assumed to have a structural arrangement similar to that of the α-$LiAlO_2$ phase, which is also hexagonal. Thus, if the slurry is dried at a low temperature and the hydrate phase remains intact prior to firing, a predominant α-phase is likely to be obtained. Alpha-phase contents as high as 75% were produced by the slurry process by drying at a temperature of 110°C. On the other hand, if the slurry is dried at a high temperature and the hydrate is decomposed by losing all the hydration water, very little α-phase will be formed in the electrolyte. As shown in Table 1.10, only 2% to 8% α-phase was produced when the slurry was dried either at 155°C for 20 to 66 hours or at 130°C for 64 to 68 hours. Thus, a very wide range of α-phase contents (possibly 0% to 100%) may be produced by the slurry process by varying the drying conditions.

The composition of the so-called $LiAlO_2 \cdot yH_2O$ phase was determined as follows: An electrolyte containing γ-$LiAlO_2$ was first washed with 30% acetic anhydride/70% glacial acetic acid and then with methanol to remove all the carbonates. The remaining pure $LiAlO_2$ was boiled with water for 2 hours to complete the hydrolysis. (If only 1/2 hour was allowed for the boiling, 28% $LiAlO_2$ did not undergo the hydrolysis). The hydrate that had the same X-ray diffraction pattern as that prepared by the slurry process (Table 1.11) was identified as $Li_2O \cdot 2Al_2O_3 \cdot 11H_2O$ by both chemical analysis and density measurements, as shown below —

	Composition, wt %		Density, g/cm^3	
	Theoretical	Observed	Observed	X-Ray (As $Li_2O \cdot 2Al_2O_3 \cdot 11H_2O$)
Li_2O	6.9	7.1		
$2Al_2O_3$	47.2	47.8	2.11	2.10
$11H_2O$	45.9	45.1		
	100.0	100.0		

In addition, the two following mechanisms are both possible for the hydrolysis reaction —

$$3\,(Li_2O \cdot Al_2O_3) + 11H_2O \rightarrow Li_2O \cdot Al_2O_3 \cdot 11H_2O + (2Li_2O) \cdot Al_2O_3 \qquad (1)$$

Mass Balance: 1 0.50 1.092 0.409

$$\text{and, } 2\,(Li_2O \cdot Al_2O_3) + 12H_2O \rightarrow Li_2O \cdot 2Al_2O_3 \cdot 11H_2O + 2LiOH \qquad (2)$$

Mass Balance: 1 0.819 1.638 0.182

The first reaction was identified as the probable mechanism based on the following experimental data:

	Weight Ratio, Hydrate/$LiAlO_2$	Dissolved Material Solution Composition	Loss, %
Possible mechanism (1)	1.092	$(2Li_2O) \cdot Al_2O_3$	40.9
Possible mechanism (2)	1.638	LiOH	18.2
Experimental data	1.12	$(2Li_2O) \cdot Al_2O_3$	43.6

By knowing the $LiAlO_2$ hydrolysis mechanism, it is possible to estimate the amount of hydration water in the hydrate by simply calculating the weight ratio of hydrate over $LiAlO_2$.

Table 1.11. A COMPARISON OF X-RAY DIFFRACTION PATTERNS OF $LiAlO_2\cdot yH_2O$ AND $LiH(AlO_2)_2\cdot 5H_2O$

		Relative X-Ray Intensity at Indicated d-spacing						
LiAlO $\cdot yH_2O$	d	4.42	4.36	3.81	2.538	2.492	2.226	1.899
ASTM 20-618	I	20	20	70	40	70	40	70
Hydrate From Slurry	d	4.40	4.33	3.77	2.525	2.488	2.222	1.892
(14A-2)	I	7	6	50	14	34	17	25
Hydrate From γ-$LiAlO_2$	d	4.35	4.31	3.75	2.522	2.481	2.217	1.888
$LiH(AlO_2)_2\cdot 5H_2O$	I	17	14	51	14	29	25	30

Note: Peak heights were used to obtain relative X-ray intensity.

The five electrolytes prepared by the slurry process in general had very high product yields, ranging from 94% to 97%. The chemical compositions of the electrolytes were determined and are listed in Table 1.10. The compositions agreed well with the corresponding target compositions listed in Table 1.9.

The prepared electrolyte materials were first hot-pressed into thermal expansion tiles of 0.7-inch in diameter x 0.2-inch thick for the dilatometer thermal cycling test. If no slumping occurred during the two cycling tests between room temperature and 650°C, the materials were used to fabricate tiles 1 inch in diameter x 0.07-inch thick for evaluating the lab-scale cell performance of the new electrolytes. The pressing conditions and resulting tile densities for the five different electrolytes are listed in Table 1.12. They all passed the dilatometer thermal cycling test. The test results are shown in Figures 1.16 through 1.20. The $LiAlO_2$ size and shape were observed by SEM, as shown in Figures 1.21 through 1.25.

Two additional alternative electrolyte compositions were prepared by a two-step firing process. However, both of them failed the thermal cycling screening test. After slurry preparation by the potassium-free process, they were fired as follows —

Electrolyte	AD55-LN-1B	AD56-T-1B
1st firing		
Prior addition	--	K_2CO_3
°C — hour	600°C — 22 hrs	600°C — 22 hrs
2nd firing		
Prior addition	Na_2CO_3	Na_2CO_3
°C — hour	600°C — 10 hrs	600°C — 10 hrs

Table 1.12. A SUMMARY OF PRESS CONDITION AND TILE DENSITY FOR SIX ELECTROLYTES

	Tile		Pressing Conditions		Density, g/ml		Dimensions, inch	
Electrolytes	No.	Type*	°C	psi	Observed	Estimated	Diameter	Thickness
AD55-2D	2832	TE	480	3550	2.382	2.35	.6981	.1822
	2882	3 cm^2	475	3550	2.385	2.35	.9952	.0694
AD55-50-2	2897	TE	490	3550	2.349	2.26	.6982	.1871
	2894	3 cm^2	490	3550	2.362	2.26	.9962	.0697
AD55-50-1	2855	TE	475	3550	2.328	2.24	.6984	.1864
	2858	3 cm^2	475	3550	2.348	2.24	.9991	.069
AD55-LN	2851	TE	480	3550	2.392	2.28	.6993	.1873
	2862	3 cm^2	480	3550	2.322	2.28	.9989	.0708
AD56T-3	2898	TE	387	3550	2.325	2.29	.70	.1755
	2888	3 cm^2	387	3550	2.349	2.29	.9935	.0692
AD56T-1	2842	TE	396	3550	2.241	2.28	.6999	.1975
	2889	3 cm^2	390	3550	2.338	2.28	.9970	.0716

---

*TE: thermal expansion tiles of 0.7-inch-diameter x 0.2-inch thick

3cm^2: tiles of 1-inch-diameter x 0.07 inch-thick having 2 layers of Kanthal A-1 20-mesh screens

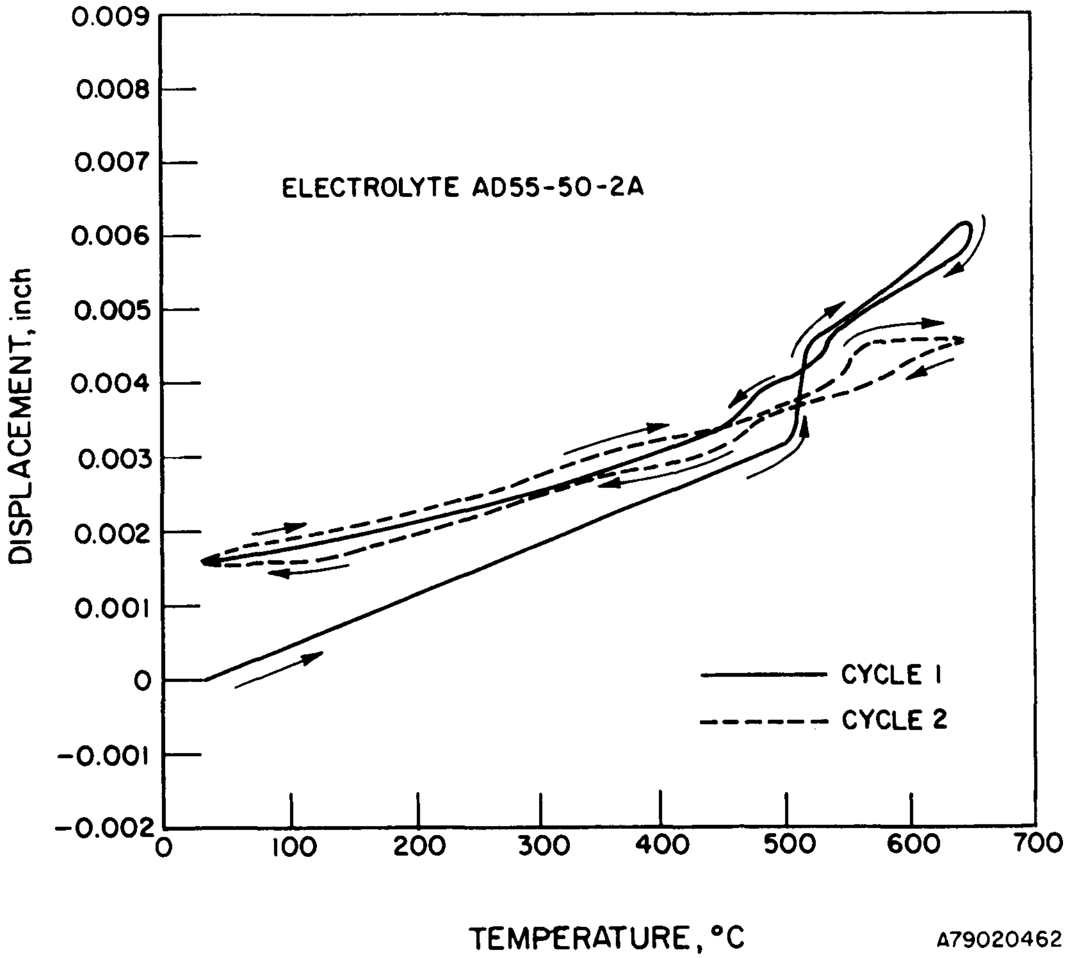

Figure 1.16. RESULTS OF THERMAL CYCLING TEST OF TILE NO. 2897 PRESSED FROM AD55-50-2A

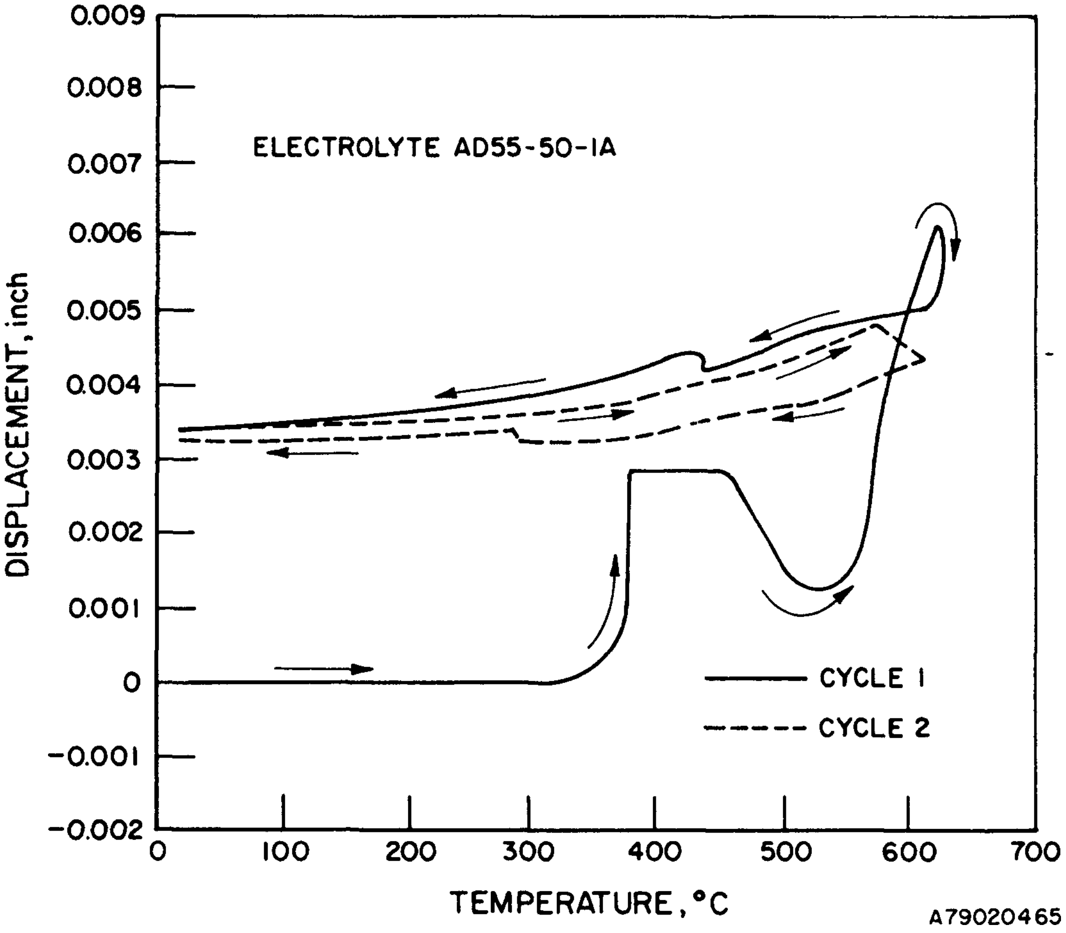

Figure 1.17. RESULTS OF THERMAL CYCLING TEST OF TILE NO. 2855 PRESSED FROM AD55-50-1A

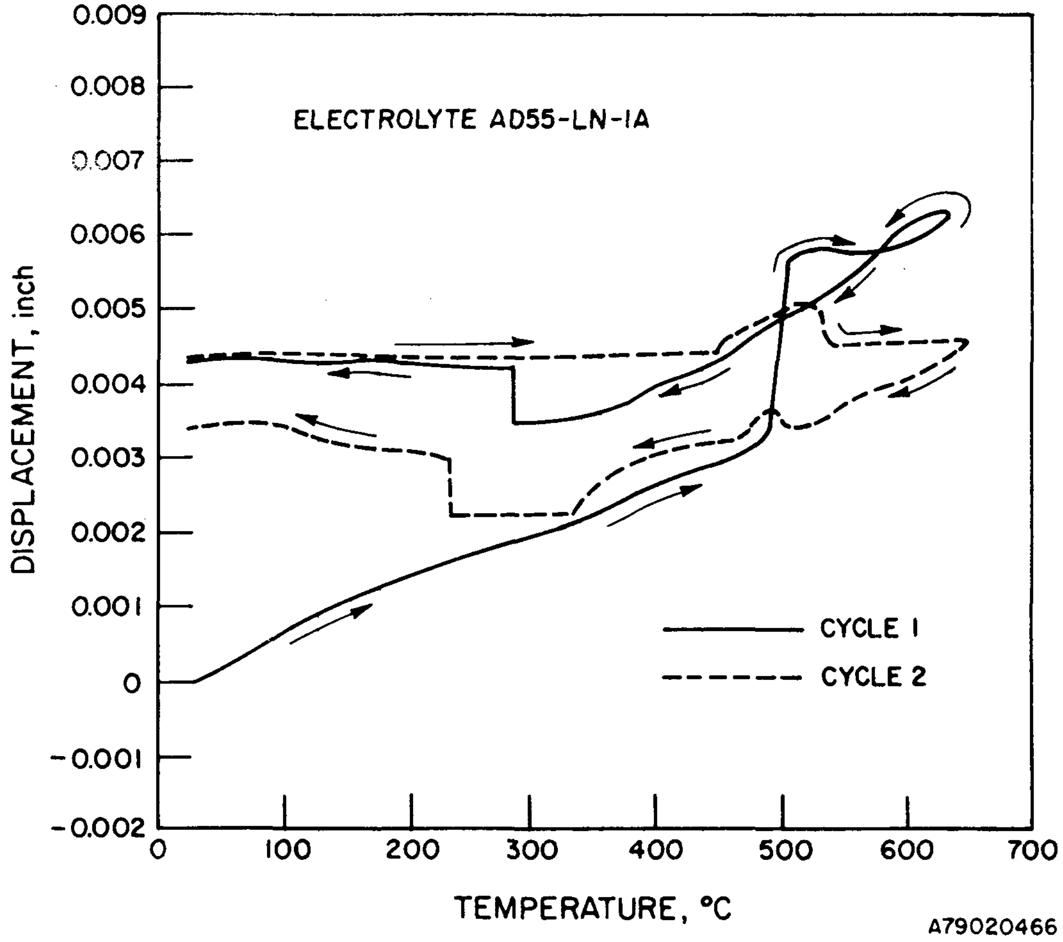

Figure 1.18. RESULTS OF THERMAL CYCLING TEST OF TILE NO. 2851 PRESSED FROM AD55-LN-1A

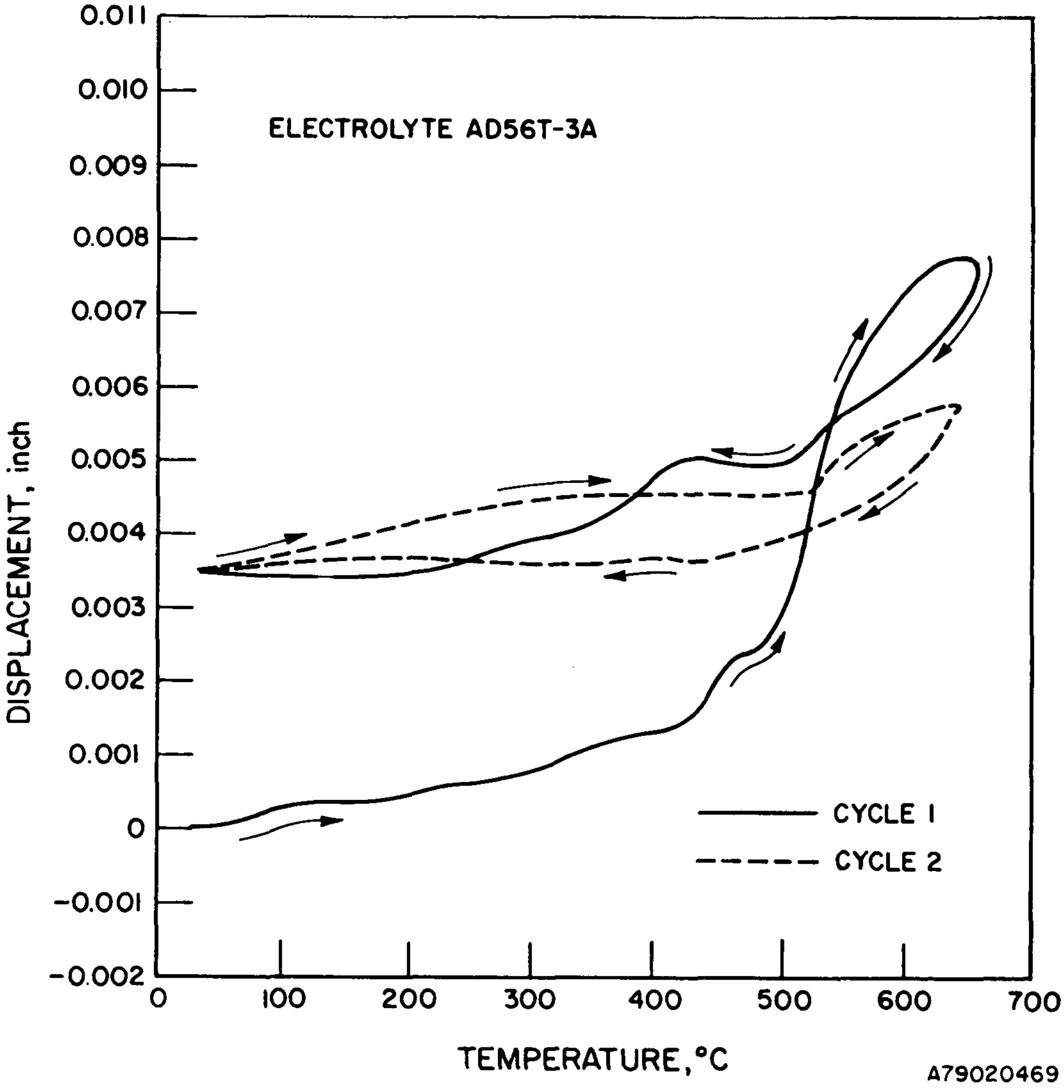

Figure 1.19. RESULTS OF THERMAL CYCLING TEST OF TILE NO. 2898 PRESSED FROM AD56T-3A

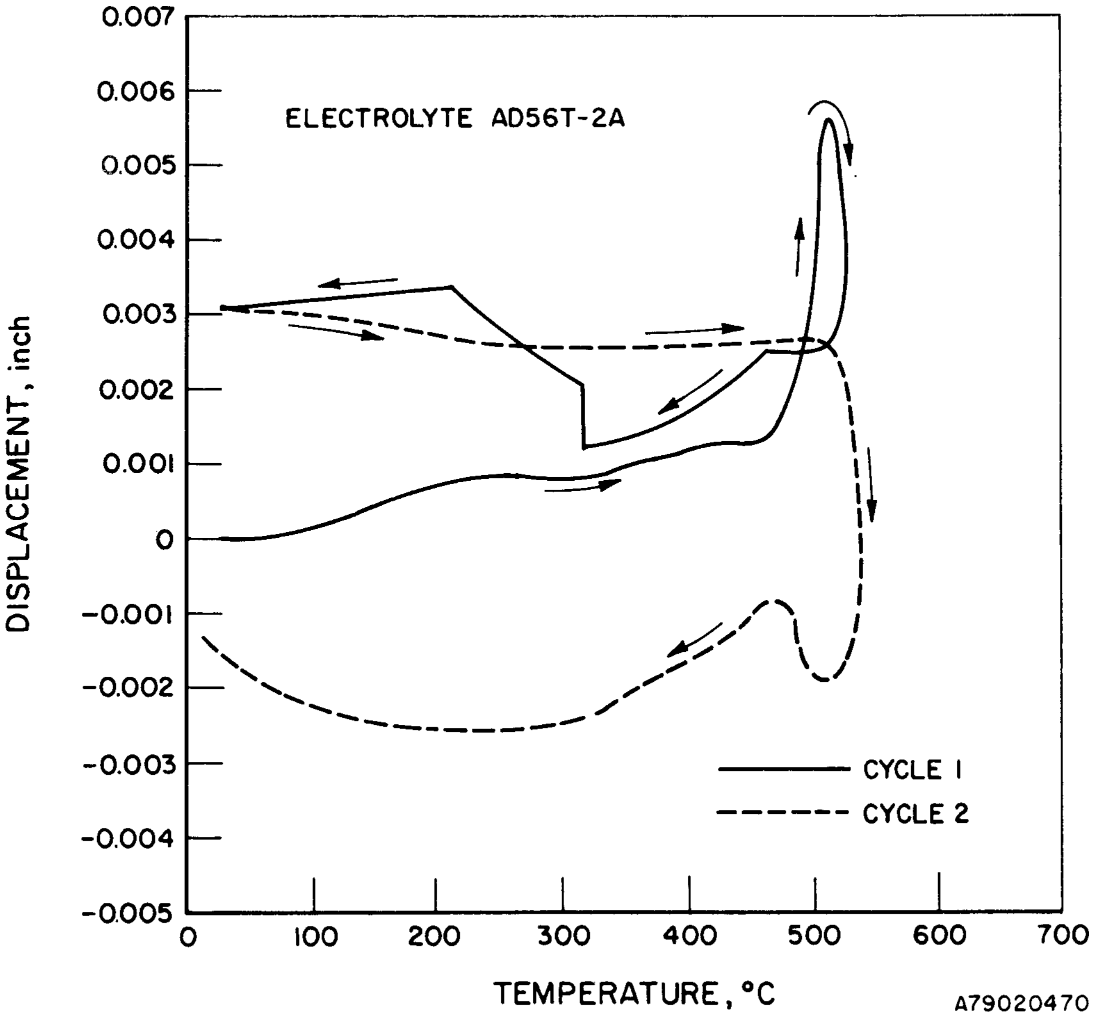

Figure 1.20. RESULTS OF THERMAL CYCLING TEST OF TILE NO. 2842 PRESSED FROM AD56T-2A (SAME AS AD56T-1A)

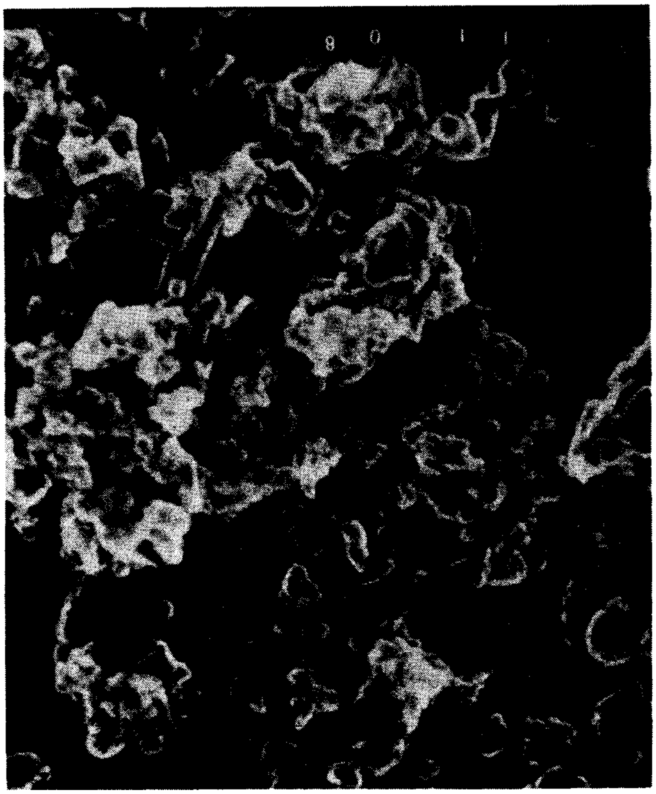

Figure 1.21. SEM MICROGRAPH OF $LiAlO_2$ WASHED FROM ELECTROLYTE AD55-50-2A (20,000 X)

Figure 1.22. SEM MICROGRAPH OF $LiAlO_2$ WASHED FROM ELECTROLYTE AD55-50-1A (20,000 X)

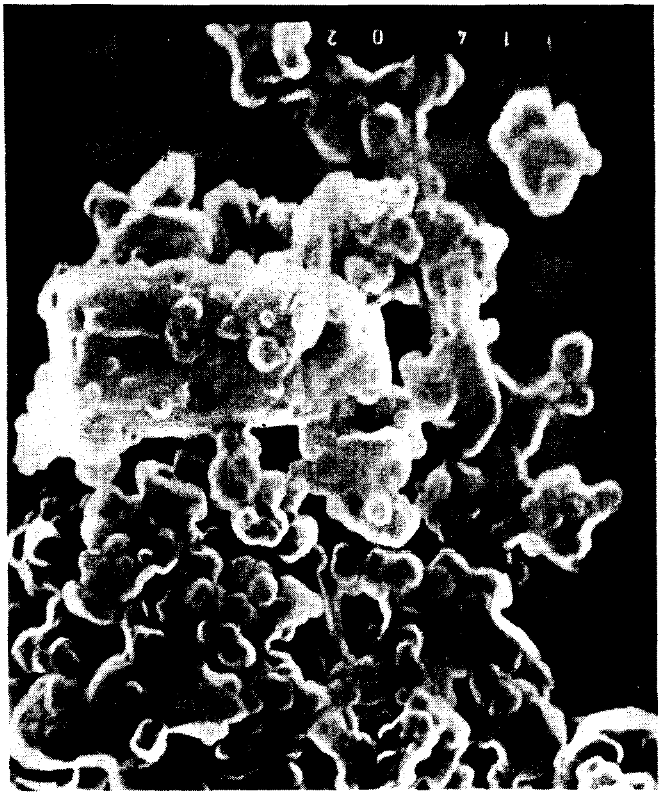

Figure 1.23. SEM MICROGRAPH OF $LiAlO_2$ WASHED FROM ELECTROLYTE AD55-LN-1A (20,000 X)

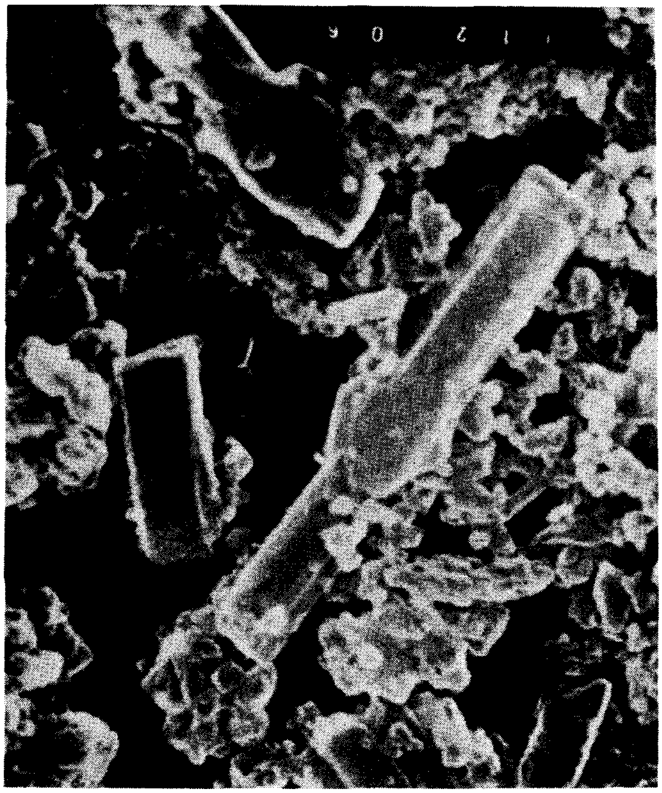

Figure 1.24. SEM MICROGRAPH OF $LiAlO_2$ WASHED FROM ELECTROLYTE AD56-T3A (20,000 X)

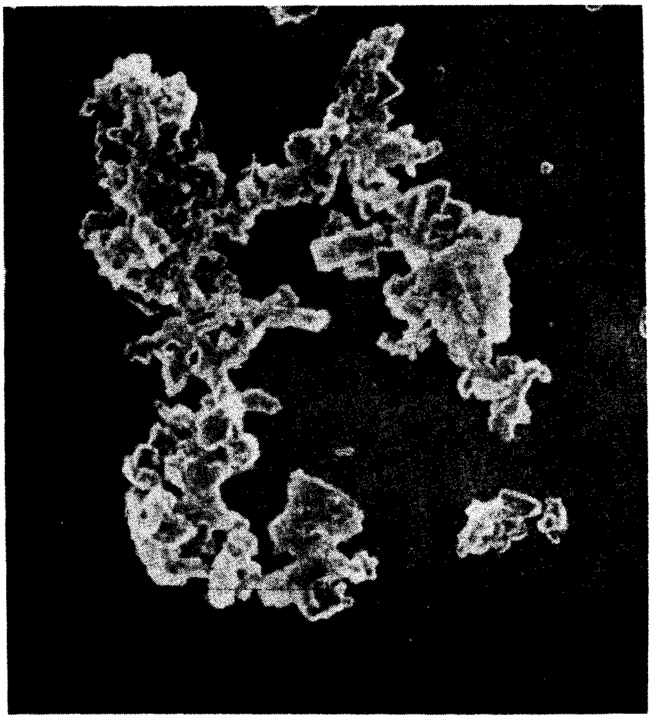

Figure 1.25. SEM MICROGRAPH OF $LiAlO_2$ PARTICULES WASHED FROM ELECTROLYTE AD56-T2A (6000X)

The test results of the two-stage fired materials were compared with those for one-stage firing in Table 1.13. The phase assemblages were almost identical for the two different firing stages. However, the surface areas of the two-stage fired materials were lower than those after one-stage firing (9 versus 13.7 m^2/g for AD55LN-1B and -1A, and 10.2 versus 10.5 m^2/g for AD56T-1B and -1A). The two materials prepared by two-stage firing were not tested in 3-cm^2 laboratory cells because of failure during the thermal cycling test. However, in view of the following considerations, it may be worthwhile to proceed with the evaluation of these two materials.

a. Their counterparts of one-stage fired materials had excellent cell performance (914 mV at 160 mA/cm^2 for AD56T-1A and 879 mV for AD55-LN-1A) compared with the goal performance of 840 mV at 160 mA/cm^2 for high-Btu (reformed methane) fuel.

b. Their phase assemblage and the surface area were similar to those of their counterparts. The evaluation of the two electrolytes by 3-cm^2 cell tests should provide insight into the following questions: (a) Will Kanthal screens be strong enough to prevent the cracking during thermal cycling? (b) What are the important factors, for example, phase assemblage, crystal morphology, surface area, etc., controlling the cell performance and correlation with thermal cycling performance?

Laboratory-scale (3 cm^2) cells were assembled and tested in order to evaluate the performance difference of the five new electrolytes. The cells were tested under the operating conditions shown below —

Operating temperature: 650°C

Fuel: High-Btu of equilibrium composition 60% H_2, 7.4% CO_2, 10% CO, and 22.6% H_2O

Oxidant: 68% air, 29.2% CO_2, and 2.8% H_2O

Utilizations: 7.5% fuel, 15% oxidant (based on 200 mA/cm^2)

Anode: Co + 10% Cr

Cathode: NiO (oxidized _in situ_ from porous Ni)

The cell performance goal under these conditions was a cell potential of 840 mV at 160 mA/cm^2. The test results were listed earlier in Table 1.10. Three of the five new electrolytes had cell potentials of 914, 905, and 879 mV, each of which exceeded the goal potential of 840 mV at 160 mA/cm^2, while the remaining two electrolytes had much lower performances (660 and 675 mV). The two poorly performing electrolytes had phase assemblages

Table 1.13. COMPARISON OF ONE- (600°C - 22 HRS) VERSUS TWO-STAGE (600°C - 22 + 10 HRS) FIRING OF ELECTROLYTE MATERIALS

	AD55-LN-1A	AD55-LN-1B	AD56T-1A	AD56T-1B
Starting Material, wt %				
Al_2O_3	52.2	52.2	51.8	51.8
LiOH	47.8	47.8	48.2	48.2
Slurry Mixing	25°C - 1 hr	25°C - 1 hr	25°C - 1 hr	25°C - 1 hr
Slurry Drying	155°C - 66 hrs	155°C - 66 hrs	155°C - 20 hrs	155°C - 20 hrs
Weight Ratio	1.03	1.03	1.0	1.0
Dry Slurry + CO_2	25°C - 16 + 24 hrs	25°C - 20 hrs	25°C - 20 hrs	25°C - 20 hrs
Weight Ratio	1.25	1.26	1.21	1.22
Firing	600°C - 22 hrs	600°C - 22 + 10 hrs	600°C - 22 hrs	600°C - 22 + 10 hrs
% Yield Product	96.1	96.3	97.1	94.5
Composition, wt/mol %				
Li_2Co_3	25/52.2	22.8/49.5	26/56.8	25/56.7
K_2Co_3	--	--	10.2/12.0	9.9/12.0
Na_2CO_3	32.9/47.8	33.3/50.5	20/5/31.2	10.8/31.3
$LiAlO_2$	42.1/--	43.9/--	43.3/--	45.3/--
Washed $LiAlO_2$				
Surface Area, m^2/g	13.7	9.0	10.5	10.2
Density, g/cm^3	2.66	2.66	2.66	2.66
$\alpha/\beta/\gamma$	7/80/3	7/81/12	8/90/2	8/89/3
Behavior During Dilatometer Screening Test	Little yield Upon melting	Slumped Upon melting	Little yield Upon melting	Slumped Upon melting

similar to those showing high performance ($\alpha/\beta/\gamma$ composition was 4/96/0 versus 3/94/3, 7/90/3, and 8/90/2). However, the former were dried at 130° to 135°C for 64 to 68 hours, while the latter were dried at 155°C for 20 to 66 hours. As expected on the basis of drying conditions, the two inferior electrolytes had higher surface areas (18.5 and 17.5 versus 10.1, 13.7, and 10.5 m^2/g) and smaller particle sizes. (See Figures 1.21 through 1.25.) Whether the difference in cell performance between the two groups of electrolytes is due to carbonate compositional differences, differences in $LiAlO_2$ properties resulting from different drying temperatures, or other factors, it should be investigated. A correlation between cell performance and carbonate composition is outlined in the phase diagram for the Li_2CO_3/Na_2CO_3 system in Figure 1.26. A compositional range of interest is indicated in this figure.

1.1.2.14. Fabrication of Electrolyte Tiles

The normal tile pressing conditions established during this program were 475° to 485°C temperature and 3550 psi pressure. The H-21 steel tool mold was heated in the hot press to the desired temperature; this took about 3 hours. Then the heater control was carefully adjusted so that the temperature fluctuation during the next hour was within ± 1°C. The pressure was then applied in four equal increments for 5 minutes at each pressure. At the end of the pressing period, the pressure was released and the mold was allowed to cool in the press furnace. The tile density thus obtained was usually greater than 95% of theoretical, which is suitable for cell testing. If the tile density was lower than 95%, increasing the pressing temperature up to 485°C generally resulted in improved tile density. When tiles pressed at 485°C still produced low densities, the pressure was increased to above 3550 psi; this is because the pressing temperature is limited by the melting point of the electrolyte.

1.1.2.15. Pot Test of Tiles

Electrolyte tile stability was investigated in a simulated anode environment to study the nature and extent of $LiAlO_2$ transformations and thus obtain a better understanding of $LiAlO_2$ instabilities in fuel cells. The results will also serve as a guide in determining the $LiAlO_2$ characteristics needed for optimum fuel cell performance and endurance. Each test

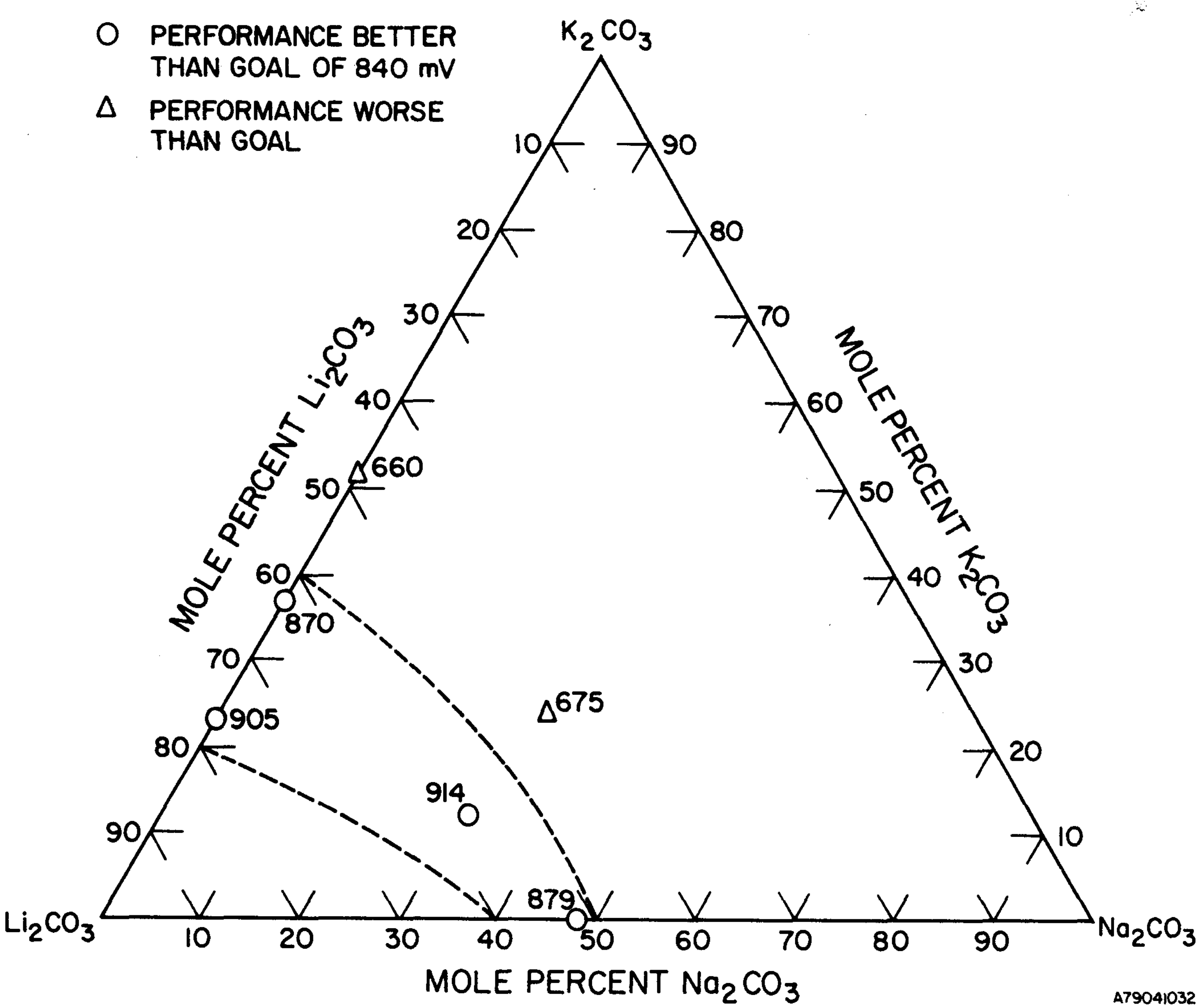

Figure 1.26. COMPOSITIONS OF INTEREST IN THE Li_2CO_3-Na_2CO_3-K_2CO_3 SYSTEM AS JUDGED BY CELL POTENTIAL AT 160 mA/cm^2 of 3-cm^2 CELLS

specimen consisted of an electrolyte tile coupled with a porous anode sandwiched between two stainless steel perforated sheets as supports. The sandwich was held together with stainless steel clips. The electrolyte tiles were pressed from six different electrolyte batches, and the electrodes were sampled from six different materials described in Subtask 1.1.1. The test specimens were placed on porous alumina supports inside a three-zone Lindberg tube furnace and maintained under a constantly flowing stream of anode gas at 650°C. Two samples of each tile/anode couple were tested.

The test was started with a low-Btu fuel gas mixture (21.1% H_2, 9.2% CO_2, 17.8% CO, 5.6% H_2O, balance N_2 at equilibrium), but was changed to a high-Btu mixture (60.0% H_2, 7.4% CO_2, 10% CO, and 22.6% H_2O) after ~100 hours because of a gas flow blockage attributed to carbon deposition from the low-Btu mixture. After 250 hours of testing, the furnace was shut off and allowed to cool. One sample from each tile/anode couple was taken for analysis. The remaining samples were tested for an additional 750 hours (total exposure = 1000 hours) and then analyzed.

The anodes separated cleanly from the electrolyte tiles after the test. After separation from the electrodes, the electrolyte tiles were measured to determine the changes in weight and dimensions. A small piece of tile, approximately 0.5 gram, was saved from each sample for analysis of electrolyte composition, and the remainder was washed with 70% acetic acid/30% acetic anhydride solution to obtain the $LiAlO_2$ particles. The $LiAlO_2$ was analyzed for phase composition, surface area, and microstructure. The results of these various analyses of the tile materials are presented in Table 1.14. Physically the tiles did not deform or lose weight appreciably, except for tile AD55-2B, which was tested for 1000 hours. This tile was badly cracked and had lost 18% of its original weight. These observations probably indicate poor carbonate-retaining properties of α-$LiAlO_2$, as the tile contained 88% α — the highest among all the tiles tested.

The chemical composition of the electrolyte tiles remained essentially unchanged after 250 hours; this was expected because of small changes in tile weights. The analyzed compositions after 1000 hours of testing are not yet available, but should provide information regarding any preferential loss of one alkali component over the other under simulated anode conditions.

The electrolyte tiles that did not contain any Kanthal A-1 reinforcement were analyzed for metallic elements contained in the coupling anodes to obtain indications of anode/electrolyte interactions. The results of the 250-hour tests are shown in Table 1.15. The levels of Co and Ni, as analyzed by atomic absorption spectroscopy, were fairly low, while Cr levels were significantly higher. More detailed analyses of the carbonate and aluminate components are desirable to isolate and understand the possible effects of such chemical interactions on $LiAlO_2$ stability.

Changes in $LiAlO_2$ phase composition indicated the following:

a. Transformation to and from the γ-phase is insignificant under the described environment.

b. When the α-phase is initially present in small percentages (<5%), the β to α transformation is much slower, as observed for AD55-6A and AD55-50-1A tiles, than when initial α contents are higher.

c. Not enough data are available to assess the effect of carbonate composition on the rate of the β to α transformation.

The following observations were made from the $LiAlO_2$ stability data shown in Table 1.14 —

- In all the tile materials studied, there was a tendency to form α-phase $LiAlO_2$ at the expense of β-phase.
- When the α-phase was initially present in small concentrations (<5%), the β to α transformation was much slower than for higher initial α contents.
- All materials showed a decrease in $LiAlO_2$ surface area as a result of high-temperature exposure to the simulated fuel environment.
- Not enough data are available to assess the effect of carbonate composition on the rate of the β to α transformation.
- Transformation from β- to γ-$LiAlO_2$ was insignificant under the test conditions studied.
- The greatest stability with respect to α formation and surface area loss was exhibited by electrolyte AD55-6A, which was originally 100% β of rod-like morphology.

These results will be compared with $LiAlO_2$ stability data currently being obtained on materials extracted from cells operated for as long as 3000 hours under this program to obtain a better understanding of the mechanism and kinetics of $LiAlO_2$ transformations under actual operating conditions.

Table 1.14. LiAlO$_2$ STABILITY RESULTS FOR VARIOUS TILE/ANODE COUPLES TESTED UNDER SIMULATED ANODE ENVIRONMENT

Electrolyte	Coupling Anode Material	Test Period, Hours	Percent Change in Tile				Electrolyte Composition				LiAlO$_2$ Composition, α/β/γ	LiAlO$_2$ Surface Area, m^2/g	Mean Pore Size, μ
			Weight	Diameter	Thickness	Density	LiAlO$_2$	Li$_2$CO$_3$	K$_2$CO$_3$	Li$_2$CO$_3$:K$_2$CO$_3$ Molar Ratio			
AD55-2B	Ni	0	0	0	0	0	45.0	26.2	28.8	1.71	75/25/0	12.2	
	(480-31-42)	250	- 3.5	-0.1	+ 2.9	- 6.4	43.4	25.6	30.9	1.55	80/20/0	7.0	0.40
		1000	-18.0	-0.2	+11.5	-27.2					88/12/0	5.5	
AD55-2D	Ni+10% Ni Cr	0	0	0	0	0	44.1	26.7	29.2	1.71	29/70/1	24.7	0.19
	(416-71-4)	250	- 3.9	+0.1	+ 6.8	- 5.3	43.6	26.9	29.4	1.71	65/32/3	12.9	0.28
		1000	- 9.7	0	- 1.8	- 8.5					60/37/3	9.7	
AD55-6A	CO+10% WC	0	0	0	0	0	45.7	25.5	28.8	1.66	0/100/0	15.8	0.18
	(416-66-1)	250	- 1.9	-0.2	+ 3.4	- 5.1	47.1	25.5	27.4	1.74	3/97/0	11.8	0.21
		1000	- 8.8	-0.2	- 1.8	- 7.1					2/98/0	9.7	
AD55-12A	Co+10% Ni Ca	0	0	0	0	0	48.9	19.0	32.1	1.11	27/59/14	13.4	
	(416-66-3)	250	- 2.9	+0.2	+ 4.1	- 7.5	47.5	21.3	31.1	1.277	43/40/17	8.1	
		1000	- 8.5	-0.4	+ 2.7	-10.9					69/19/12	5.0	
AD55-LN-1A	Co+10% Cr	0	0	0	0	0	42.1	25.0	32.9*	1.09*	7/90/3	13.7	
	(416-66-6)	250	- 4.2	-0.2	- 0.7	- 4.7	46.3	23.0	30.7*	1.07*	22/77/1	8.4	0.30
		1000	-10.8	-0.3	+ 9.7	-25.4					67/33/0	3.5	
AD55-50-1A	CO	0	0	0	0	0	48.5	32.8	18.7	3.27	3/94/3	10.1	0.35
	(480-31-62)	250	- 1.5	+0.6	+ 9.5	-12.3	50.0	31.4	18.7	3.15	9/89/2	7.1	
		1000	- 5.8	0	+ 3.1	- 9.0					26/71/3	4.1	

---

*Na$_2$CO$_3$ substituted for K$_2$CO$_3$

Table 1.15. ANALYSIS OF ANODE METALLIC ELEMENTS IN ELECTROLYTE TILES AFTER 250 HOURS OF TESTING

Electrolyte Tile	Coupling Anode	Chemical Analysis		
		% Co	% Cr	% Ni
AD55-2B	Ni (480-31-42)	-	-	0.066
AD55-2D	Ni + 10% Ni Cr (416-71-4)	-	0.133	0.017
AD55-6A	Co + 10% WC (416-66-1)	<0.036	-	-
AD55-12A	Co + 10% Ni Cr (416-66-3)	<0.036	0.198	0.022
AD55-LN-1A	Co + 10% Cr (416-66-6)	0.025	0.010	-
AD55-50-1A	Co (480-31-62)	<0.036	-	-

1.2. Cost-Effective Electrolyte Tiles

As the development of the molten-carbonate fuel cell system proceeds into the demonstration and commercialization stages, large quantities of electrolyte tiles will be required. A 5-MW demonstration system operating at an ECAS-projected[10] power density level of 127 W/ft^2 will require 39,370 ft^2 of tile. Similarly, each 100 MW of installed fuel cell plant capacity corresponds to over 785,000 ft^2 of tile requirement. Thus, if the molten-carbonate fuel cell system is to have a significant impact on electrical power production, then a tile fabrication process capable of mass-production of high-quality tiles at a low cost clearly must be developed.

The fabrication processes used in the conventional powder metallurgy, ceramics, glass, and plastics industries were evaluated for their potential ability to form the composite alkali carbonate/lithium aluminate tile into thin, high-density ($\geq$95% of theoretical) shapes with relatively small tolerances. Although systems studies currently being performed may identify other suitable configurations, most attention was given to the fabrication of thin (~0.05 to 0.07 inch in thickness), square or rectangular tiles with cross-sectional areas of 2 to 4 ft^2. A rather tight tolerance will have to be maintained on the thickness and parallelism of such tiles to minimize potential problems associated with gas leakage through wet seals and to maintain geometric compatibility at gas manifolds, etc., when many cells are assembled into a package. Incorporating reinforcement structures and openings for gas transfer are also being considered.

The processes evaluated can be divided into two classes of operations: a) cold forming and b) hot forming. The cold-forming class of operations can be further subdivided into those operations requiring the application of a load to form the "green" body and those, such as slip casting, requiring no pressure or a nominally low pressure. A list of the processes considered is given in Table 1.16.

It is apparent that a number of related problem areas need to be addressed when choosing processes for experimental testing, such as —

- Can "green" tile bodies be fired to the required density after a cold-forming operation without warping, cracking, or blistering?
- Binders and plasticizers used in conjunction with cold forming need to be compatible with $LiAlO_2$ and the carbonate in a nonaqueous solvent.

Table 1.16. MASS-PRODUCTION PROCESSES UNDER EVALUATION FOR FABRICATION OF ELECTROLYTE TILES

Cold Forming		
Pressure	Pressureless	Hot Forming
Die Pressing	Slip Casting	Hot Pressing
Anvil Pressing	Tape Casting	Hot Extrusion
Isostatic Pressing		Hot Rolling
Extrusion		Hot Stamping
Roll Compaction		Fusion Casting
		Injection Molding

- For hot-forming processes, the rheological behavior, or plastic deformation response, of the tile to the temperature/pressure conditions needs to be experimentally determined.
- In any mass-production process involving processing of a powder, the flow of the powder from storage hoppers into the forming cavity must be reliably maintained. Spray-drying of powders with binders to form spherical agglomerates of fine particles is widely used in the conventional ceramics industry to provide the necessary powder flowability. An adequate nonaqueous spray drying process will probably have to be identified for the electrolyte powder.
- Consideration needs to be given to the use of reinforcement within the tile body and to the incorporation of gas-transfer holes.
- The overall impact of using low-cost raw materials on tile processing and quality must be evaluated.

After preliminary evaluation of the above processing considerations, contacts were made with production or research and development groups of five major companies involved in the high-volume production of technical ceramics and glasses. Based on its experience and expertise in fabricating a wide range of high-quality technical ceramic products, Coors Porcelain Co., Golden, Colorado was selected to identify and perform experimental feasibility studies on potential cost-effective tile fabrication processes, under subcontract to IGT. The following section summarizes the tile fabrication studies performed by Coors Porcelain. Cell test evaluation results of tiles provided by Coors to IGT are presented in Section 2.1.1. Cell performance levels attained with tiles fabricated by the simulated roll compaction/warm laminate/hot stamping process were comparable with those from conventionally hot-pressed tiles, confirming the potential of this process.

1.2.1. Summary of Tile Fabrication Studies Performed by Coors Porcelain Co.

The objective of this project was to investigate potential ceramic fabrication processes applicable to cost-effective mass production of molten carbonate fuel cell electrolyte tiles and to provide samples of tiles for evaluation.

The most feasible fabrication method at this stage of the development seems to be a three-stage process. First, the electrolyte powder is formed into a thin sheet by roll compaction. (Tape casting or sheet extrusion and calendering are also possibilities.) Next, warm lamination is used to incorporate Kanthal reinforcement screens between electrolyte sheets. Finally, the laminates are hot-stamped to achieve final densification and to cut the tiles to size.

Roll compaction, tape casting, sheet extrusion, and calendering were selected over iso-pressing, dry pressing, and slip casting because they are the most cost-effective methods of producing large thin sheets. Also, the resulting sheets are flexible and, consequently, are easy to handle and more amenable to lamination.

Of the three methods, roll compaction appears to be the most favorable as it is faster than tape casting and less complicated than sheet extrusion and calendering.

The scope of the project was, therefore, to examine the electrolyte powder and its response to various preparation and fabrication techniques. These results will provide the necessary insight into the viability of the conceptual "roll compaction/warm laminate/hot stamp" process.

The project was divided into the following areas: electrolyte powder characterization, the response of the powder to dry ball-milling, and the cold- and hot-pressing characteristics of milled and unmilled powders.

1.2.1.1. Characterization

The material used for this project was DOE electrolyte powder from Lot No. AD55-2D. The powder was characterized using scanning electron microscopy, thermal gravimetric analysis (TGA) and B.E.T. gas adsorption.

SEM photographs show that the as-received powder consists of agglomerates ranging from a few microns to 250 microns. (See Figure 1.27.) Other than size, the particles all have a similar appearance; $LiAlO_2$ particles cannot be differentiated from carbonate particles. An energy dispersive X-ray (EDAX) on several particles showed them all to contain potassium, lithium, and aluminum cations; it appears that the agglomerates are composed of both $LiAlO_2$ and carbonate particles.

A particle-size distribution was obtained by measuring the agglomerates shown in Figure 1.27. The results are listed in Table 1.17. The range of particle sizes observed (28% smaller than 10 microns and 5% larger than 100 microns) is usually not conducive to forming compacts with a homogenous microstructure.

Table 1.17. PARTICLE SIZE DISTRIBUTION FOR AS-RECEIVED AND MILLED POWDERS

Size Range,	As-received Powder	4-Hour Milled Powder	6.5-Hour Milled Powder
	Distribution, %		
0-10	28%	53%	80%
10-30	26%	39%	14%
30-50	26%	7%	5%
50-100	15%	1%	1%
100-200	4%	0	0
>200	1%	0	0

A TGA was run up to 1000°C, with a heating rate of 5°C/minute. The sample began to lose weight gradually at 150°C. The weight loss was then linear up to 850°C, where the total weight loss was 4%. Between 850° and 1000°C, the sample lost weight rapidly; an additional 22% was lost for a total weight loss of 26%. These results indicate that the sample did not contain a significant amount of water, and that only one species was responsible for the observed weight loss. This species is probably the carbonate salts; it appears that they evaporate slowly up to 850°C, at which point they begin to vaporize rapidly.

The surface area was measured by B.E.T. gas adsorption to be 1.4 m^2/gram. This is significantly smaller than the 19.6 m^2/gram surface area of the

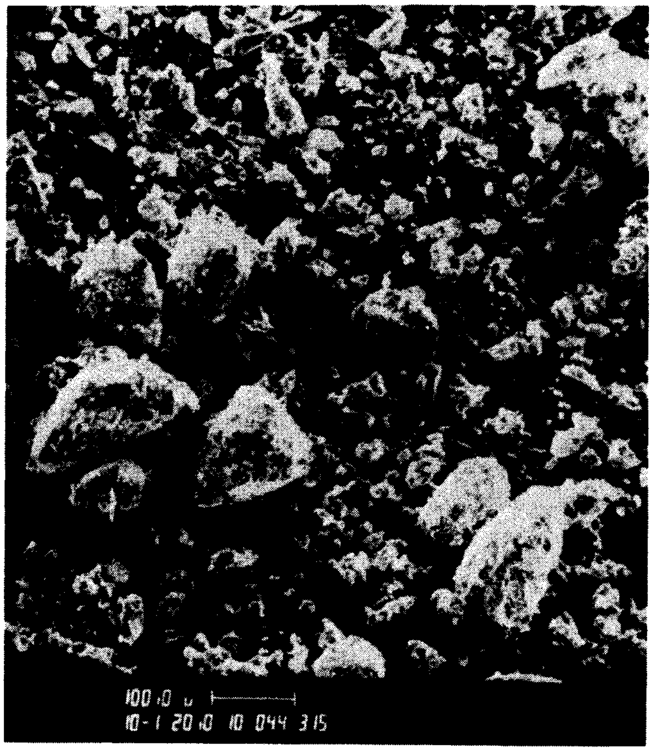

Figure 1.27. SEM PHOTOGRAPH OF AD55-2D
AS-RECEIVED POWDER (100 X)

washed $LiAlO_2$ particles measured at IGT. These results, combined with the EDAX data, indicate that the agglomerates are made of high surface area $LiAlO_2$ particles bound together by carbonate salts.

In conclusion, the most striking feature of the as-received AD55-2D powder is the presence of large agglomerates. How they react under an applied pressure could have a profound effect on the powder compact's "green" density. If the agglomerates do not break down, it could result in large pores and/or low density regions that would decrease the compact's overall density. Thus, the powder was subjected to various milling conditions in an attempt to break up these agglomerates and observe the effect on the powder's compaction characteristics.

1.2.1.2. Dry Ball-Milling Tests

The as-received powder was milled in a high-alumina ball-mill (6-in.-ID) charged with a high-alumina medium (0.4-in. diameter) to a powder ratio of 6:1. All milling runs were made at 90 rpm.

When milled, the as-received powder stuck excessively to the sides of the mill and the medium. This reduced the milling action and made testing laborious, so a combination grinding aid and lubricant was added. This successfully solved the caking problem.

Powder samples (containing the grinding aid) were milled for runs of 2, 4, 6.5, and 66 hours. SEM photos of the 4 and 66-hour milled powders are shown in Figures 1.28 and 1.29, respectively. It is evident that the ball-milling was effective in breaking down the agglomerates. For example, the largest agglomerates for the 66-hour powder were approximately 30 microns compared with 250 microns for the as-received powder. The particle size distributions for the as-received, 4 and 6.5-hour milled powders are listed in Table 1.17.

1.2.1.3. Cold Pressing Tests

The compaction response of the as-received and milled powder was examined using a characterization technique described by Niesz.[11] Pressure-density data for the as-received and 6.5-hour milled powders was obtained from 5 to 60,000 psi. This data was used to make a plot of percent-theoretical-density versus logarithm of pressure (see Figure 1.30).

Figure 1.28. SEM PHOTOGRAPH OF 4-HOUR MILLED POWDER (120 X)

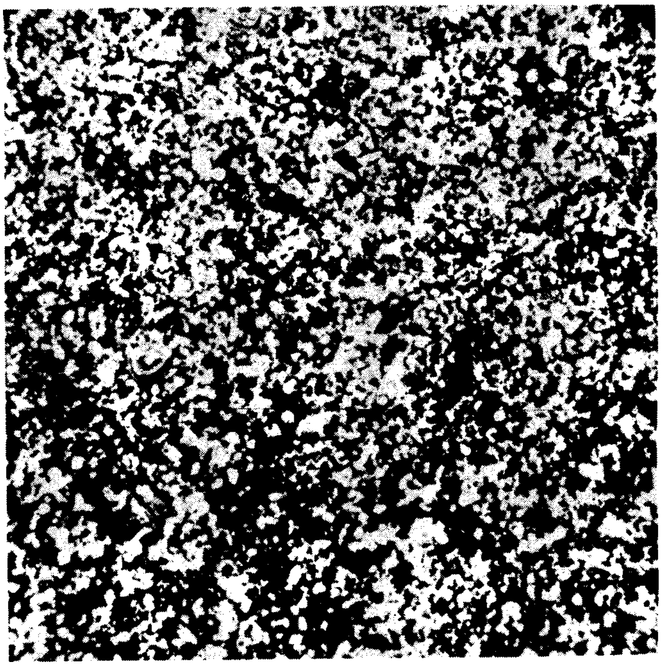

Figure 1.29. SEM PHOTOGRAPH OF 66-HOUR MILLED POWDER (120 X)

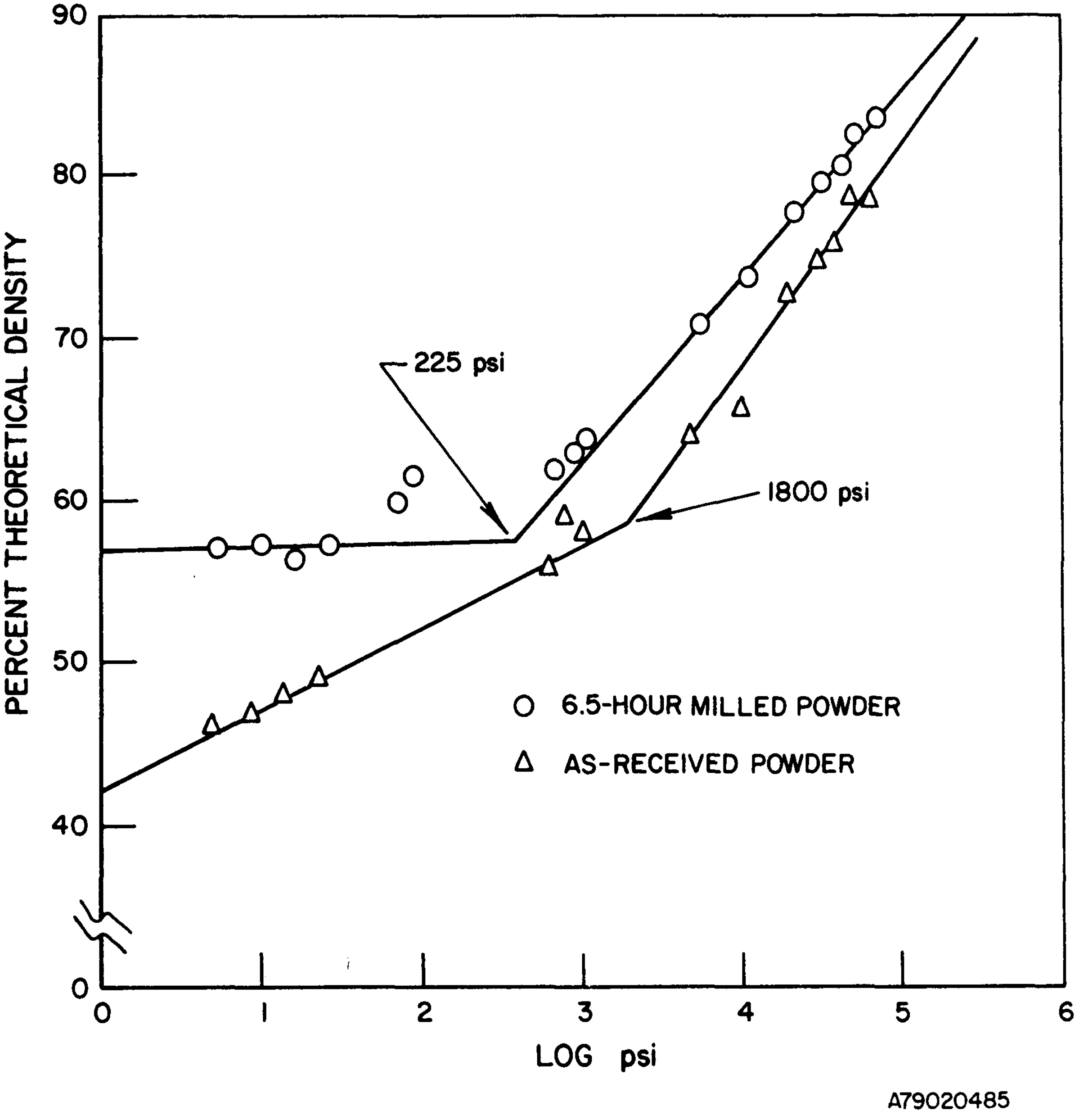

Figure 1.30. COMPACTION RESPONSE OF MILLED AND AS-RECEIVED POWDERS

Such plots are useful because they usually contain several linear regions which are each controlled by different compaction mechanisms. The intersections of the linear regions can be used to evaluate the strength of the powders being compacted.

Figure 1.30 shows that each plot has two linear regions. Looking at the low-pressure regions, it can be seen that the tap density (where log psi equals 0) for the 6.5-hour milled powder is higher than that of the as-received powder. The lower density for the as-received powder is probably the result of large porous agglomerates, such as the ones shown in Figure 1.27. Milling the powder breaks down these porous agglomerates and enables the powder to pack with fewer inhomogeneities; both of these effects result in higher densities.

When the pressure is applied initially, compaction is achieved by particle sliding and rearrangement. Thus, compaction in the low-pressure region is controlled by particle-particle friction. The slope in this region is steeper for the as-received powder compacts because their coarser pore structure allows more particle rearrangement before the available interstices are filled and the agglomerates impinge on one another.

The 6.5-hour milled powder compact densities did not increase significantly until the applied pressure was great enough to break up or crush the agglomerates. This induced more particle rearrangement, which is controlled by the strength of the agglomerates. This compaction mechanism is evidenced by the high-pressure linear regions in Figure 1.30.

The intersection of the high- and low-pressure regions correlated with the strength of the agglomerates. The intersection for the 6.5-hour milled powder, 225 psi, is lower than for the as-received powder, 1800 psi, so milling the powder reduces the strength of the agglomerates as well as their size. This enables the milled powder to be compacted to higher densities over the entire range of the pressures examined.

These tests provided encouraging results. They showed that ball milling enables the DOE powder to be pressed to over 80% of its theoretical density (2.0 grams/cc) at pressures comparable to those exerted during roll compaction.

1.2.1.4. Hot-Pressing Tests

All hot-press tests were made using the tooling shown in Figure 1.31. The die is made out of TZM molybdenum, and the spacers and punch are made out of Poco graphite. The die cavity is 1.019 inches in diameter. The tooling was heated using an induction furnace, and the parts were pressed in an air atmosphere.

Initial tests showed that the standard hot-pressing schedule used at IGT to make electrolyte tiles can be streamlined considerably. The standard schedule calls for as-received powder (precompacted only by the weight of the pressing apparatus) to be heated to 485°C and pressed for 5-minute intervals at 1100, 2200, and 3550 psi. It was found that parts can be pressed to an acceptable density (95% of theoretical) at 485°C by applying a load of 750 psi for an instant (the time it takes to release the hydraulic fluid from the ram, which is approximately 2 seconds). Following this schedule, parts were pressed to 96% of theoretical density (2.34 grams/cc).

The microstructure for such a part is shown in Figure 1.32. Porosity is observed in both the partially densified agglomerates and in the interstices formed by the packed agglomerates. Some areas may also contain free carbonate, although further microstructural analysis is required to confirm this.

The fact that the schedule could be streamlined to such an extent was encouraging because it indicates that the hot-stamping stage of the conceptual fabrication process may be possible. Reducing the pressure to this extent means the load required to hot-stamp a 4-ft^2 tile is reduced from 1000 tons to 220 tons.

Unfortunately, it was not quite as easy to hot-press the 6.5-hour milled powder to greater than 95% of theoretical density. When the powder (precompacted by approximately 40 psi due to the weight of the apparatus) was heated and pressed at 1000 psi for an instant, the density was only 2.01 grams/cc. To reach a density of 2.34 grams/cc, it was necessary to press at 7700 psi.

Subsequently, the 6.5-hour milled material was calcined in air at ~500°C overnight to assure complete removal of the milling aid. It was found that this treatment permitted a 2.32 g/cm^3 tile density to be achieved after pressing for 1 second at 1000 psi and 485°C. Thus, the higher pressure

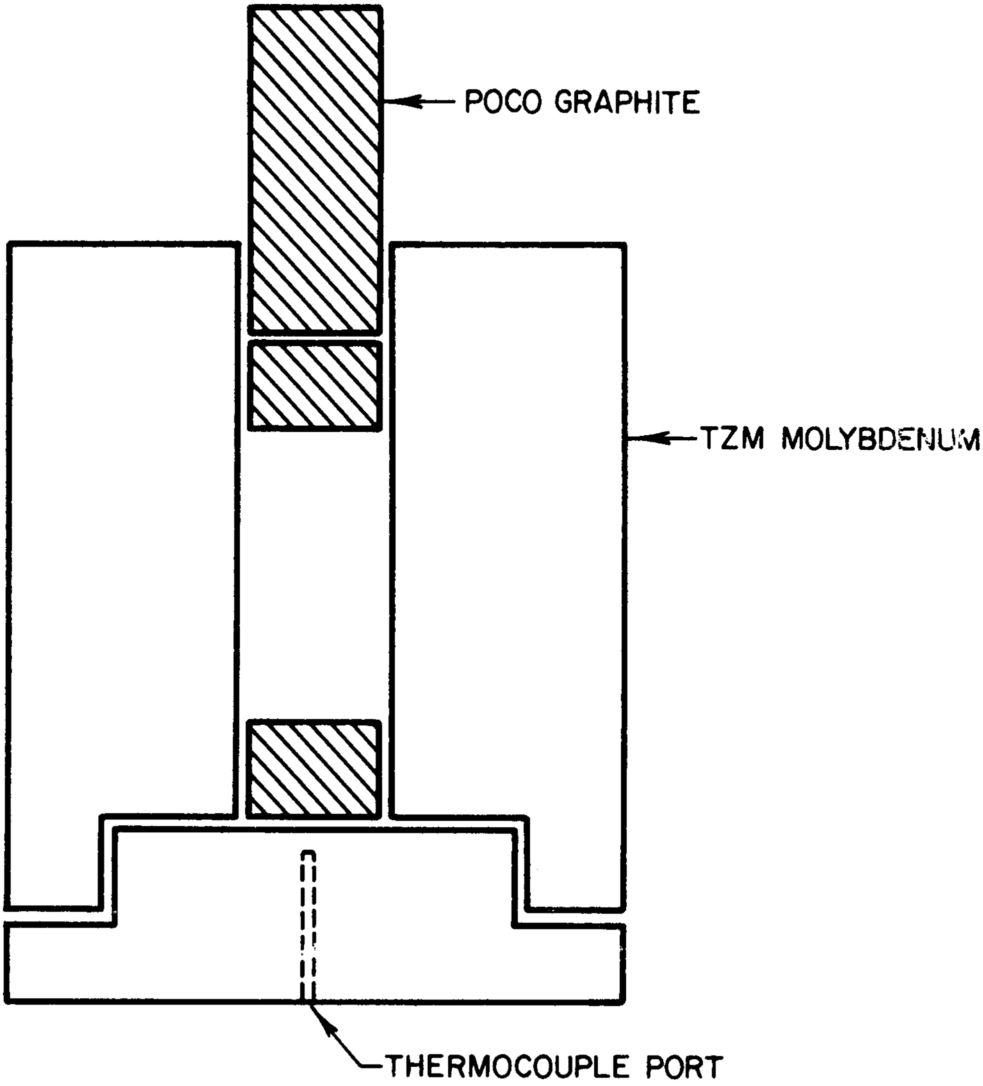

A79020464

Figure 1.31. HOT PRESS TOOLING (0.8 in. = 1 in.)

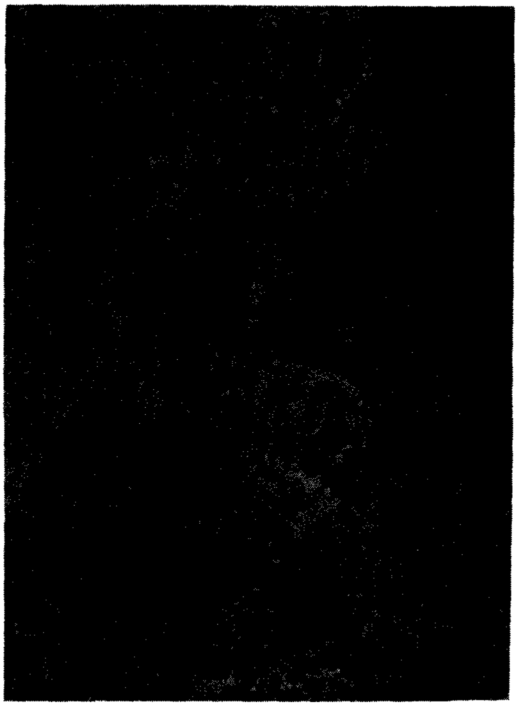

Figure 1.32. POLISHED SECTION OF AS-RECEIVED POWDER
HOT PRESSED AT 750 PSI AND 485°C
DENSITY = 2.34 gm/cc. (200 X)

required to achieve high density in the initial milling experiments was associated with incomplete removal of the milling aid rather than agglomerate size and carbonate redistribution effects.

Figure 1.33 shows the microstructure of a 6.5-hour milled sample with a density of 2.34 grams/cc. The microstructure is much finer and more homogenous than that of as-received powder samples with a comparable density. (See Figure 1.32.) It will be very instructive to determine how the cell performances, mechanical strengths, and bubble pressures of the two types of microstructure compare.

For the next stage of the development program, a fabrication technique that roughly simulates a roll compaction/warm lamination/hot stamping process was used to make electrolyte tiles.

First, two as-received powder wafers were pressed to 40,000 psi (this is comparable to the pressure exerted during roll compaction). A disc of Kanthal screen was placed between the wafers and they were loaded into the hot press. They then were heated to 485°C and pressed at 1000 psi.

Figure 1.34 shows the microstructure of such a sample. The white oval in the photograph is the result of light reflecting off of the Kanthal wire. It can be seen that the wafers knitted together well, and that the Kanthal wire was well incorporated into the electrolyte. Cold pressing the powder at 40,000 psi broke up agglomerates, so the $LiAlO_2$ particles are finer than in the samples pressed below 1800 psi (See Figure 1.32.) The electrolyte density of this sample is 2.35 grams/cc.

A similar fabrication technique was used to prepare samples with 6.5-hour milled powder, with the only difference being that the samples were hot-pressed at 7700 psi. A typical microstructure is shown in Figure 1.35. Again, the wafers knitted together and the wire was well incorporated into the electrolyte. The microstructure is fine and homogenous; hopefully, this will increase the strength and enable such tiles to withstand the fuel cell environment better than the as-received powder tiles.

The fabrication technique used to make the sample tiles does not simulate a roll compaction/warm lamination/hot stamping process exactly. A roll compaction process may produce a different microstructure, and there may be

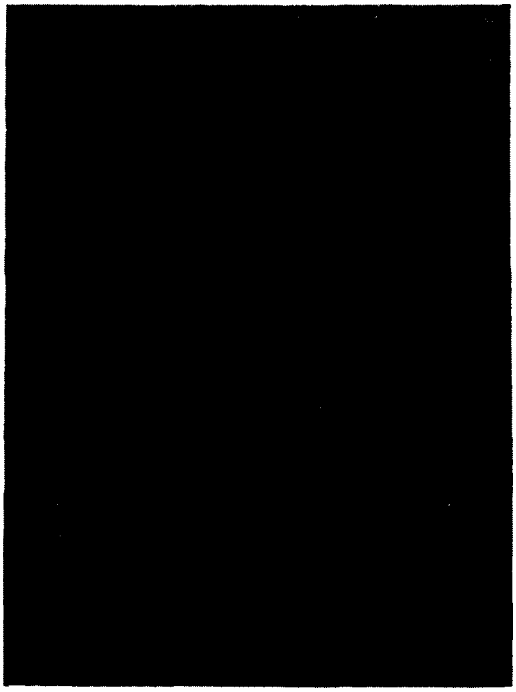

Figure 1.33. POLISHED SECTION OF 6.5-HOUR MILLED POWDER
PRESSED AT 7700 PSI
DENSITY - 2.34 gm/cc (200 X)

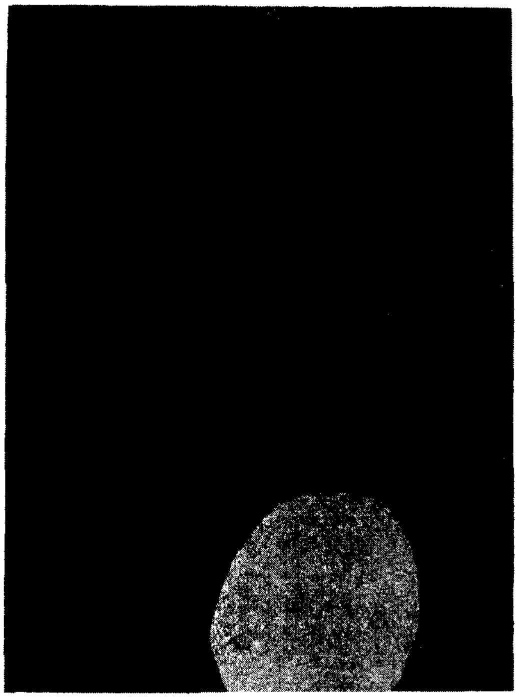

Figure 1.34. POLISHED SECTION OF ELECTROLYTE TILE SAMPLE MADE USING AS-RECEIVED POWDER (200 X)

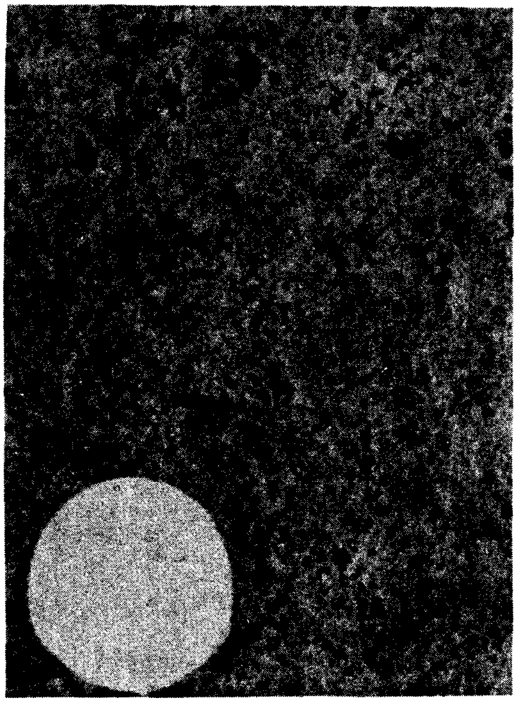

Figure 1.35. POLISHED SECTION OF ELECTROLYTE TILE SAMPLE MADE USING 6.5-HOUR MILLED POWDER (200 X)

problems with binder burnout. However, the results do indicate that such a process using hot stamping or hot rolling as the final operation is possible.

1.2.1.5. Summary

AD55-2D electrolyte powder is made of agglomerates ranging from a few microns to 250 microns. When this powder is cold- and hot-pressed, the microstructures are coarse and inhomogeneous. Milling the powder breaks down these agglomerates and enables parts to be pressed with finer and more homogeneous microstructures.

The most feasible fabrication method for mass producing electrolyte tiles seems to be a roll compaction/warm lamination/hot stamping process. Initial tests have been performed that indicate such a process is possible. Scale-up of such a process, the study of nonaqueous spray-drying operations, the use of binders and plasticizers, and the study of tile microstructural effects, etc., should be pursued in the next phase of this work.

1.3. Cell and Component Development. Bench-Scale Cell Testing

1.3.1. Introduction and Summary

The objective of this subtask is to test in bench-scale cells (1 atm pressure) the components developed under Subtask 1.1, to —

a. Demonstrate their performance capabilities on low-Btu fuel gas
b. Identify the physical and chemical changes occurring in cell components during operation.

The goals of this subtask were to —

1. Demonstrate the performance of 0.74 volts at 160 mA/cm^2 on low-Btu fuel gas and standard oxidant at 75% fuel and 50% CO_2 utilizations
2. Demonstrate Goal a performance after 1000 hours of operation with 10 ppm H_2S in the low-Btu fuel gas.

During fiscal year (FY) 1978, we operated four bench-scale cells to evaluate the components that IGT developed for DOE. The results of these cells show that —

- Bench-scale cells assembled with tiles pressed with electrolyte powders prepared by the modified aqueous slurry process are capable of yielding power outputs equal to, or better than, those of cells assembled with state-of-the-art electrolytes. As with state-of-the-art tiles, pressed densities greater than 95% of theoretical are necessary to obtain performance levels at, or above, 740 mV at 160 mA/cm^2, with low-Btu fuels.

- Bench-scale cells assembled with Co + 10% Cr anodes yield power outputs equal to, or better than, those of cells assembled with state-of-the-art anodes.
- A bench-scale cell assembled with an AD55-2C electrolyte tile (modified aqueous slurry process) and a Co + 10% Cr anode attained, or surpassed, the Goal 1 performance level of 740 mV at 160 mA/cm^2 with 75% fuel and 50% CO_2 (oxidant) utilizations for 60 hours, thus demonstrating the performance capabilities of the components developed during FY 1978.
- A similar cell is presently in operation to demonstrate the performance capability when the low-Btu fuel gas contains 10 ppm H_2S. This cell will continue to operate during the FY 1979 program.

In addition, some preliminary wet-seal efficiency tests showed that, early in life, these cells are capable of withstanding a pressure differential of up to 15-in. water column across the wet seals, for periods of 1 to 2 hours, without a significant increase in leakage. However, additional testing is necessary to verify these results and to evaluate the capability of the tiles to withstand such pressure differentials without increased reactant crossover (bubble pressure). This testing will be conducted during the FY 1979 program.

1.3.2. Bench-Scale Cell Tests

Four bench-scale cells (94-cm^2 active electrode area) were operated during FY 1978 to evaluate the electrolyte tiles and electrodes developed under Subtask 1.1. The first two cells were assembled with state-of-the-art electrodes to evaluate an electrolyte prepared by the aqueous slurry process (without the uncertainties that would be introduced when using unproven electrodes). Once the electrolyte was proven and its performance capabilities demonstrated, two other cells were assembled with DOE electrodes and tiles and their performance demonstrated. Tables 1.18 through 1.21 list the components used in these four assemblies and their characteristics. A description of the performance behavior of these four cells follows.

Cell DOE 78-1

This cell was assembled to evaluate one of the first large tiles (6-5/8 inch-diameter) pressed with electrolyte AD55-2C (56.4% carbonates; $\alpha/\beta/\gamma$ $LiAlO_2$ = 53/47/0). These early tiles were of lower density (~2.0 g/cm^3) as we were experimenting with pressing temperatures and pressures to determine the optimum conditions to obtain tiles in the 2.3 g/cm^3 density range. However, we felt it was necessary to begin bench-scale cell testing, in spite

Table 1.18. CELL COMPONENT CHARACTERISTICS FOR CELL DOE 78-1

CURRENT COLLECTORS -	Anode	● Type 316 Stainless Steel Perforated Plate
		● 3/32-in.-diam holes on staggered 5/32-in. centers
		● 47 holes/in.^{2}
		● 67% coverage
	Cathode	● Type 316 Stainless Steel Perforated Plate
		● No. 7 straight, 0.057-in.-diam holes
		● 144 holes/in.^{2}
		● 62% coverage
ELECTROLYTE TILE -	Batch:	AD55-2C
	H.P. No.:	247 at 480°C and 3550 psi (before cold-pressing
	Reinforcement:	2.08 vol % Kanthal
	Thickness:	1.969 mm, avg
	Weight:	57.6915 grams
	Density:	2.019 g/cc (84.4% of theoretical density)

Table 1.19. CELL COMPONENT CHARACTERISTICS FOR CELL DOE 78-2

CURRENT COLLECTORS - Anode

- Type 316 Stainless Steel Perforated Plate
- 3/32-in.-diam holes on staggered 5/32-in centers
- 47 holes/in.^{2}
- 67% coverage

Cathode

- Type 316 Stainless Steel Perforated Plate
- No. 7 straight, 0.057 in.-diam holes
- 144 holes/in.^{2}
- 62% coverage

ELECTROLYTE TILE -

Batch: AD55-2C
H.P. No.: 250 at 487°C and 7000 psi (before cold-pressing)
Reinforcement: 2.07 vol % Kanthal
Thickness: 1.811 mm, avg
Weight: 57.14 grams
Density: 2.305 g/cc (96% of theoretical density)

Table 1.20. CELL COMPONENT CHARACTERISTICS FOR CELL DOE 78-3

Characteristic	Anode*	Cathode
Manufacturer	Gould Inc.	Gould Inc.
Material	Co + 10% Cr	Nickel
Part No.	416-66-5	480-31-29
Mean Pore Size, μ	3.2	8.9
80% Pore Spectra, μ	1.7 to 5.2	4.5 to 16.5
Pore Spectra Porosity, %	80.1	79.6
Surface Area, m^2/g	0.566	0.155
Thickness, mm	0.79	0.53
Weight, grams	13.9	10.5

CURRENT COLLECTORS -

Anode

- Type 316 Stainless Steel Perforated Plate
- 3/32-in.-diam holes on staggered 5/32-in centers
- 47 holes/in.^{2}
- 67% coverage

Cathode

- Type 316 Stainless Steel Perforated Plate
- No. 7 straight, 0.057-in.-diam holes
- 144 holes/in.^{2}
- 62% coverage

ELECTROLYTE TILE:

Batch: AD55-2C

H.P. No.: 251, at 492°C and 7000 psi (before cold-pressing)

Reinforcement: 2.08 vol % Kanthal

Thickness: 1.776 mm, avg

Weight: 56.0 grams

Density: 2.309 g/cc (96.5% of theoretical density)

---

*Anode wet-seal protected with aluminized coating.

Table 1.21. CELL COMPONENT CHARACTERISTICS FOR CELL DOE 78-4

Characteristic	Anode*	Cathode
Manufacturer	Gould Inc.	Gould Inc.
Material	Co + 10% Cr	Nickel
Part No.	416-66-6	--
Mean Pore Size, μ	3.03	9.05
80% Pore Spectra, μ	1.69 to 7.61	4.5 to 15.87
Pore Spectra Porosity, %	76.49	76.76
Surface Area, m^2/g	0.461	0.139
Thickness, mm	0.79	0.41
Weight, grams	16.81	11.36

CURRENT COLLECTORS - Anode

- Type 316 Stainless Steel Perforated Plate
- 3/32-in.-diam holes on staggered 5/32-in. centers
- 47 holes/in.^{2}
- 67% coverage

Cathode

- Type 316 Stainless Steel Perforated Plate
- No. 7 straight, 0.057-in.-diam holes
- 144 holes/in.^{2}
- 62% coverage

ELECTROLYTE TILE:

Batch: AD55-2D
H.P. No.: 254, at 480°C and 3550 psi (before cold-pressing)
Reinforcement: 2.06 vol % Kanthal
Thickness: 1.875 mm, avg
Weight: 58.25 grams
Density: 2.271 g/cc

---

*Anode wet-seal protected with aluminum foil.

of the low-density tiles to obtain preliminary cell performance data with the new electrolyte. In addition, to ascertain electrolyte performance capabilities without the uncertainties that new, unproven electrodes could introduce, it was decided that the first few electrolyte tests had to be conducted with proven, state-of-the-art electrodes.

The components used in the assembly of Cell DOE 78-1 are listed in Table 1.18 The cell operated for 315 hours and was voluntarily terminated after it demonstrated that, in spite of a lower density tile (2.02 g/cm^3), electrolyte AD55-2C was capable of sustaining a performance just 10 mV lower (at 160 mA/cm^2) than state-of-the-art electrolytes when the fuel is the product gas from steam-reformed naphtha. We expected to match or surpass state-of-the-art performance with higher density tiles. The performance parameters for this cell are shown in Figures 1.36 and 1.37. Notice in Figure 1.36 that the initial rate of performance gain of Cell DOE 78-1 is slow. This is because of the low density tile: As the carbonate melts and expands, it fills the void volume of the tile instead of the pores of the electrodes, and as a result, a longer time is needed for the cell to reach its full performance potential.

Cell DOE 78-2

This cell was a repeat of Cell DOE 78-1, except that the electrolyte tile (AD55-2C) was of high density (2.305 g/cm^3; 96% of theoretical). As expected, because of the higher density, the initial rate of performance gain was much faster than that of DOE 78-1: Approximately 100 hours to reach peak power output versus 250 hours for DOE 78-1.

Cell DOE 78-2 operated for a total of 315 hours, the first 200 hours on a fuel simulating the product gas from steam-reformed naphtha, and the last 115 hours on a low-Btu, air-blown, coal gasification product (standard oxidant during the 315 hours). Figure 1.36 presents the cell's performance while on a steam-reformed naphtha fuel, and shows that cells assembled with electrolyte AD55-2C are capable, at least during the first 200 to 300 hours, of sustaining performance levels comparable to those of state-of-the-art cells (~770 mV at 160 mA/cm^2; 75% fuel and 50% CO_2 utilizations). Figure 1.37 includes a life-graph of Cell DOE 78-2, which shows that when the fuel was changed to the low-Btu gas, a significant loss of performance occurred (~100 mV

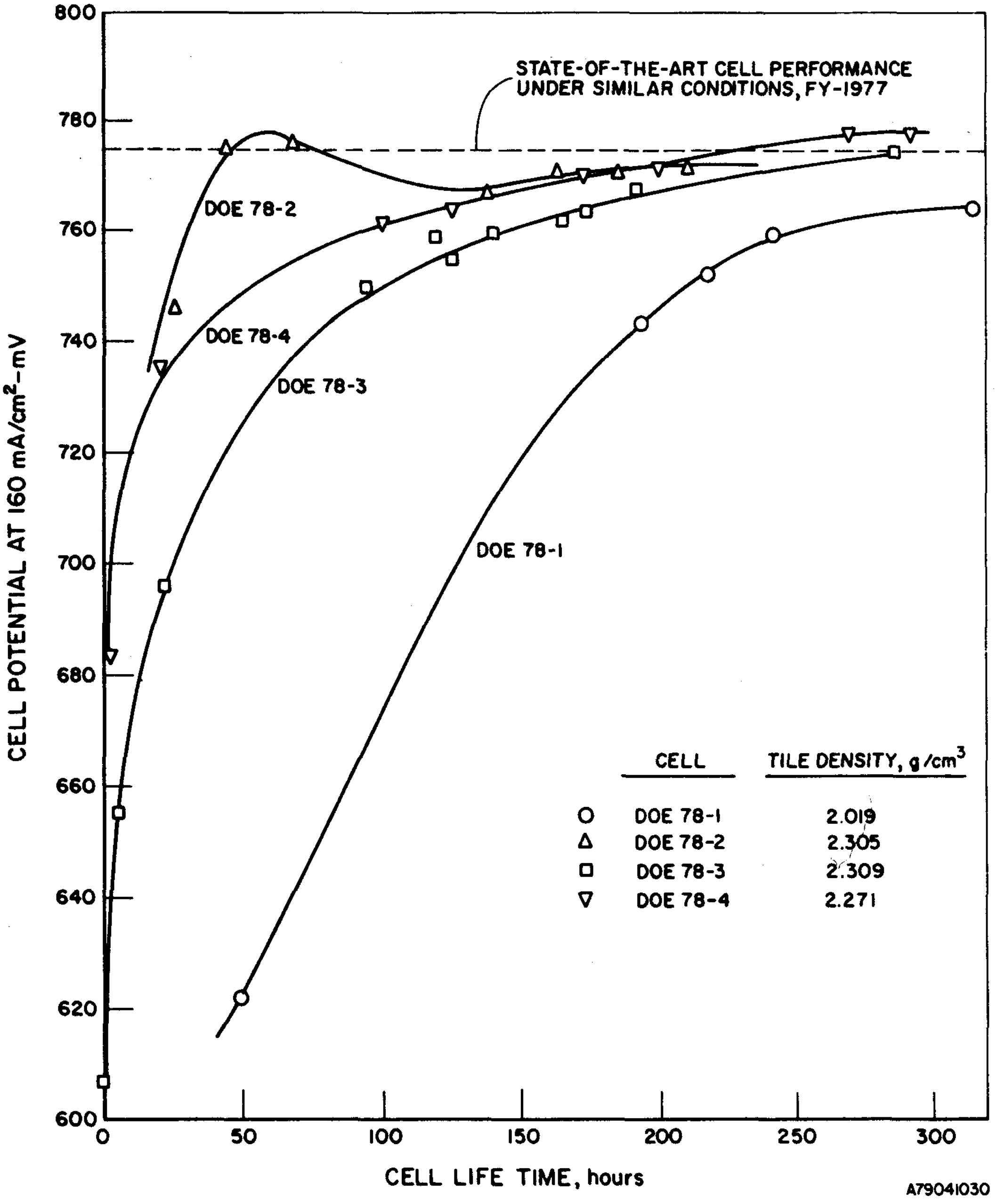

Figure 1.36. INITIAL CELL PERFORMANCE BEHAVIOR WITH SIMULATED PRODUCT FROM STEAM-REFORMED NAPHTHA (75% Fuel and 50% CO_2 Utilizations)

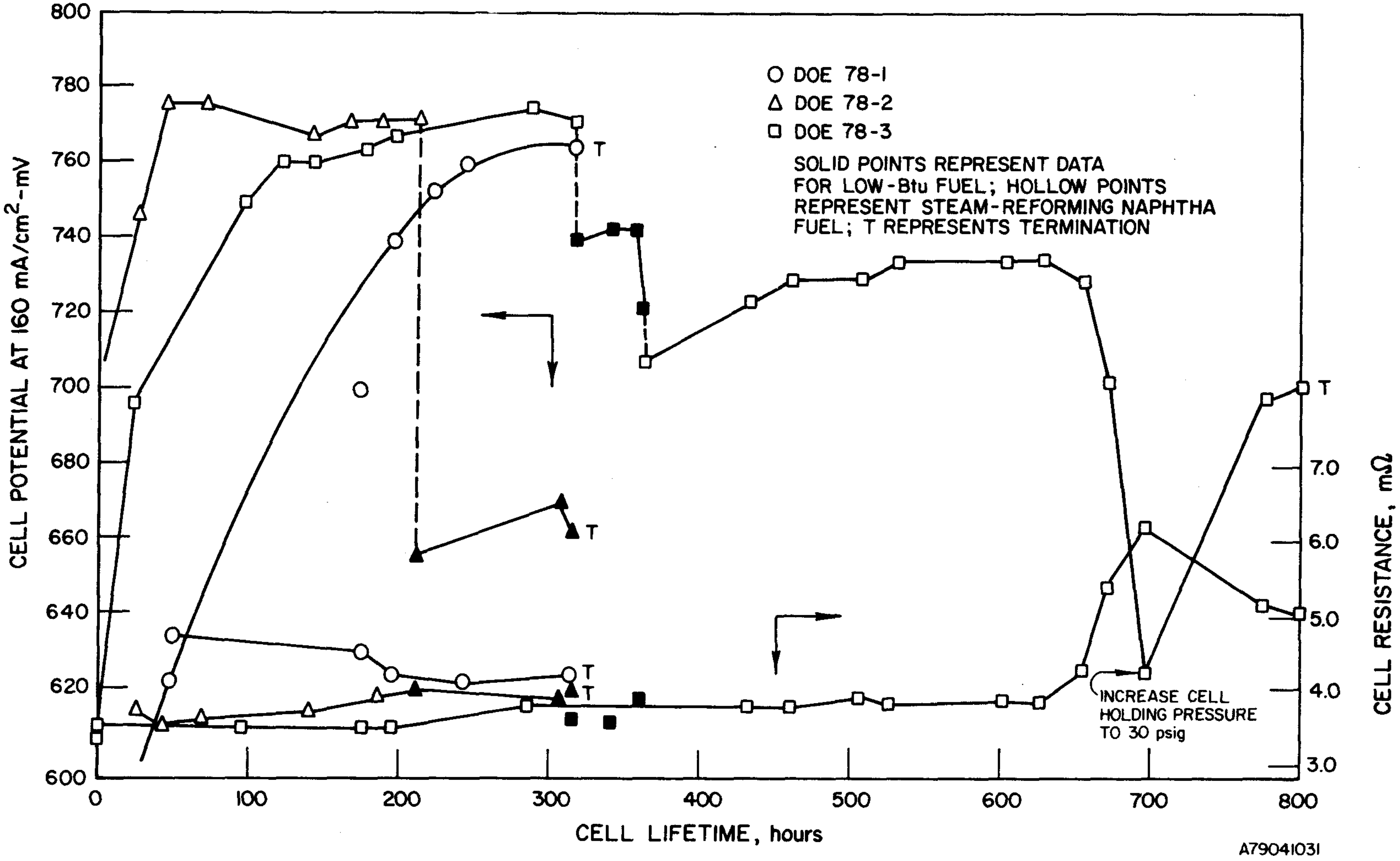

Figure 1.37. LIFEGRAPHS OF CELLS DOE 78-1, 78-2, AND 78-3

at 160 mA/cm^2). This performance drop was in excess of that predicted by Nernst. No change in IR-losses were observed, which indicates that the losses were due to electrode polarization. As shown in Figure 1.38 , the slope of the constant conversion polarization curve suddenly changes beyond 100 mA/cm^2, indicating mass transport limitations (diffusion).

The highest performance on low-Btu fuel was 670 mV at 160 mA/cm^2 (75% fuel and 50% CO_2 utilizations), which is 70 mV below the FY 1977 level (and Goal 1). Because of the low power output, the cell was terminated.

Upon disassembly, the tile layer between the anode and the Kanthal screen by the fuel outlet section of the cell separated, remaining bonded to the electrode, as shown in Figure 1.39. This indicates either a zone of high carbonate losses and/or a fault in the as-pressed tile. An area of anode oxidation was evident (Figure 1.39), possibly corresponding to a crack in the tile, or to fuel flow maldistribution; the anode side corresponding to the oxidant inlet showed discoloration. A small area of the wet seal was corroded (Figure 1.39) to a serious degree, considering the short operating time. Qualitatively, we can say that the low cell performance was associated with the tile problem by the anode outlet and the crack or flow maldistribution on one side of the cell.

Cell DOE 78-3

Cells DOE 78-1 and 78-2 demonstrated that electrolyte AD55-2C was capable of sustaining acceptable cell performance with steam-reformed naphtha fuel. Lab-scale cells (3-cm^2) demonstrated that Co + 10% Cr anodes were stable and capable of high performance. Cell DOE 78-3 was assembled with these components (see Table 1.20 for specifications) for evaluation in bench-scale hardware. Figures 1.36 and 1.37 show cell performance with steam-reformed naphtha and low-Btu coal gasification fuels. During the first 285 hours, the cell operated with the H_2-rich fuel, reaching a peak output of 775 mV at 160 mA/cm^2 (75% fuel and 50% CO_2 utilizations). After 285 hours, the fuel was changed to low-Btu gas. For the next 60 hours, cell performance fluctuated between 739 and 747 mV at 160 mA/cm^2 (75% fuel and 50% CO_2 utilizations), meeting Goal 1 of this program.(See Figure 1.38 also.) At 360 hours, cell output on low-Btu fuel suddenly dropped. Reinstating the H_2-rich fuel proved ineffective; cell performance reached only 735 mV at 160 mA/cm^2, 40 mV

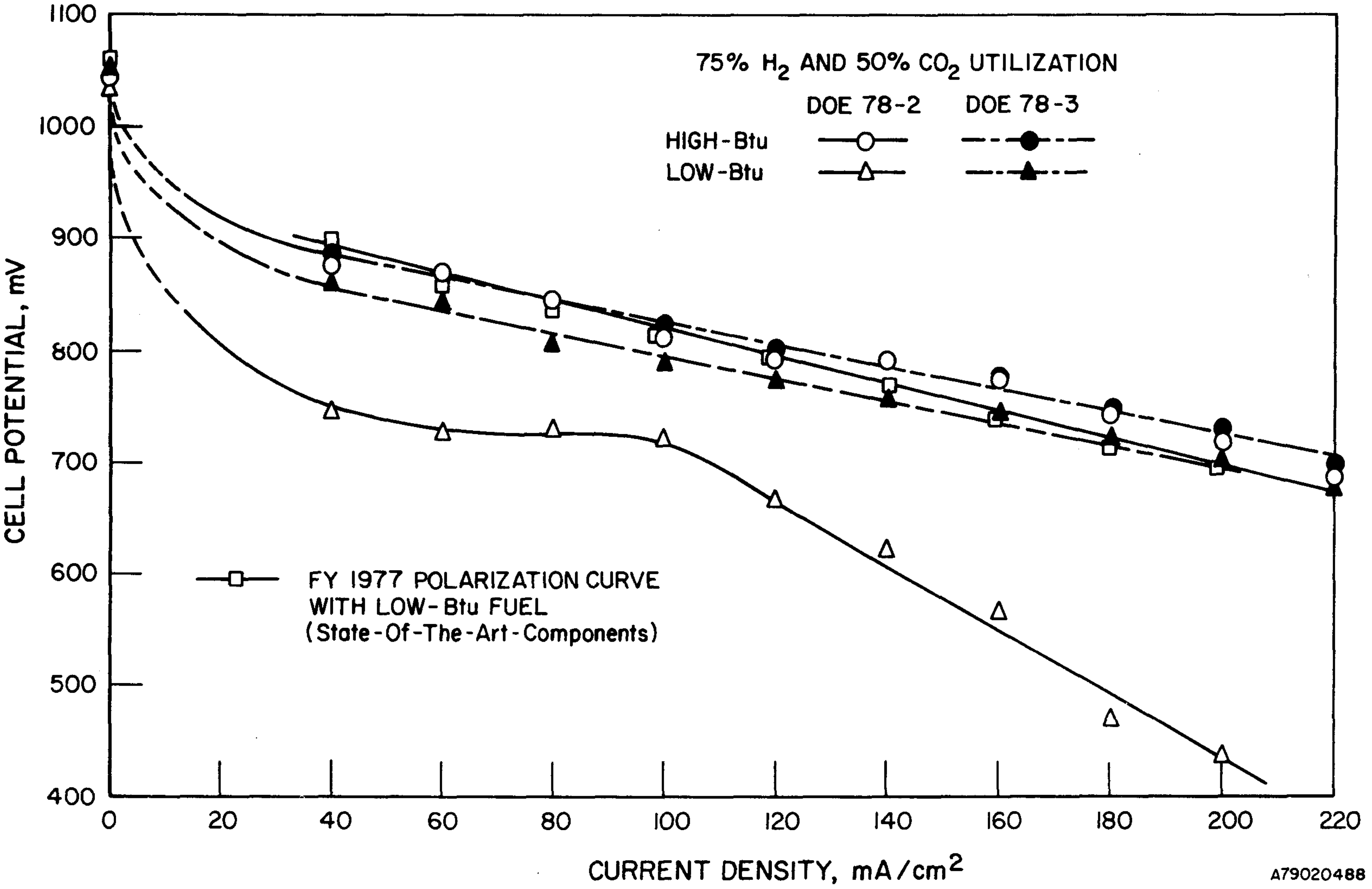

Figure 1.38. CONSTANT CONVERSION POLARIZATION CURVES OF CELLS DOE 78-2 AND 78-3

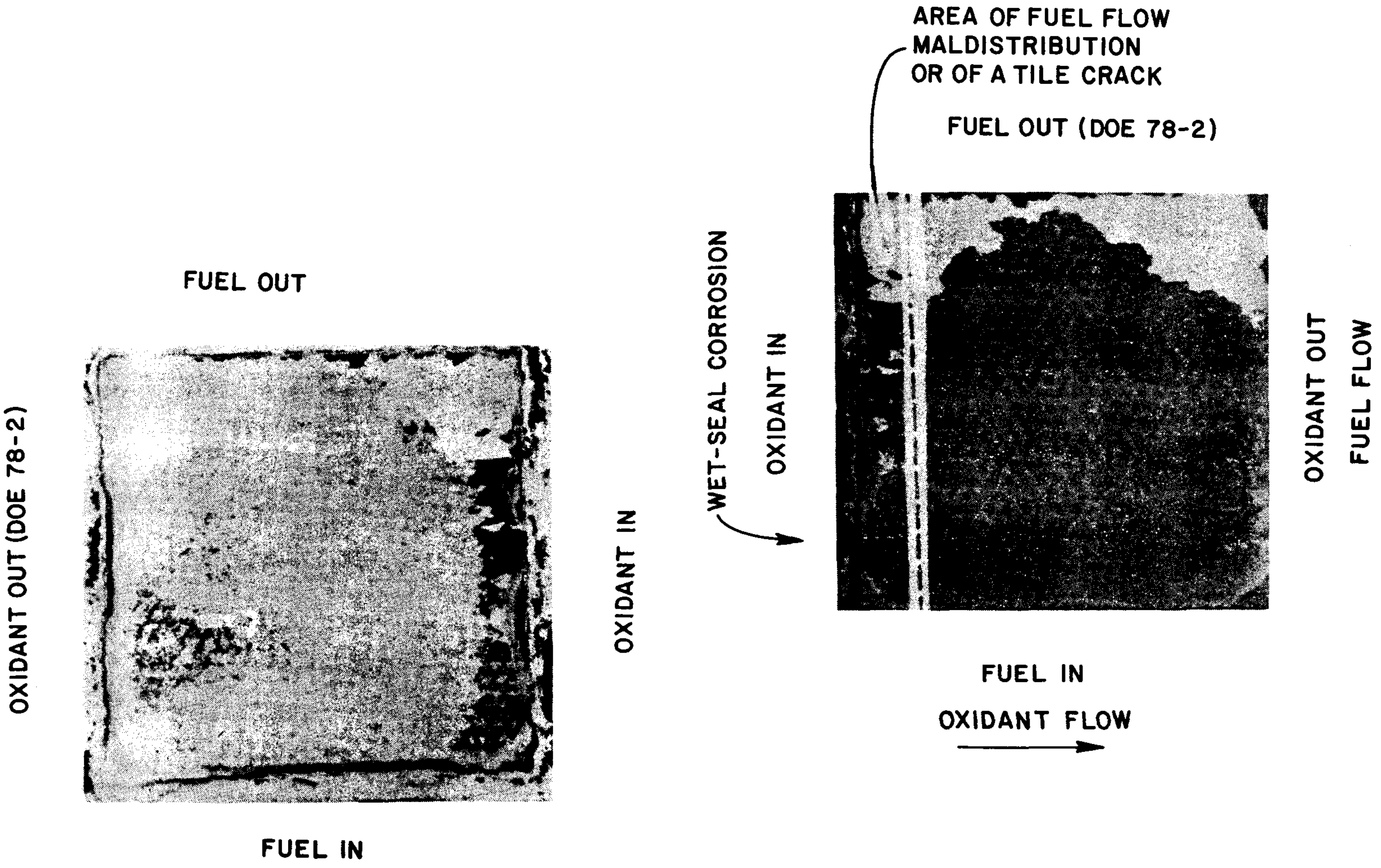

Figure 1.39. ANODE OF CELL DOE 78-2 AFTER DISASSEMBLY

lower than at 285 hours. The H_2-rich fuel flow was maintained for 300 hours, but the cell did not recover. At 650 hours of operation, cell performance dropped to 625 mV at 160 mA/cm^2. This sudden drop was accompanied by a similarly sudden increase in cell IR (3.8 to 5.4 mΩ). A cell holding pressure increase from 15 to 30 psig resulted in a recovery of up to 715 mV at 160 mA/cm^2. At 800 hours, the cell was terminated to investigate the reasons for its performance behavior. During its lifetime, anode and cathode wet-seal efficiencies were always above 98%.

After disassembly, the following observations and conclusions were made —

a. The drop in performance after the successful 60 hours of operation on low-Btu fuel (at 360 hours lifetime) was caused by carbon deposition by the fuel inlet. (See Figure 1.40.)

b. The drop in performance at 650 hours was caused by loss of contact at the anode/electrolyte interface as a result of carbon build-up.

c. The loss of carbonate from the cell package also contributed, though to a much lesser extent, to cell decay. (See the corners and side of the assembly of Figure 1.40.)

Cell DOE 78-4

This cell was assembled for the dual purpose of evaluating Electrolyte AD55-2D ($\alpha/\beta/\gamma$ $LiAlO_2$ = 29/66/5) and evaluating the effect of H_2S (10 ppm on low-Btu fuel) on cell performance endurance, and components. A Co + 10% Cr anode, similar to the one in Cell DOE 78-3, was used in the assembly. (See Table 1.21 for component specifications.) The cell has now operated for 290 hours on a fuel simulating steam-reformed naphtha. Its performance at 160 mA/cm^2, 75% fuel and 50% CO_2 utilizations, is shown in Figure 1.36.

This cell will continue to operate during FY 1979. We plan to —

a. Feed a sulfur-free, low-Btu, air-blown coal gasification fuel for approximately 200 hours

b. Feed a similar fuel, but with approximately 10 ppm H_2S to evaluate the effect on performance

c. Reinstate the sulfur-free fuel to evaluate performance recovery

d. If possible, operate the cell for ~2000 hours

e. Conduct complete analyses of the terminated cell components to determine carbonate losses and changes in component characteristics.

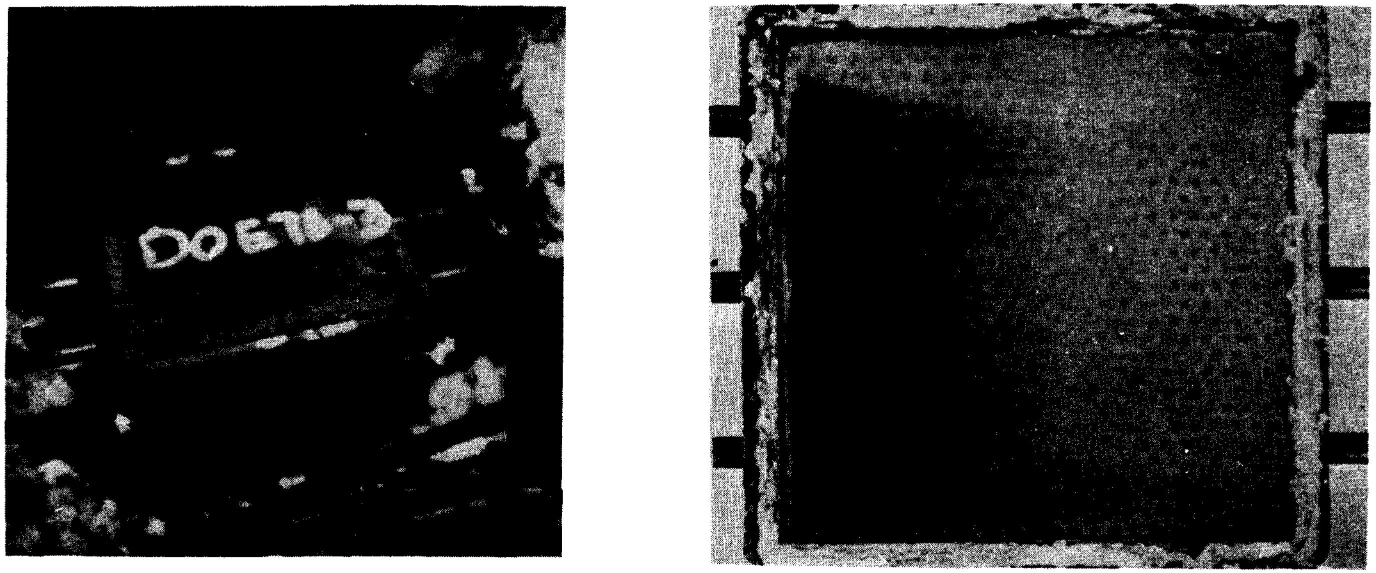

Figure 1.40. ASSEMBLY AND ANODE OF DOE 78-3 AFTER TERMINATION

During the operation of Cell DOE 78-3 on low-Btu fuel, carbon deposition occurred, in spite of the fact that enough steam was present to thermodynamically control carbon formation by the Boudovard reaction. Consequently, we will further increase the water content of the low-Btu fuel, starting with Cell DOE 78-4, to make certain that carbon formation does not impair cell component evaluation and endurance testing.

1.3.3. Conclusions

Based on the data generated with the bench-scale cell tests conducted during FY 1978, we conclude that Goal 1 performance, 740 mV at 160 mA/cm^2 at 75% fuel (low-Btu coal gasification) and 50% CO_2 (standard oxidant) utilizations, can be attained with a cell assembled with electrolyte tiles fabricated with powders prepared by the modified aqueous slurry process, a Co + 10% Cr anode, a Ni cathode, and perforated plate current collectors. A tile density above 95% of theoretical is required to initially obtain a rapid rate of performance gain to attain peak performance.

TASK 2. FUEL CELL ELECTROLYTE OPTIMIZATION

2.1. Testing in Laboratory- and Bench-Scale Cells

2.1.1. Laboratory-Scale Testing

Introduction

Laboratory-scale (3 cm^2) fuel-cell tests were used to evaluate the performance of cells assembled with the standard composition tile and electrode components developed in this program and of tiles with carbonate compositions other than the standard 62 mole percent Li_2CO_3/38 mole percent K_2CO_3 eutectic. A schematic diagram of a laboratory-scale cell is shown in Figure 2.1. The tile and electrode studies were carried out at 650°C with fuel compositions corresponding either to reformed natural gas (60% H_2, 7.4% CO_2, 10% CO, 22.6% H_2O) or to a simulated low-Btu air-blown coal gasification product (21.1% H_2, 9.2% CO_2, 17.7% CO, 5.6% H_2O, 1.1% CH_4, bal N_2), and an oxidant consisting of 30% CO_2/70% air (humidified at room temperature). The reactant gas utilizations were 7.5% H_2 in the fuel and 15.0% CO_2 in the oxidant, based on a 200 mA/cm^2 current density. Besides cell potential, IR-free anode and cathode polarizations and IR-losses at 160 mA/cm^2 are reported with respect to a 66.7% CO_2/33.3% O_2 gold reference electrode. Most of the lab-scale testing was devoted to the testing of tiles and anode structures, although a limited amount of H_2S contaminant testing was also performed. The approach followed was first to test tiles developed in Subtask 1.1.2 and then cell-test new anode structures from Subtask 1.1.1 with the most promising tiles. To do this, tiles fabricated from electrolyte batches that showed promising results in screening tests were coupled with state-of-the-art electrodes and tested for performance and stability. Once the performance and stability levels were known, the new tiles were coupled with the developmental electrodes to evaluate their performance with the new electrodes, making it possible to discriminate between a poor performance associated with the electrolyte and that as a result of poor electrode stability.

2.1.1.1. Laboratory-Scale Cell Testing of Tiles

The first two cells, DOE-A1 and DOE-A2, had state-of-the-art electrodes and electrolyte tiles fabricated from Electrolytes AD55-2A (50 hours at 685°C) and AD55-2A, respectively. These two electrolytes were prepared by the

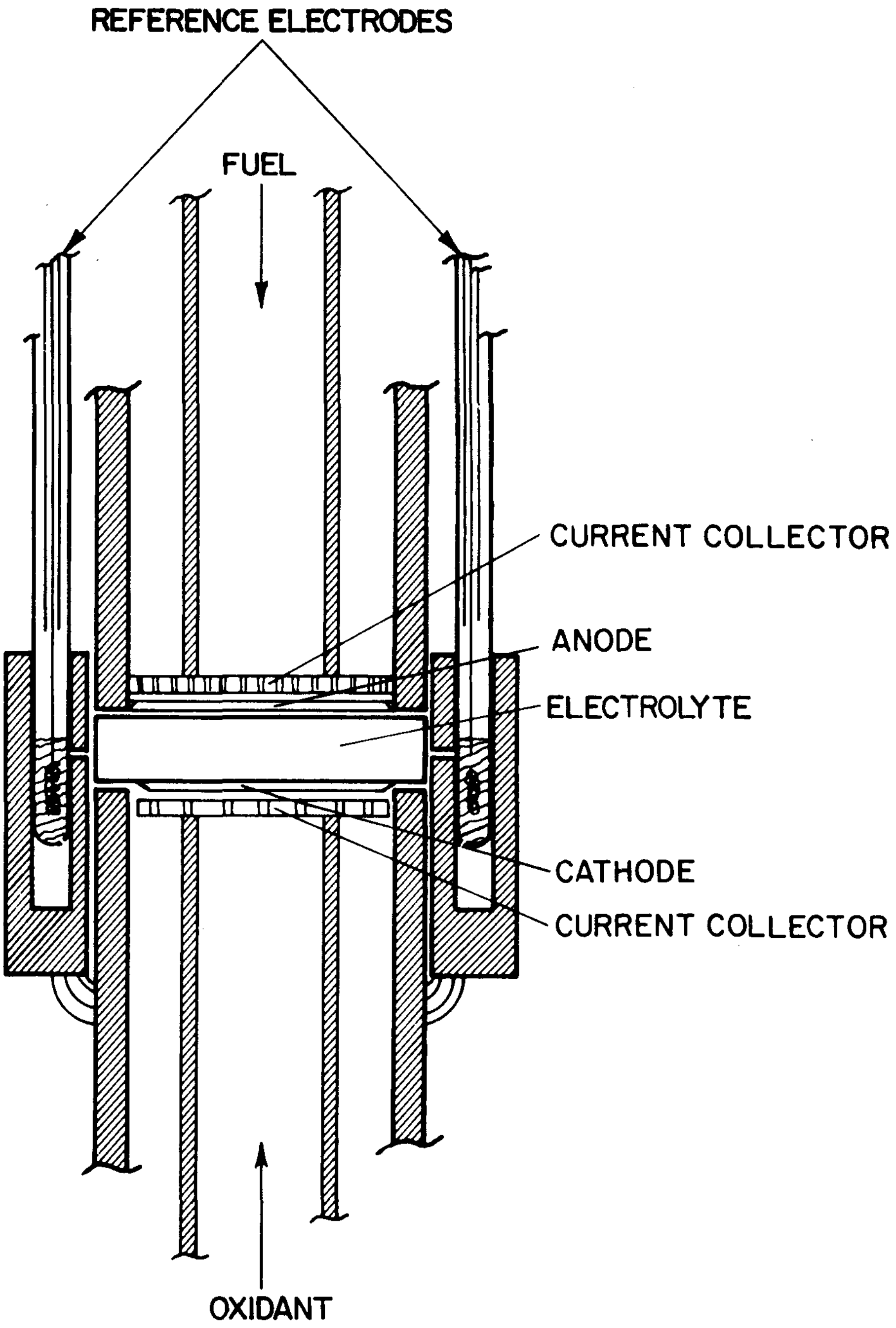

A78041086

Figure 2.1. SCHEMATIC DIAGRAM OF LABORATORY-SCALE FUEL CELL ASSEMBLY

aqueous slurry process described in Task 1 of this report. The main difference between the two electrolytes was that the AD55-2A had a significantly higher surface area: 20.7 m^2/g versus 11.0 m^2/g for the AD55-2A (50 hours at 685°C).

Cell DOE-A1 operated nearly 1200 hours on high-Btu fuel and standard oxidant. The cell performance at 160 mA/cm^2 is shown in Figure 2.2. As seen in the figure, the cell potential increased from 815 mV to 870 mV during the first 300 hours of operation and remained nearly at that level during the rest of the test period. The performance goal under these conditions (840 mV at 160 mA/cm^2) was thus surpassed by 30 mV with this test.

Cell DOE-A2 operated over 3500 hours with high- and low-Btu fuels. High-Btu fuel was used up to 1536 hours of operation and low-Btu from 1536 hours until termination of the test at 3536 hours. As seen in the cell performance plot of Figure 2.3, DOE-A2 showed 816 mV at 160 mA/cm^2 initially and reached the goal cell potential of 840 mV at 160 mA/cm^2 after 60 hours of operation with high-Btu fuel. The cell further improved to 870 mV at 250 hours and to 875 to 885 mV during the 600 to 1500 hour period. During the 600 to 1500 hour period, this cell performance was 10 to 15 mV better than that of cell DOE-A1, which contained the AD55-2A (50 hours 685°C) electrolyte tile.

The fuel in Cell DOE-A2 was changed from high-Btu to low-Btu after 1536 hours of operation. Within 1 to 2 hours, the cell potential at 160 mA/cm^2 had dropped 50 mV because of higher anode polarization. The cell was operated for 2000 hours on low-Btu fuel until its termination at 3536 hours. During operation with low-Btu fuel, the cell potential at 160 mA/cm^2 decreased gradually from 835 mV at 1526 hours to 745 mV at 3536 hours. Of the 90 mV loss, we can discount ~20 mV lost in anode open circuit when the humidity of the low-Btu fuel was increased (from 5.6% to 10%) to avoid carbon deposition. Therefore, a rate of performance loss of ~35 mV/1000 hours was obtained. Most of the performance loss (~25 mV/1000 hours) was due to higher IR-losses.

The performance of these cells, DOE-A1 and DOE-A2, surpassed the performance goal at 160 mA/cm^2 with high-Btu fuel (840 mV) by 30 and 45 mV, respectively. These results demonstrated that acceptable electrolytes can be prepared by the aqueous slurry process, and that tiles pressed from such electrolytes will show good cell performance and stability if the electrodes

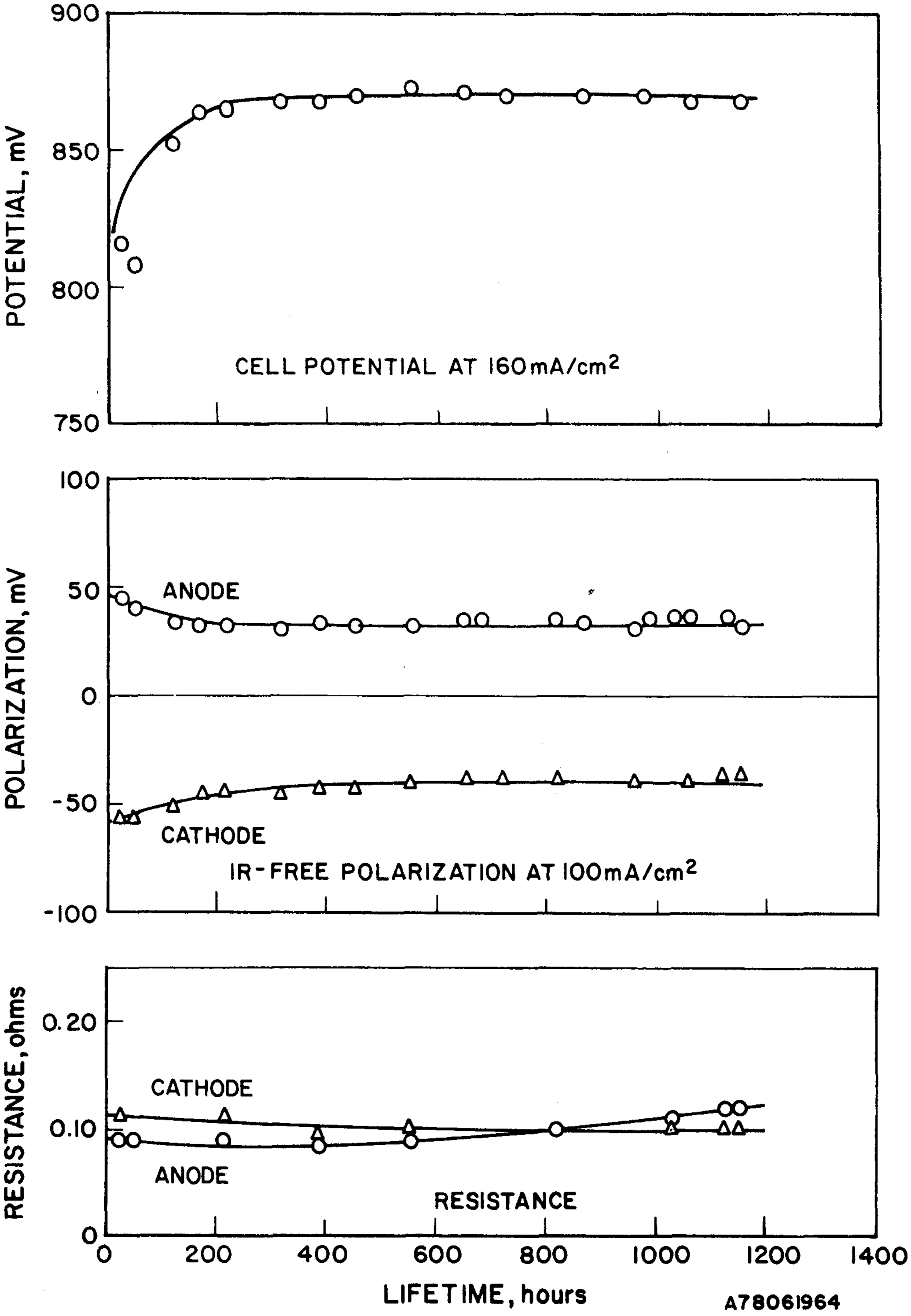

Figure 2.2. PERFORMANCE OF LABORATORY-SCALE CELL DOE-A1 USING DEVELOPMENTAL TILE AND STATE-OF-THE-ART ELECTRODES

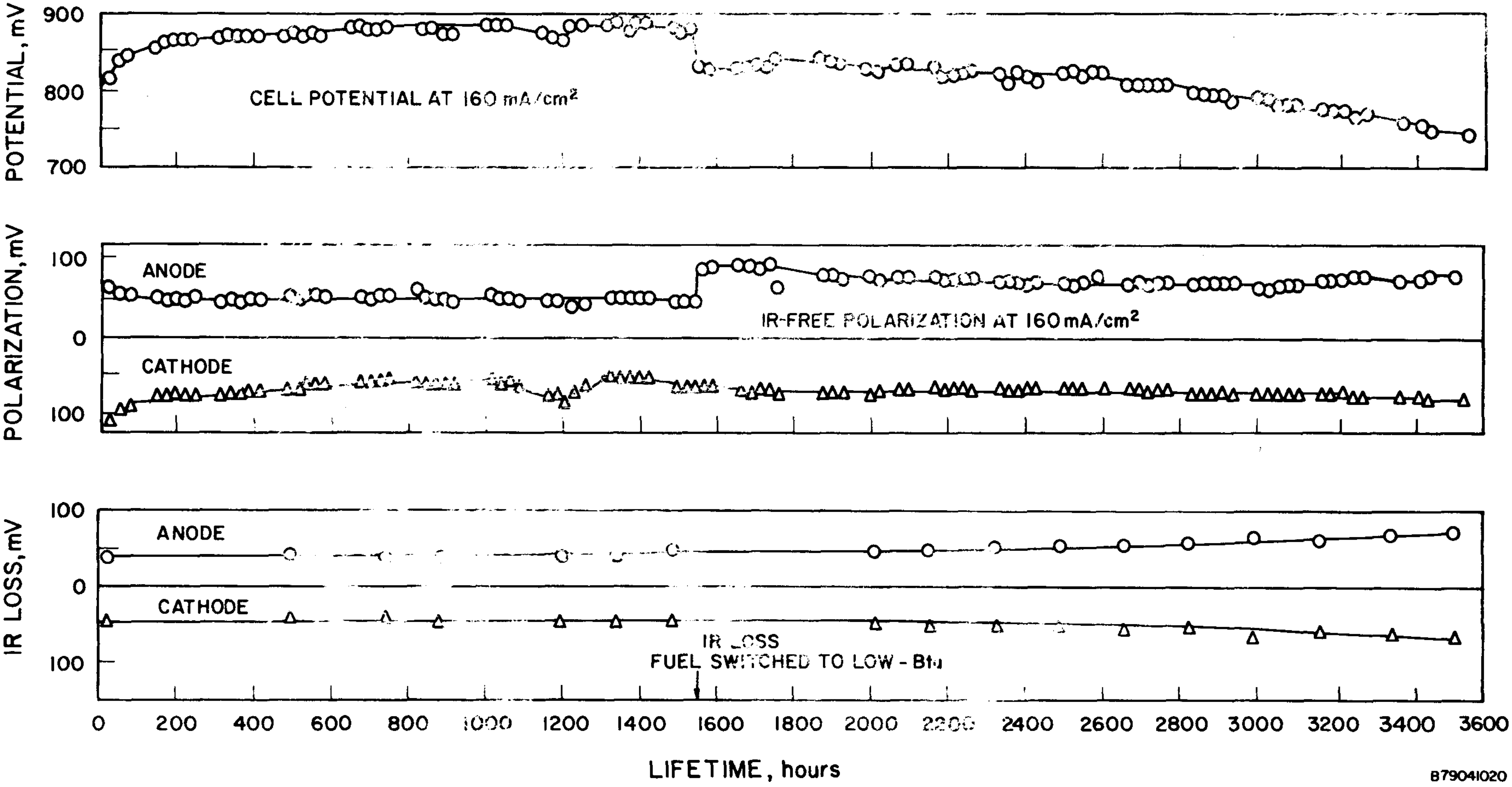

Figure 2.3. PERFORMANCE OF CELL DOE-A2 AT 160 mA/cm^2 USING DEVELOPMENTAL TILE AND STATE-OF-THE-ART ELECTRODES

and tiles are properly matched and the electrodes are structurally stable (do not lose surface area, porosity or experience other physiochemical changes). Tiles pressed from electrolyte powders prepared by the aqueous slurry process were used in the anode stability studies, alternate electrolyte composition studies, H_2S contaminant effect work, and evaluation of cost effective tile fabrication techniques. Results of these cell-test studies are described in turn.

Testing of Porous Anode Structures

Acceptable performance and stability of the fuel cell are directly dependent on the stability of its components. Because any major structural changes of the cell components will affect the performance stability, correlation of cell performance stability with analysis of structural changes can be used to identify the solve cell performance degradation problems associated with component aging effects. One of the components susceptible to instabilities during prolonged high-temperature operations is the porous sintered anode structure.

In the previous section the performance level and short term stability were reported for laboratory-scale cells assembled with developmental tiles pressed from the most promising electrolyte batches, when coupled with state-of-the-art electrodes. Good performance (870 to 885 mV at 160 mA/cm^2) and stability were observed. In this section we present the results of laboratory-scale cell tests when such developmental tiles are coupled with developmental anode structures. These cells were, in general, operated for short times (500 to 1000 hours) but those showing good stability were operated for longer periods (up to 3000 hours). The porous anode structures tested were fabricated from nickel or cobalt powder, in some cases with 10% sintering inhibitor (nichrome, chromium or tungsten carbide) as a second-phase dispersion. The cell stability was studied with both high- and low-But fuels. The cells operated for this purpose are listed in Table 2.1.

Cells DOE-1 (100% Ni, 6.0μ mps anode) and DOE-2 (100 Ni, 7.9μ mps anode) were assembled with AD55-2A (50 hrs at 685°C) electrolyte and operated on high-But fuel. The results were presented in the January to March Progress Report. The cell potential at 160mA/cm^2 of cell DOE-1 reached only 770 mV after 400 hours of operation and declined thereafter. Cell DOE-2 showed a cell potential of 840 to 845 mV at 160 mA/cm^2 during the first 200 hours of testing, but it was not stable and dropped to 700 mV at 600 hours. The drop in potential in both cells was associated with an increase in the anode polarization.

Cell DOE-3 (Co-10% NiCr, 3.7μ mps anode) achieved the goal performance of 840 mV at 160 mA/cm^2 during the first several hundred hours of operation on high-Btu fuel, but experienced a gradual decline thereafter. At 720-hours lifetime, the cell holding force was increased, and the cell potential increased from 820 to 860 mV. As shown in Figure 2.4, this change in holding force resulted in a decrease in anode polarization and a slight increase in cathode polarization. Upon switching to low-Btu fuel at 864 hours, the cell potential decreased significantly, from 859 mV to 782 mV, as a result of a large increase in anode polarization. The performance with low-Btu fuel increased during the following 350 hours, and then decreased during the period of 1248 to 2040 hours at a rate of 90 mV/1000 hours. In contrast with Cell DOEA-2, whose performance decline was caused by increased electrode IR losses, the losses in DOE-3 were associated with a continuing increase in anode polarization. The IR losses in DOE-3 were fairly constant during the lifetime of the cell.

Cells DOE-4 and DOE-5 both exceeded the performance goal on high-Btu fuel at the beginning of life.(See Figures 2.5 and 2.6.) Peak cell potentials of 898 mV and 886 mV at 160 mA/cm^2 were attained by DOE-4 and DOE-5, respectively, before switching to low-Btu fuel. Changing from high- to low-Btu fuel resulted in cell potential losses of 40 mV and 38 mV, respectively, for these two cells, which were also associated with anode polarization increases. Cells DOE-4 and DOE-5 showed very stable performance on low-Btu fuel with cell potential loss rates of 20 mV/1000 hours in both cells. These cells operated for 2000 hours (DOE-4) and 3000 hours (DOE-5).

Cell DOE-8 (Co-10% NiCr, 3.7μ mps anode, 9.6μ mps cathode) was operated with low-Btu fuel. The maximum cell potential at 160 mA/cm^2 was only 800 mV because of somewhat high anode polarization (~90 mV versus ~60 to 70 mV with the Co-10Cr anodes in DOE-4 and DOE-5). The cell, however, showed very stable performance, and the cell potential dropped only 20 mV from 800 mV at 144 hours

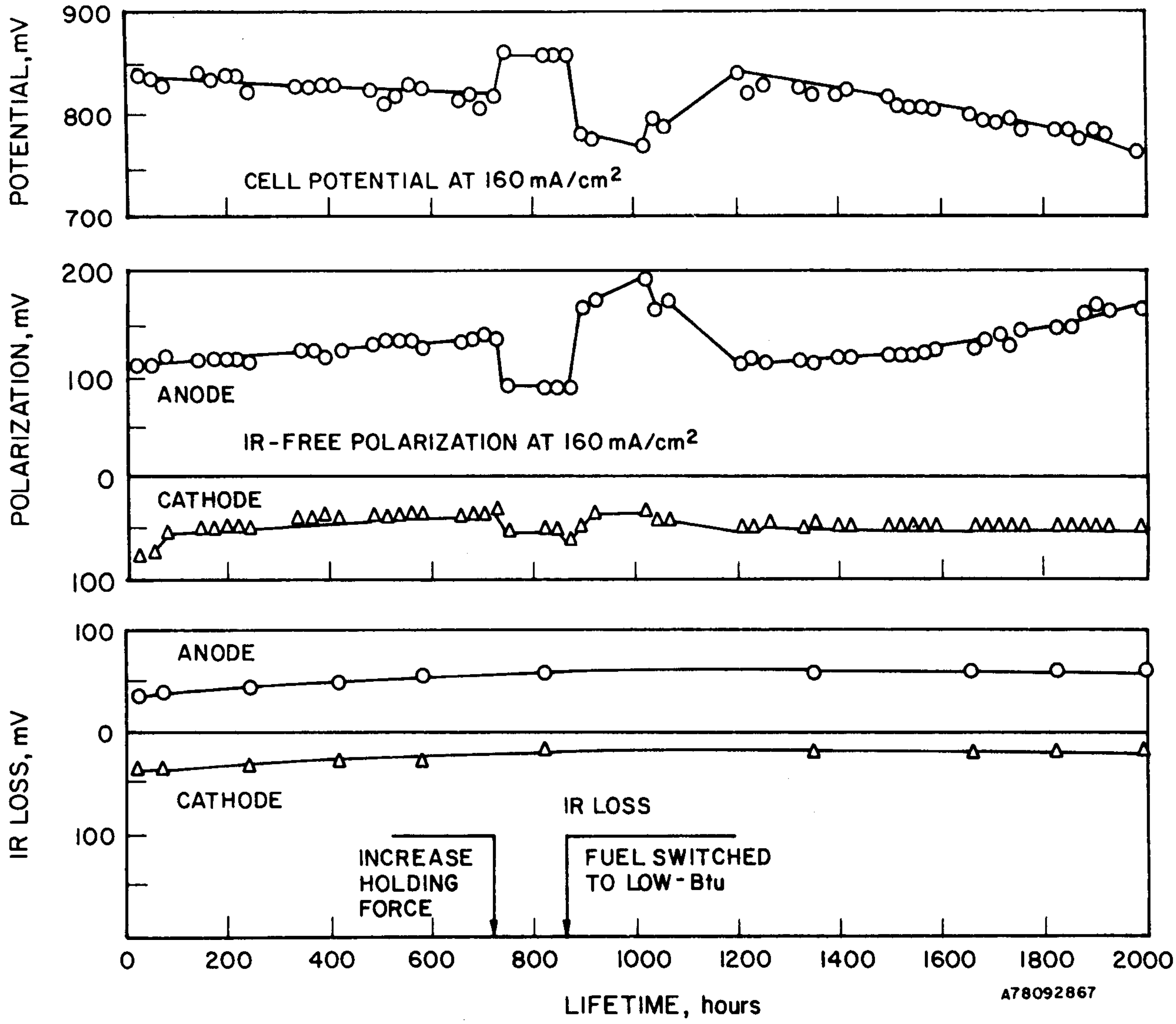

Figure 2.4. PERFORMANCE OF CELL DOE-3 AT 160 mA/cm^2

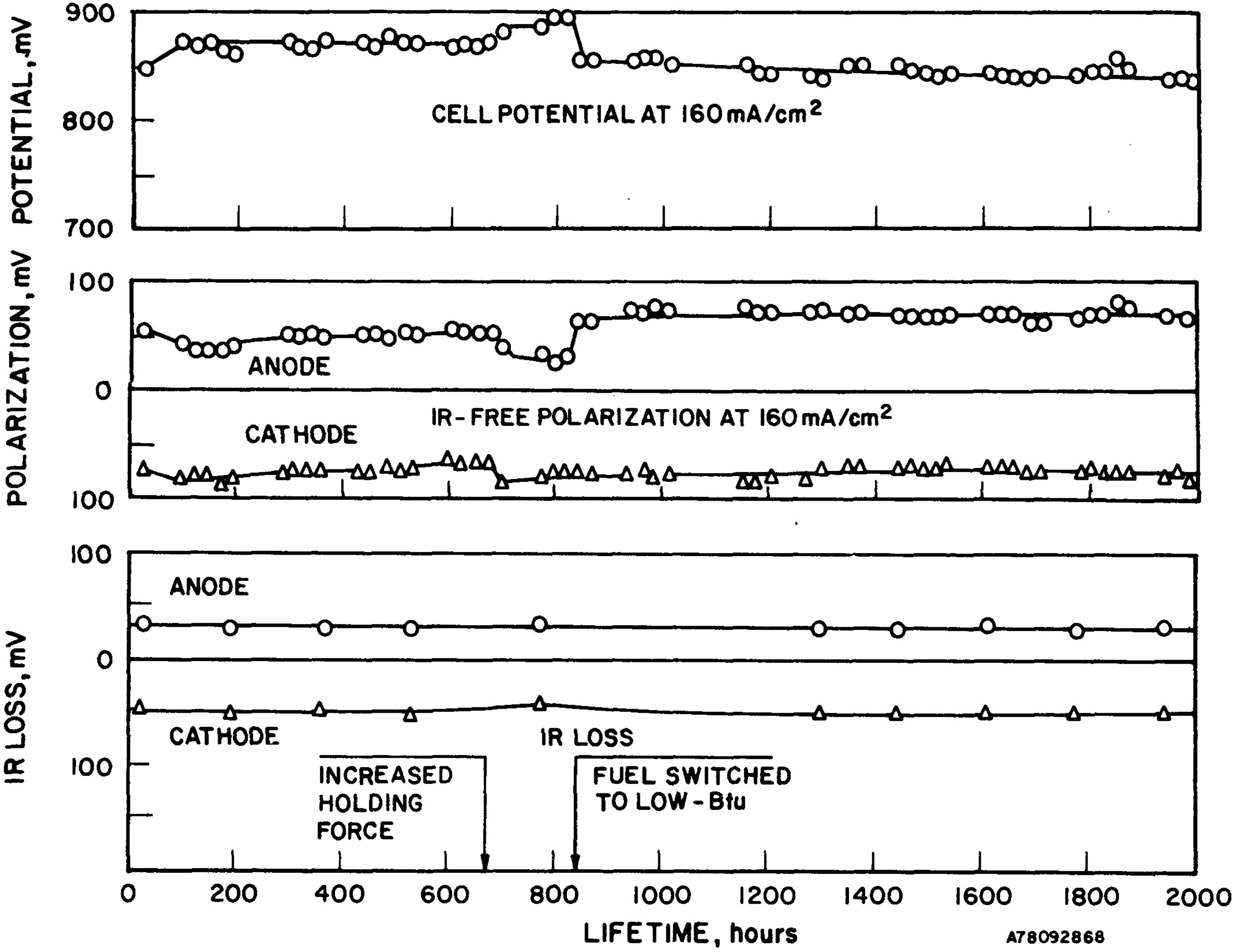

Figure 2.5. PERFORMANCE OF CELL DOE-4 AT 160 mA/cm^2

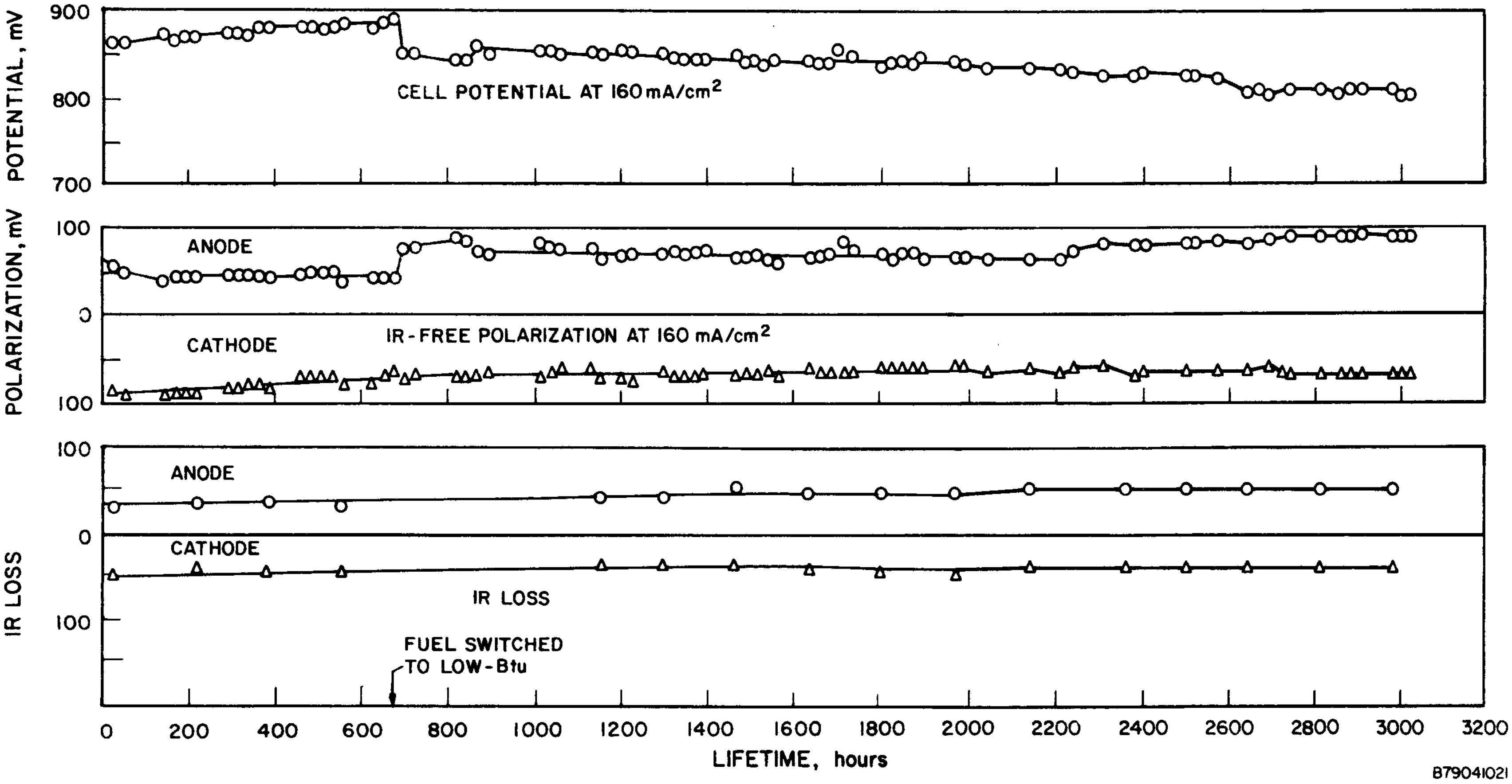

Figure 2.6. PERFORMANCE OF CELL DOE-5 AT 160 mA/cm^2

to 780 mV at termination (1824 hours). The rate of cell potential loss at 160 mA/cm^2 was 12 mV/1000 hours. Again the loss is related to higher anode polarization. The cell performance plot is shown in Figure 2.7.

Cell DOE-10 (100% Co, 4.1μ mps anode, 9.6μ mps cathode), which was operated only with low-Btu fuel, showed good performance (850 mV at 160 mA/cm^2) up to 70 hours of operation. The cell potential dropped rapidly to 770 mV after 170 hours and showed very unstable performance therafter. As seen in Figure 2.8, very large performance fluctuations resulted from a very unstable anode polarization. Cell DOE-11 (Co-10% WC 4.6μ mps, 9.6μ mps cathode) showed similar fluctuations in the cell performance from day to day. Again, as seen in Figure 2.9, a very unstable anode polarization was responsible for the fluctuations. Cell DOE-11 also was operated only on low-Btu fuel.

Cells DOE-17 (Co-10% NiCr, 3.7μ mps anode), DOE-18 (Co-10% WC, 4.6μ mps anode), DOE-19 (Co, 4.1μ mps anode), and DOE-22 (Ni-10% NiCr, 7.0μ mps anode) were started with tiles pressed from AD55-2D electrolyte batch and operated on high-Btu fuel for the purpose of determining the cell performance and stability with these components. The results are shown in Figure 2.10. In general, they followed a similar pattern to that of cells with the same type of anode operated on low-Btu fuel (Cells DOE-8, DOE-10, and DOE-11). The cells with the Co-10% NiCr and Ni-10% NiCr anodes (DOE-17 and DOE-22) showed good initial performance levels (850 and 860 mV at 160 mA/cm^2) and a rate of performance decay of 36 mV/1000 hours and 100 mV/1000 hours, respectively. The cells with the 100% Co (DOE-19) and Co-10% WC (DOE-18) anodes, showed very erratic performance because of large fluctuations in the anode polarization, similar to that seen in Cells DOE-10 and DOE-11 with the same types of anodes. The cathode polarization and the IR losses were generally stable in all the cells operated for anode studies.

The results of these laboratory-scale cell tests can be summarized as follows —

a. When developmental tiles were used, a good cell performance (870 to 885 mV at 160 mA/cm^2 on high-Btu fuel) was obtained. This performance was attained by coupling tiles pressed from electrolyte batches prepared by the aqueous slurry process with electrodes of known good stability (state-of-the-art). Good cell performance stability up to 3500 hours of operation (DOE-A type cells) was demonstrated with these developmental tiles.

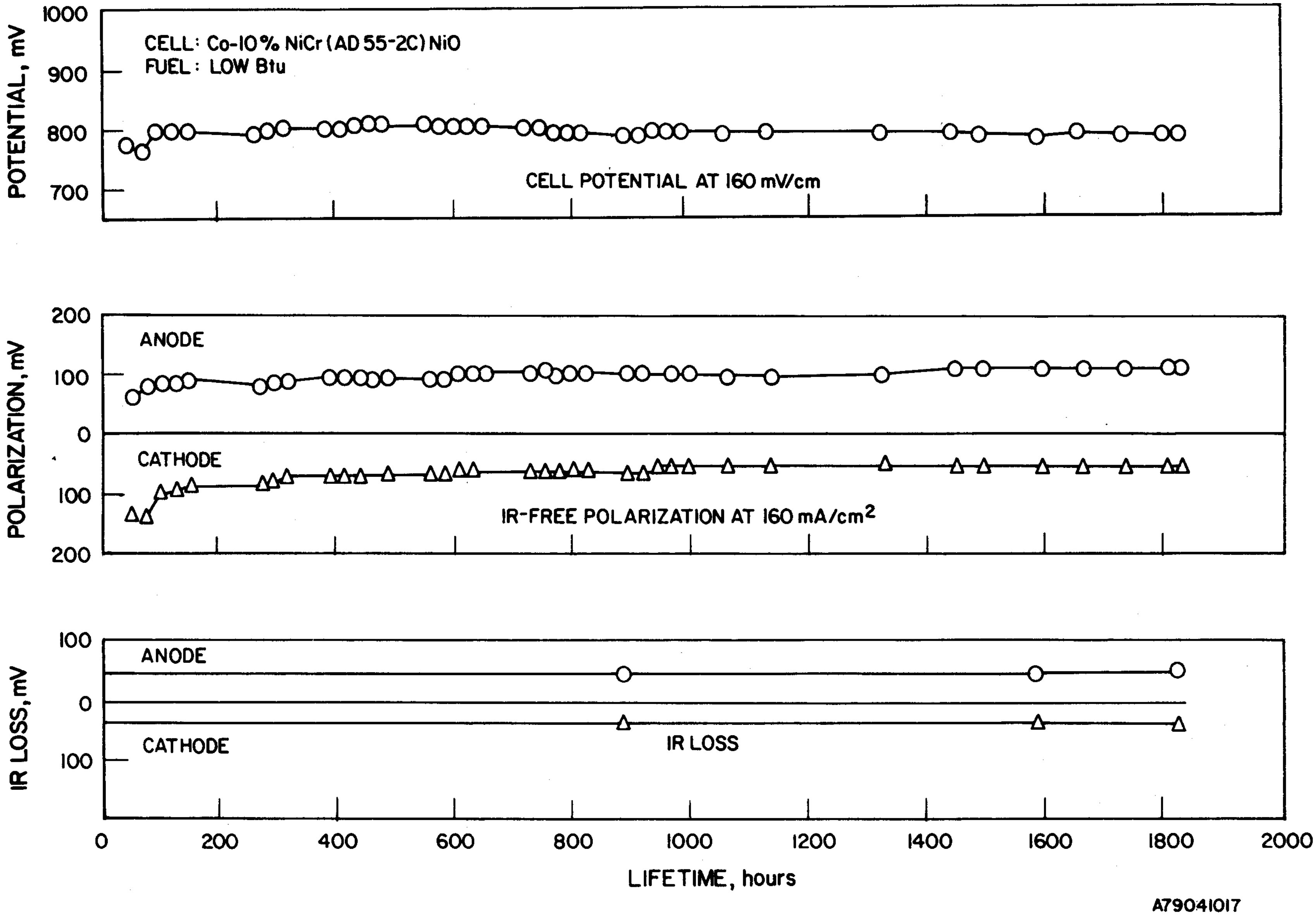

Figure 2.7. PERFORMANCE OF CELL DOE-8 AT 160 mA/cm^2 USING A Co-10% NiCr ANODE

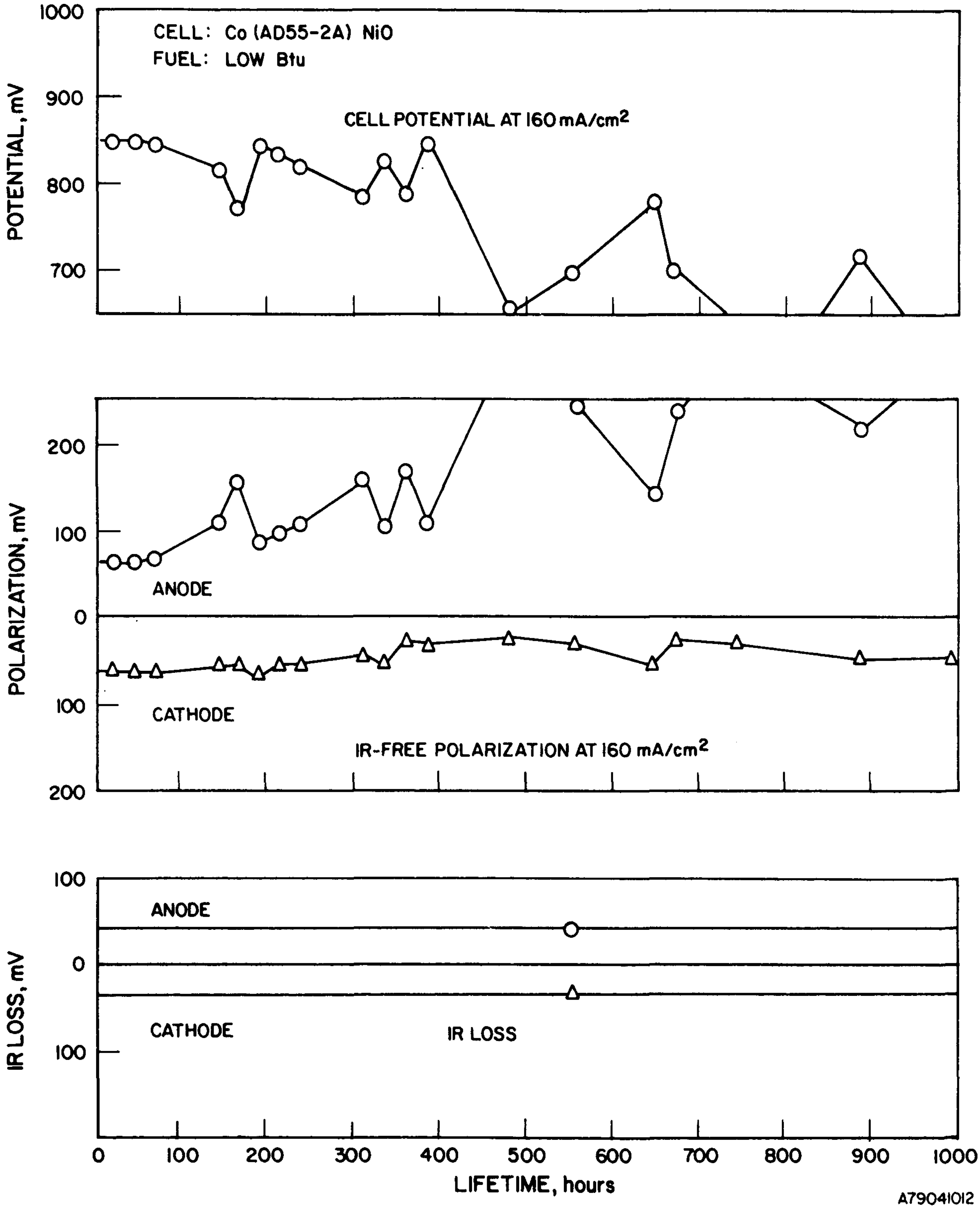

Figure 2.8. PERFORMANCE OF CELL DOE-10 AT 160 mA/cm^2 USING A 100% Co ANODE (High-Btu Fuel)

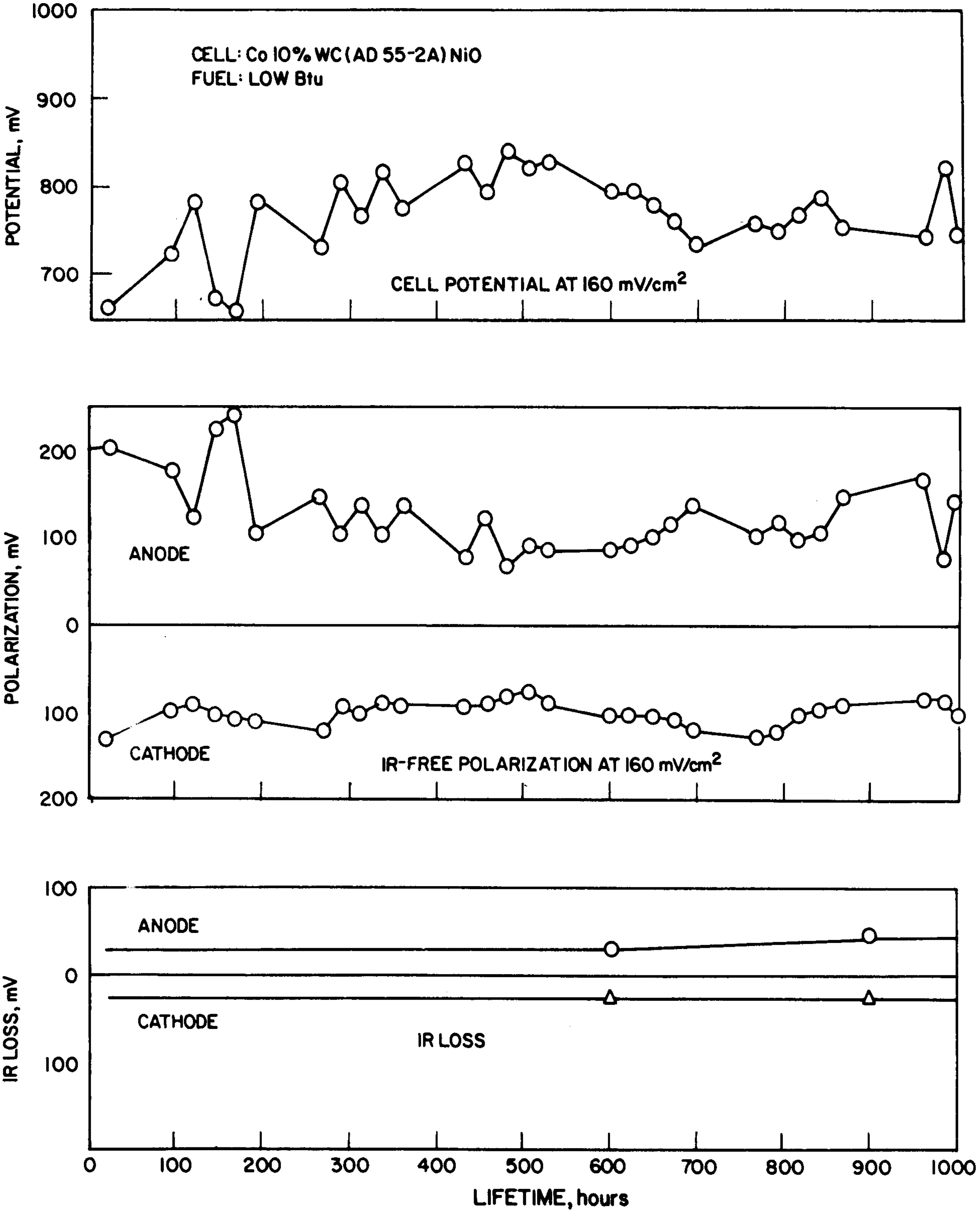

A79041011

Figure 2.9. PERFORMANCE OF CELL DOE-11 AT 160 mA/cm^2 USING a Co-10% WC ANODE

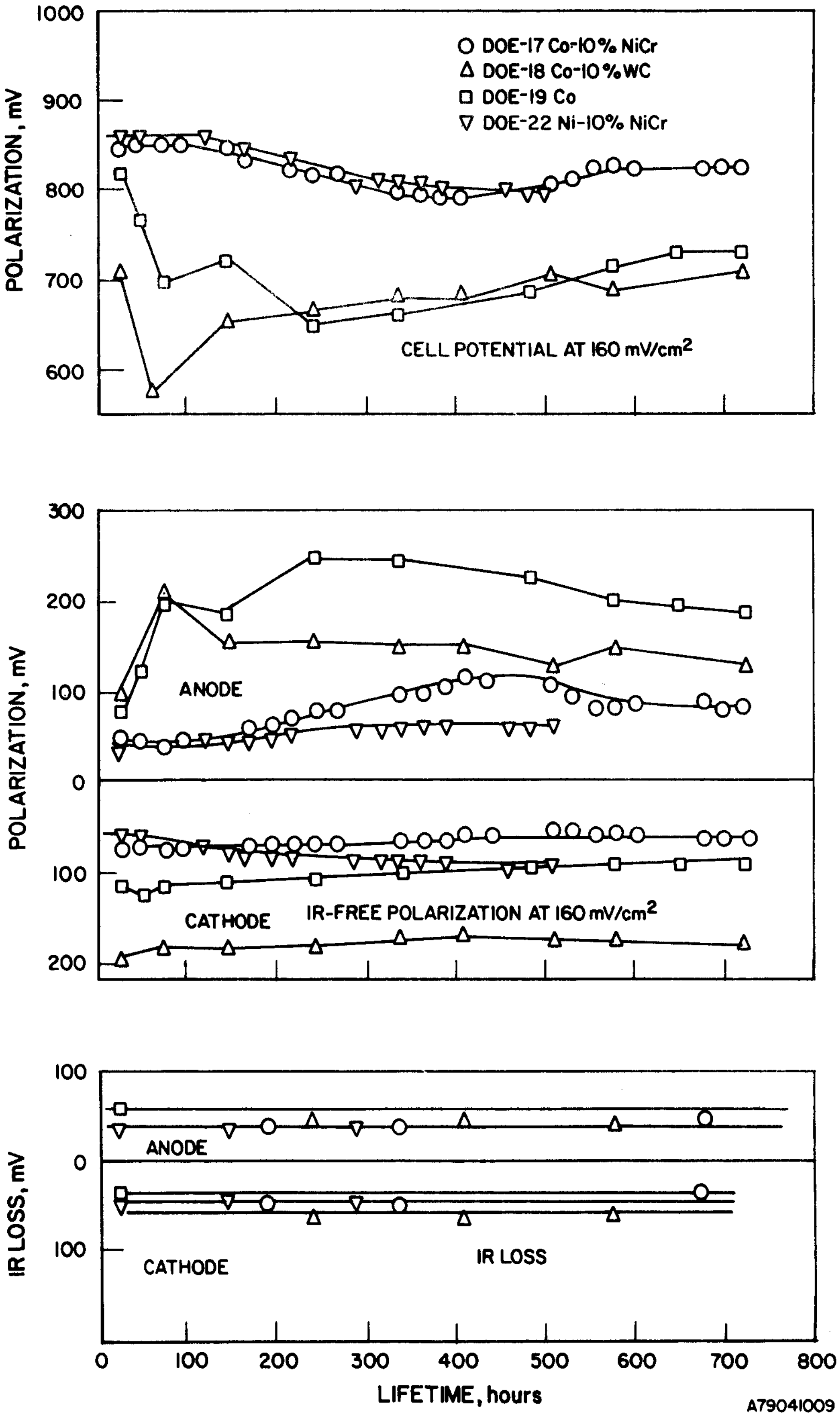

Figure 2.10. PERFORMANCE OF CELLS DOE-17, DOE-18, DOE-19, AND DOE-22 AT 160 mA/cm² USING Co-10% NiCr, Co-10% WC, Co-100%, AND Ni-10% NiCr ANODES, RESPECTIVELY

b. When Co-10% Cr anodes were used in conjunction with developmental tiles of demonstrated good stability, good cell performance (as high as 898 mV at 160 mA/cm^2 with high-Btu fuel in DOE-4 and stability up to 3000 hours in DOE-5) was attained.

c. When Co-10% NiCr or Ni-10% NiCr anodes were used with developmental tiles, good performance (860 mV at 160 mA/cm^2 with high-Btu fuel in DOE-22), but only fair stability, were obtained.

d. When Co, Ni, or Co-10% WC anodes were used, only fair performance and extremely poor stability were observed. The poor stability was associated with very rapid increases and fluctuations in the anode polarization. These results demonstrate the need for stabilizing the anode and the superiority of chromium over nichrome and tungsten carbide in providing this stability through retardation of matrix sintering.

2.1.1.2. Testing of Alternative Electrolyte Compositions

Cell testing of alternative electrolyte compositions was carried out after such electrolytes prepared by the aqueous slurry process showed good properties in the characterization and screening tests. These alternative electrolyte studies were performed in cells assembled with electrolytes prepared by the aqueous slurry process described in Subtask 1.1.2. The cells were assembled with Co-10% Cr anodes and NiO cathodes and were operated on high-Btu fuel/standard oxidant for a maximum of 500 hours. In addition to obtaining the cell performance with electrolytes of various carbonate compositions at 650°C, the performances with two ternary electrolytes, the eutectic (melting point 397°C) and one ternary off-eutectic (melted completely at 590°C), was also obtained at 550° and 600°C as shown in Figures 2.11 through 2.19 and Table 2.1.

As seen in Figure 2.11 and as discussed above, the cell potential at 160 mA/cm^2 of Cells DOE-A1 and DOE-A2 was in the upper end of the performance band of the state-of-the-art cells. When these new developmental tiles with the 62 Li/38 K baseline composition were tested with the Co-10% Cr anode/NiO cathode combination, the cell potential at 160 mA/cm^2 was 870 to 895 mV (curves 1 and 2 in Figure 2.12) versus 840 to 875 mV for state-of-the-art cells (seen in Figure 2.11). The cell potential at 160 mA/cm^2 was further improved to 903 mV by using a 75 mole percent Li_2CO_3/25 mole percent K_2CO_3 electrolyte and to 912 mV by using a 57 mole percent Li_2CO_3/31 mole percent Na_2CO_3/12 mole percent K_2CO_3 composition. Good performance (883 mV at 160 mA/cm^2) was also obtained when a 52 mole percent Li_2CO_3/48 mole percent Na_2CO_3

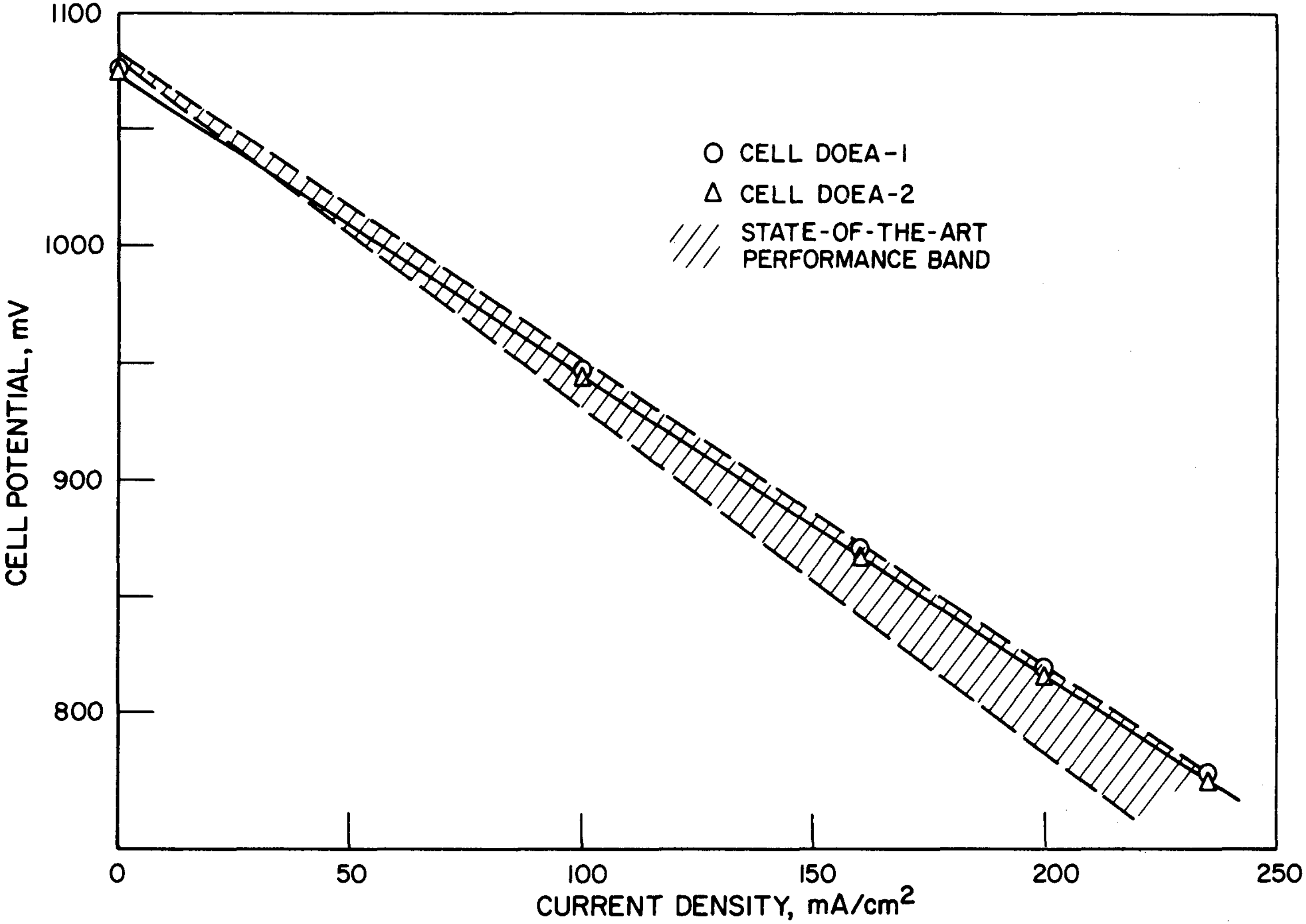

A79030490

Figure 2.11. POLARIZATION OF CELLS DOE-A1 AND DOE-A2 COMPARED WITH STATE-OF-THE-ART CELLS

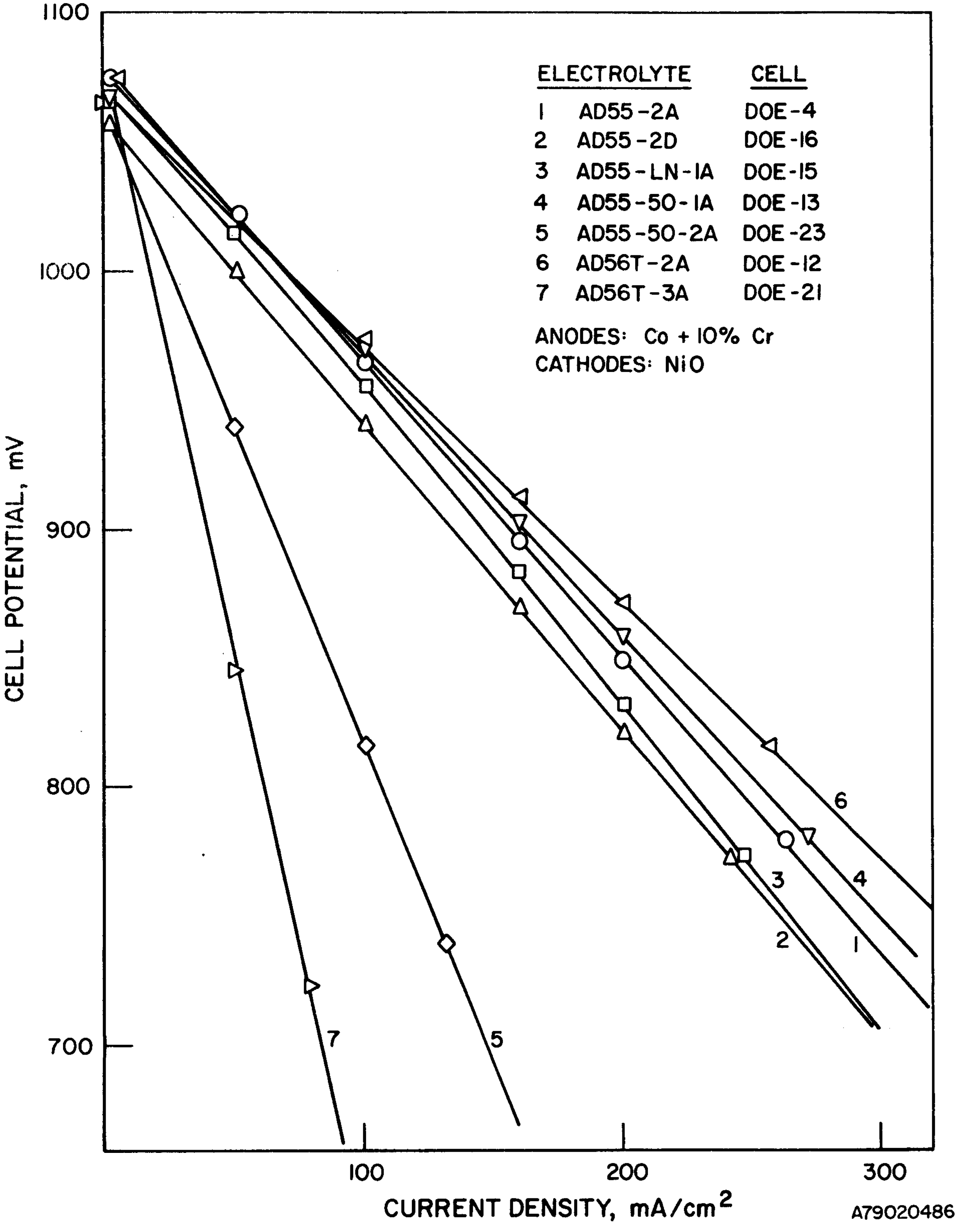

Figure 2.12. PERFORMANCE OF LABORATORY-SCALE CELLS WITH DIFFERENT ELECTROLYTE COMPOSITIONS (Reformed Methane Fuel)

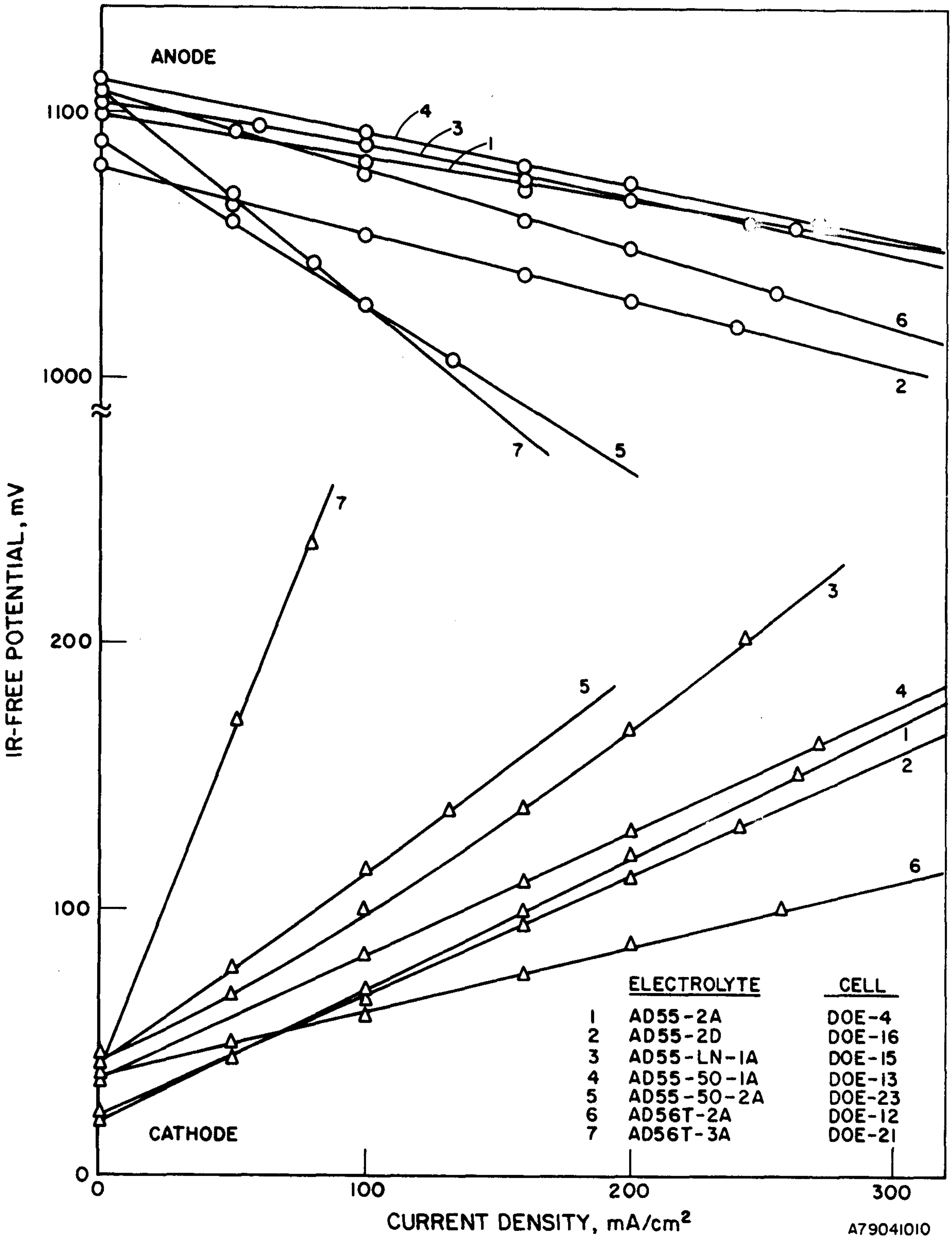

Figure 2.13. IR-FREE ANODE AND CATHODE POLARIZATION WITH DIFFERENT ELECTROLYTE COMPOSITIONS

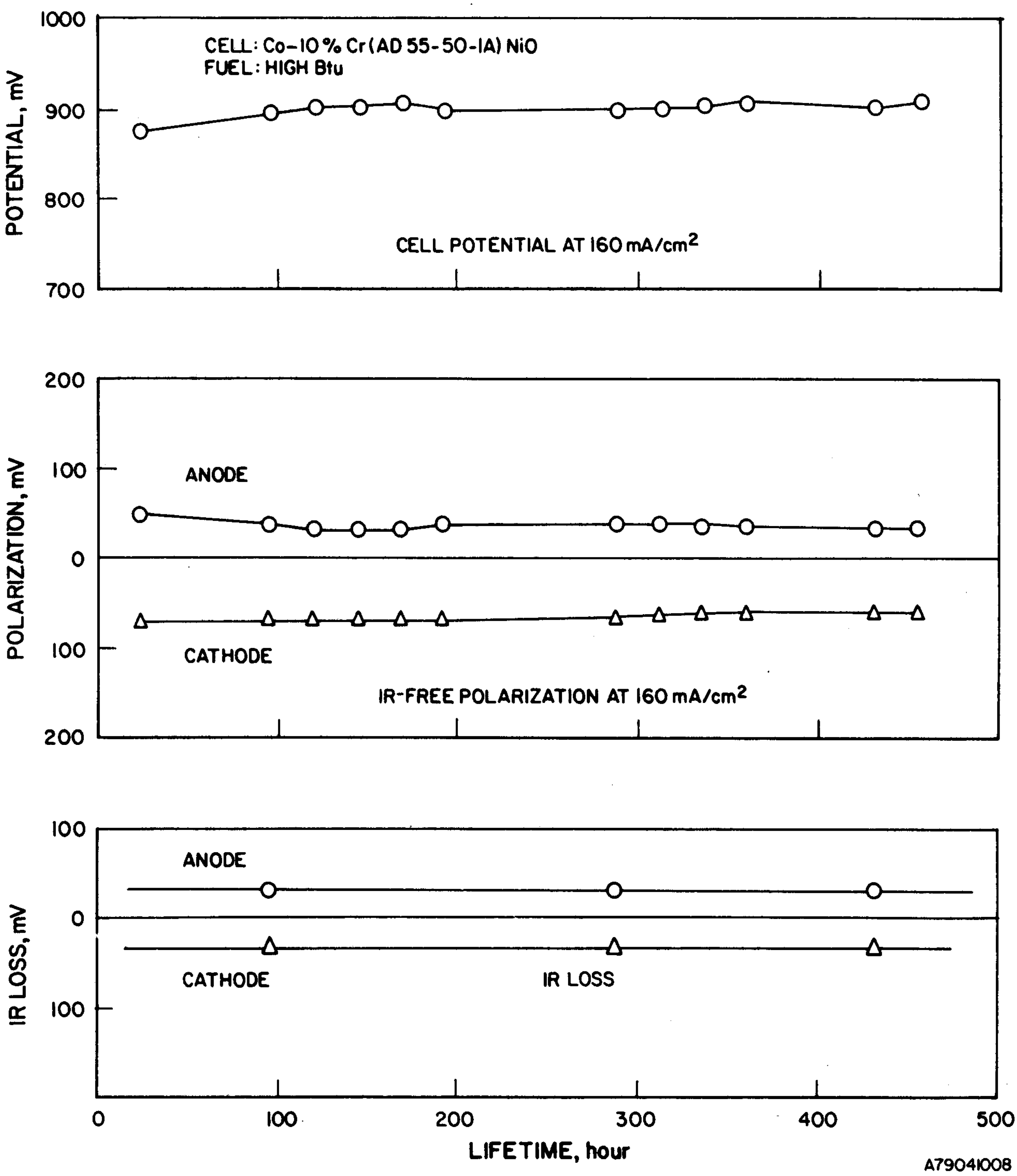

Figure 2.14. PERFORMANCE OF CELL DOE-13 AT 160 mA/cm^2

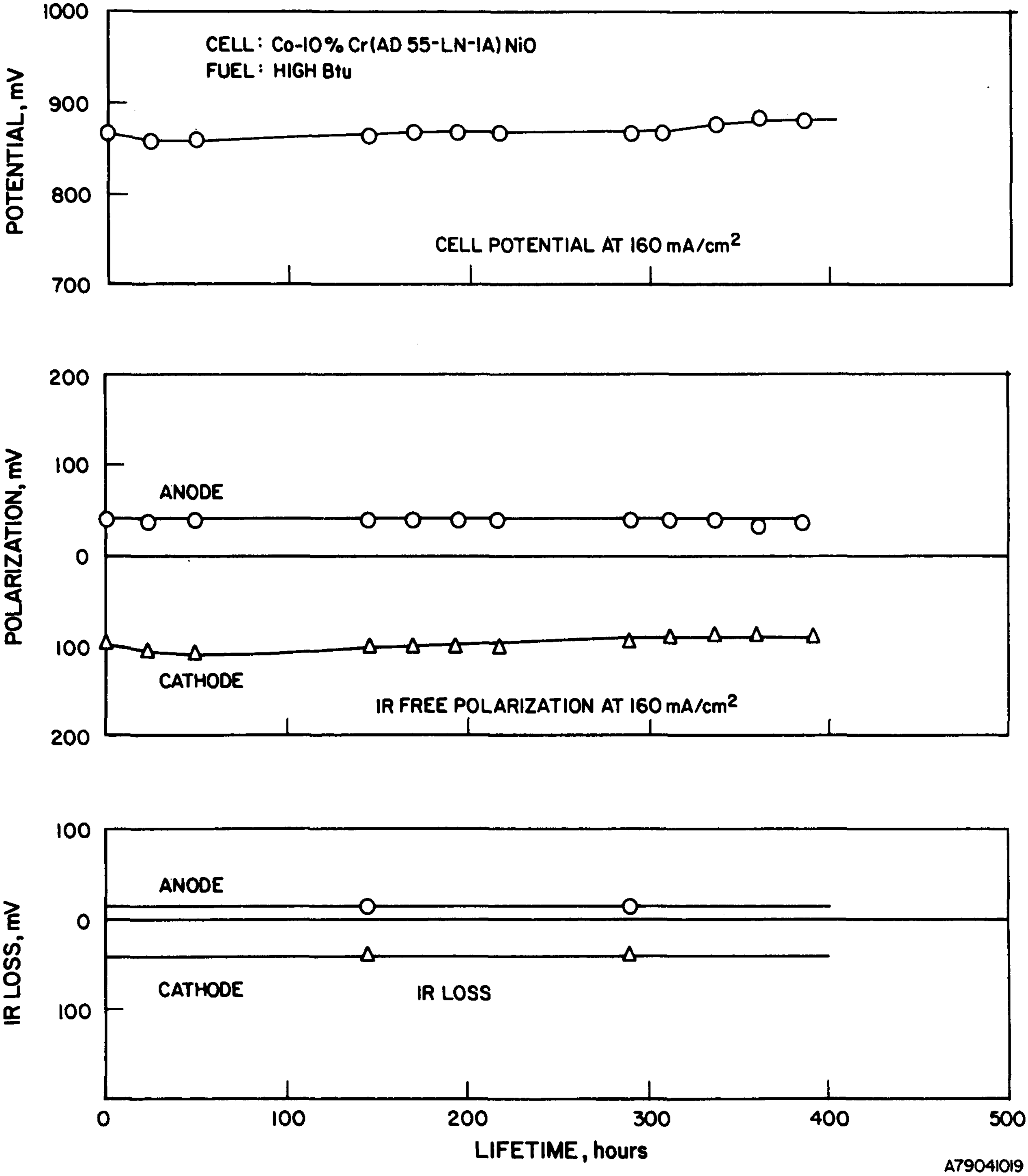

Figure 2.15. PERFORMANCE OF CELL DOE-15 AT 160 mA/cm^2

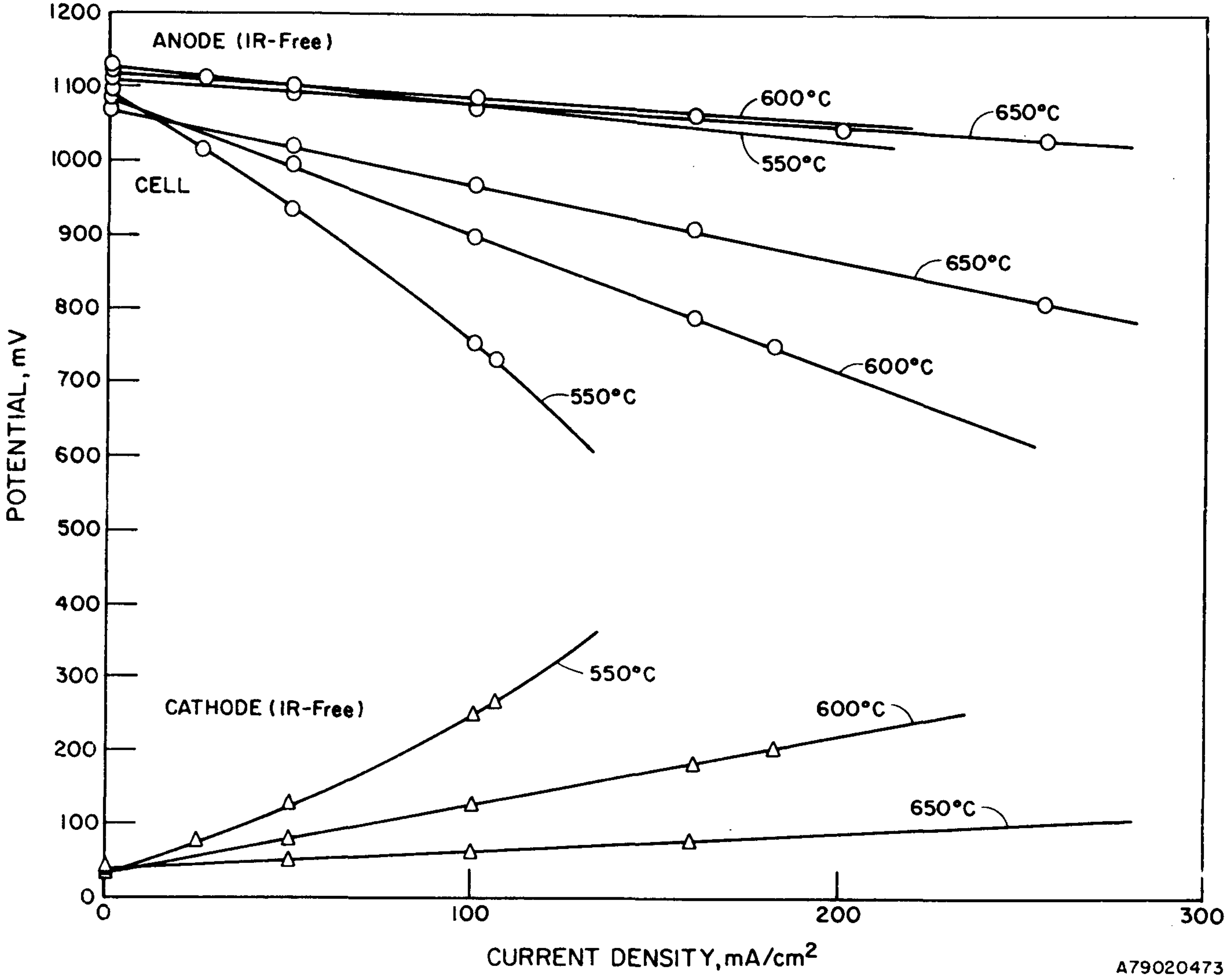

Figure 2.16. ANODE, CATHODE, AND CELL POTENTIAL VERSUS CURRENT DENSITY AT 550°, 600° AND 650°C OF CELL DOE-12 ASSEMBLED WITH A TERNARY OFF-EUTECTIC ELECTROLYTE

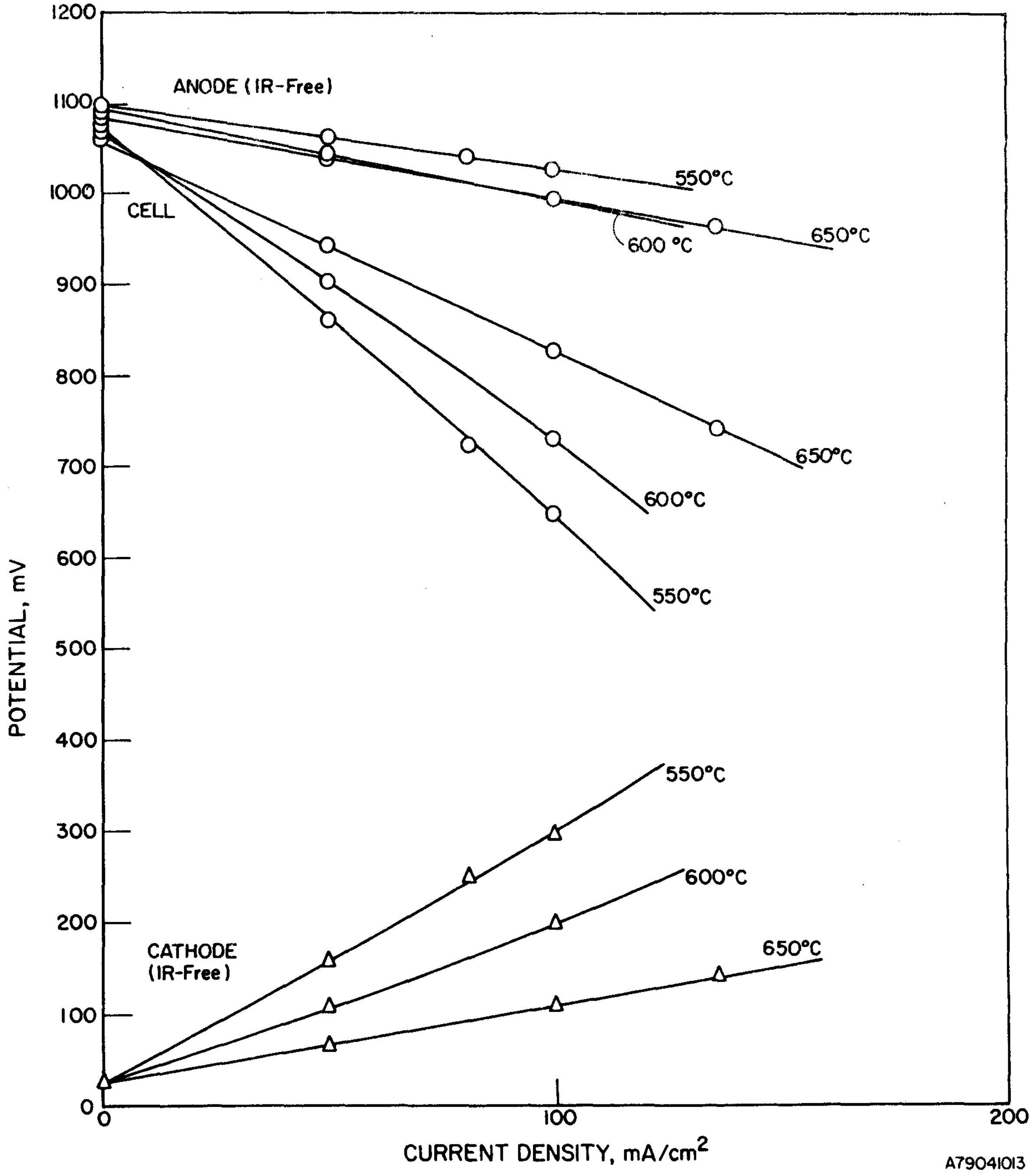

Figure 2.17. ANODE, CATHODE, AND CELL POTENTIAL VERSUS CURRENT DENSITY AT 550°, 600°, AND 650°C OF CELL DOE-20 ASSEMBLED WITH A TERNARY EUTECTIC ELECTROLYTE

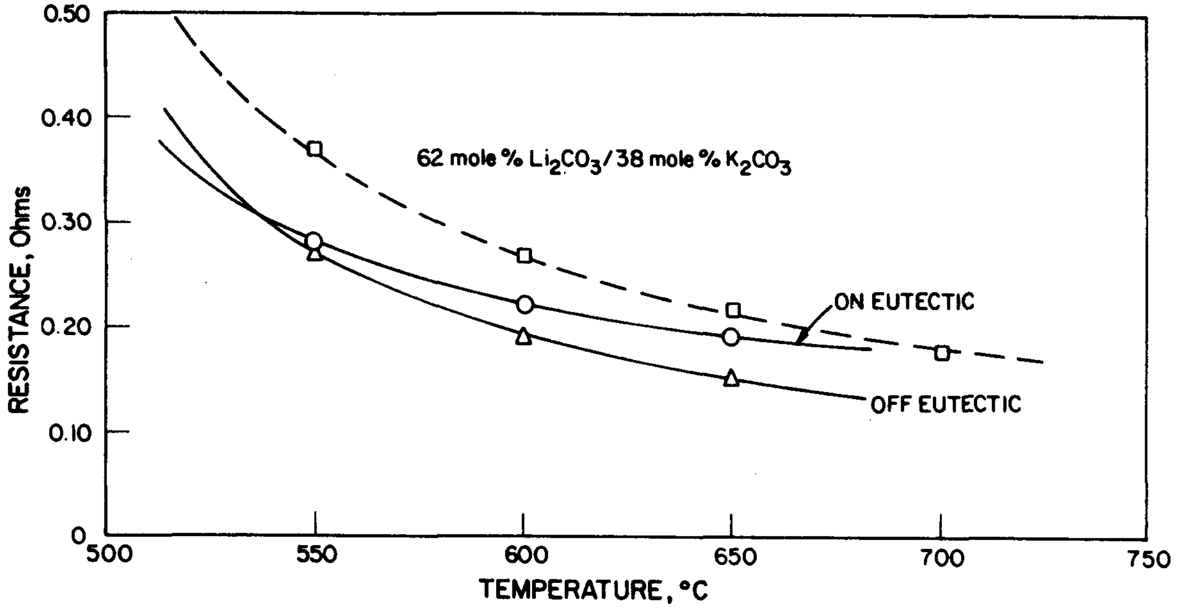

Figure 2.18. VARIATION IN THE RESISTANCE WITH TEMPERATURE FOR CELLS DOE-12 AND DOE-20 WITH TERNARY ELECTROLYTES COMPARED WITH 62 Li/38 K ELECTROLYTE

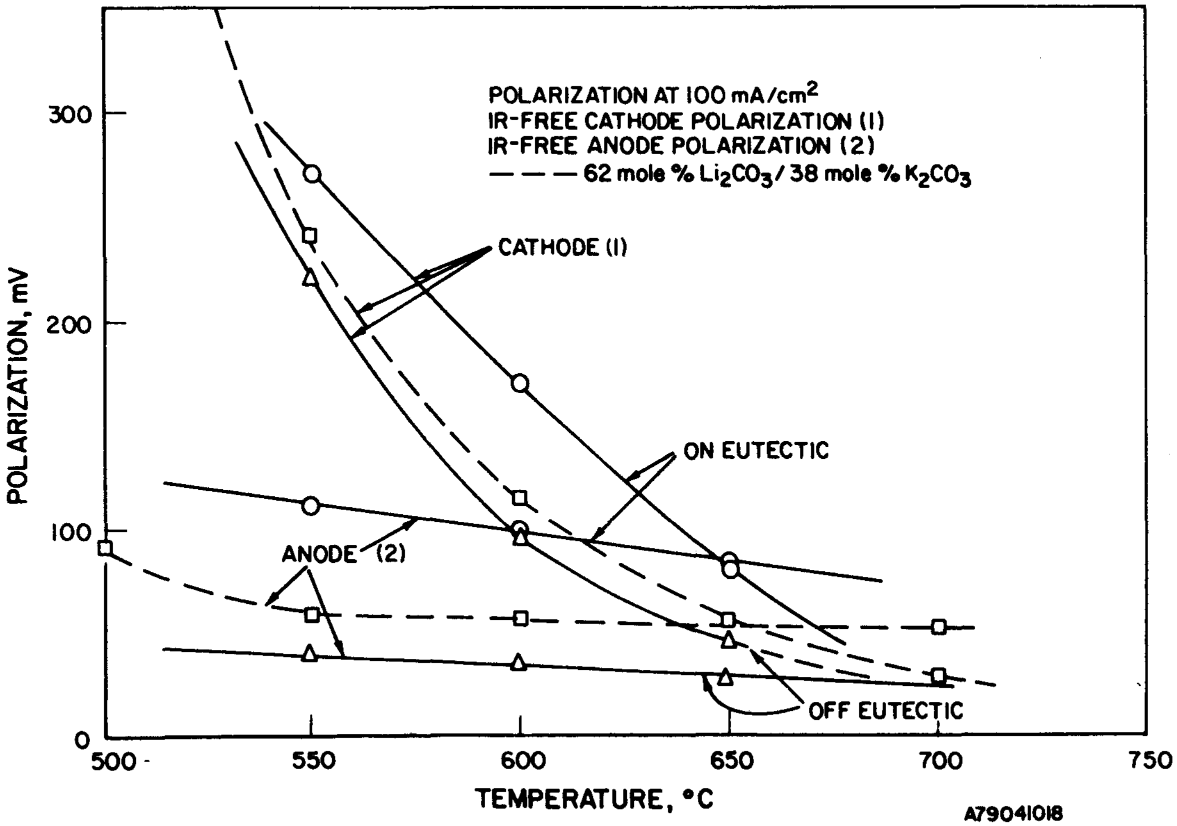

Figure 2.19. VARIATION IN THE ANODE AND CATHODE POLARIZATION WITH TEMPERATURE OF CELLS WITH TERNARY ELECTROLYTES

Table 2.1. LABORATORY-SCALE CELL TESTING OF ANODE STRUCTURES

Cell No.	Anode	Cathode	Type of Electrolyte (Tile)	Rating of Anode (Performance/Stability)
DOE-1	Ni-6.1μ mps (480-31-44)	Ni-9.6μ mps (480-31-27)	AD55-2A (50 hr 685°C) (2755)	Fair/poor
DOE-2	Ni-7.9μ mps (480-31-36)	Ni-9.6μ mps (480-31-27)	AD55-2A (50 hr 685°C) (2756)	Good/poor
DOE-3	Co-10% NiCr 3.7μ mps (416-66-3)	Ni-9.6μ mps (480-31-27)	AD55-2A (2760)	Good/fair
DOE-4	Co-10% Cr 3.2μ mps (416-66-51)	Ni-9.6μ mps (480-31-27)	AD55-2A (2778)	Good/good
DOE-5	Co-10% Cr 3.0μ mps (416-86-6)	Ni-9.6μ mps (480-31-27)	AD55-2A (50 hr 685°C) (2783)	Good/good
DOE-8	Co-10% NiCr 3.7μ mps (416-66-3)	Ni-9.6μ mps (480-31-27)	AD55-2C (2821)	Fair/good
DOE-10	Co-4.1μ mps (480-31-62)	Ni-9.6μ mps (480-31-27)	AD55-2A (2787)	Good initially/very poor
DOE-11	Co-10% WC 4.6μ mps (416-66-1)	Ni-9.6μ mps (480-31-27)	AD55-2A (2788)	Good initially/very poor
DOE-17	Co-10% NiCr 3.7μ mps (416-66-3)	Ni-9.6μ mps (480-31-27)	AD55-2D (2871)	Good/fair
DOE-18	Co-10% WC 4.6μ mps (416-66-1)	Ni-9.6μ mps (480-31-27)	AD55-2D (2876)	Poor/poor
DOE-19	Co-4.1μ mps (480-31-62)	Ni-9.6μ mps (480-31-27)	AD55-2D (2878)	Fair/poor
DOE-22	Ni-10% NiCr 7.0μ mps (416-71-4)	Ni-9.6μ mps (480-31-27)	AD55-2D (2879)	Good/fair

electrolyte was used, as shown in curve 3 of Figure 2.12. The cell potential at 160 mA/cm^2 was extremely low (~670 mV and 680 mV) with a 50 mole percent Li_2CO_3/50 mole percent K_2CO_3 and the ternary eutectic (397°C melting point), respectively.

Figure 2.13 illustrates the variation in the anode and cathode potentials at 650°C as a function of carbonate composition. In general, with the exception of curves 5 and 7, which are very steep, the curves of anode potential are nearly parallel so the anode polarization (at 160 mA/cm^2) remains at 38 ± 8 mV. The curves for the cathode potential, on the other hand, vary considerably, and the cathode polarization values range from 36 mV for the AD56T-2A (ternary off-eutectic) electrolyte to 140 mV for the AD55-LN-1A (Li/Na) electrolyte (See Table 2.2.) These results indicate that the improvement being observed in the cell potential comes primarily from decreased cathode polarization. As seen in Table 2.1, the improvement in cell conductivity also resulted when the AD55-50-1A (75 mole percent Li_2CO_3/25 mole percent K_2CO_3) and the AD55-LN-1A (Li/Na) electrolytes were used. This last electrolyte, however, showed above average (91 mV at 160 mA/cm^2) cathode polarization. The poor performance of the AD55-50-2A (50 mole percent Li_2CO_3/50 mole percent K_2CO_3) and the AD56T-3A (ternary eutectic) electrolytes was caused by a combination of factors: cathode polarization and poor cell conductivity, as seen in Table 2.2. One repeat test with the ternary eutectic electrolyte showed low performance levels similar to the first one.

Although additional data would be desirable, these alternative electrolyte studies indicate that improved cell performance can be obtained with at least two, and perhaps three, other types of electrolyte. The AD56T-2A (ternary off-eutectic) electrolyte showed the best performance, followed by the AD55-50-1A (75 mole percent Li_2CO_3/25 mole percent K_2CO_3) electrolyte. The AD55-LN-1A (52 mole percent Li_2CO_3/48 mole percent Na_2CO_3) showed the lowest cell resistance; however, the cathode polarization was greater than average, and the cell performance was only as good as the performance with the standard electrolyte. If comparable cathode polarization could be obtained, this composition would also show a better performance than that with the standard electrolyte.

Table 2.2. SUMMARY OF LAB-SCALE CELL TEST RESULTS FOR ALTERNATIVE ELECTROLYTE COMPOSITIONS

Electrolyte (Code)	AD55-2A 1	AD55-2D 2	AD55-LN-1A 3	AD55-50-1A 4	AD55-50-2A 5	AD56T-2A 6	AD56T-3A 7
Final $LiAlO_2$ $\alpha/\beta/\gamma$	53/47/0	29/66/5	7/90/3	3/94/3	4/96/0	8/90/2	2/98/0
S.A. (m^2/g)	20.2	19.6	13.7	10.1	18.5	10.5	17.5
Wt. % $LiAlO_2$	45.0	44.1	42.1	48.5	45.6	43.3	43.4
Wt. % Li_2CO_3	26.2	26.7	25.0	32.8	18.6	26.0	18.2
Wt. % Na_2CO_3	--	--	32.9	--	--	20.5	19.7
Wt. % K_2CO_3	28.8	29.2	--	18.7	35.8	10.2	18.7
Mol % Li_2CO_3	63.0	63.1	52.2	76.6	49.2	56.8	43.4
Mol % Na_2CO_3	--	--	47.8	--	--	31.2	32.7
Mol % K_2CO_3	37.0	36.9	--	23.4	50.8	12.0	23.9
Cell Potential (mV at 160 mA/cm^2)	896	870	883	903	$\sim$670	912	$\sim$680
IR-Drop (mV at 160 mA/cm^2)	77	77	57	77	135	72	91
IR-Free Polarization (mV at 160 mA/cm^2) Total $\left[\frac{\text{Anode}}{\text{Cathode}}\right]$	$106\left[\frac{30}{76}\right]$	$113\left[\frac{42}{71}\right]$	$128\left[\frac{37}{91}\right]$	$102\left[\frac{34}{68}\right]$	$\sim 250\left[\frac{130}{120}\right]$	$85\left[\frac{49}{36}\right]$	$276\left[\frac{136}{140}\right]$
Total Losses (mV at 160 mA/cm^2)	183	190	185	169	$\sim$385	157	$\sim$483

Short term stability data were obtained for two of the alternative electrolyte compositions, Cell DOE-13 (75 mole percent Li_2CO_3/25 mole percent K_2CO_3) and Cell DOE-15 (52 mole percent Li_2CO_3/48 mole percent Na_2CO_3), and are presented in Figures 2.14 and 2.15. As seen in Figure 2.14, the AD55-50-1A electrolyte (75 mole percent Li_2CO_3/25 mole percent K_2CO_3) showed good stability up to 456 hours when the test was voluntarily terminated. The performance of Cell DOE-15 (52 mole percent Li_2CO_3/48 mole percent Na_2CO_3), shown in Figure 2.15, was still improving when the test was terminated at 386 hours.

Cell performance data were also obtained between 550° and 650°C with the AD56T-2A off-eutectic ternary electrolyte and the AD56T-3A eutectic ternary electrolyte. The compositions of these electrolytes are shown in Table 2.1, and the results appear in Figures 2.16 through 2.19. As illustrated in the figures, the performance with both ternary electrolytes was extremely poor at 550°C. The performance of off-eutectic, however, improved very rapidly with temperature, and at 650°C showed the best performance of all the electrolytes tested (912 mV at 160 mA/cm^2). The cell performance with the eutectic ternary also showed improvement with temperature but remained very poor, even at 650°C (680 mV at 160 mA/cm^2).

As seen in Figures 2.16 and 2.17, the anode potential curves at 550°, 600°, and 650°C are approximately parallel for both electrolytes, indicating that the anode polarization had not been affected much by temperature. The slope of the cathode potential curves, on the other hand, decreased sharply as the temperature increased as a result of a rapid decrease in the cathode polarization. The anode and cathode polarizations of the ternary eutectic, however, remained much higher, even at 650°C. Another factor contributing to the poor performances observed at 550°C is, as seen in Figure 2.18, the conductivity of the electrolytes. At 550°C the internal resistance of the cell is much higher than at 650°C and much larger IR losses are observed. For example, the IR losses increased from 72 and 91 mV to 130 and 135 mV for the ternary off-eutectic and eutectic, respectively, when the temperature was lowered from 650 to 550°C.

The changes with temperature of the anode and cathode polarization are shown in Figure 2.19. The anode polarization is not affected if the temperature is 550°C or higher. The cathode polarizations, however, decrease very rapidly when the temperature is increased from 550° to 650°C. The same effect of temperature on the anode and cathode polarization was observed with the standard electrolyte (62 mole percent Li_2CO_3/38 mole percent K_2CO_3; melting point 487°C), as seen in Figure 2.19. Lower solubilities of O_2 and CO_2 at the lower temperature and/or slower reaction kinetics may be responsible for the observed increases in the cathode polarization.

2.1.1.3. Laboratory-Scale Cell Testing With Sulfur Contaminants

Cell DOE-16 (Co-10% Cr anode, AD55-2D electrolyte, NiO cathode) was operated on clean and sulfur-containing low-Btu fuel to observe the effects of the sulfur contaminants on the cell performance. (See Figure 2.20.)

The cell was operated for the first 144 hours with clean high-Btu fuel to reach a steady performance level. A loss of 30 mV (15 mV anode OCV and 15 mV in anode polarization) occurred when the fuel was switched to sulfur-free low-Btu fuel. Flow of a low-Btu fuel with 5 to 10 ppm H_2S + COS was started after 190 hours of operation. A loss of 40 mV (10 mV anode OCV and 30 mV anode polarization) occurred after 24 hours, followed by an additional 20 mV loss during the next 180 hours of operation with the sulfur-containing fuel. At the 495-hour mark, the fuel was switched to clean, low-Btu fuel to observe cell recovery. Within 24 hours, the cell showed essentially complete recovery by regaining 40 mV at 160 mA/cm^2 (again 10 mV anode OCV plus 30 mV anode polarization). No further performance recovery was observed during the next 80 hours. Flow of the sulfur containing low-Btu fuel was restarted after 620 hours of operation with similar results, that is, a drop of 10 mV in anode OCV and 30 mV in anode polarization at 160 mA/cm^2 had occurred 24 hours after switching fuels. Since then, the cell has operated with the sulfur-containing fuel. There is no adequate explanation for the 45 mV recovery observed between 930 to 978 hours. However, a new cylinder of low-Btu fuel with 10 ppm H_2S, with a minor difference in composition introduced after 930 hours of operation, may have been responsible. Gas chromatographic analyses of the new cylinder were carried out about 100 hours after the new cylinder was started. The results indicated that 5 to 10 ppm of sulfur compounds entered the cell from the humidifier and 5 to 10 ppm exited the cell; no significant loss of sulfur by reaction with the tile or other cell components was detectable.

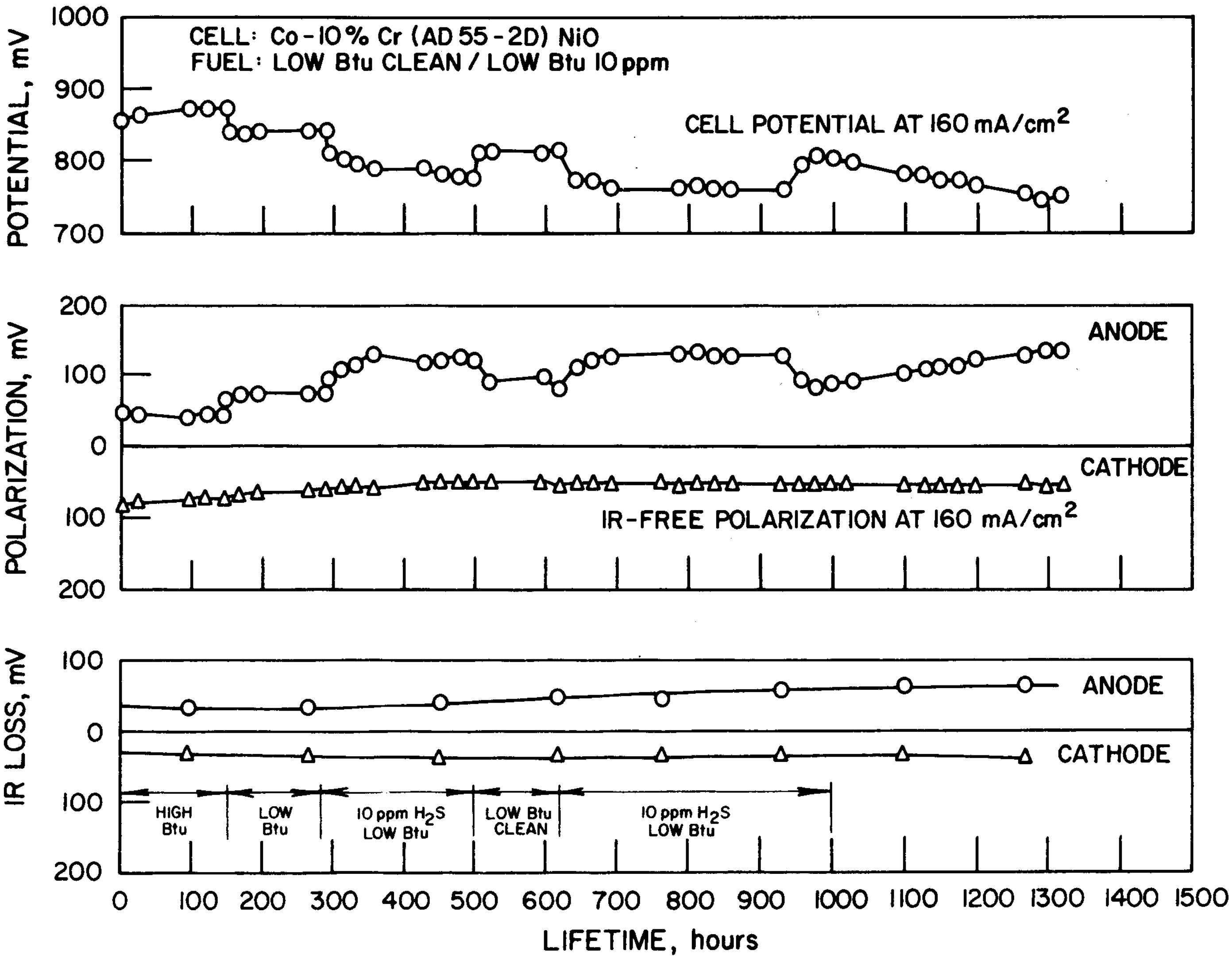

A79030495

Figure 2.20. EFFECT OF H_2S CONTAMINANT ON PERFORMANCE OF CELL DOE-16

The results from Cell DOE-16 seem to indicate that two different loss mechanisms occur when the cell is operated with the sulfur-containing fuel. The first loss-of-performance, occurring within 24 hours of switching to the sulfur-containing fuel, may be related to either changes in the activity of the ions in the melt that would result in the loss of anode open circuit and polarization, or to effects of reversible interactions between sulfur species and the cobalt anodes. These changes were reversible, and the cell recovered the loss when clean fuel was reintroduced. A second loss-of-performance, occurring gradually with time, is related to increases in the anode polarization and IR losses. This loss may have been caused by structural changes of the anode electrode and corrosion of the anode current collector. Such changes would cause irreversible losses of performance.

2.1.1.4. Laboratory-Scale Cell Testing of Tiles Fabricated by Coors Porcelain Co.

Electrolyte tiles fabricated by Coors Porcelain Co. under their cost-effective manufacturing studies were tested in laboratory-scale cells to compare their performance with tiles hot-pressed at IGT from the same powder batch (AD55-2D). The tiles were coupled with Co-10% Cr anodes and NiO cathodes and tested with a reformed naphtha fuel and standard oxidant (70% air-30% CO_2) at 650°C. This fuel gas was 75% H_2/25% CO_2 humidified at 58°C to yield an equilibrium composition at 650°C of 51.4% H_2, 28.1% H_2O, 9.9% CO, and 10.6% CO_2.

A summary of as-built data and performance levels of the three cells operated with Coors tiles is given in Table 2.3. The cells required approximately 400 hours to reach stable performance levels, which were in the range of 835 to 865 mV at a current density of 160 mA/cm^2. Lifetime performance plots of the cells through 1000 hours of testing are shown in Figures 2.21 through 2.23. These performances with tiles fabricated by Coors can be compared with that of Cell DOE-16 (Figure 2.20) which used clean, reformed methane fuel. Comparative cell polarization curves are shown in Figure 2.24. Although the performance band for the Coors-fabricated tiles is slightly lower than that of Cell DOE-16, a significant part of this difference resulted from the difference in fuel gas compositions used in the two series of tests — DOE-16 used reformed methane, while the Coors cells operated on reformed naptha. The slope of the cell polarization curve for Cell C-2 is actually less than that for Cell DOE-16, namely 1.055 $mV/mA/cm^2$ versus 1.180 $mV/mA/cm^2$.

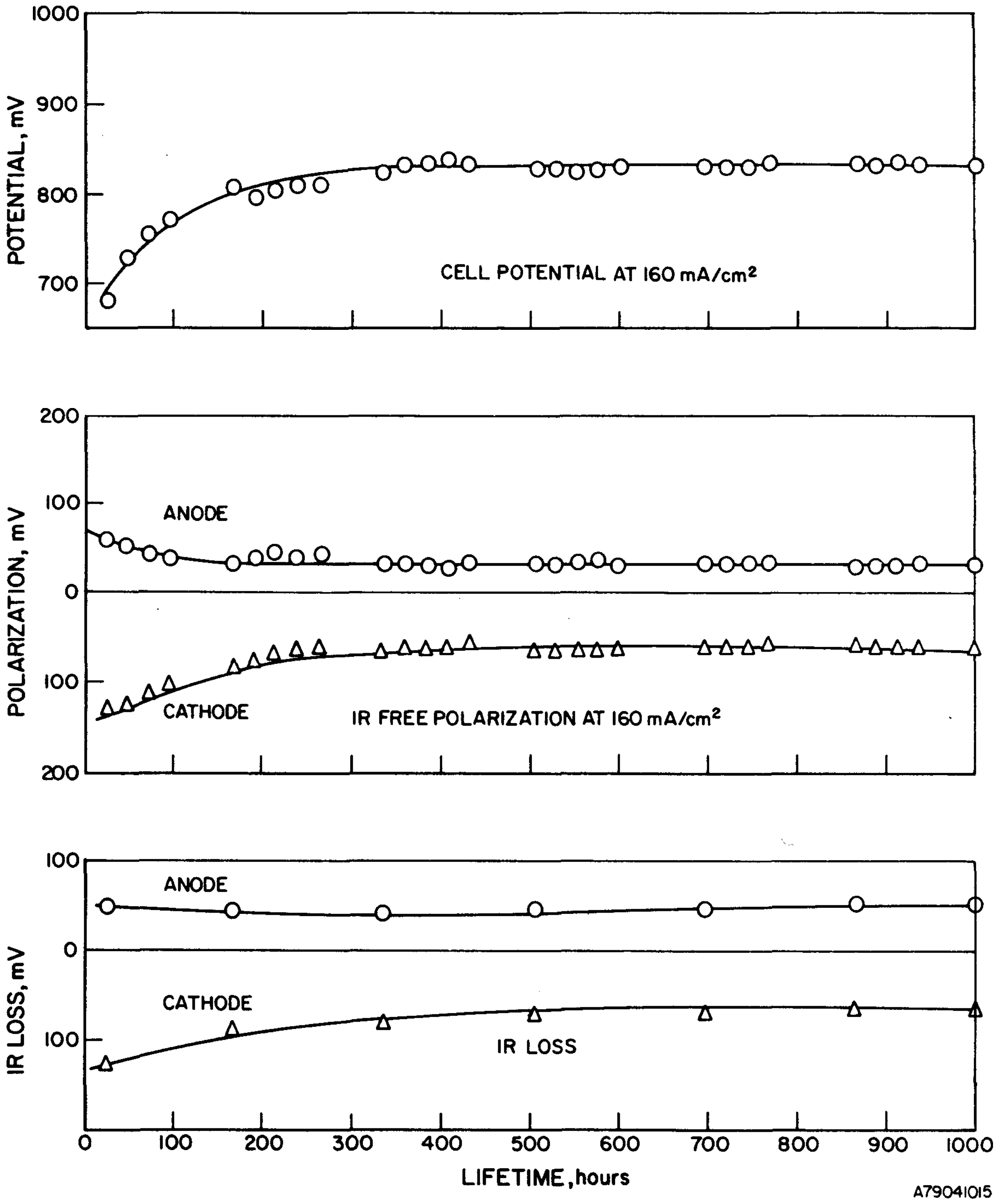

Figure 2.21. PERFORMANCE OF CELL C-1 WITH COORS TILE NO. 1
(Reformed Naphtha Fuel)

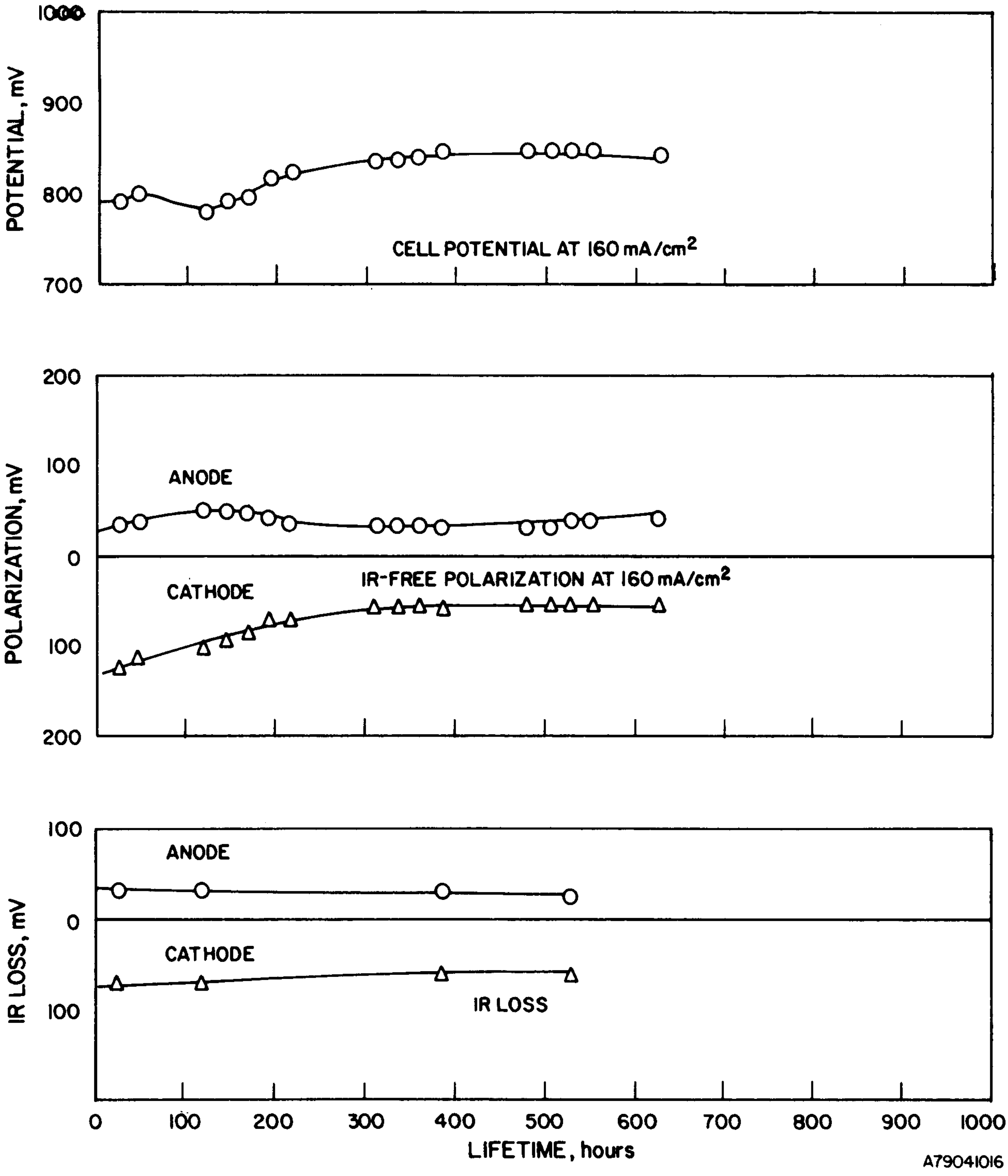

Figure 2.22. PERFORMANCE OF CELL C-2 WITH COORS TILE NO. 28 (Reformed Naphtha Fuel)

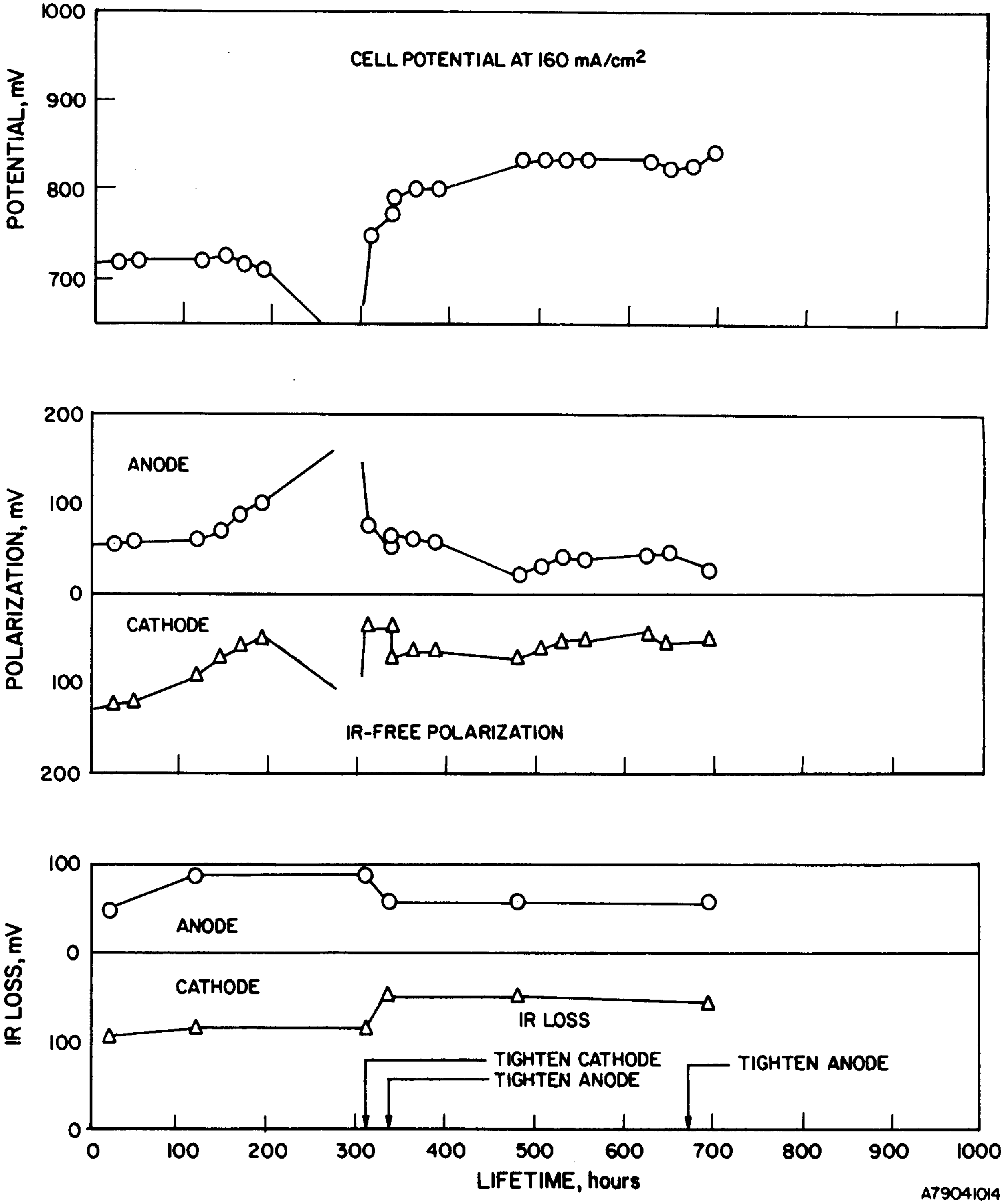

Figure 2.23. PERFORMANCE OF CELL C-3 WITH COORS TILE NO. 32 (Reformed Naphtha Fuel)

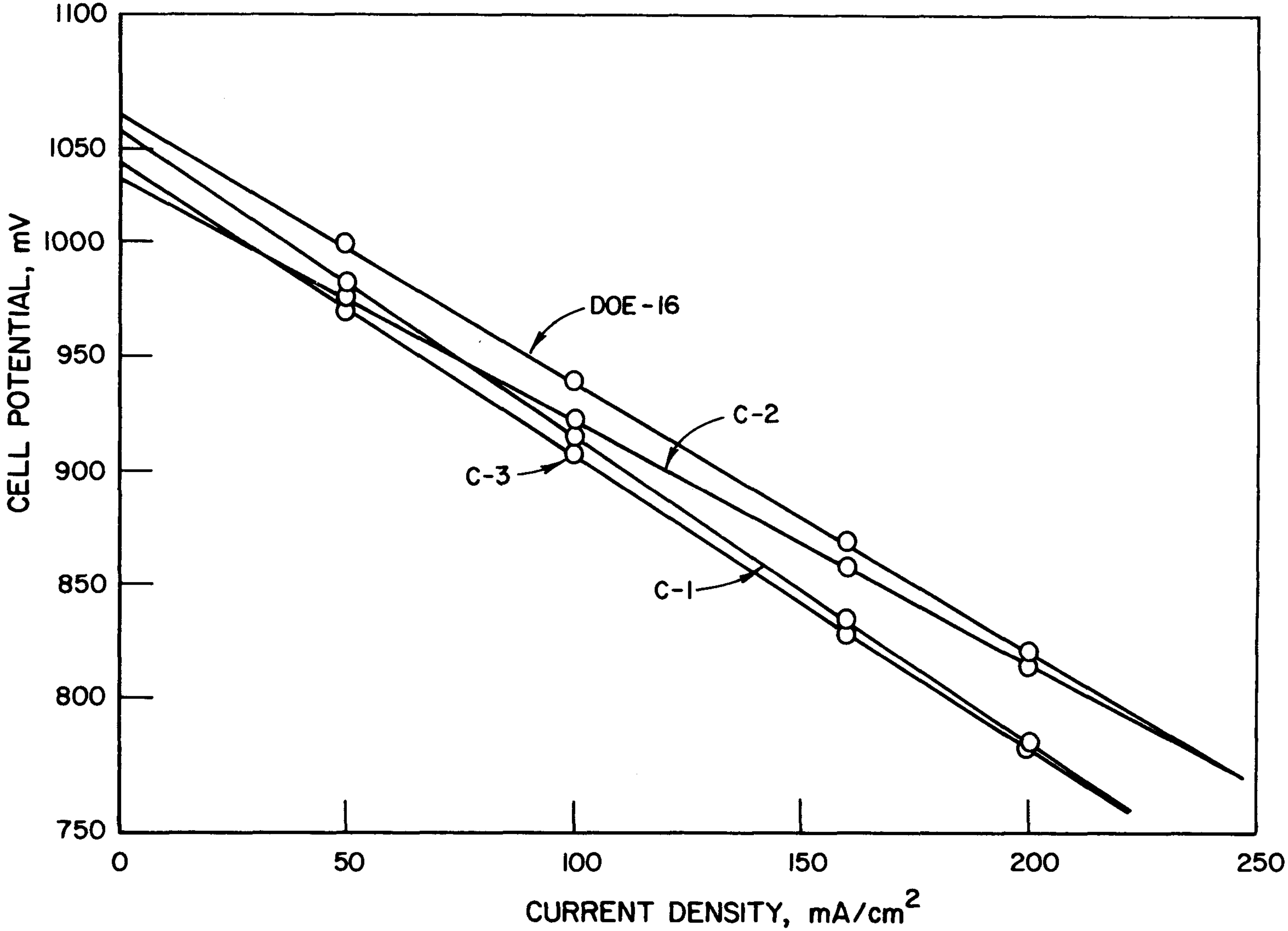

A79020468

Figure 2.24. CELL POLARIZATION CURVES FOR CELLS DOE-16 (Reformed Methane Fuel) AND C-1, C-2, AND C-3 (Reformed Naphtha Fuel) AT 650°C

Table 2.3. LABORATORY-SCALE CELLS OPERATED WITH COORS TILES*

Cell	Tile Data	Cell Performance at 160 mA/cm^2
C-1	Tile No. 1 pressed from as-received powder at 485°C and 10,000 psi for 5 min. 0.070-in. thick – no Kanthal screen. Density 2.44 g/cm^3.	835 mV
C-2	Tile No. 28 pressed from as-received powder at 485°C and 1000 psi for ~1 sec. 0.048-in. thick – no Kanthal screen. Density 2.33 g/cm^3.	865 mV
C-3	Tile No. 32. Two wafers cold-pressed at 40,000 psi and laminated with 1 Kanthal screen at 485°C and 1000 psi for 1 sec. Density 2.28 g/cm^3. 0.076-in. thick.	840 mV

* Tested at 650°C with reformed naphtha fuel/standard oxidant. Co-10% Cr anode/NiO cathode.

The comparable performance between tiles fabricated by Coors' simulated roll-compaction/warm-laminate/hot-stamp process with conventionally hot-pressed tiles is very encouraging. Further development of this potentially cost-effective tile mass production process appears to be warranted by these results.

2.1.2. Fuel Cell Electrolyte Optimization – Bench-Scale Cell Tests

The objective of this subtask was to demonstrate, in a bench-scale, the performance capability of a "new" electrolyte, other than the 62 mole percent Li_2CO_3/38 mole percent K_2CO_3 binary composition, for a period of 2000 hours. The capability of operation at temperatures below 650°C was one of the requirements imposed on this new electrolyte.

As previously discussed under Subtask 2.1.1., we identified two "new" electrolyte compositions that yielded better cell performance than the Li/K binary at 650°C. However, when the operating temperature was lowered to 600° and 550°C, laboratory-scale tests showed a significant lowering of cell performance, caused mainly by increased cathode polarization. Consequently, no bench-scale tests were operated. Instead, additional emphasis was placed on identifying the mechanism(s) responsible for the increase in cathode polarization with decreasing operating temperatures. Detailed discussions on the "new" electrolytes, their compositions, and performance behavior were included in Section 2.1.1.

2.2. Development Models to Predict Cell Performance

Summary

A mathematical model has been developed which predicts the performance of a scaled-up molten-carbonate fuel cell with crossflow of fuel and oxidant for various inlet gas compositions, gas flow rates, and operating pressures. The model takes into account the water gas equilibrium of CO and, in pressurized operation, the methane steam-reforming equilibrium. It contains only a single adjustable parameter, the effective impedance, which may be adjusted locally or given an average value. For all inlet gas compositions, the performance at 75% conversion predicted by the model agrees to within 4% with experimental data if an appropriate average value is assigned to the effective impedance. The effective cell impedances thus obtained agree fairly well with estimates based on the limited data available for small-scale cell performance. Therefore, as more data for differential-conversion cells with various inlet gas compositions become available, the performance of scaled-up cells may be predicted with excellent accuracy by means of the current model.

The current distribution predicted by the model is more uniform at high, average current densities (and the same conversion, 75%); also, it is more uniform for low-Btu gas than for reformed natural gas (RNG). The performance of cells in pressurized operation (10 atm) is predicted satisfactorily if the methanation equilibrium is accounted for.

To obtain estimates of the local concentration and surface (activation) overpotentials, a simple porous electrode model has been combined with the cross-flow model. The results indicate that ohmic potential drop in the electrode film is not negligible and needs to be included in further work.

Introduction

The objective of this subtask was to develop mathematical models capable of predicting the current distributions within a molten carbonate fuel cell as a function of feed gas compositions, gas flow rates, flow geometries, gas utilizations, and operating pressure.

The half-cell reactions occurring in this cell are —

Anode: $H_2 + CO_3^{=} \rightarrow CO_2 + H_2O + 2e^-$ (3)

$CO + CO_3^{=} \rightarrow 2CO_2 + 2e^-$ (4)

Cathode: $2e^- + CO_2 + 1/2O_2 \rightarrow CO_3^{=}$ (5)

The CO present in the fuel may react electrochemically as shown in Equation 2, but at the cell operating temperature of 650°C, the water-gas shift equilibrium —

$CO + H_2O \rightleftarrows CO_2 + H_2$ (6)

is attained more rapidly. Hence, in the various stages of the model development, it was assumed that the direct CO-oxidation reaction did not contribute to the current density.

The model development was carried out in the following stages —

1. Prediction of the current distribution for the crossflow and CO-flow configurations by a) the use of a fixed impedance value, b) inclusion of the effect of the water-gas shift reaction, c) adjustment of the impedance value to match experimental data, and d) inclusion of the effect of higher operating pressures

2. Incorporation of a microscopic, multi-parameter, porous electrode model for the crossflow configuration.

A detailed account of the work performed is given below.

2.2.1. Basic Crossflow Model

In the initial modeling study, Equations 3 and 5 only were considered. The shift reaction (Equation 6) was neglected. The model was generated by formulating mass balances on the anode and cathode sides, which resulted in one equation each for local conversion at the anode and cathode. These two equations were coupled by the cell potential balance. The potential balance equation was obtained by combining the Nernst potential (local equilibrium potential) and an assumed linear current-overpotential relationship in such a way that the cell terminal potential was constant. The detailed derivation of the equations are presented in Appendix A.

The assumption that current and overpotential are linearly related is based on measurements in small-scale (3-cm^2) cells with 7.5% and 15% oxidant utilizations.[10] It should be kept in mind that their approximately linear polarization behavior results from a complex interaction of activation overpotential, concentration overpotential, and ohmic resistance in the electrode pores; it does not necessarily indicate that the electrode is operating in the linear region of the activation overpotential.

The resulting three equations contain three unknowns: the local current density, the local cumulative fuel conversion (λ = moles of H_2 consumed/moles of H_2 at inlet), and the local cumulative oxidant conversion (μ = moles of CO_2 consumed/moles of CO_2 at inlet). They also contain three operational parameters in dimensionless form; the cell terminal potential, the oxygen-to-hydrogen stoichiometric ratio at the cell inlet, and the effective impedance.

2.2.1.1. Initial Results for Hydrogen-Rich Fuel

We developed a computer program to solve these three equations. The inputs to the program are: anode and cathode gas compositions and flow rates, standard anode and cathode potentials, terminal voltages, length of the anode and cathode gas channels, number of sections in the x and y directions, temperature, pressure, and effective impedance. Only the effective impedance is an adjustable parameter; in the computations reported here, it has been assigned an average value for the entire cell. Initially, this value was based on polarization measurements in small-scale fuel cells (3-cm^2 electrode area, 7.5% fuel conversion) using reformed natural gas. Figure 2.25 and 2.26 compare the experimental data (obtained from 100-cm^2 cells) and the predicted curves for reformed natural gas and reformed naphtha fuels.

Although the agreement between the prediction and experimental data is fairly good, the fuel conversion exceeds 75% at most current densities. This suggests that the effective cell impedance is underestimated by the initial value assigned on the basis of small-scale cell polarization data. Consequently, in later computations (Section 3) the cell impedance was varied until a 75% fuel conversion resulted. However, the effect of including the water gas equilibrium was first investigated, using the same impedance value as employed in Figures 2.25 and 2.26.

As an illustration of the data produced by the model calculations, Table 2.4 is a sample printout that shows the current distribution, Nernst losses, overpotentials, and local anode and cathode conversions across the cell, which has been divided into 100 subdivisions (a 10 x 10 matrix). (Refer to Figure A-1 for the directions "across" the cell.) The fuel is reformed natural gas. For a terminal voltage of 755 mV, the predicted current density

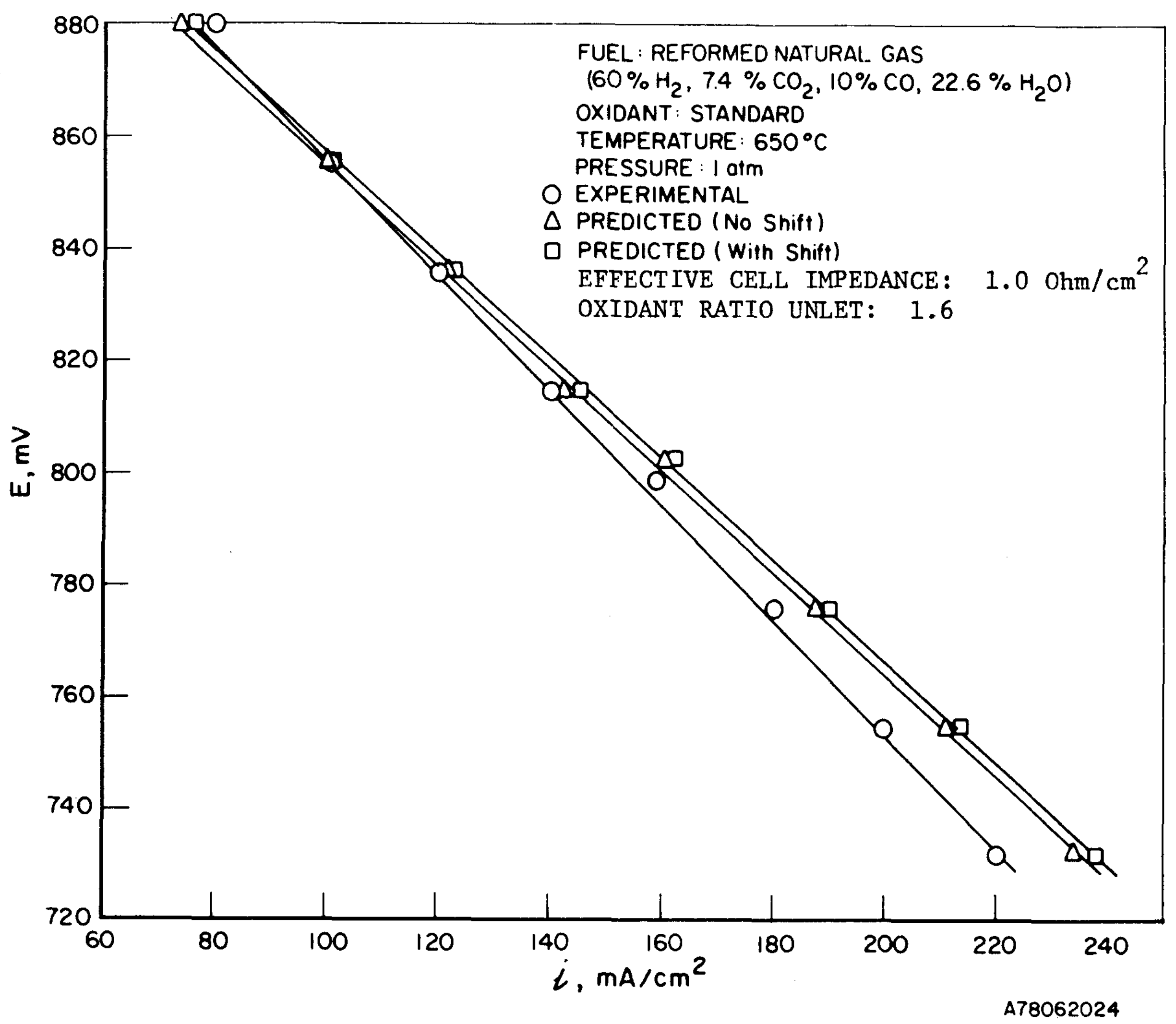

Figure 2.25. PREDICTED POLARIZATION CURVES FOR REFORMED NATURAL GAS (With and Without the CO Shift Reaction) COMPARED WITH EXPERIMENTAL DATA (Cell Impedance is Pre-Assigned)

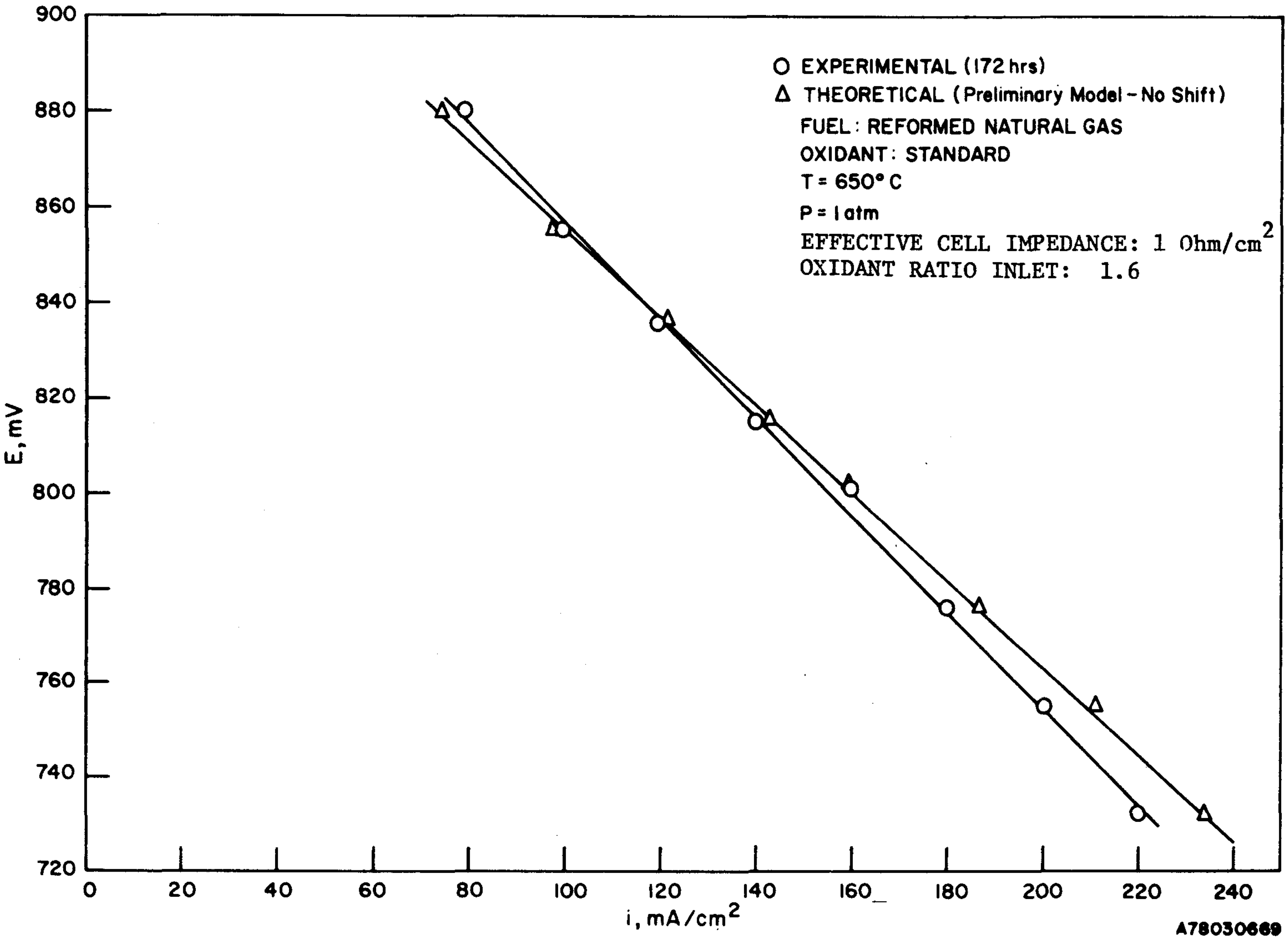

Figure 2.26. COMPARISON OF THE EXPERIMENTAL AND THEORETICAL POLARIZATION CURVES FOR A CELL USING REFORMED NATURAL GAS AS THE FUEL

using the "small-scale cell" impedance (1.025 ohm cm^2) is 211.39 mA/cm^2, as compared with the experimental value of 200 mA/cm^2. Isocurrent-density lines have been drawn throught the data of Table 2.4, Section A. In the last two righthand columns of Sections A and B of Table 2.4, the current density increases from top to bottom. The dependency on current density of both anode and cathode conversions across the cell matrix at a given overall cell potential is shown in Figure 2.27. As expected, Table 2.4 shows that the separate Nernst losses and the overpotential plus ohmic resistance losses add up to a constant sum.

2.2.2. Effect of Water-Gas Equilibrium

In the second stage of the model development, the water-gas shift reaction (Equation 6) was included. The mass and potential balance equations were correspondingly modified, and these changes were incorporated into the computer program. Polarization curves were obtained for reformed natural gas (RNG), for the gas product from the partial oxidation of heavy oils (PO), and for low-Btu coal gas (LBTU) using the modified computer program. These are shown in Figures 2.28 through 2.30.

For all gas compositions, the same effective cell impedance was employed as in ection 2.2.1, except for a correction in the ohmic component. (See Section 2.2.3.) The resulting values are given in Table 2.5. The experimental polarization curve and the curve predicted with and without the shift reaction are shown for each fuel gas. For RNG (Figure 2.28), the contribution to current density from hydrogen originating from the shift reaction is not significant. This was expected because the initial CO content is low and the H_2 content high. In the cases of PO and LBTU fuels, the water-gas shift reaction contributes significantly to the current density (Figures 2.29 and 2.30) because of high initial CO contents.

2.2.3. Variation of Effective Electrode Impedance, $\mathcal{Z}$

The single adjustable parameter in the basic crossflow model is $\mathcal{Z}$, the effective electrode impedance, which is the sum of the ohmic cell resistance and the overpotential resistances, given by –

$$\mathcal{Z} = R \cdot A + \frac{\eta_A}{i} + \frac{\eta_C}{i} \tag{7}$$

where A is the area of the cell, i is the current density, and η_A (<0) and η_C (<0)

Table 2.4, Part 1. TYPICAL MODEL OUTPUT (Reformed Natural Gas, without water gas shift)

```
TOTAL IMPEDANCE=  1.025 OHM SQ-CM
AVERAGE CURRENT DENSITY (DIMENSIONLESS)=  0.087
AVERAGE ANODE CONVERSION=  0.874
AVERAGE CATHODE CONVERSION=  0.536

TERMINAL VOLTAGE= 0.7550 VOLTS
TOTAL CURRENT=19.8706 AMPS
CURRENT DENSITY= 211.39 MAMPS PER SQ-CM
```

```
A. LOCAL CURRENT DENSITIES, ROW BY ROW, DIMENSIONLESS

   0.133  0.118  0.108  0.100  0.092  0.085  0.078  0.071  0.064  0.055
   0.132  0.117  0.107  0.099  0.091  0.085  0.078  0.071  0.064  0.055
   0.131  0.116  0.106  0.098  0.091  0.084  0.078  0.071  0.064  0.056
   0.129  0.115  0.105  0.097  0.090  0.084  0.077  0.071  0.064  0.056
   0.127  0.114  0.104  0.096  0.089  0.083  0.077  0.071  0.064  0.057
   0.125  0.112  0.103  0.095  0.088  0.082  0.077  0.071  0.064  0.057
   0.122  0.110  0.101  0.094  0.088  0.082  0.076  0.070  0.064  0.058
   0.119  0.108  0.100  0.093  0.087  0.081  0.076  0.070  0.064  0.058
   0.115  0.105  0.098  0.091  0.086  0.080  0.075  0.070  0.065  0.059
   0.111  0.103  0.096  0.090  0.085  0.080  0.075  0.070  0.065  0.059
```

0.13 0.12 0.11 0.10 0.09 0.08 0.07 0.06

```
B. REAL CURRENT DENSITIES, ROW BY ROW, MAMPS PER SQ-CM

 322.85 286.48 261.19 240.73 222.41 205.77 189.41 172.55 154.33 133.09
 319.67 283.95 259.07 238.96 220.96 204.63 188.61 172.17 154.46 133.96
 316.08 281.15 256.76 237.03 219.41 203.42 187.78 171.77 154.61 134.87
 312.02 278.02 254.22 234.94 217.74 202.14 186.91 171.37 154.78 136.22
 307.36 274.52 251.41 232.67 215.94 200.78 185.99 170.96 154.98 137.21
 301.96 270.58 248.31 229.77 214.03 199.35 185.07 170.58 155.26 138.31
 295.65 266.05 244.84 227.08 211.94 197.81 184.08 170.18 155.54 139.44
 288.13 260.94 240.96 224.11 209.68 196.18 183.06 169.80 155.89 140.69
 279.04 254.97 236.58 220.85 207.24 194.45 182.01 169.47 156.34 142.06
 267.75 247.95 231.61 217.24 204.61 192.65 180.98 169.20 156.91 143.60
```

```
C. NERNST LOSSES, VOLTS

   0.026  0.059  0.082  0.101  0.117  0.132  0.147  0.163  0.179  0.198
   0.029  0.062  0.084  0.102  0.118  0.133  0.148  0.163  0.179  0.198
   0.032  0.064  0.086  0.104  0.120  0.134  0.149  0.163  0.179  0.197
   0.036  0.067  0.089  0.106  0.121  0.136  0.149  0.164  0.179  0.196
   0.040  0.070  0.091  0.108  0.123  0.137  0.150  0.164  0.179  0.195
   0.045  0.074  0.094  0.110  0.125  0.138  0.151  0.164  0.178  0.194
   0.051  0.078  0.097  0.113  0.127  0.140  0.152  0.165  0.178  0.193
   0.058  0.082  0.101  0.115  0.129  0.141  0.153  0.165  0.178  0.192
   0.066  0.088  0.104  0.118  0.131  0.143  0.154  0.165  0.177  0.190
   0.076  0.094  0.109  0.122  0.133  0.144  0.155  0.166  0.177  0.189
```

Table 2.4, Part 2. TYPICAL MODEL OUTPUT (Reformed Natural Gas, without water gas shift)

D. OVERPOTENTIAL PLUS OHMIC RESISTANCE, VOLTS

```
   0.293  0.260  0.237  0.218  0.202  0.187  0.172  0.156  0.140  0.121
   0.290  0.257  0.235  0.217  0.200  0.185  0.171  0.156  0.140  0.121
   0.287  0.255  0.233  0.215  0.199  0.184  0.170  0.156  0.140  0.122
   0.283  0.252  0.230  0.213  0.197  0.183  0.169  0.155  0.140  0.123
   0.279  0.249  0.228  0.211  0.196  0.182  0.169  0.155  0.140  0.124
   0.274  0.245  0.225  0.208  0.194  0.181  0.168  0.155  0.141  0.125
   0.268  0.241  0.222  0.206  0.192  0.179  0.167  0.154  0.141  0.126
   0.261  0.237  0.218  0.203  0.190  0.178  0.166  0.154  0.141  0.128
   0.253  0.231  0.214  0.200  0.188  0.176  0.165  0.154  0.142  0.129
   0.243  0.225  0.210  0.197  0.185  0.175  0.164  0.153  0.142  0.130
```

E. LOCAL ANODE CONVERSIONS, ROW BY ROW, FLOW DIRECTION TO THE RIGHT

```
   0.000  0.000  0.000  0.000  0.000  0.000  0.000  0.000  0.000  0.000  0.000
   0.000  0.133  0.252  0.360  0.459  0.551  0.636  0.715  0.786  0.850  0.905
   0.000  0.132  0.250  0.357  0.455  0.547  0.631  0.709  0.781  0.844  0.900
   0.000  0.131  0.247  0.353  0.451  0.542  0.626  0.704  0.775  0.838  0.894
   0.000  0.129  0.244  0.349  0.446  0.536  0.620  0.697  0.768  0.832  0.888
   0.000  0.127  0.241  0.345  0.441  0.530  0.613  0.690  0.761  0.825  0.881
   0.000  0.125  0.237  0.339  0.434  0.523  0.605  0.682  0.752  0.817  0.874
   0.000  0.122  0.232  0.333  0.427  0.515  0.597  0.673  0.743  0.808  0.865
   0.000  0.119  0.227  0.327  0.419  0.506  0.587  0.663  0.733  0.797  0.856
   0.000  0.115  0.221  0.319  0.410  0.496  0.576  0.651  0.721  0.786  0.845
   0.000  0.111  0.213  0.309  0.399  0.483  0.563  0.638  0.708  0.773  0.832
```

F. LOCAL CATHODE CONVERSIONS, ROW BY ROW, FLOW DIRECTION VERTICALLY DOWN

```
   0.000  0.000  0.000  0.000  0.000  0.000  0.000  0.000  0.000  0.000  0.000
   0.000  0.082  0.073  0.066  0.061  0.056  0.052  0.048  0.044  0.039  0.034
   0.000  0.163  0.145  0.132  0.122  0.112  0.104  0.096  0.087  0.078  0.068
   0.000  0.243  0.216  0.197  0.182  0.168  0.156  0.143  0.131  0.117  0.102
   0.000  0.322  0.286  0.261  0.241  0.223  0.207  0.191  0.174  0.157  0.136
   0.000  0.400  0.356  0.325  0.300  0.278  0.258  0.238  0.218  0.196  0.171
   0.000  0.477  0.425  0.388  0.359  0.332  0.308  0.285  0.261  0.235  0.206
   0.000  0.552  0.492  0.450  0.416  0.386  0.358  0.332  0.304  0.275  0.242
   0.000  0.625  0.558  0.511  0.473  0.439  0.408  0.378  0.347  0.314  0.277
   0.000  0.695  0.623  0.571  0.529  0.492  0.458  0.424  0.390  0.354  0.313
   0.000  0.743  0.666  0.630  0.564  0.544  0.506  0.470  0.433  0.394  0.350
```

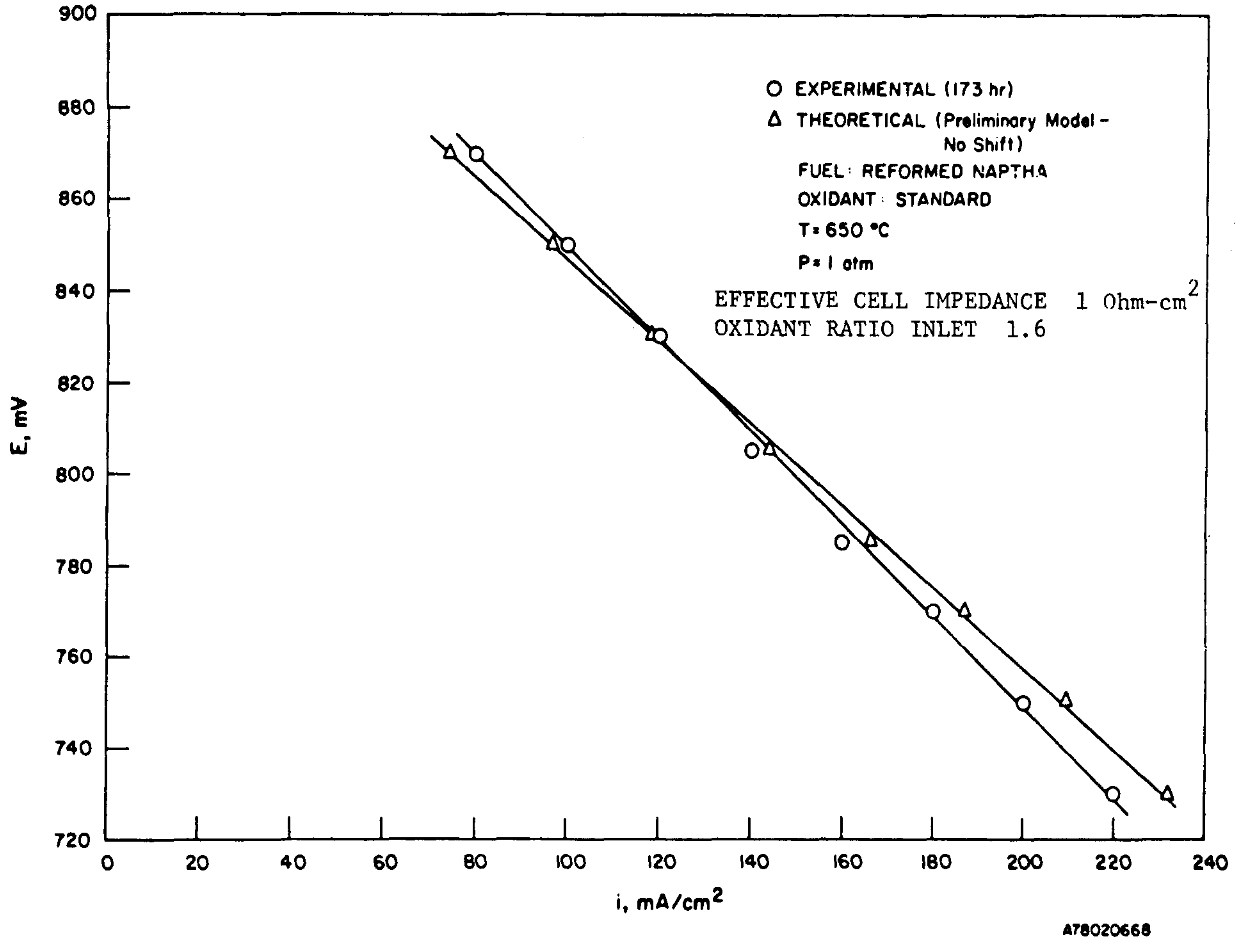

Figure 2.27. COMPARISON OF THE EXPERIMENTAL AND THEORETICAL POLARIZATION CURVES FOR A CELL USING REFORMED NAPHTHA AS THE FUEL

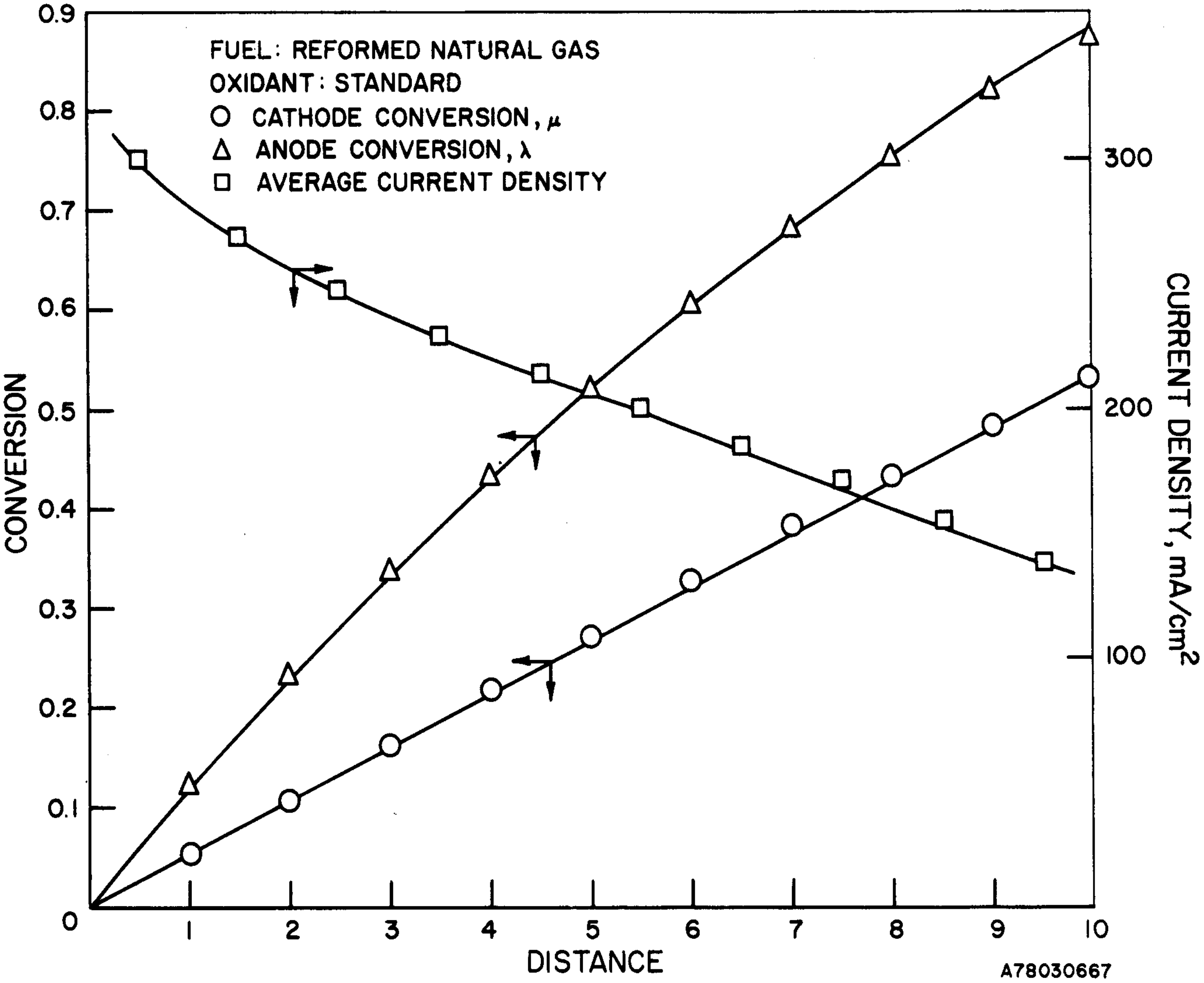

Figure 2.28. VARIATION OF CONVERSIONS AND CURRENT DENSITIES AT A CONSTANT POTENTIAL OF 755 mV

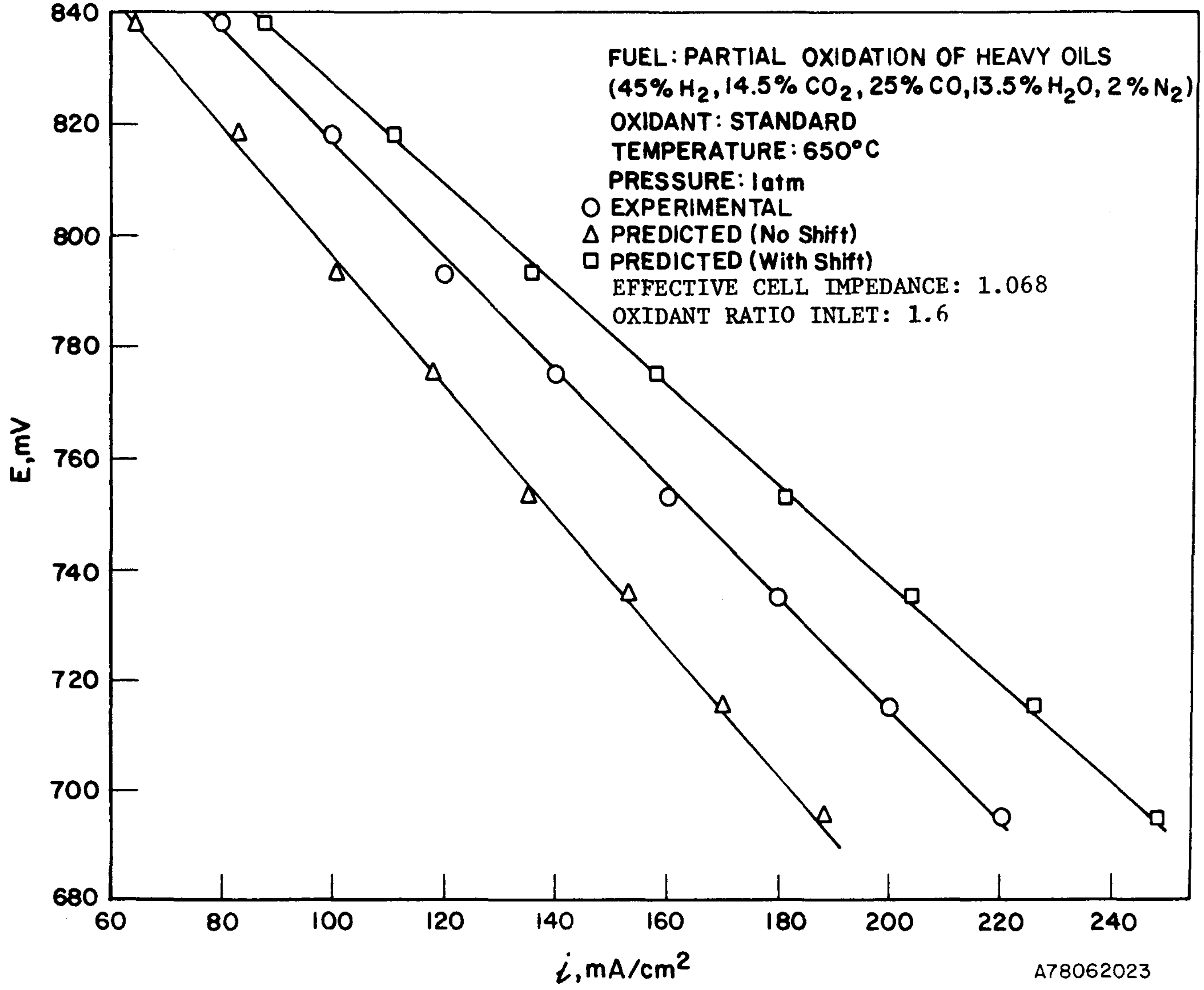

Figure 2.29. PREDICTED POLARIZATION CURVES FOR PARTIAL OXIDATION OF HEAVY OILS (With and Without the CO Shift Reaction) COMPARED WITH EXPERIMENTAL DATA (Cell Impedance is Pre-Assigned)

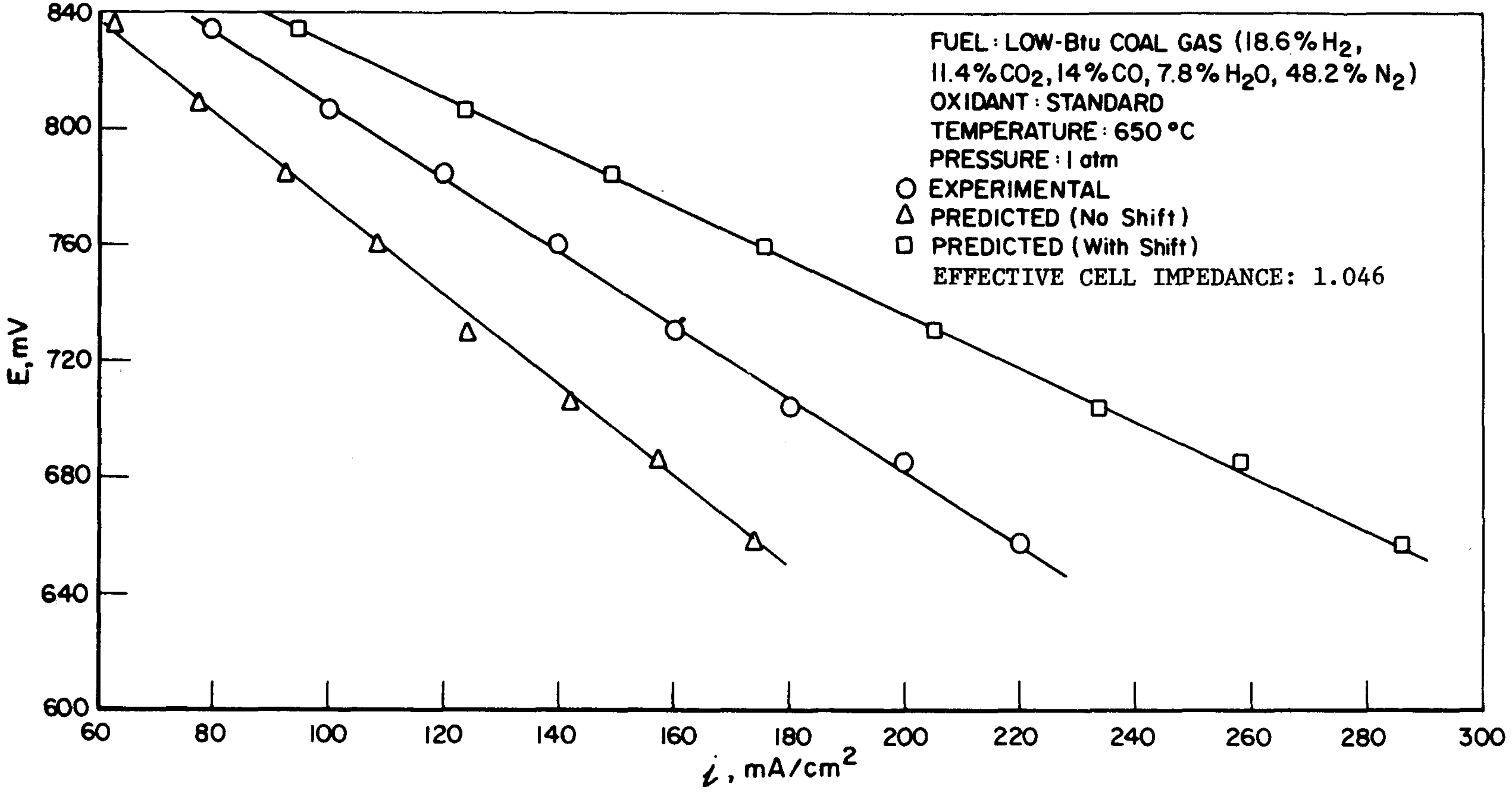

A78062022

Figure 2.30. PREDICTED POLARIZATION CURVES FOR LOW-Btu COAL GAS (With and Without the CO Shift Reaction) COMPARED WITH EXPERIMENTAL DATA (Cell Impedance is Pre-Assigned)

Table 2.5. INITIAL VALUES OF EFFECTIVE CELL IMPEDANCE ($\mathcal{Z}$) AND VALUES OBTAINED AFTER ADJUSTMENT FOR 75% FUEL CONVERSION (at 200 mA/cm^2)

	Initial	Adjusted
Reformed natural gas	1.00*	1.19
Low-Btu coal gas	1.046**	1.604

* Z_{ohm} = 0.400

$A_a = \eta_a/i = 0.225$

$Z_c = \eta_c/i = 0.375$

** Z_{ohm} = 0.446

$Z_a = \eta_a/i$ 0.225

$Z_c = \eta_c/i$ 0.375

are the anode and cathode overpotentials. The cell resistance, R, was obtained with an oscilloscope by a current interruption technique on 100-cm^2 cells. (In large cells, the fuel and oxidant gases flow perpendicular to each other.) However, the values of η_A and η_C were estimates, based on polarization measurements on small cells (3 cm^2) equipped with reference electrodes (Table 2.5). Given this value of $\mathcal{Z}$, together with the cell potential, gas compositions, and flow rates, the model predicts the current density and anode and cathode conversions. The average anode conversion initially obtained was generally different from the experimental 75% conversion achieved in 100-cm^2 cells. We therefore adjusted the value of $\mathcal{Z}$ to yield an overall anode conversion of 75%. The predicted average current densities with the shift reaction based on the new values of $\mathcal{Z}$ agree to within 4% of the experimental current densities. Figures 2.31 and 2.32 compare the predicted polarization curves with the experimental curves for two feed gases.

Figure 2.33 shows effective cell impedance values at 75% fuel conversion. The values are fairly constant with increasing load.* The difference in trend between reformed natural gas and low-Btu gas suggests that the H_2 and H_2O components of the fuel gas are responsible for increasing polarization

---

* The single deviating point for RNG does not appear to be correct.

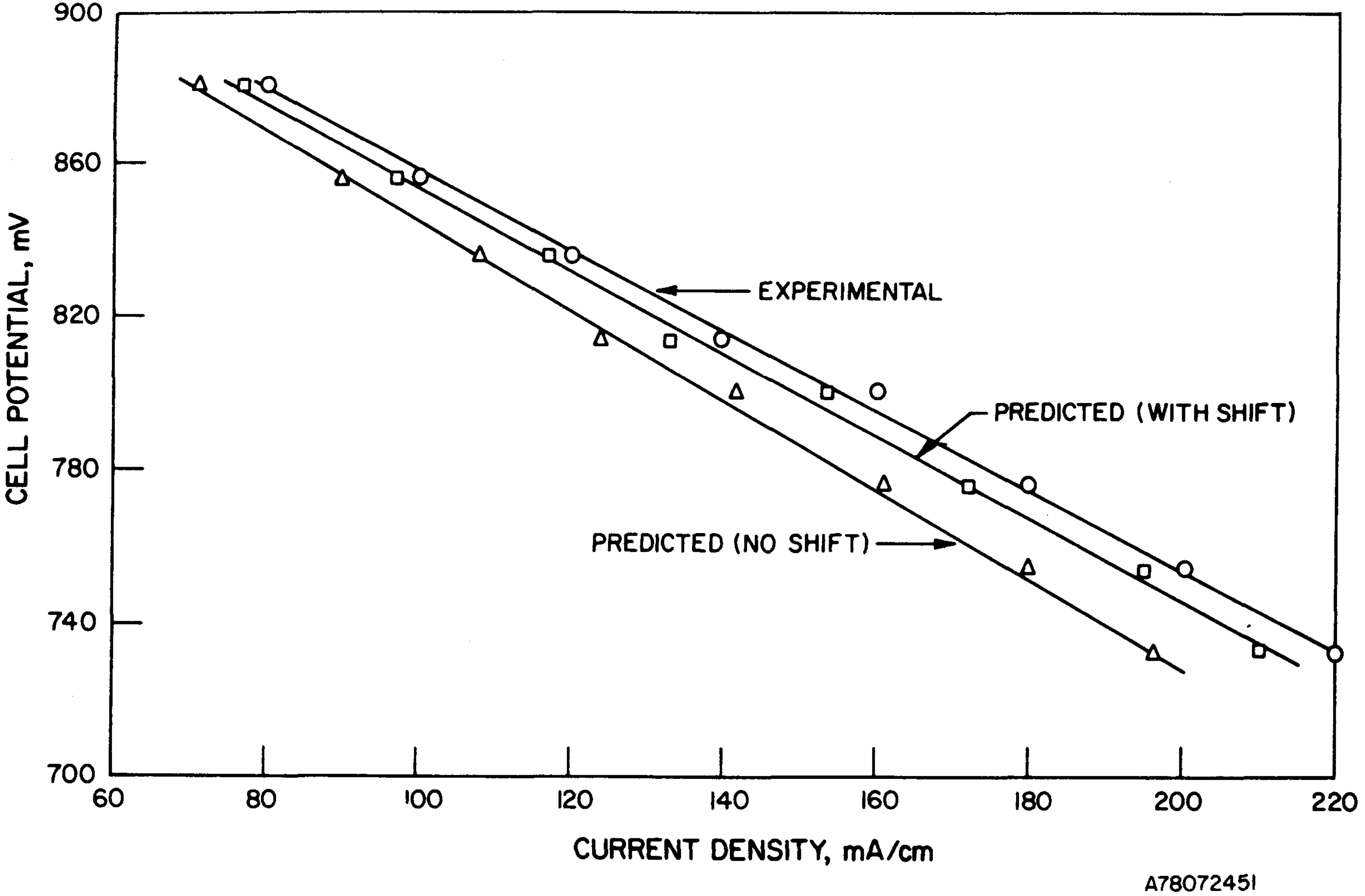

Figure 2.31. COMPARISON OF EXPERIMENTAL AND PREDICTED CURRENT DENSITIES
(Cell Impedance Value Adjusted for 75% Conversion)
(Fuel: Reformed Natural Gas)

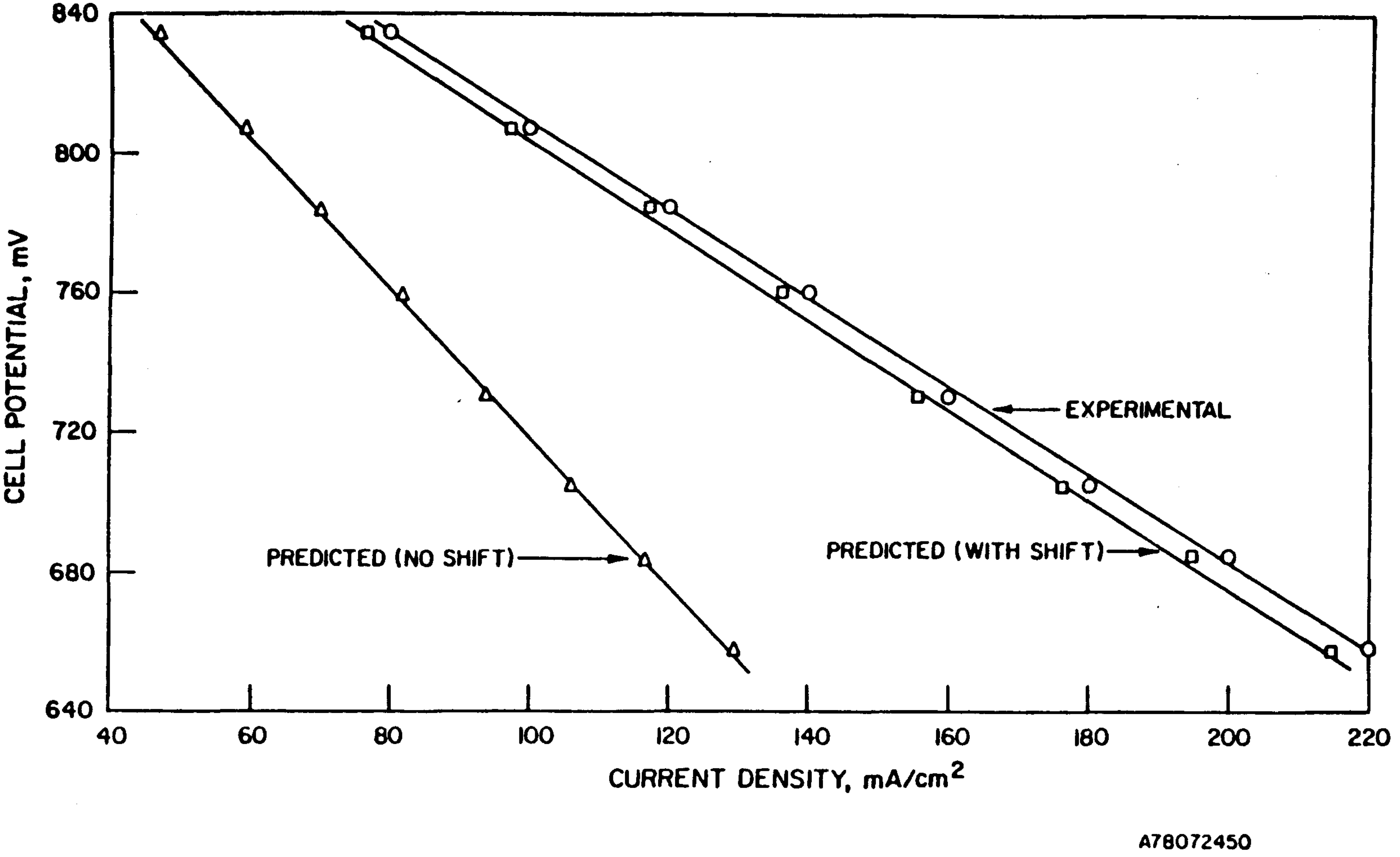

Figure 2.32. COMPARISON OF EXPERIMENTAL AND PREDICTED CURRENT DENSITIES
(Cell Impedance Value Adjusted for 75% Conversion)
(Fuel: Low-Btu Coal Gas)

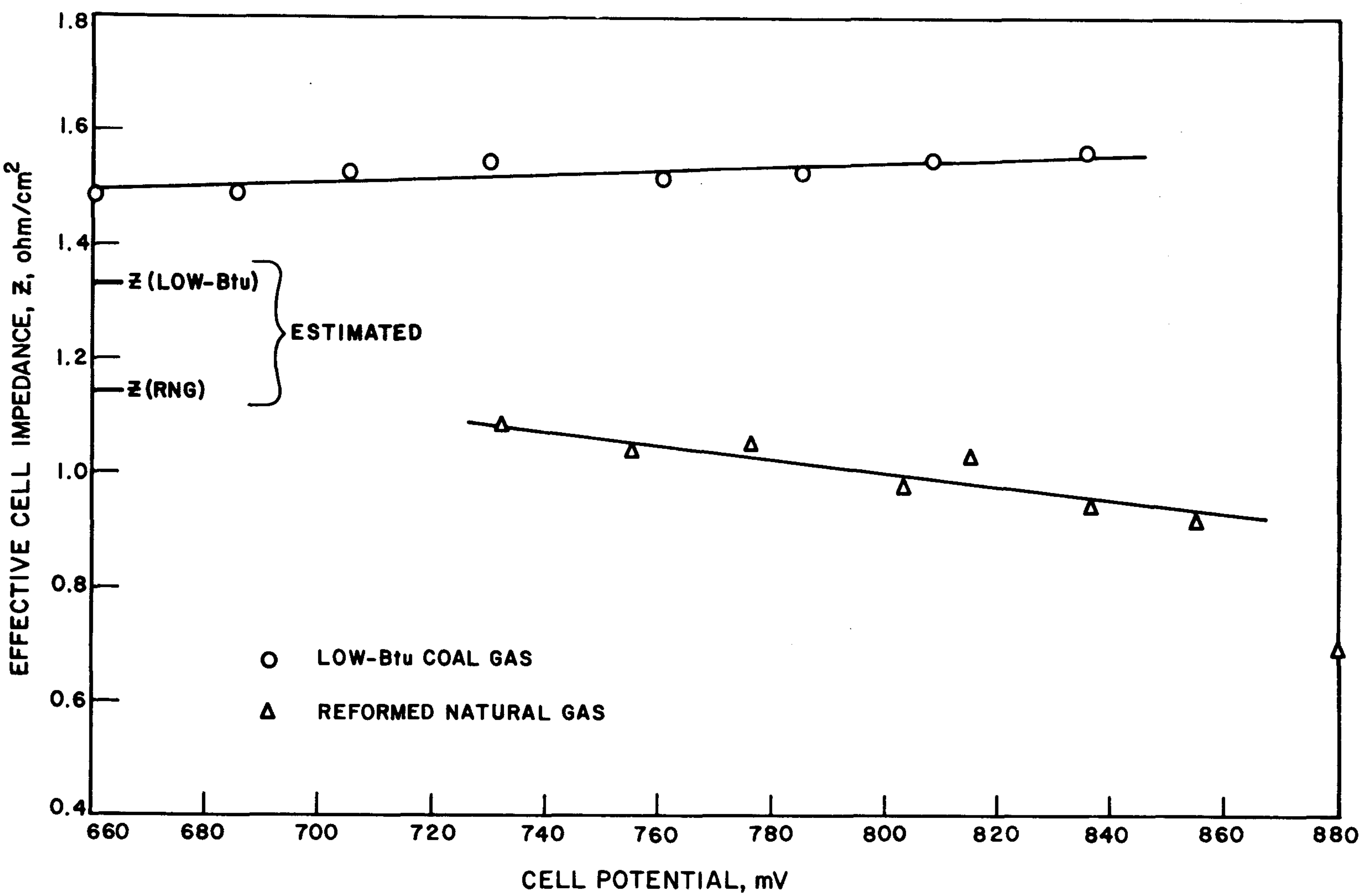

A78123711

Figure 2.33. EFFECTIVE CELL IMPEDANCE AT 75% FUEL CONVERSION

resistance at increasing current density. This is so because only in H_2 and H_2O content are the average gas compositions in the cell significantly different when comparing reformed natural gas and low-Btu gas. (See Table 2.6.)

Table 2.6. ESTIMATED ELECTRODE IMPEDANCE VALUES

	Reformed Natural Gas		Low-Btu Gas	
	Inlet	Outlet	Inlet	Outlet
H_2	60	9.9	18.6	3.8
CO_2	7.4	4.0	11.4	35.5
CO	10	4.4	14.0	3.9
H_2O	22.6	45.7	7.8	17.6
Z (Anode)	0.315		0.455	
Z (Cathode)	0.428		0.428	
R (Ohmic)*	0.400		0.446	
Z (Cell)	1.143		1.329	
Z (Exp) at 200 mA/cm^2	1.05		1.49	

Low H_2O values in the bulk fuel gas appear to be favorable for a relative decrease of polarization as the current density is increased at a constant 75% fuel conversion.

It is of interest to compare the effective cell impedance of Figure 2.33 with estimates of this parameter constructed from small-scale (3 cm^2) cell polarization data. Polarization curves (at 7.5% fuel conversion) for a limited number of gas compositions are available.[10] These allow an estimate of the effective electrode impedance corresponding to the average gas compositions on the fuel side and on the oxidant side. The estimates are shown in Table 2.6.

There is a reasonably good agreement for both reformed natural gas and low-Btu gas. The low-data are underestimated probably because the available small-cell electrode impedance data do not allow the effect of the CO and H_2O concentrations to be accounted for. However, it is clear that more small-scale cell data on a variety of gas compositions will make accurate predictions of the performance of scaled-up cells possible.

2.2.3.1. Current Distribution

In general, it was observed that as the value assigned to Z was increased, the current distribution became more uniform. This is illustrated in Table 2.7 (Fuel: RNG).

Table 2.7. UNIFORMITY OF CURRENT DISTRIBUTION AS A FUNCTION OF Z

Z, ohm/cm^2	Ratio of Highest to Lowest Current Density
0.625	4.8
0.825	4.2
1.025	3.8
1.225	3.4
1.425	3.1
1.625	2.95
5.0	1.7
10.0	1.4

The current distribution was always of the same type as shown in Table 2.4, with the highest current density at the inlet of fuel and oxidant, and lowest at the outlet of the oxidant.

2.2.4. Effects of Pressure on Current Distribution

Increasing the operating pressure of molten carbonate fuel cells results in performance improvements (Nernst gains) because of the increase in the partial pressure of the reactants. Higher pressure should also be expected to produce increases in gas solubilities and mass transport rates, and, hence, additional improvements in cell performances.

Pressure favors the carbon deposition and methanation reactions —

$$2CO \rightleftarrows C + CO_2 \qquad (8)$$

$$CO + 3H_2 \rightleftarrows CH_4 + H_2O \qquad (9)$$

Equilibrium inlet compositions, taking into account the above two equations and the water-gas shift reaction —

$$CO + H_2O \rightleftarrows CO_2 + H_2 \qquad (10)$$

were calculated at 1, 5, and 10 atmospheres at 650°C for fuels obtained from various processes.

The mass balance and potential balance equations were rewritten, and a new computer program was developed. The new mass balance equations on the anode side are presented in Appendix B.

Figure 2.34 compares experimental and predicted polarization curves for reformed naphtha at 10 atm. The predicted current densities agree very well with the experimental values. The experimental data were obtained at constant flows rather than at constant conversions. Hence, only one value of each fuel and oxidant flow rate was used as an input to the model.

The current distribution is not significantly altered by increasing pressures. The table below compares the ratio of the highest to the lowest current densities obtained for steam reformed naphtha at 1 and 10 atm (for an average current density of 200 mA/cm^2).

Pressure, atm	Ratio of Highest to Lowest Current Density
1	2.11
10	1.94

2.2.5. Modification of Linear Model for Coflow Mode of Operation

When both the fuel and oxidant gases flow in the same direction (coflow), the current distribution is expected to be less uniform when compared with the crossflow mode of operation. To quantify this, we developed a model to predict the current density for the coflow mode.

A computer program was written and polarization curves generated for —

a. RNG without shift reaction
b. RNG with shift reaction
c. LBTU with shift reaction.

Figures 2.35 and 2.36 compare the average current distribution along the 10-cm cell length for the crossflow and coflow configurations for cases a and c. As would be expected, the current density distribution is considerably less uniform in the case of coflow as compared with crossflow. Particularly high current densities can be ssen for coflow at the cell entrance, where both fuel and oxidant are at their highest concentrations.

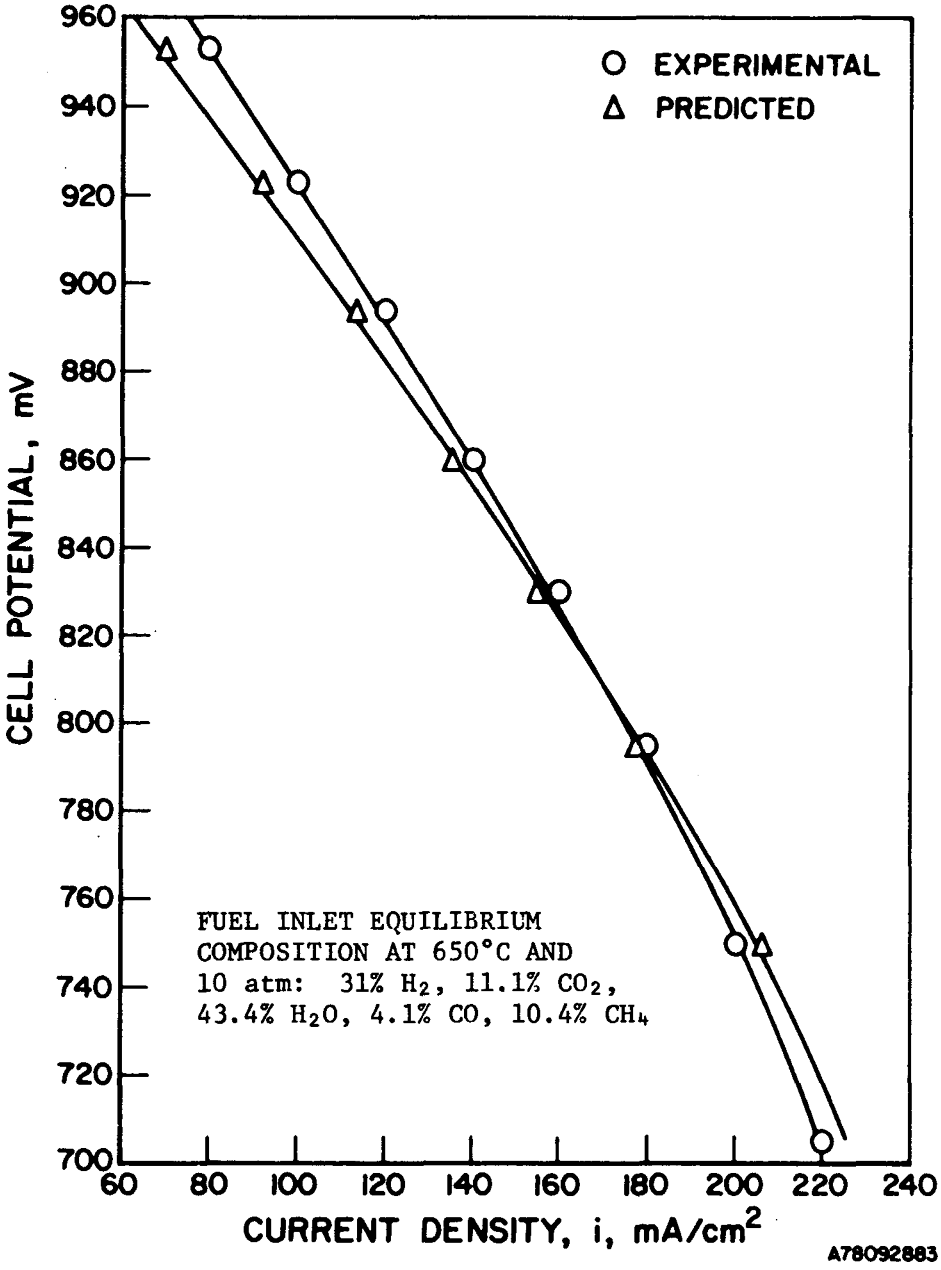

Figure 2.34. COMPARISON OF EXPERIMENTAL AND PREDICTED POLARIZATION CURVES FOR REFORMED NAPHTHA AT 10 atm PRESSURE

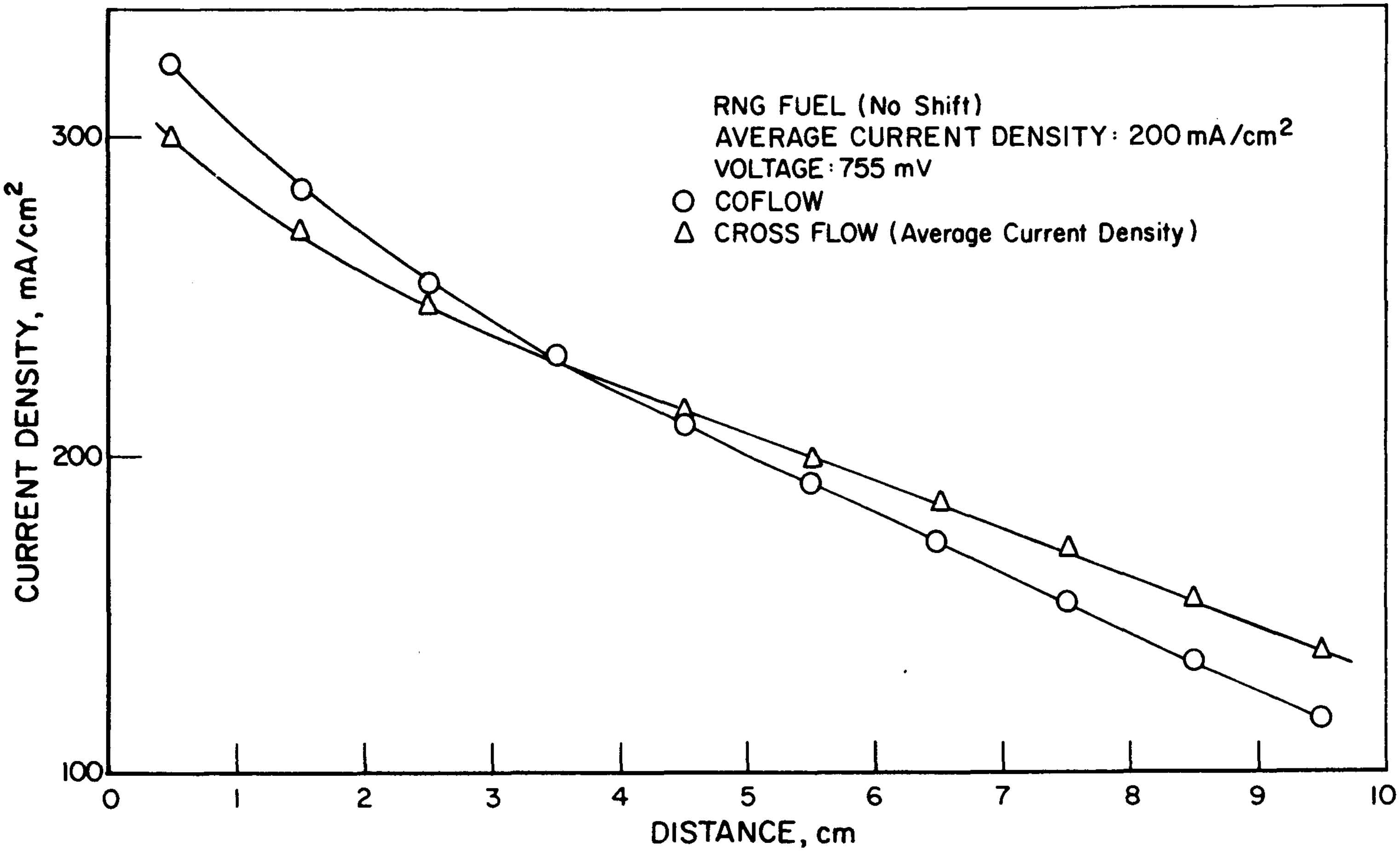

A78062021

Figure 2.35. VARIATION IN CURRENT DENSITY WITH CELL LENGTH FOR REFORMED NATURAL GAS (Without CO Shift Reaction) FOR THE COFLOW AND CROSSFLOW CONFIGURATIONS

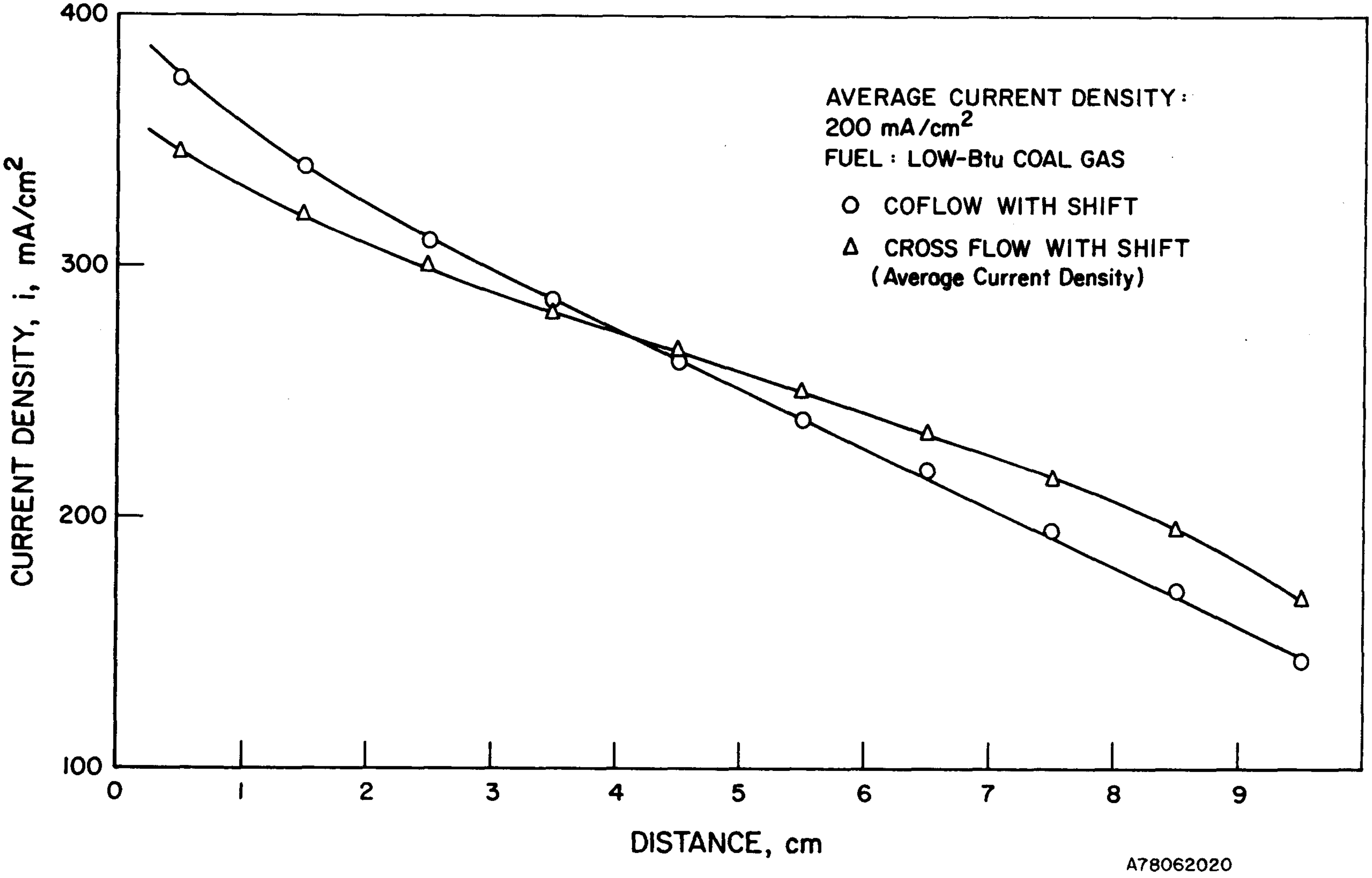

Figure 2.36. VARIATION IN CURRENT DENSITY WITH CELL LENGTH FOR LOW-Btu COAL GAS (With CO Shift Reaction) FOR THE COFLOW AND CROSSFLOW CONFIGURATIONS

Figures 2.37 and 2.38 show the predicted polarization curves for RNG without the shift reaction and LBTU with the shift reaction for the coflow and crossflow configurations. Overall average current densities were predicted to be only slightly lower for the coflow mode. From our calculations, the crossflow configuration would appear to be preferred to the coflow mode because the current distribution is more uniform in the former.

The contribution of the shift reaction to the current density is more significant for the coflow mode than the crossflow mode. This is illustrated in Table 2.8, where the ratio of the current density at the cell entrance to that at the cell exit is shown for each of the two flow modes with and without the shift reaction. At 880 mV, the shift reaction increases this ratio by 37% for the coflow mode, whereas for the crossflow mode, the predicted increase is only 16%.

Table 2.8. RATIO OF CURRENT DENSITIES AT ENTRANCE AND EXIT OF CELL FOR COFLOW AND CROSSFLOW MODES (Fuel: RNG)

Cell Potential, mV	Coflow		Crossflow	
	Without Shift	With Shift	Without Shift	With Shift
880	10.88	6.85	5.15	4.42
732	2.58	2.08	2.10	1.92

2.2.6. Incorporation of a Porous Electrode Model

In the crossflow performance model discussed above, a constant effective cell impedance, Ƶ, has been used. By adjusting this parameter, we are able to obtain the average cell potential for different gas compositions. However, from this model, one cannot identify the magnitude of the surface and concentration overpotentials at each electrode.

The development of the porous electrode model, therefore, is aimed at the integration of electrode kinetic data and the mass transfer and ohmic resistances in the crossflow model. We reviewed various porous electrode models described in the literature with the view of selecting one that could easily be incorporated into the existing crossflow model. The thin-film model of Wasan, *et al*[11] was considered appropriate for a first exploration.

In the thin-film model (Figure 2.39), the pores are assumed to be only partially filled with the electrolyte. A thin electrolyte film extends over

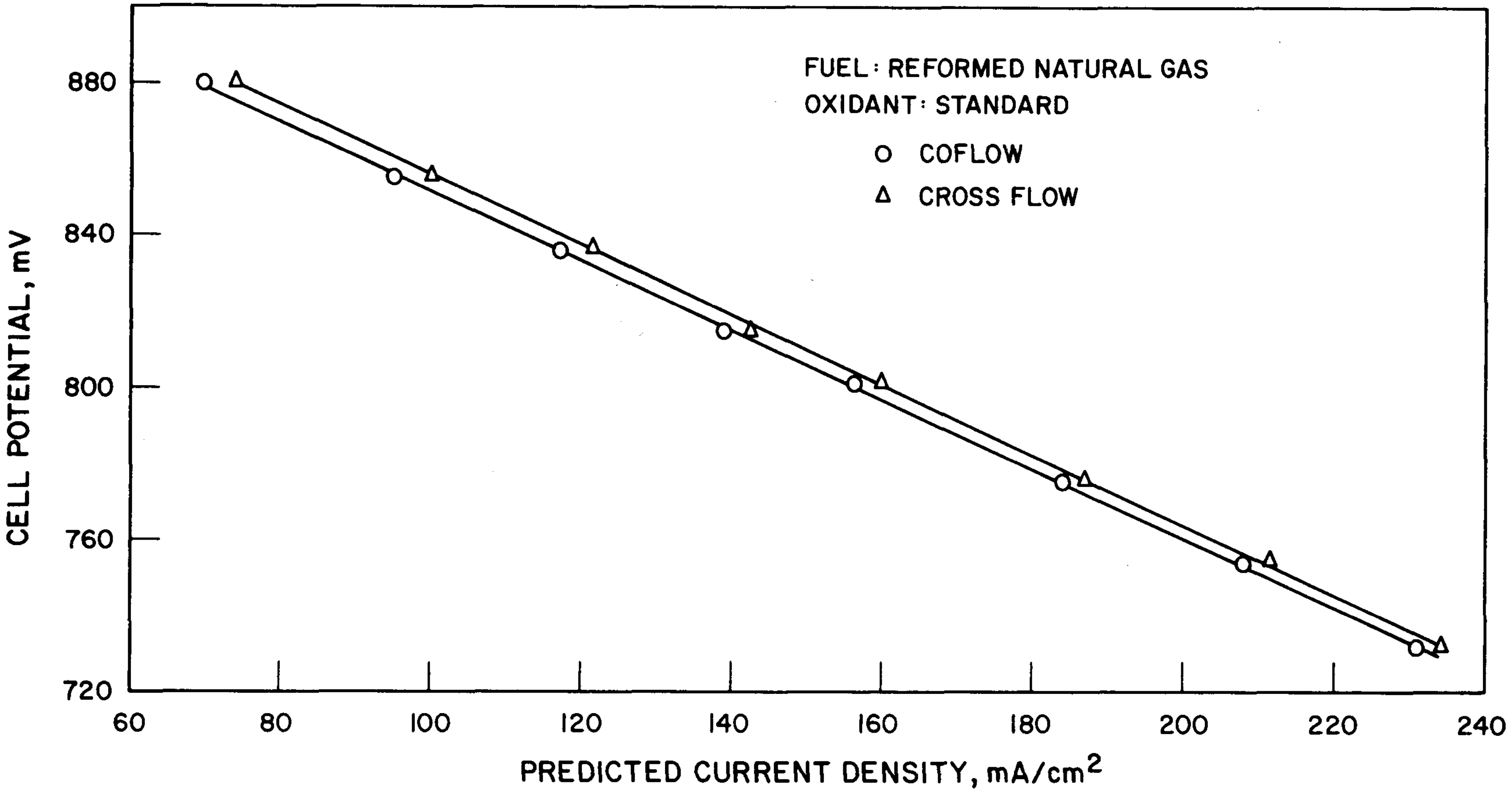

A78062006

Figure 2.37. PREDICTED POLARIZATION CURVES FOR REFORMED NATURAL GAS USING COFLOW AND CROSSFLOW CELL CONFIGURATIONS (CO Shift Reaction Not Considered)

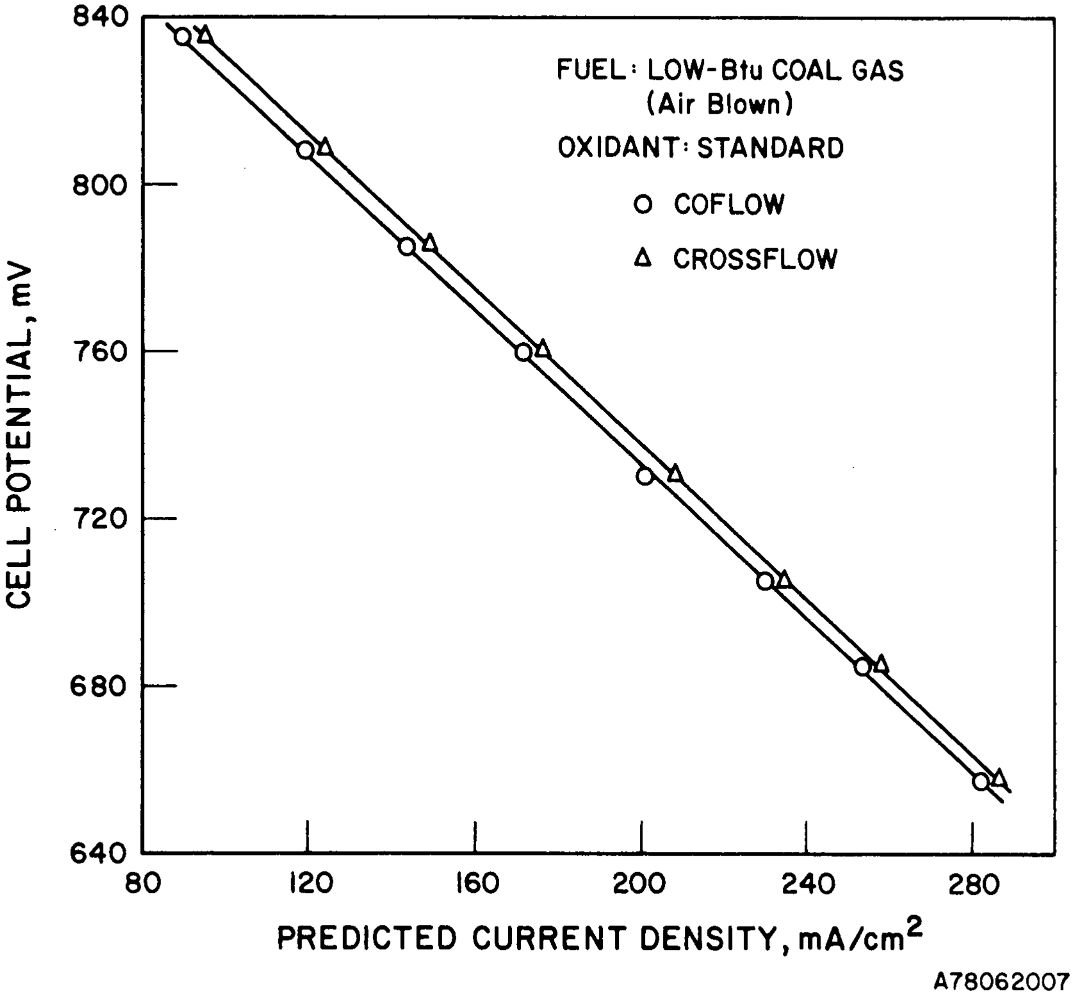

Figure 2.38. PREDICTED POLARIZATION CURVES FOR LOW-Btu COAL GAS USING COFLOW AND CROSSFLOW CELL CONFIGURATIONS (CO Shift Reaction Considered)

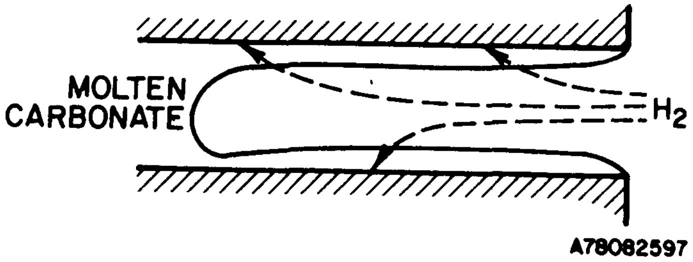

Figure 2.39. THIN FILM MODEL

the internal surface of the pore. The electron transfer step takes place at the solid-liquid interface, after the hydrogen has diffused through the gas and liquid phases to the porous electrode. The thin-film model can account for mass transfer resistance in the gas phase and in the electrolyte. Current distribution is determined by a balance between the electrode reaction kinetics and mass transfer resistance. Ohmic resistance may be predominant in the gas phase (along the pore length) or in the liquid phase (along the electrolyte film).

We critically examined some of the simplifying assumptions made in the development of the thin-film model according to Wasan *et al*. These are —

a. Anode reaction is first order in hydrogen concentration.

b. Film thickness and pore radius are uniform.

c. Ohmic potential drop in the electrolyte film is negligible.

d. Sufficiently high polarization exists, which justifies the use of the Tafel expression.

e. Diffusion of reactant gas through the metal phase is negligible.

Assumption a is made only in the first approximation; it was relaxed in our incorporation of the thin-film model in the crossflow model. Assumption b is made necessary by a lack of pertinent data. Assumption c is not plausible, *a priori*, and will be examined in more detail later on. Assumption d is also a first approximation assumption and was relaxed in the later stages of this modeling study. Assumption e is justified by the electrode geometry. Assumption f is questionable because hydrogen diffusion through nickel is by no means negligible, as has been shown qualitatively by Tantram et al.[12] Until recently, sufficient data were not available to estimate the importance of this effect; however, we have estimated the magnitude of the limiting current density corresponding solely to hydrogen diffusion through nickel. The following values were used in the calculations:

Solubility of H_2 in Ni at 650°C = 2.44×10^{-5} g mol/cc atm (from Ref. 13)
Diffusivity of H_2 in Ni at 650°C = 3×10^{-5} cm^2/sec (from Ref. 14)
Pore radius = 2.5μ
Effective metal passage radius = 1.25μ

Using the limiting current expression given by Wasan et al. for flooded pores, the ratio of limiting currents in the electrolyte compared with those in the metal is 0.18. Because H_2 can reach the electrode surface more easily through the metal than through the electrolyte, current limitation by hydrogen transfer through the electrolyte in flooded pores is unlikely. We also looked into the possibility of H_2O-transfer being current-limiting. Because reliable values of diffusivities and Henry coefficients for water in the electrolyte are not available, we assume similar values as for hydrogen. Consequently, we can say that the transport of either H_2 or H_2O through the electrolyte film may be current-limiting.

The expression obtained from Reference 10 for the current density, i, is —

$$i = \Pi NLnFC_{H_2}^{bulk} D_{H_2}^{gas} \qquad (11)$$

where —

n = number of electrons transferred per mole of hydrogen (=2)
F = Faraday's constant
$C_{H_2}^{bulk}$ = Concentration of H_2 in the gas stream outside the pores
$D_{H_2}^{gas}$ = diffusivity of H_2 in the gas stream
L = length of a pore
N = number of pores per cm^2.

The dimensionless parameter Z* is an index of gas-phase mass-transfer resistance relative to resistance associated with mass-transfer across the liquid film and with slow kinetics of the electrode reaction.

---

* Note that Z is different from the Z that has been used to denote the effective electrode impedance.

$$Z = 2\,\frac{R_P}{\delta}\,\frac{D_{H_2}^{liq}}{D_{H_2}^{gas}}\,\frac{C_{liq}^{sat}}{C_{H_2}^{bulk}}\,\frac{1}{1 + W} \qquad (12)$$

where —

R_p = radius of a pore

δ = film thickness

$D_{H_2}^{liq}$ = diffusitivity of H_2 in the electrolyte

C_{liq}^{sat} = solubility of H_2 in the electrolyte.

The dimensionless parameter W reflects the relative importance of electrode-kinetic resistance compared with mass-transfer resistance across the film and is given by —

$$W = \frac{D_{H_2}^{liq}}{k_1 \delta} \qquad (13)$$

The potential-dependent rate constant of the reaction, k_1, is related to the exchange current density, i_o, by —

$$k_1 = \frac{i_o \exp\,(\alpha_a nF/RT)}{nFC_{liq}^{sat}} \qquad (14)$$

where η = overpotential (anodic).

Substituting for k_1 from Equation 14, in Equation 13,

$$W = \frac{D_{H_2}^{liq} nFC_{liq}^{sat}}{\delta i_o \exp\,(\alpha_a \eta F/RT)} \qquad (15)$$

Substituting Equation 15 in Equation 12, we obtain —

$$Z = 2\frac{R_P}{\delta}\,\frac{D_{H_2}^{liq}}{D_{H_2}^{gas}}\,\frac{C_{liq}^{sat}}{C_{H_2}^{bulk}}\quad \frac{1}{1 + \frac{D_{H_2}^{liq} nFC_{liq}^{sat}}{\delta i_o \exp\,(\alpha_a \eta F/RT}} \qquad (16)$$

Now, $C_{liq}^{sat} = H_{H_2} \cdot P_{H_2}$ (17)

and $C_{H_2}^{bulk} = P_{H_2}$ (18)

where H_{H_2} = Henry coefficient of H_2

and $C^{bulk}_{H_2}$ = partial pressure of H_2.

Combining Equations 16, 17, and 18 and substituting for Z in Equation 9, we obtain —

$$i = \pi LNnFP_{H_2} D^{gas}_{H_2} 2R_p D^{liq}_{H_2} H_{H_2} \quad \frac{i_o \exp\ (\alpha\eta F/RT)}{\delta i_o \exp\ (\alpha\eta F/RT) + D^{liq}_{H_2} nFP_{H_2} H_{H_2}} \tag{19}$$

Dividing by the "gas current," A, Equation C.22, we obtain —

$$\frac{i}{A} = J = \frac{2\pi LNR_p nFP_{H_2} H_{H_2} D^{liq}_{H_2}}{A\delta} \quad \frac{1}{\dfrac{D^{liq}_{H_2} nFP_{H_2} H_{H_2}}{\delta i_o \exp\ (\frac{\alpha\eta}{RT})}} \tag{20}$$

Equation 20 relates local current density, i, to anodic overpotential, η_A. The three parameters to be specified are α, and the other two are related to Z and W. η for the anode is comprised of η (kinetic) and η (mass-transfer).

From Equation 20,

$$\eta_{anode} = \frac{RT}{\alpha_a F} \ln \frac{JQ_{2A}}{Q_{1A-J}} \tag{21}$$

$$\text{where } Q_{1A} = \frac{2\pi NLR_p nFP_{H_2} H_{H_2} D^{liq}_{H_2}}{A\delta} \tag{22}$$

$$\text{and } Q_{2A} = \frac{D^{liq}_{H_2} nFP_{H_2} H_{H_2}}{\delta i^H_o} \tag{23}$$

An equation similar to Equation 20 was developed for the cathode side also, from which —

$$\eta_{cathode} = \frac{RT}{\alpha_c F} \ln \frac{Q_{1C} - J}{JQ_{2C}} \tag{24}$$

$$\text{where } Q_{1C} = \frac{2\pi NLR_p nFb_{O_2} H_{O_2} D^{liq}_{O_2}}{A\delta} \tag{25}$$

$$\text{and } Q_{2C} = \frac{D^{liq}_{O_2} nFb_{O_2} H_{O_2}}{\delta i^{O_2}_o} \tag{26}$$

The potential balance equation (Equation C.33) was modified to include the expressions for the anode and cathode overpotentials (Equations 21 and 24), and a new computer program was developed.

The additional inputs to the computer program are —

1. Anode and cathode pore lengths (assumed to be the anode and cathode thickness)
2. Anode and cathode pore radii
3. Electrolyte film thickness
4. Diffusivities of H_2 and O_2 in the electrolyte
5. Diffusivities of H_2 and O_2 in the fuel and oxidant gases, respectively
6. Henry coefficient of H_2 and O_2
7. Hydrogen and oxygen exchange current densities
8. Apparent transfer coefficients of fuel oxidation and oxygen reduction.

The electrode kinetic parameters (i_o, α) generated in the electrochemical half-cell (under Task 2.3) were used in the model. The dependence of the hydrogen exchange current density on the partial pressures of the reactants was found to be —

$$i_o \alpha (P_{H_2})^{0.25} (P_{H_2O})^{0.18} (P_{CO_2})^{0.25} \tag{27}$$

The oxygen exchange current density was assumed to be dependent as follows (from Ref. 15) —

$$i_o \alpha (P_{O_2})^{0.375} (P_{CO_2})^{-1.25} \tag{28}$$

These relationships were also included in the computer program, and polarization curves were generated for reformed natural gas fuel without CO conversion.

The model is sensitive to changes in the oxygen-exchange current density, but not to changes in the hydrogen-exchange current density because the anode is not kinetically limited. This is the result of the high-exchange current density ($</1$ mA/cm^2) assumed for hydrogen and of the large surface area of the anode. The assumption c of the model, that is, a negligible ohmic drop in the electrode film is, consequently, no longer valid because the current distribution will become very non-uniform at the electrode (i_o <1mA/cm^2); at the oxygen electrode the kinetic and mass-transfer resistance are of nearly equal magnitude and the current distribution is more uniform.

Figure 2.40 shows the effect of varying the oxygen-exchange current density on the polarization curves. Keeping the hydrogen-exchange current density constant at 40 mA/cm^2, it can be seen that an i_o of at least 2mA/cm^2 for the oxygen reaction is necessary to achieve a good fit with the experimental data.

Table 2.9 is a sample computer printout that shows the current distribution, Nerst losses, ohmic losses, and anode and cathode overpotentials (split up as surface and concentration overpotentials).

The difference between the open circuit voltage of 1074 mV and the terminal potential of 855 mV (average current density 100 mA/cm^2) is the result of the following losses:

Nernst loss	125.1 mV	
Ohmic loss (Bulk + Film)	35.9 mV	
Anode activation loss	0.2 mV	(negligible)
Anode concentration polarization loss	0.4 mV	(negligible)
Cathode activation loss	15.9 mV	
Cathode concentration polarization loss	41.4 mV	
Total	218.9 mV	

The very small anodic losses can be explained by the porous electrode model, which does not take into account that the anode current is non-uniformly distributed and that a considerable ohmic drop occurs in current conduction along the electrode film. Together, these factors increase the measured overpotential by one order of magnitude. This also explains the deviations of the predicted performance curve from the experimental curve at high current densities, where a tendency toward limiting current behavior appears (Figure 2.40).

Thus, it is necessary to account for the ohmic drop in the electrode pores so as to reach a good agreement between model predictions and experimental performance.

Table 2.9, Part 1. PREDICTED CURRENT DISTRIBUTION, NERNST LOSSES, OVERPOTENTIALS, AND CONVERSIONS AT CONSTANT POTENTIAL
(Fuel: PO)

LOCAL CURRENT DENSITIES, ROW BY ROW, DIMENSIONLESS

0.143	0.133	0.123	0.113	0.101	0.088	0.074	0.057	0.040	0.025
0.143	0.128	0.119	0.110	0.100	0.088	0.074	0.059	0.043	0.028
0.131	0.124	0.116	0.108	0.099	0.088	0.076	0.062	0.047	0.032
0.124	0.118	0.112	0.105	0.097	0.088	0.077	0.065	0.051	0.036
0.117	0.113	0.108	0.102	0.095	0.088	0.078	0.067	0.054	0.040
0.110	0.107	0.103	0.099	0.093	0.087	0.079	0.070	0.058	0.045
0.103	0.101	0.098	0.095	0.091	0.086	0.079	0.071	0.062	0.049
0.095	0.094	0.093	0.091	0.088	0.084	0.079	0.073	0.064	0.054
0.087	0.088	0.088	0.087	0.085	0.083	0.079	0.074	0.067	0.058
0.080	0.081	0.082	0.082	0.082	0.080	0.078	0.075	0.070	0.062

REAL CURRENT DENSITIES, ROW BY ROW, MAMPS PER SQ-CM

171.21	159.09	147.35	134.98	121.33	105.87	88.21	68.52	48.16	29.85
171.21	153.22	142.82	131.73	119.38	105.27	89.05	70.76	51.41	33.29
156.42	148.02	138.96	129.29	118.41	105.88	91.33	74.67	56.50	38.53
146.53	141.82	134.29	126.05	116.54	105.54	92.62	77.60	60.76	43.34
140.27	135.22	129.11	122.32	114.23	105.00	93.74	80.42	65.07	48.46
131.67	128.15	123.62	118.29	111.88	104.07	94.52	83.32	69.17	53.64
122.74	120.88	117.74	113.85	108.97	102.79	95.01	85.18	73.64	58.94
113.62	113.09	111.52	109.03	105.66	101.10	95.08	87.17	77.00	64.31
104.43	105.11	104.85	103.81	101.89	98.95	94.68	88.64	80.35	69.60
95.20	96.94	97.74	98.07	97.70	96.31	93.77	89.61	83.27	73.90

NERNST LOSSES, VOLTS

0.028	0.063	0.088	0.109	0.127	0.144	0.160	0.175	0.189	0.201
0.031	0.065	0.090	0.109	0.127	0.143	0.159	0.174	0.187	0.199
0.033	0.066	0.089	0.109	0.126	0.141	0.156	0.170	0.184	0.196
0.036	0.067	0.090	0.109	0.125	0.140	0.154	0.168	0.181	0.192
0.039	0.069	0.091	0.109	0.124	0.138	0.152	0.165	0.177	0.189
0.042	0.070	0.091	0.109	0.124	0.137	0.150	0.162	0.174	0.186
0.046	0.072	0.092	0.109	0.123	0.136	0.148	0.159	0.171	0.182
0.050	0.075	0.094	0.109	0.122	0.134	0.146	0.156	0.167	0.178
0.054	0.077	0.095	0.109	0.122	0.133	0.143	0.153	0.163	0.173
0.059	0.080	0.097	0.110	0.122	0.132	0.141	0.151	0.160	0.169

Table 2.9, Part 2. PREDICTED CURRENT DISTRIBUTION, NERNST LOSSES, OVERPOTENTIALS, AND CONVERSIONS AT CONSTANT POTENTIAL

(Fuel: PO)

OHMIC RESISTANCE,VOLTS

0.061	0.056	0.052	0.048	0.043	0.037	0.031	0.024	0.017	0.011
0.061	0.054	0.051	0.047	0.042	0.037	0.031	0.025	0.018	0.012
0.055	0.052	0.049	0.046	0.042	0.037	0.032	0.026	0.020	0.014
0.053	0.050	0.048	0.045	0.041	0.037	0.033	0.027	0.021	0.015
0.050	0.048	0.046	0.043	0.040	0.037	0.033	0.028	0.023	0.017
0.047	0.045	0.044	0.042	0.040	0.037	0.033	0.029	0.024	0.019
0.043	0.043	0.042	0.040	0.039	0.036	0.034	0.030	0.026	0.021
0.040	0.040	0.039	0.039	0.037	0.036	0.034	0.031	0.027	0.023
0.037	0.037	0.037	0.037	0.036	0.035	0.033	0.031	0.028	0.025
0.034	0.034	0.035	0.035	0.035	0.034	0.033	0.032	0.029	0.026

ANODE SURFACE OVERPOTENTIAL,VOLTS

0.0003	0.0003	0.0002	0.0002	0.0002	0.0002	0.0002	0.0001	0.0001	0.0001
0.0004	0.0003	0.0002	0.0002	0.0002	0.0002	0.0002	0.0001	0.0001	0.0001
0.0003	0.0003	0.0002	0.0002	0.0002	0.0002	0.0002	0.0001	0.0001	0.0001
0.0003	0.0002	0.0002	0.0002	0.0002	0.0002	0.0002	0.0001	0.0001	0.0001
0.0003	0.0002	0.0002	0.0002	0.0002	0.0002	0.0002	0.0002	0.0001	0.0001
0.0003	0.0002	0.0002	0.0002	0.0002	0.0002	0.0002	0.0002	0.0001	0.0001
0.0002	0.0002	0.0002	0.0002	0.0002	0.0002	0.0002	0.0002	0.0001	0.0001
0.0002	0.0002	0.0002	0.0002	0.0002	0.0002	0.0002	0.0002	0.0001	0.0001
0.0002	0.0002	0.0002	0.0002	0.0002	0.0002	0.0002	0.0002	0.0001	0.0001
0.0002	0.0002	0.0002	0.0002	0.0002	0.0002	0.0002	0.0002	0.0001	0.0001

ANODE CONCENTRATION OVERPOTENTIAL,VOLTS

0.0000	0.0001	0.0002	0.0003	0.0004	0.0006	0.0008	0.0009	0.0010	0.0008
0.0049	0.0001	0.0002	0.0003	0.0004	0.0005	0.0007	0.0009	0.0009	0.0009
0.0000	0.0001	0.0002	0.0003	0.0004	0.0005	0.0006	0.0008	0.0009	0.0009
0.0000	0.0001	0.0002	0.0002	0.0003	0.0004	0.0006	0.0007	0.0009	0.0009
0.0000	0.0001	0.0001	0.0002	0.0003	0.0004	0.0005	0.0007	0.0008	0.0009
0.0000	0.0001	0.0001	0.0002	0.0003	0.0004	0.0005	0.0006	0.0008	0.0009
0.0000	0.0001	0.0001	0.0002	0.0002	0.0003	0.0004	0.0006	0.0007	0.0008
0.0000	0.0001	0.0001	0.0001	0.0002	0.0003	0.0004	0.0005	0.0006	0.0008
0.0000	0.0000	0.0001	0.0001	0.0002	0.0002	0.0003	0.0004	0.0006	0.0007
0.0000	0.0000	0.0001	0.0001	0.0001	0.0002	0.0003	0.0004	0.0005	0.0006

Table 2.9, Part 3. PREDICTED CURRENT DISTRIBUTION, NERNST LOSSES, OVERPOTENTIALS, AND CONVERSIONS AT CONSTANT POTENTIAL
(Fuel: PO)

```
CATHODE SURFACE OVERPOTENTIAL,VOLTS

-0.0314-0.0292-0.0271-0.0249-0.0224-0.0196-0.0164-0.0127-0.0090-0.0056
-0.0320-0.0270-0.0252-0.0234-0.0213-0.0189-0.0161-0.0129-0.0095-0.0062
-0.0259-0.0248-0.0235-0.0221-0.0204-0.0185-0.0161-0.0134-0.0102-0.0071
-0.0233-0.0226-0.0216-0.0206-0.0193-0.0178-0.0159-0.0136-0.0108-0.0079
-0.0207-0.0204-0.0198-0.0191-0.0182-0.0171-0.0156-0.0137-0.0114-0.0087
-0.0182-0.0182-0.0179-0.0176-0.0170-0.0163-0.0152-0.0138-0.0119-0.0095
-0.0157-0.0160-0.0161-0.0160-0.0158-0.0154-0.0148-0.0137-0.0123-0.0102
-0.0135-0.0139-0.0142-0.0144-0.0145-0.0144-0.0142-0.0136-0.0126-0.0110
-0.0114-0.0120-0.0124-0.0128-0.0132-0.0134-0.0135-0.0133-0.0128-0.0116
-0.0094-0.0101-0.0107-0.0113-0.0118-0.0123-0.0127-0.0129-0.0128-0.0120
```

```
CATHODE CONCENTRATION OVERPOTENTIAL,VOLTS

-0.0985-0.0698-0.0509-0.0370-0.0260-0.0173-0.0105-0.0056-0.0024-0.0009
-0.0901-0.0717-0.0529-0.0388-0.0277-0.0187-0.0117-0.0065-0.0030-0.0011
-0.1047-0.0759-0.0564-0.0419-0.0304-0.0211-0.0136-0.0079-0.0040-0.0016
-0.1071-0.0789-0.0597-0.0449-0.0328-0.0232-0.0154-0.0094-0.0050-0.0022
-0.1096-0.0819-0.0622-0.0474-0.0354-0.0257-0.0175-0.0110-0.0062-0.0030
-0.1119-0.0845-0.0652-0.0503-0.0382-0.0281-0.0198-0.0131-0.0077-0.0040
-0.1142-0.0875-0.0683-0.0533-0.0411-0.0308-0.0222-0.0151-0.0096-0.0052
-0.1150-0.0900-0.0714-0.0565-0.0442-0.0338-0.0249-0.0175-0.0115-0.0067
-0.1160-0.0922-0.0746-0.0597-0.0474-0.0369-0.0279-0.0202-0.0137-0.0086
-0.1165-0.0940-0.0769-0.0630-0.0508-0.0403-0.0311-0.0232-0.0163-0.0106
```

```
LOCAL ANODE CONVERSIONS, ROW BY ROW, FLOW DIRECTION TO THE RIGHT

  0.000   0.000   0.000   0.000   0.000   0.000   0.000   0.000   0.000   0.000   0.000
  0.000   0.143   0.276   0.399   0.512   0.613   0.702   0.775   0.832   0.873   0.898
  0.000   0.143   0.271   0.390   0.500   0.600   0.688   0.762   0.821   0.864   0.892
  0.000   0.131   0.254   0.370   0.478   0.577   0.666   0.742   0.804   0.852   0.884
  0.000   0.124   0.243   0.355   0.460   0.557   0.646   0.723   0.788   0.838   0.875
  0.000   0.117   0.230   0.338   0.440   0.536   0.623   0.702   0.769   0.823   0.864
  0.000   0.110   0.217   0.320   0.419   0.513   0.599   0.678   0.748   0.806   0.851
  0.000   0.103   0.204   0.302   0.397   0.488   0.574   0.653   0.724   0.786   0.835
  0.000   0.095   0.189   0.283   0.374   0.462   0.546   0.626   0.699   0.763   0.817
  0.000   0.087   0.175   0.263   0.349   0.434   0.517   0.596   0.670   0.737   0.795
  0.000   0.080   0.161   0.242   0.324   0.406   0.486   0.564   0.639   0.709   0.771
```

Table 2.9, Part 4. PREDICTED CURRENT DISTRIUBITON, NERNST LOSSES, OVERPOTENTIALS, AND CONVERSIONS AT CONSTANT POTENTIAL

(Fuel: PO)

```
LOCAL CATHODE CONVERSIONS, ROW BY ROW, FLOW DIRECTION VERTICALLY DOWN

   0.000   0.000   0.000   0.000   0.000   0.000   0.000   0.000   0.000   0.000   0.000
   0.000   0.086   0.080   0.074   0.068   0.061   0.053   0.044   0.034   0.024   0.015
   0.000   0.172   0.156   0.145   0.134   0.121   0.106   0.089   0.070   0.050   0.032
   0.000   0.250   0.231   0.215   0.198   0.180   0.159   0.135   0.107   0.078   0.051
   0.000   0.324   0.302   0.282   0.262   0.238   0.212   0.181   0.146   0.109   0.073
   0.000   0.395   0.369   0.347   0.323   0.296   0.264   0.228   0.186   0.141   0.097
   0.000   0.461   0.434   0.409   0.382   0.352   0.316   0.275   0.228   0.176   0.124
   0.000   0.522   0.494   0.468   0.439   0.406   0.368   0.323   0.271   0.213   0.153
   0.000   0.579   0.551   0.524   0.494   0.459   0.419   0.371   0.314   0.251   0.186
   0.000   0.631   0.604   0.576   0.546   0.510   0.468   0.418   0.359   0.292   0.220
   0.000   0.679   0.652   0.625   0.595   0.559   0.516   0.465   0.404   0.333   0.257

OHMIC RESISTANCE=  0.400 OHM SQ-CM
AVERAGE CURRENT DENSITY (DIMENSIONLESS)=  0.085
AVERAGE ANODE CONVERSION=  0.848
AVERAGE CATHODE CONVERSION=  0.509

TERMINAL VOLTAGE= 0.8550 VOLTS
TOTAL CURRENT= 9.5430 AMPS
CURRENT DENSITY= 101.52 MAMPS PER SQ-CM

AVERAGE NERNST LOSS= 0.1251 VOLTS
AVERAGE OHMIC LOSS= 0.0359 VOLTS
AVERAGE ANODE SURFACE OVERPOT= 0.0002 VOLTS
AVERAGE ANODE CONCN. OVERPOT= 0.0004 VOLTS
AVERAGE CATHODE SURFACE OVERPOT=-0.0159 VOLTS
AVERAGE CATHODE CONCN. OVERPOT=-0.0414 VOLTS
```

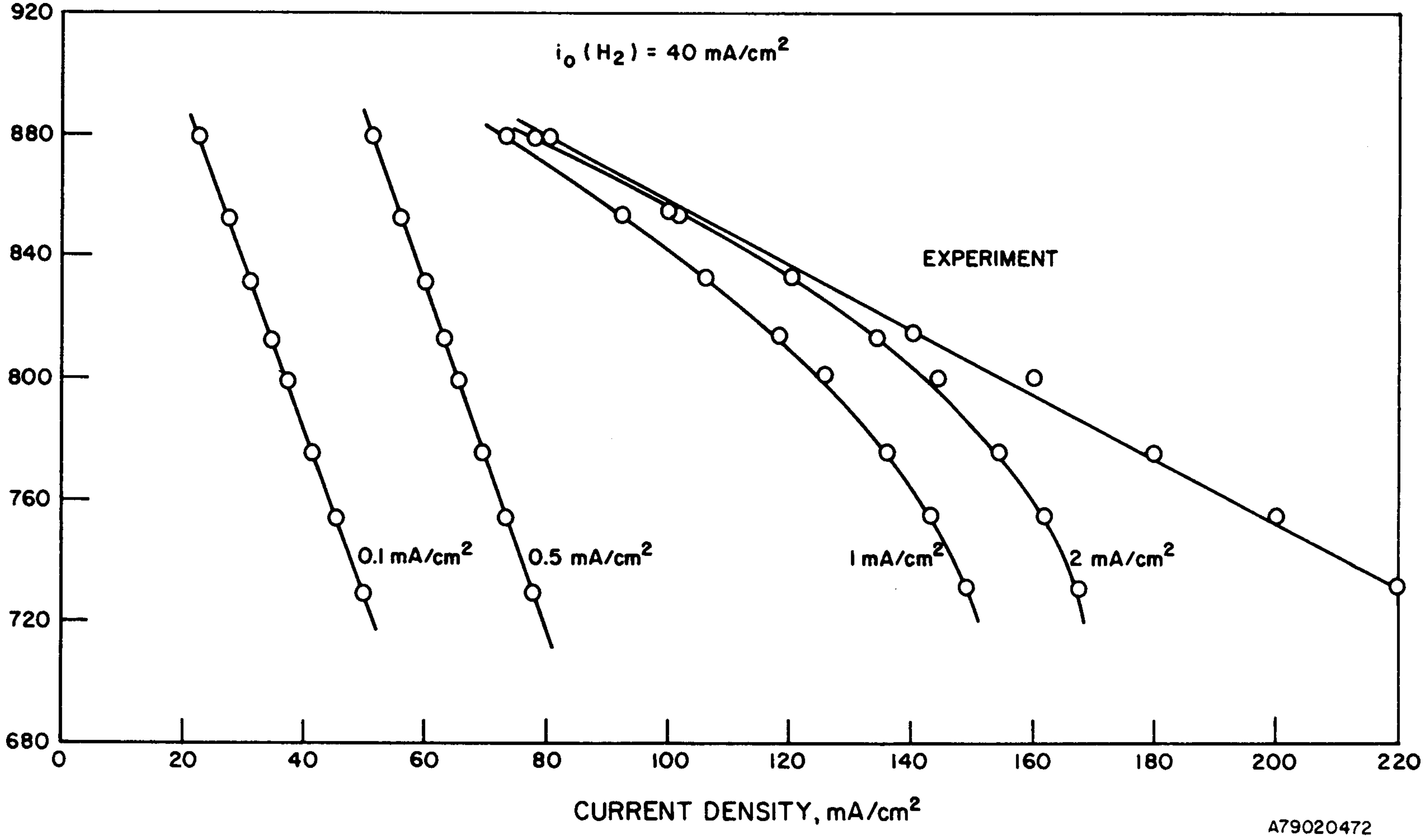

Figure 2.40. EFFECT OF VARYING OXYGEN EXCHANGE CURRENT DENSITY

2.3. Electrochemical Measurements

Summary

The rate of the fuel oxidation process at nickel and cobalt anodes has been shown to exhibit mixed- or diffusion-control with wire electrodes immersed in carbonate melts. The electrode kinetics for fuel oxidation at these two anode materials were evaluated in three selected molten carbonate mixtures. Activation kinetics under the probable diffusion-controlled conditions present in the electrochemical half-cell were measured using a potential step technique. For all the molten carbonate mixtures used in the course of this study, the highest exchange current values were found on nickel anodes, with the highest values being measured in the ternary eutectic melt (43.5% Li_2CO_3/31.5% Na_2CO_3/25% K_2CO_3). For this ternary melt, the exchange current density on nickel varied from 78 mA/cm^2 for intermediate-Btu fuel to 22 mA/cm^2 for low-Btu fuel at 650°C. The exchange current density was found to have a reaction order of around 0.25 for hydrogen, carbon dioxide, and water. The electrochemical performance of these two anode materials in the three selected melts is discussed, and a tentative reaction mechanism for the oxidation reaction is suggested.

Oxygen reduction kinetics were studied on a gold electrode, also using the potential step techniques. Exchange current density values of about 5 mA/cm^2 typically were found. Under the conditions present in the half-cell, a stable NiO electrode was not achieved, and, consequently, a extended study of the electrode kinetics could not be performed, as was done for the anode.

2.3.1. Introduction

Several factors can be expected to govern the selection of the molten carbonate melt which is supported in the lithium aluminate ($LiAlO_2$) matrix of the molten carbonate fuel cell tile. The major factors can be summarized as follows: a) ionic conductivity, b) the solubility of the reactants and reaction products, c) the diffusion coefficients of reactants and products, d) the rate of the electrochemical anodic and cathodic reactions, e) electrolyte vapor pressure, and f) stability of the lithium aluminate matrix with each selected molten carbonate mixture.

From a cell lifetime standpoint, minimizing electrolyte vaporization loss and maximizing the stability of $LiAlO_2$ appear to be of paramount importance because they appear to be the major effects influencing cell deterioration and the corresponding cell lifetime. From a cell performance viewpoint, the ionic conductivity (a), the gaseous solubility (b), the diffusivity (c), and the electrochemical rates (d) are important. This portion of the molten carbonate fuel cell program focuses on identifying the electrochemical rates as a function of operating temperature, gas composition, electrolyte composition, and electrode materials.

To date, few workers have reported on the influence of molten carbonate composition on the electrochemical performance of the molten carbonate fuel cell, using representative electrode materials. The electrode kinetics, particularly for the hydrogen oxidation reaction, have not been quantified. It has also been difficult to correlate experimental data performed in electrochemical half-cells with conditions present at the porous electrode of a fuel cell because the relative contribution to cell polarization from the diffusional effects of either the reaction or the reaction products will be expected to differ in each case. The small amount of data available on electrode kinetics for the hydrogen oxidation reaction has been of a somewhat preliminary nature.[17] Polarization data to this date for hydrogen oxidation have indicated little effect caused by the nature of the metal,[18,19] indicating rapid activation kinetics for the anodic reaction with a probable strong dependency of the overall rate on diffusional effects. Experimental evidence has indicated that polarization at such electrodes for the hydrogen oxidation reaction in molten carbonates may be influenced more by the local build-up of reaction products (H_2O, CO_2) than by the diffusion of hydrogen in the melt.[20] Some recent work has been reported on open circuit potential measurements for hydrogen dissolved in lithium carbonate/potassium carbonate melts on gold electrodes[21] in which reasonable agreement was found between calculated and experimental thermodynamic values. Some work has been reported on the oxidation of hydrogen with completely immersed electrodes[22,23] and, with a view of obtaining data under conditions more representative of that present at the gas/liquid/solid interfaces within the porous electrode of the fuel cell, some work has been performed on partially raised electrodes in molten carbonate melts.[24,25] The latter work has shown that the diffusion of reactants through the thin-film electrolyte miniscus plays a significant role in the overall rate of the anodic reaction. From chronopotentiometric measurements performed in a lithium/sodium carbonate melt using a completely immersed smooth platinum electrode, diffusion control of the anodic process was indicated.[26]

As will be discussed later, the study of the activation kinetics for the hydrogen oxidation reaction on a nickel or cobalt electrode in molten carbonate melts requires the application of techniques which will enable effective separation of activation kinetics from the diffusion-control conditions that have been shown to exist in the electrochemical half-cell. The majority of the prior electrode kinetic work in molten carbonate melts has focused on oxygen reduction at gold electrodes fully immersed in lithium carbonate/sodium carbonate/potassium carbonate electrolytes.[27,28] This work concluded that the exchange current density for the oxygen reduction reaction was closely dependent on the partial pressures of CO_2 and O_2 to the respective powers, $P_{CO_2}{}^{-5/4}$ and $P_{O_2}{}^{3/8}$. These kinetic data were obtained by analysis of current voltage characteristics obtained at different sweep rates under the diffusion-controlled conditions present.

Objective

The objective of the experimental work has been to measure activation kinetic data in three molten carbonate mixtures with a view to identifying the preferred electrolyte composition for the electrolyte tile based upon such electrochemical data. Emphasis has focused on the hydrogen oxidation reaction on nickel and cobalt anodes where little work has, as indicated earlier, been reported. Electrolyte compositions chosen for evaluation have included binary and ternary mixtures of alkali-metal carbonates. Work has been focused particularly on the following electrolyte compositions: 62 mole percent Li_2CO_3/38 mole percent K_2CO_3 (Li/K), which has a high ionic conductivity and a reasonably high reactant gas solubility; 52 mole percent Li_2CO_3/48 mole percent Na_2CO_3 (Li/Na), which combines good electrolyte conductivity and a high sodium content for low vapor pressure for minimizing electrolyte vaporization losses; and the ternary 43.5 mole percent Li_2CO_3/31.5 mole percent Na_2CO_3/25 mole percent K_2CO_3 (Li/Na/K), to evaluate electrochemical performance at temperatures below 650°C.

Electrochemical techniques used in the course of this work have included linear voltage sweep, steady state potentiostatic, and potential step[29] methods. The latter technique was found particularly useful for identification of kinetic current values under the diffusion-controlled conditions present in the electrochemical half-cell.

2.3.2. Experimental Procedures

Materials for the anode nickel wire and cobalt rod were purchased from commercial sources (Materials Research Corp., Orangeburg, New York). All measurements were performed in the electrochemical half-cell systems shown in Figure 2.41. Humidification of the inlet gas was performed by passing it through a heated saturator. All lines from the saturator to the cell were heated to prevent condensation. A gold wire bubbled with 33.3% O_2/66.7% CO_2 inside an alumina tube served as a reference electrode. The wire communicates with the melt through a small hole (0.015-in diameter) at the bottom of the tube. The potential of the working electrode was controlled by a Wenking ST72 potentiostat. The potentiostat has a rise time of about 7 microseconds when a step voltage is applied. A piece of round, gold foil was used as the counterelectrode. The electrolyte was prepared from a mixture of Li_2CO_3, Na_2CO_3 and K_2CO_3 (Mallinckrodt, Analytical Reagent).

A Tacussel type GSTP2B pulse/sweep generator was used to control the potentiostat. The output voltage of the Tacussel generator was monitored with a digital voltmeter (Fluke, type 8020A). Steady-state, linear voltage sweep and transient pulse techniques were used to study the current-voltage relationships of the electrode. The signals were recorded on a Hewlett-Packard 7046 X-Y recorder. Signals from the transient techniques were displayed and photographed on a Tektronix Type 547 oscilloscope. In order to eliminate errors caused by mass transfer effects, the transient potentiostatic technique was used so that more precise kinetic information could be obtained. The measurements were performed with appropriate IR compensation using a feedback circuit. A Lindberg Hevi-Duty SB furnace with 3-zone temperature control was used to heat the cell. The temperature of the melt was read by means of an alumina-sheathed thermocouple and was displayed on a digital readout (Newport Laboratories Inc., Model 267A-KC1-07).

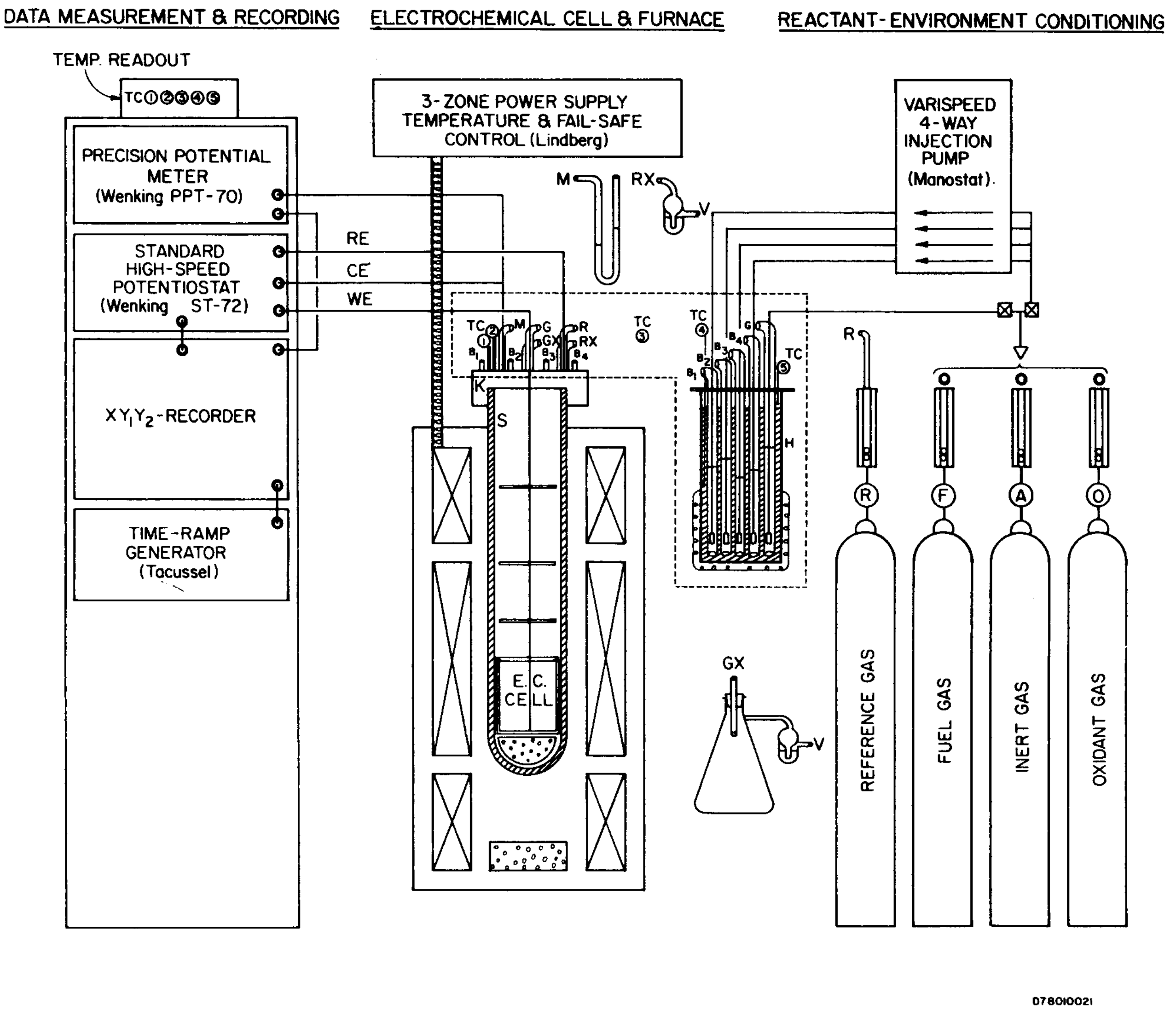

LEGEND

TC 1, 2, 3, 4, 5 - thermocouples
RE - reference electrode
CE - counterelectrode
WE - working electrode
M - manometer
G - cell blanketing gas supply
R - reference gas
B_1, B_2, B_3, B_4 - gas bubbler tubes
GX - gas knock-out pot
RX - reference gas exit
V - vent to hood
H - temperature-controlled humidifier with insulated heated envelope
K - feedthrough head for furnace tube
S - heavy alumina furnace tube and hermetic enclosure of E.C. cell

Figure 2.41. APPARATUS FOR HIGH-TEMPERATURE ELECTROCHEMICAL KINETICS STUDIES

2.3.3. Experimental Results

Before comparative activation kinetic data could be obtained for the hydrogen oxidation reaction, it was essential to determine whether the rate of the anodic reaction in the electrochemical half-cell shown in Figure 2.41 was influenced by activation, diffusion, or mixed control. Mixed control would be present if the rate of the kinetic and diffusional process had similar values. If, in fact, diffusion or mixed control were present, then some dependency of the current density on both the linear voltage sweep rate and the fuel bubbling rate into the molten carbonate mixture would be expected. The first objective was, therefore, to gain some qualitative insight into the relative contributions to the overall rate by activation and diffusion control under such experimental conditions.

Figures 2.42 and 2.43 show linear voltage sweep measurements at various sweep rates for a completely immersed nickel wire anode in the ternary Li/Na/K melt at 650°C, under conditions of continuous bubbling (50 mℓ/min) and with the fuel-bubbling turned off immediately before the linear voltage sweep, respectively. The fuel composition during the course of these measurements corresponded to intermediate-Btu fuel, that is, 40% H_2, 17% CO_2, 10% CO, and 33% H_2O. (See Table 2.10.) In both cases, we can see a dependency of the measured current density on the voltage sweep rate; the higher the sweep rate, the higher the observed current density. If we compare the measured current at a fixed voltage sweep rate, higher values were obtained for the melt subjected to continuous bubbling. For example, with a sweep rate of 0.15 mV/sec in the anodic direction, if we measured the current density at an anodic overpotential of 20 mV, the current densities were, respectively, 0.35 and 0.11 mA/cm^2, with and without continuous fuel bubbling. For the completely immersed nickel wire, both the dependency of the current density on the linear voltage sweep rate and on fuel-bubbling suggests diffusion or mixed control at the anode, either of the electroactive species or of reaction products away from the reaction site. Upon potentiostatting either nickel- or cobalt-working electrodes at high anodic overpotentials above 100 mV, some modification from the initial current/voltage characteristics was observed. Examples of such steady-state polarization curves for nickel and cobalt fully immersed in the Li/Na/K melt subjected to continuous bubbling with low-Btu fuel are shown in

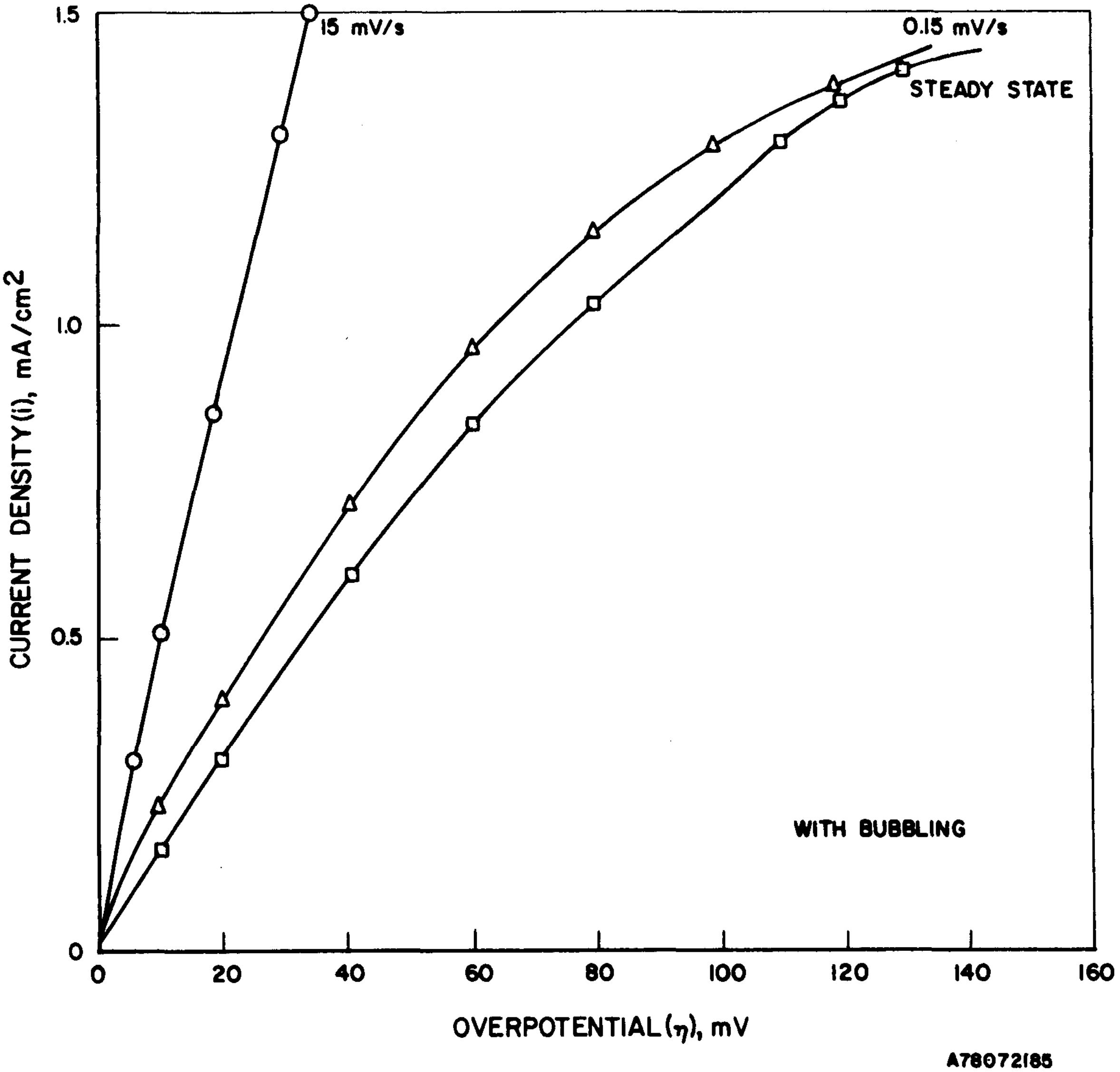

Figure 2.42. DEPENDENCY OF POLARIZATION CURVE ON LINEAR VOLTAGE SWEEP RATE FOR A FULLY IMMERSED NICKEL WIRE (Fuel Continuously Bubbled into Melt)

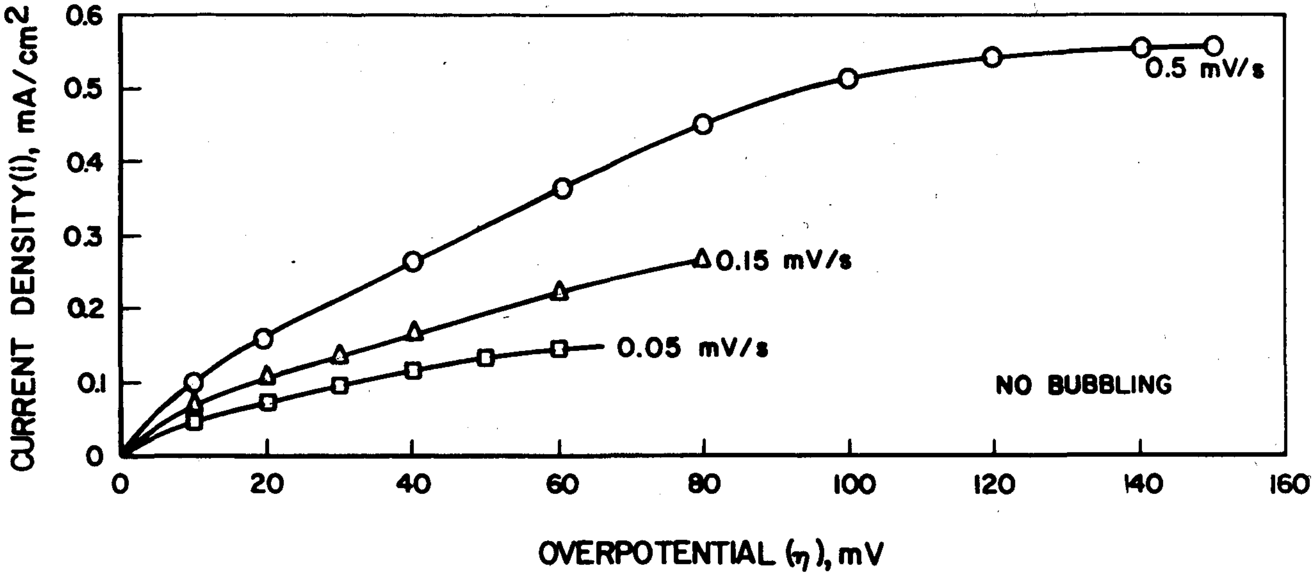

A78072184

Figure 2.43. DEPENDENCY OF POLARIZATION CURVE ON LINEAR VOLTAGE SWEEP RATE FOR A FULLY IMMERSED NICKEL WIRE (No Fuel Bubbling into Melt at Time of Measurement)

Table 2.10. FUEL GAS COMPOSITION CALCULATED FROM THE WATER-GAS-SHIFT EQUILIBRIUM REACTION (Numbers in Parentheses Correspond to the Humidifier Temperature)

	Mole Percent Fraction of Gases at 650°C					
	H_2	CO_2	H_2O	CO	CH_4	N_2
High Btu (53°C)	60.0	7.42	22.47	10.11		
Intermediate Btu (71°C)	40.5	16.4	32.8	10.3		
Low Btu (36°C)	21.16	9.16	5.54	17.76	1.13	45.25
Very low Btu (36°C)	11.71	5.71	4.40	7.75	0.57	69.86
High Btu (71°C)	53.68	8.08	31.11	7.12		

Figures 2.44 and 2.45, respectively. These measurements were performed over a temperature range of 550° to 700°C. Generally, the higher the melt temperature the higher the recorded current at a given overpotential. These steady-state polarization curves differ from those obtained initially on new electrodes in that they exhibited rapidly increasing currents at high anodic overpotentials (~150 mV for nickel and ~100 mV for cobalt). Once the high anodic potentials were removed, approximately 30 minutes was required to reach the initial open circuit potential. However, if upon removal of the anodic overpotential the working electrode was potentiostatted back to its initial open-circuit potential, then large (several mA/cm^2) cathodic currents were observed. It can be speculated that the sudden increase in currents at high anodic overpotentials is due to electrode surface oxidation.

A nickel or cobalt wire which is completely immersed in a molten carbonate electrolyte may be somewhat unrepresentative of those electrochemical conditions present at a porous anode within the molten carbonate fuel cell. Here, it is usually assumed that the porous anode will be covered with a thin film of the molten carbonate mixture originating from the electrolyte tile. Although there may well be some pores within this nickel electrode that may be completely flooded with electrolyte, the more favorable site for the anodic reaction would be expected to exist where a thin film of the molten carbonate electrolyte is present within an open pore of the sintered porous anode. Here, optimum conditions would exist for the supply of electroactive species and the removal of reaction products. Because the rate

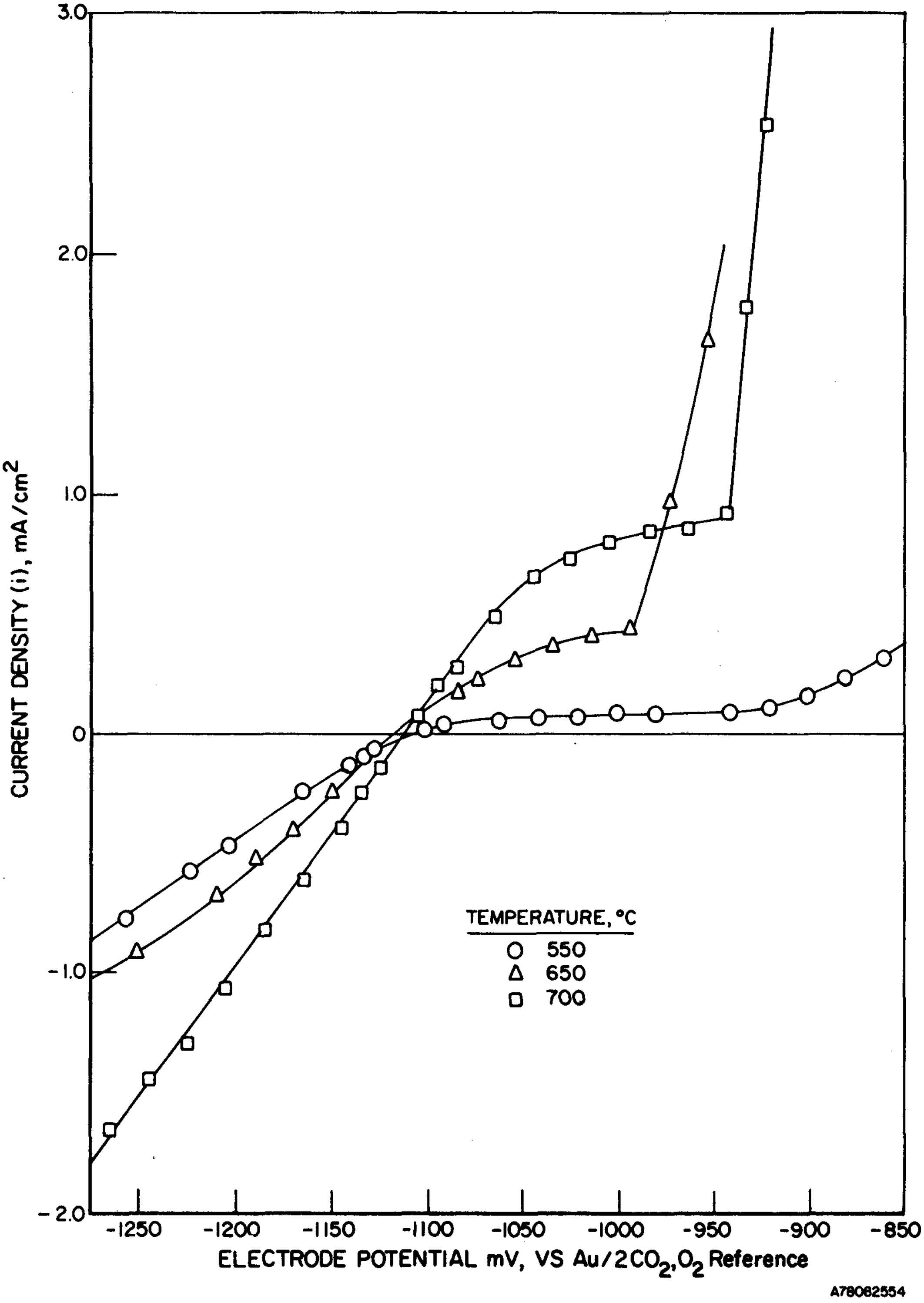

Figure 2.44. STEADY-STATE POLARIZATION CURVES FOR NICKEL IN Li/Na/K CARBONATE MELT

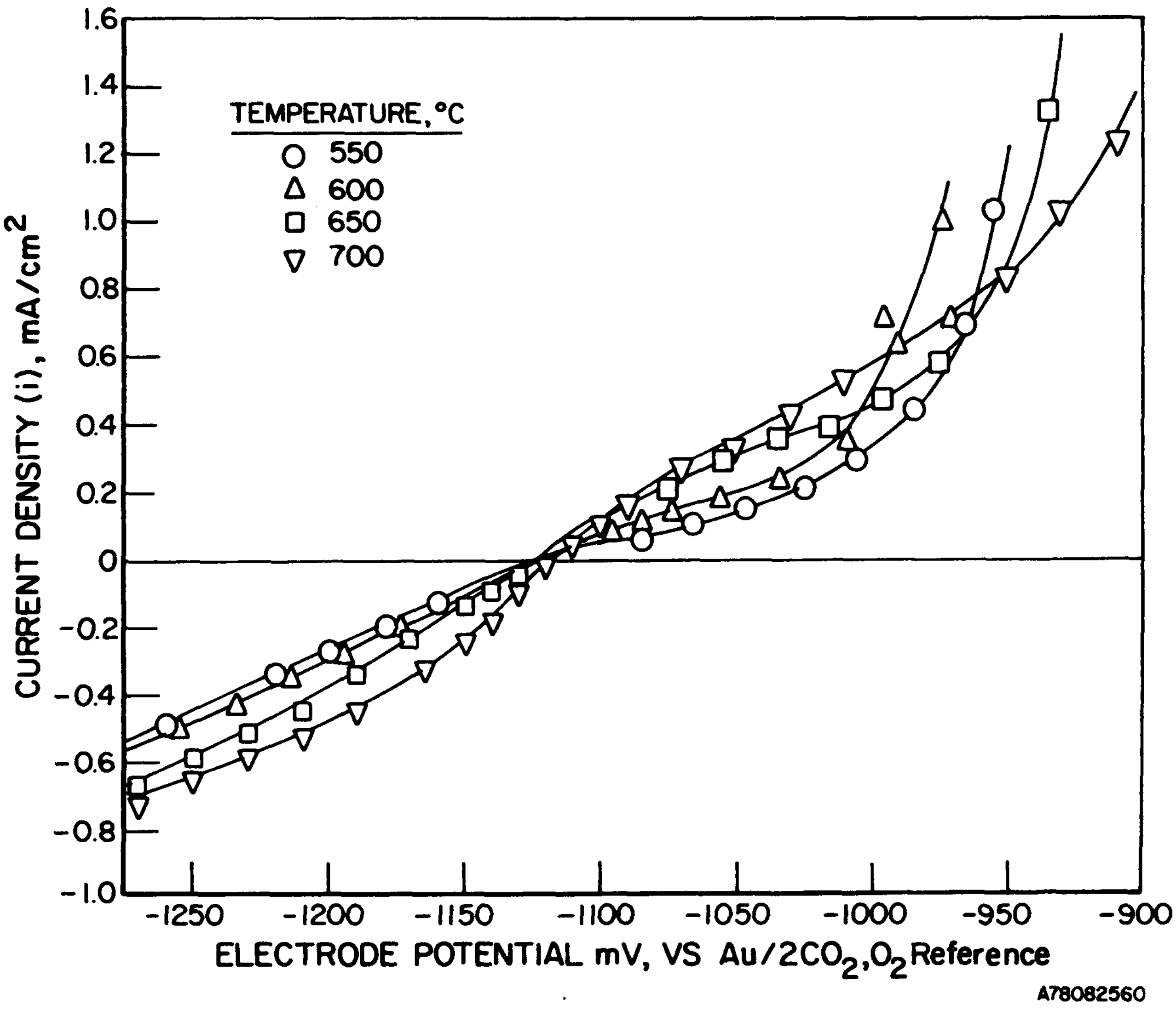

Figure 2.45. STEADY-STATE POLARIZATION CURVES FOR COBALT IN Li/Na/K CARBONATE MELT

of the overall electrochemical processes occurring within the molten carbonate fuel cell will be more rapid at electroactive sites that are covered with a thin film of the electrolyte, linear sweep measurements were performed on a nickel wire partially raised out of the melt (approximately 50%) so that the upper half of the nickel wire surface would approximate those electrochemical conditions expected at the porous electrode within the fuel cell anode. With continuous fuel-bubbling, linear voltage sweep measurements were performed with sweep rates between 0.15 mV/sec and 150 mV/sec, and a dependency of the current density on the voltage sweep rate was again observed (Figure 2.46), indicating the continued presence of diffusion- or mixed-control effects at a partially raised nickel wire. The limiting current density obtained with a sweep rate of 0.15 mV/s at an overpotential of ~150 mV can be seen to be around 3 mA/cm^2. In a porous electrode, where the ratio of real/apparent area is usually around 400, this current density would correspond to an apparent value of 1.2 A/cm^2.

2.3.4. Measurement of Electrode Kinetics

On the basis of the above observations, the extrapolation of activation kinetic data from either steady-state potentiostatic or voltage sweep measurements would give exchange current density values that would be dependent upon both the voltage sweep rate and the fuel bubbling rate. Clearly, under the diffusion conditions present, other electrochemical techniques have to be used to gain insight into the true activation kinetics. The measurement of activation kinetic parameters under the diffusion- or mixed-control conditions has been performed using transient potentiostatic techniques[29] on both nickel and cobalt electrodes under conditions of total and partial immersion in the candidate molten carbonate electrolytes. This technique involves applying a voltage step to the nickel or cobalt working electrode, and recording the current as a function of time. Under such conditions of mixed- or diffusion-control, the assumption is made that at time zero, only activation control will be present, that is, a sufficient supply of electroactive species will be present together with minimal reaction products so that any mass transfer effects will be minimized. A typical oscillograph obtained using this transient potentiostatic technique is shown in Figure 2.47. A 20-mV anodic voltage step (from the resting potential) is shown for a nickel electrode (top traces). The bottom traces show the current density variations on three

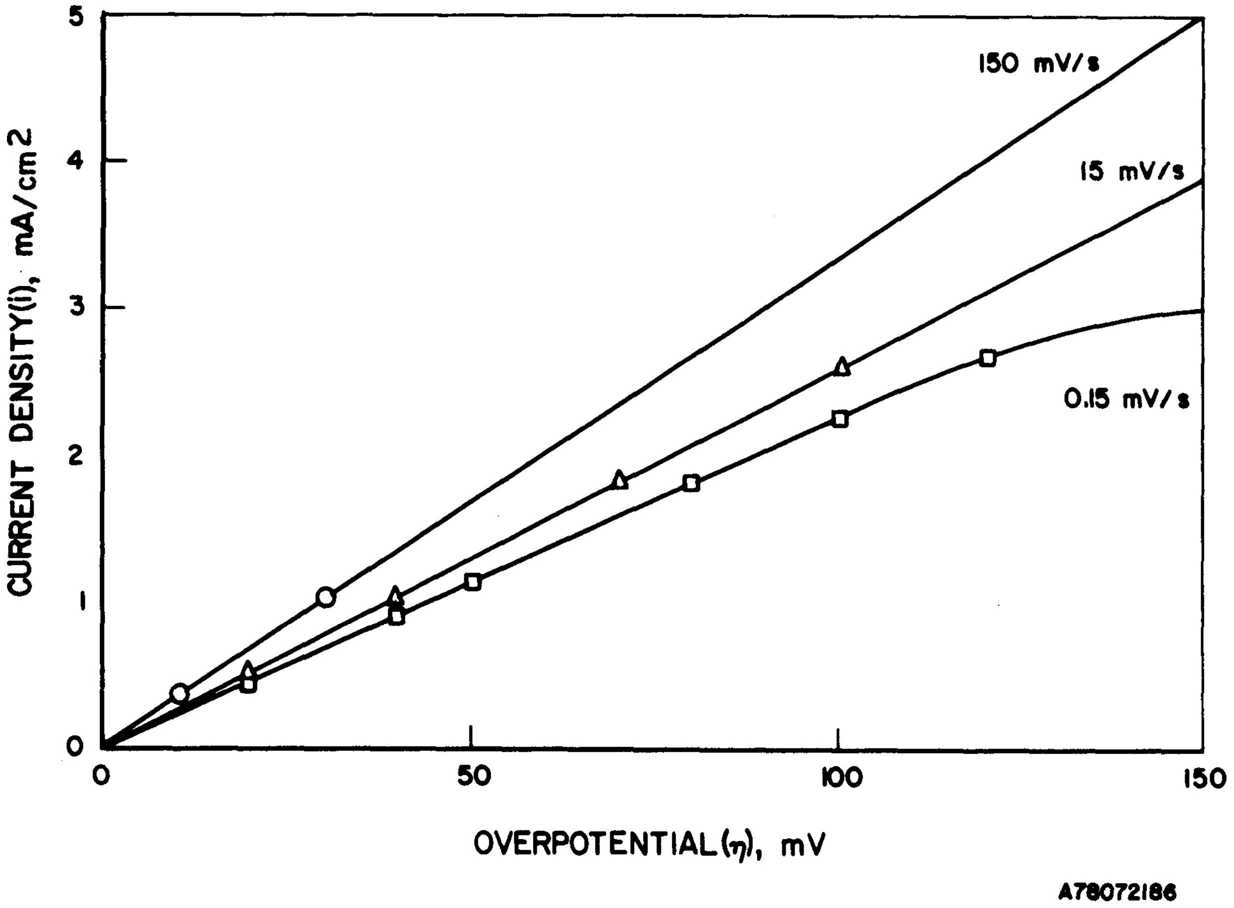

Figure 2.46. DEPENDCY OF POLARIZATION CURVE ON LINEAR VOLTAGE SWEEP RATE FOR A PARTIALLY RAISED (50%) NICKEL WIRE. INTERMEDIATE-Btu FUEL CONTINUOUSLY BUBBLED INTO Li/Na/K MELT AT 650°C

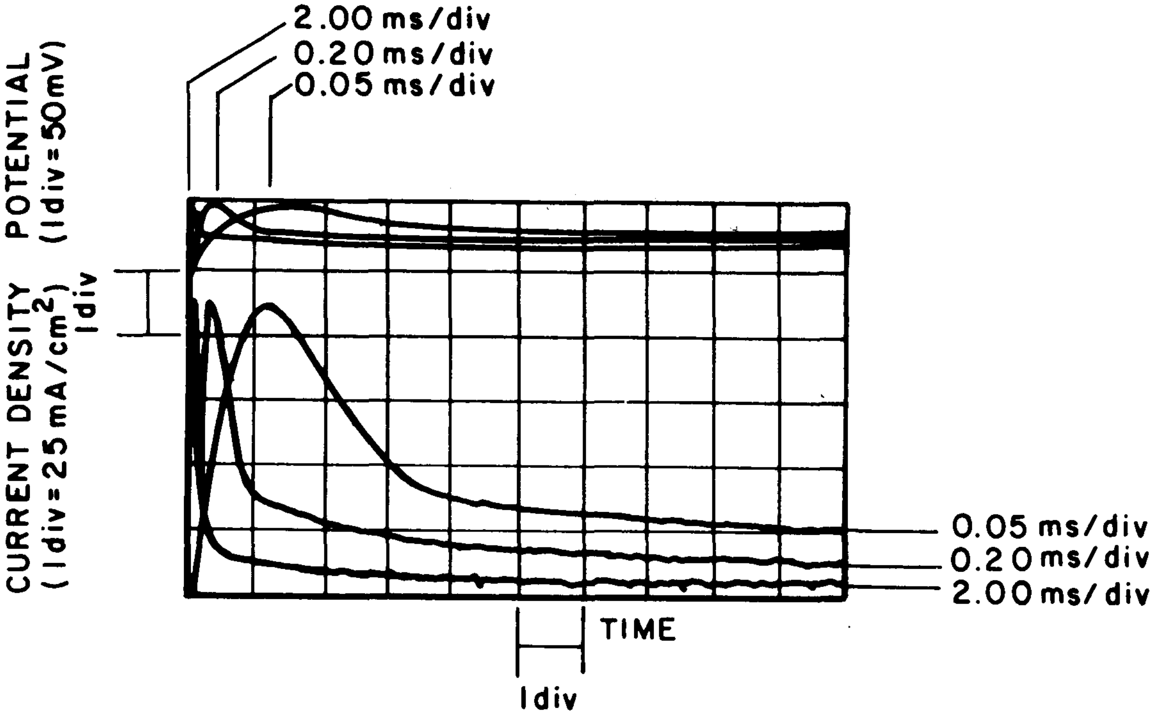

A78103210

Figure 2.47. TRANSIENT POTENTIOSTATIC MEASUREMENTS ON NICKEL IN LITHIUM-POTASSIUM MELT AT 650°C (Low-Btu Fuel With 50 ppm H_2S Introduced With Fuel)

different time scales between 0.05 ms and 2.0 ms/division. The kinetic current i(o) was obtained by extrapolating currents between 0.3 and 0.5 ms to time zero. Here the kinetic current was found to be 25 mA/cm^2 for the Li/Na/K melt at 650°C with intermediate-Btu fuel. Care was taken so that the extrapolated current values were free of interference by capacitive currents. With appropriate IR compensation, the capacitive current can be clearly distinguished. After the transient capacitive spike (Figure 2.47), the current can be seen to decrease as a result of diffusional processes.

This potential step technique has been applied to both nickel and cobalt electrodes in the three candidate molten carbonate mixtures discussed earlier. This was carried out using various fuel compositions and different temperatures so that comparative kinetic data could be obtained from the three candidate melts. Extrapolated current densities at time zero i(0) were plotted versus the applied potential steps η. Figure 2.48 shows a representative activation polarization plot for nickel in the Li/Na/K ternary melt using intermediate-Btu fuel. For an activation process, the current-voltage relationship is given by —

$$i(0) = i_o[e^{\alpha_a \eta F/RT} - e^{-\alpha_c \eta F/RT}] \qquad (29)$$

In the low overpotential region, this equation can be approximated by

$$i(0) = i_0 \, (\alpha_a + \alpha_c)\eta F/RT$$

or

$$i_o = \frac{RT}{(\alpha_a + \alpha_c)F} \; \frac{di(0)}{d\eta} \qquad (30)$$

Thus, the exchange current density i_o can be calculated from the slope of the i(0) versus the η curve. We assume a value of 2 for the sum of the apparent transfer coefficients α_a and α_c based on a total of two electron transfer processes and a stoichiometric number 1. For the specific case, i_o was calculated using Equation 30 to be 78 mA/cm^2 for a nickel electrode. This potential step technique has been applied to electrodes that have been both fully immersed and partially raised in molten carbonate mixtures. Under each experimental condition, the extrapolated current densities were in good

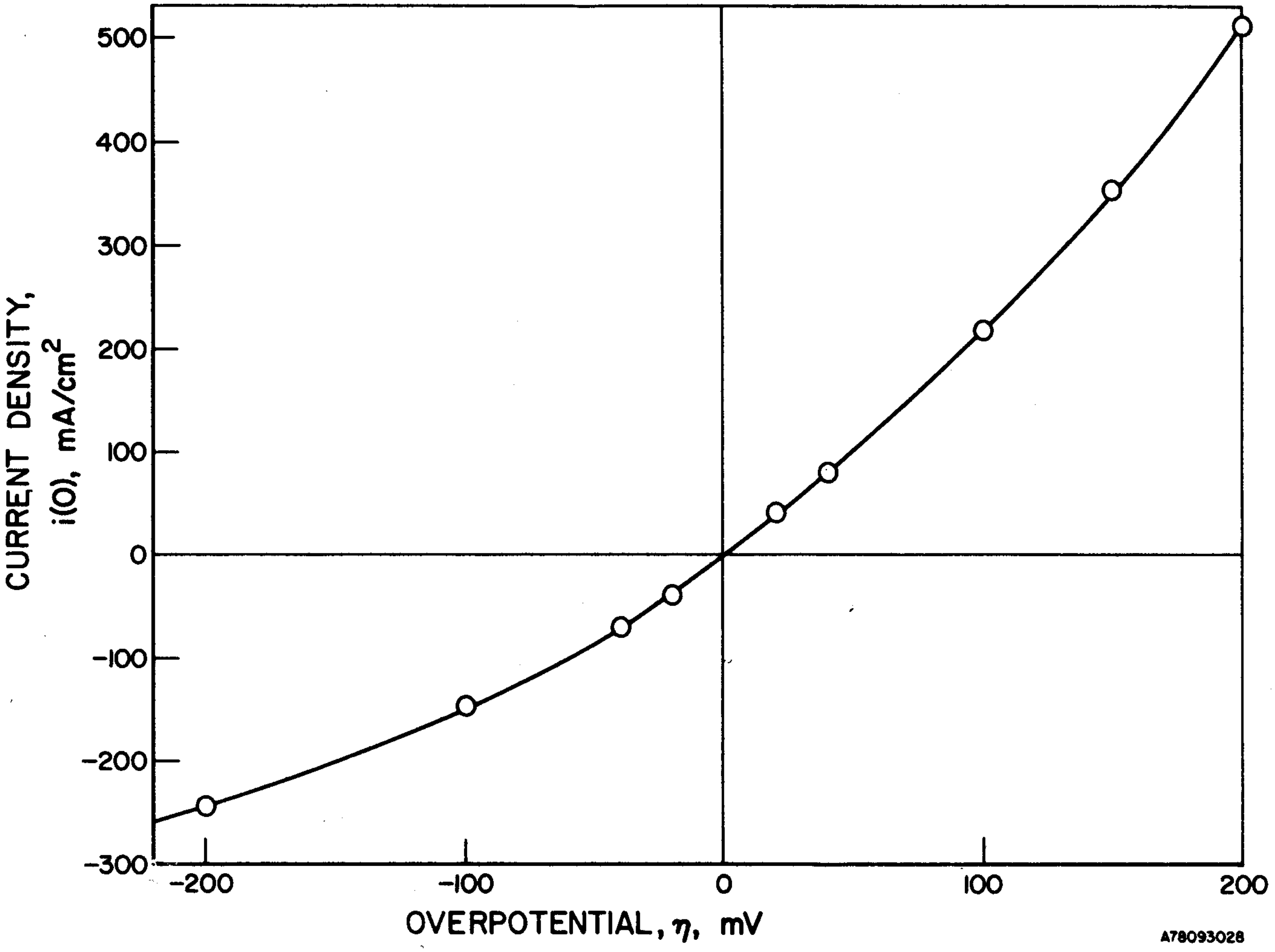

Figure 2.48. POLARIZATION CURVE AT A NICKEL ELECTRODE FROM i(0) VALUES EXTRAPOLATED VIA POTENTIAL STEP TECHNIQUE (Fuel: 40% H_2, 17% CO_2, 10% CO, and 33% H_2O at 650°C)

agreement with values obtained from fully immersed electrodes, which supports the validity of this technique for separating activation kinetic data under diffusion- or mixed-control conditions.

Exchange current density values were also obtained from Allen-Hickling plots[30] of the potential step data. For the Allen-Hickling plot, Equation 28 can be rewritten as —

$$\log \frac{i}{\exp[(\alpha_a + \alpha_c)\eta F/RT] - 1} = \log i_o - \frac{\alpha_c \eta F}{2.303\ RT} \tag{31}$$

If we assume $\alpha_a + \alpha_c = 2$, then a plot of

$$\log \frac{i}{\exp[(\alpha_a + \alpha_c)\eta F/RT] - 1} \quad \text{versus } \eta \tag{32}$$

can give the value of α_c from the slope and a value of i_o from the intercept. Typical Allen-Hickling plots of 650°C for nickel and cobalt are compared in Figure 2.49 using intermediate-Btu fuel. From the intercept at zero overpotential, exchange current densities were generally found to be higher for nickel (85 mA/cm^2) compared with cobalt (28 mA/cm^2). Good agreement was found between exchange current density values obtained from low overpotential data and Allen-Hickling plots.

From the anodic slope shown in Figure 2.49, we obtain $\alpha_a = 0.7$ and $\alpha_c = 0.3$ for nickel and $\alpha_a = 0.74$ and $\alpha_c = 1.26$ for cobalt.

The above charge transfer coefficients discussed for the ternary melt are representative of values obtained for all three melts with the temperatures and fuel compositions used in this work.

In the high anodic overpotential region, oxidation of the electrode surface may become significant (Figures 2.44 and 2.45), giving currents higher than that resulting from fuel oxidation only. This would result in higher α_a values in the anodic region. To gain more insight into the validity of α_a and α_c values corresponding to fuel oxidation at nickel and cobalt electrodes, activation data were generated on a gold electrode in the Li/K melt at 650°C using intermediate-Btu fuel as shown in Figure 2.50. The corresponding Allen-Hickling data from this activation plot are shown in

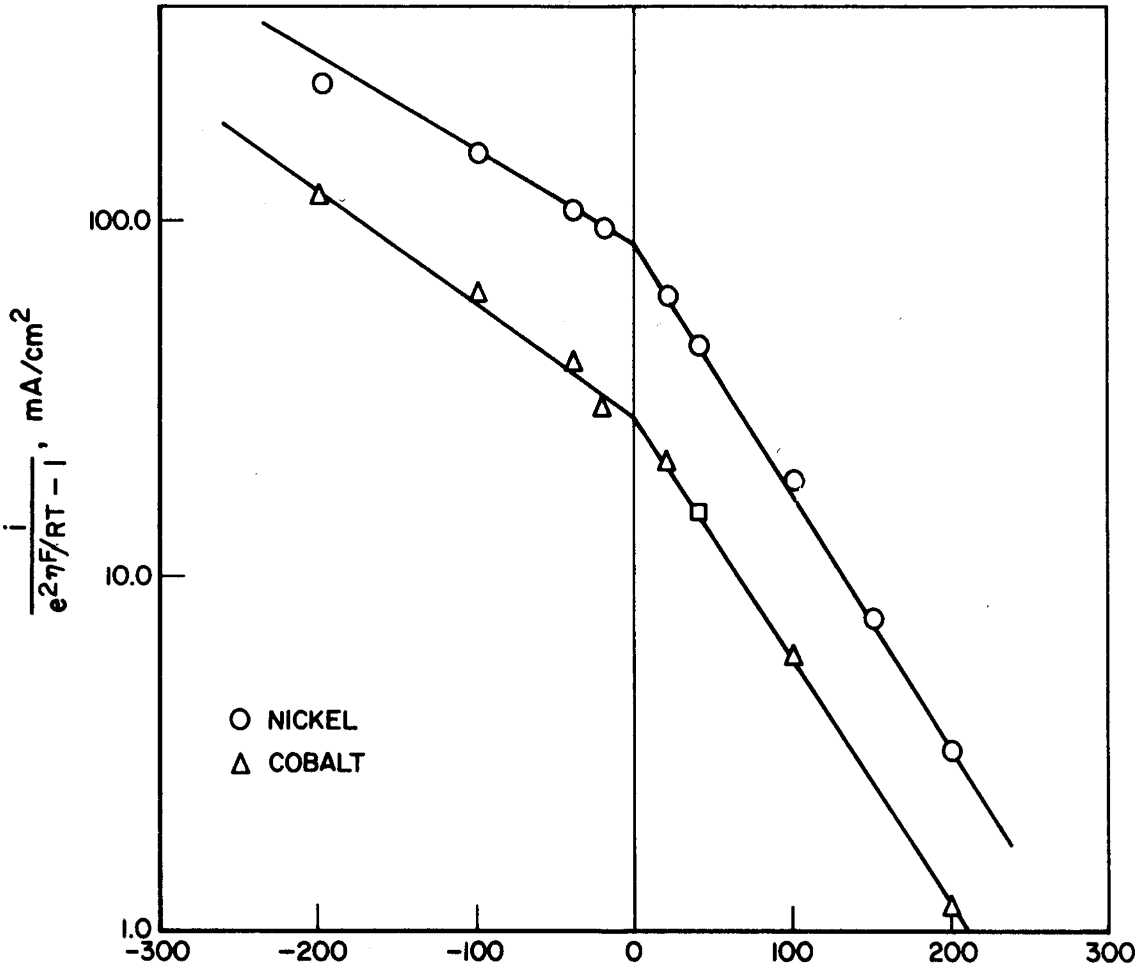

Figure 2.49. CURRENT-VOLTAGE CHARACTERISTICS FROM TRANSIENT POTENTIOSTATIC EXPERIMENTS ON GOLD IN 650°C Li/K MELT WITH INTERMEDIATE-Btu FUEL

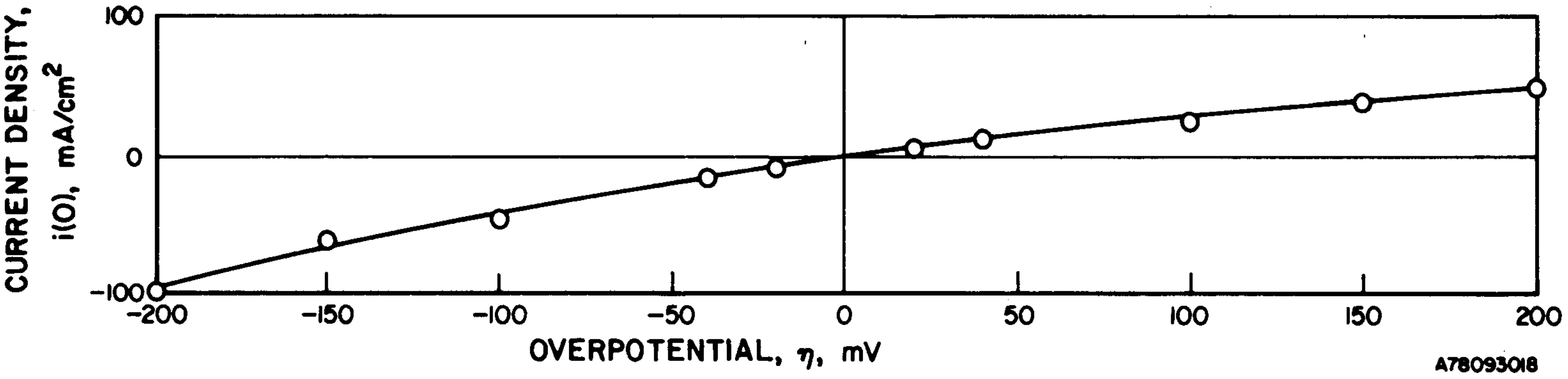

Figure 2.50. CURRENT VOLTAGE CHARACTERISTICS FROM TRANSIENT POTENTIOSTATIC EXPERIMENTS ON GOLD IN 650°C Li/K MELT WITH INTERMEDIATE-Btu FUEL

Figure 2.51. Here we obtain $i_o = 16$ mA/cm^2, $\alpha_c = 1.56$, and $\alpha_a = 0.44$. Based on these results, we can tentatively conclude that the oxidation of fuel proceeds with $\alpha_c = 1.5$ and $\alpha_a = 0.5$ in the absence of electrode oxidation effects.

Other kinetic information can be obtained by determining the dependency of the exchange current density i_o on fuel composition. The dependency of this parameter on hydrogen content is shown for both nickel and cobalt in Figures 2.52, 2.53, and 2.54 for the Li/K, Li/Na/K, and Li/Na melts at 650°C, respectively.

Although the slope of these lines would indicate an empirical reaction order for hydrogen of approximately 0.5, this can not be considered the true reaction order because it was not possible to independently vary the hydrogen content without changing the overall gas composition by the water-gas shift reaction. (See Table 2.10.)

$$H_2O + CO \rightleftarrows H_2 + CO_2 \tag{33}$$

The true reaction orders for hydrogen, carbon dioxide, and water in the fuel were calculated from the following equation —

$$i_o = k^* \, [H_2]^a [CO_2]^b [H_2O]^c \tag{34}$$

where k^* is a proportionality constant, and a, b, and c are the reaction orders of H_2, CO_2, and H_2O, respectively.

Knowing the respective concentrations of H_2, CO_2, and H_2O, then, by the water-gas shift reaction (Equation 5), the CO content is automatically fixed. If i_o is measured in four different fuels, then the four unknowns k^*, a, b, and c can be determined. The above equation can be written in the logarithmic form —

$$\log i_o = k + a \log [H_2] + b \log [CO_2] + c \log [H_2O] \tag{35}$$

where $k = \log k^*$. Using i_o values obtained with full gas compositions corresponding to high, medium, low, and very low Btu (Table 2.10), Equation 35 can be written in a matrix form.

$$\begin{pmatrix} 1.54 \\ 1.62 \\ 1.34 \\ 1.20 \end{pmatrix} \begin{pmatrix} 1 & -0.22 & -1.13 & -0.65 \\ 1 & -0.39 & -0.79 & -0.48 \\ 1 & -0.67 & -1.04 & -1.26 \\ 1 & -0.93 & -1.24 & -1.36 \end{pmatrix} \begin{pmatrix} k \\ a \\ b \\ c \end{pmatrix} \tag{36}$$

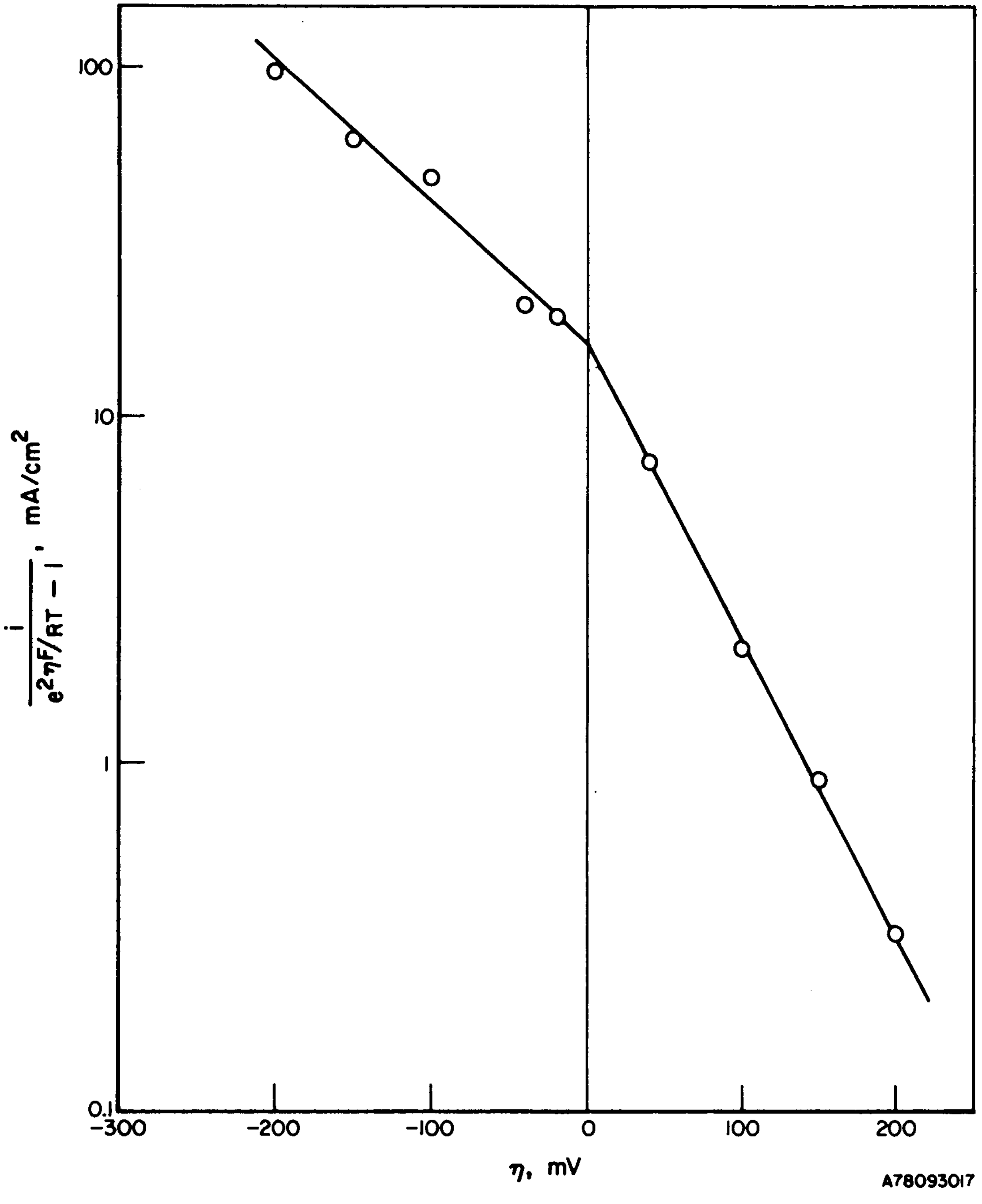

Figure 2.51. DEPENDENCY OF EXCHANGE CURRENT DENSITIES OF NICKEL AND COBALT ON HYDROGEN CONTENT USING VARIOUS FUELS (Li/K Melt at 650°C)

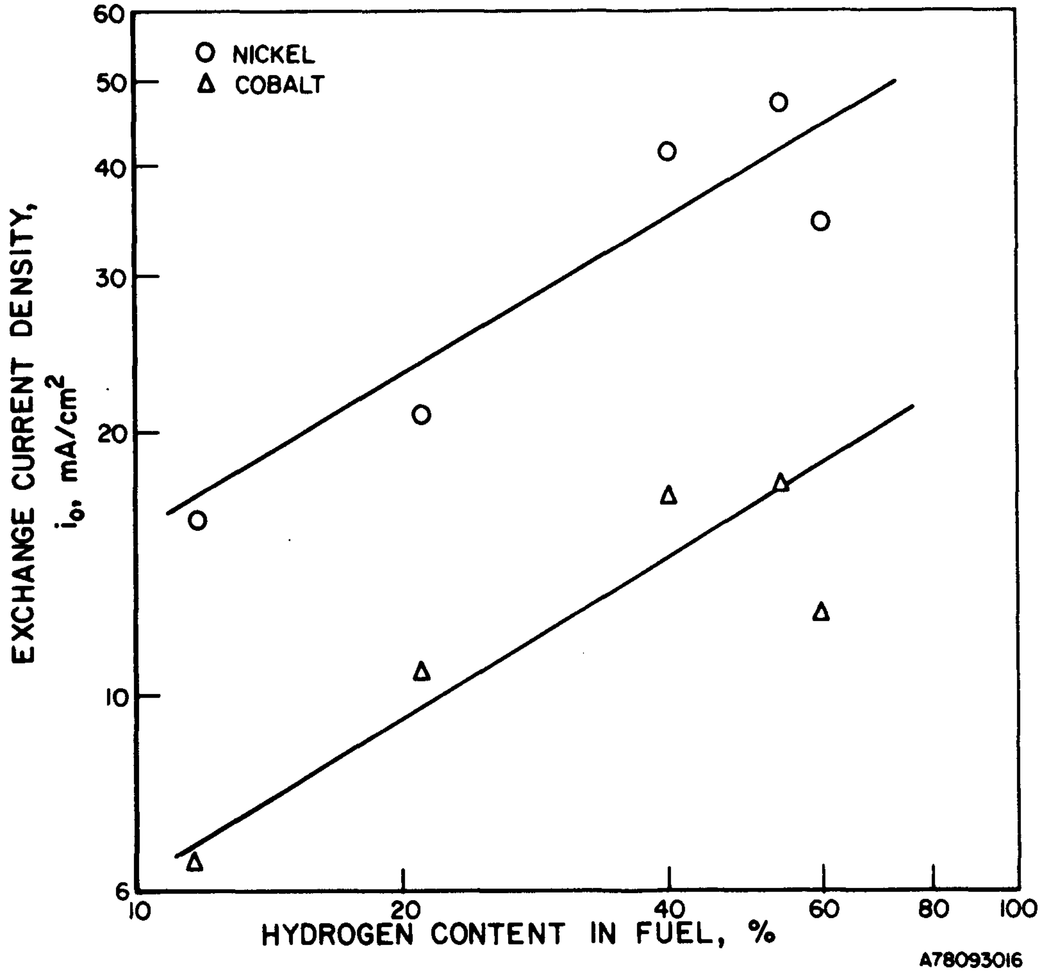

Figure 2.52. DEPENDENCY OF EXCHANGE CURRENT DENSITIES OF NICKEL AND COBALT ON HYDROGEN CONTENT USING VARIOUS FUELS (Li/Na/K Melt at 650°C)

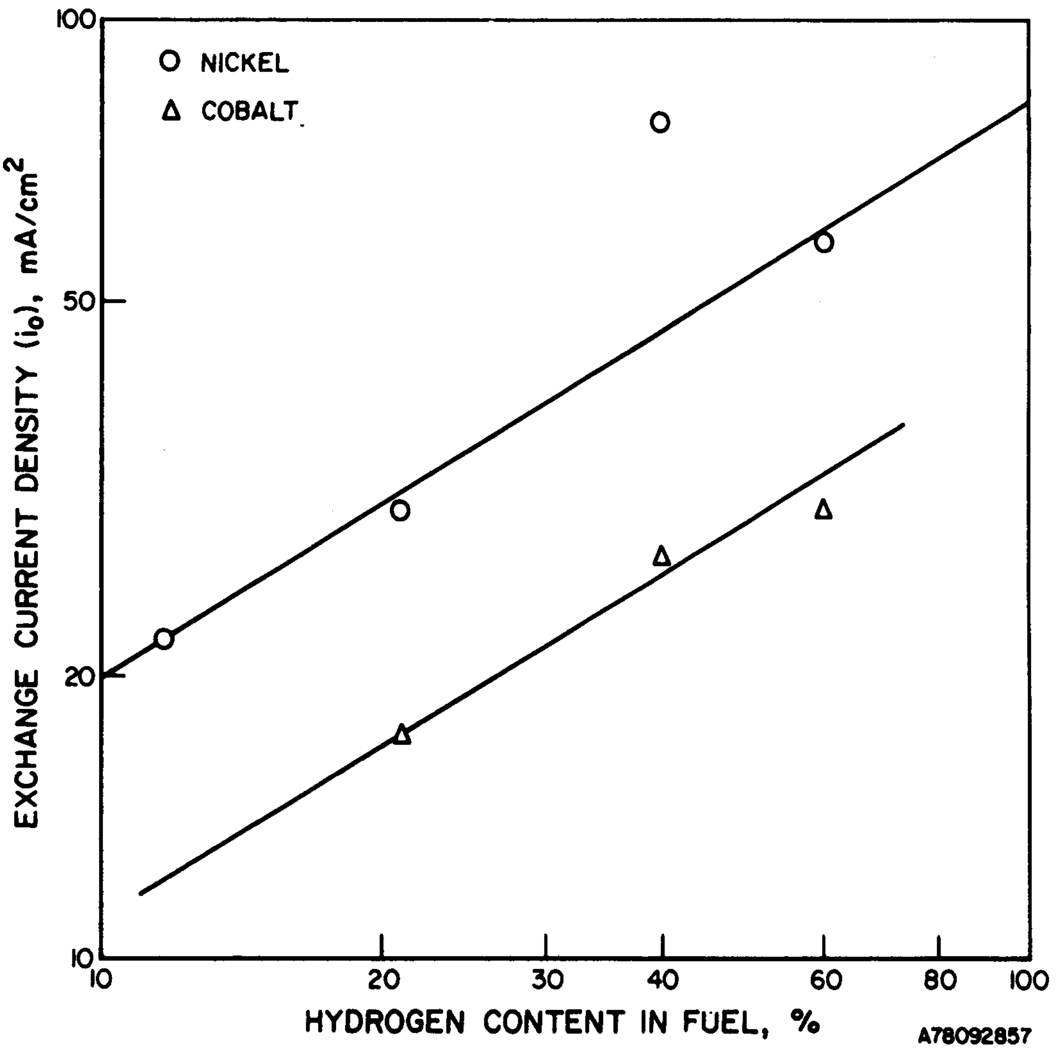

Figure 2.53. DEPENDENCY OF EXCHANGE CURRENT DENSITIES OF NICKEL AND COBALT ON HYDROGEN CONTENT USING VARIOUS FUELS (Li/Na Melt at 650°C)

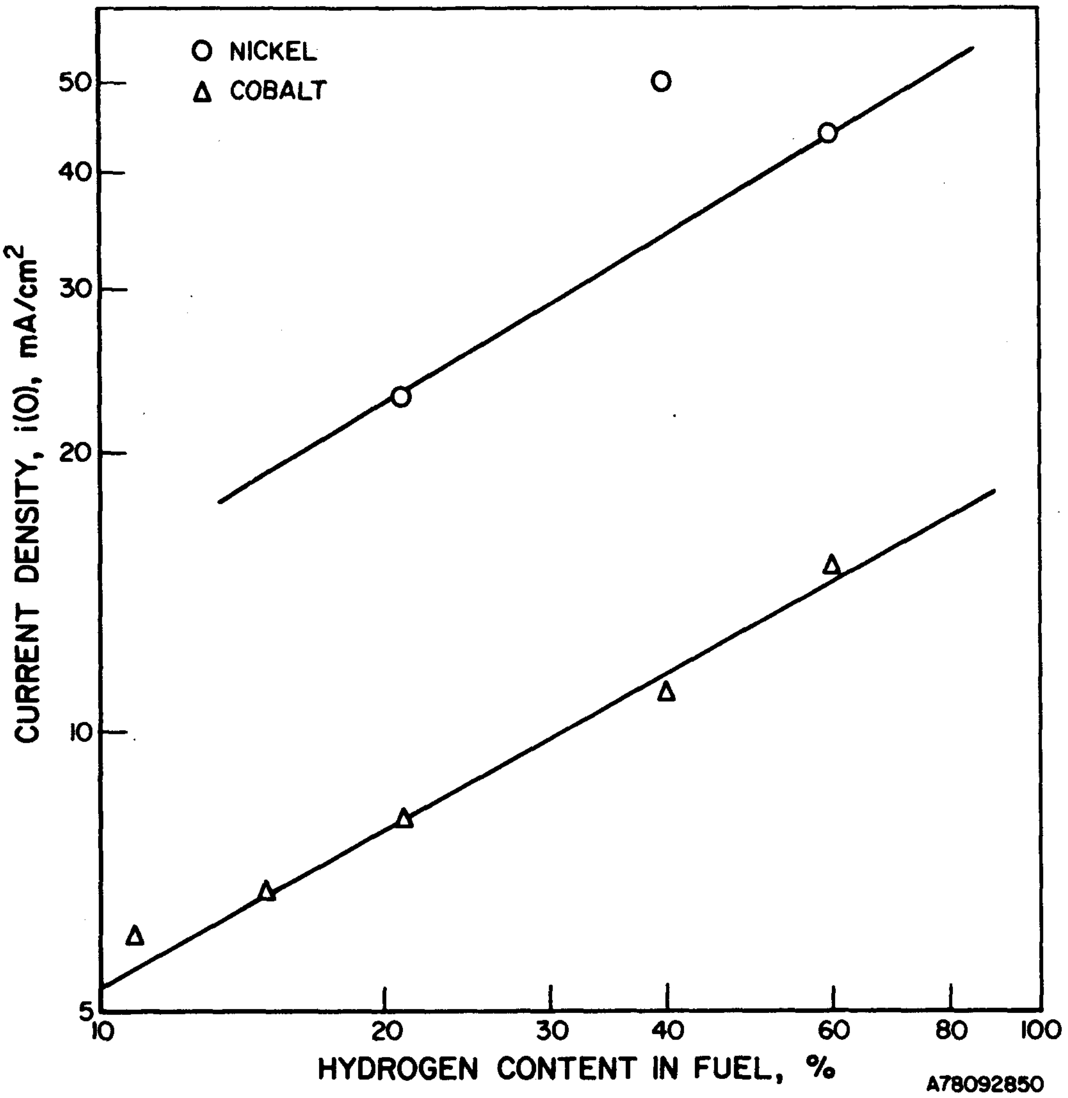

Figure 2.54. DEPENDENCY ON TEMPERATURE OF i_o VALUES OBTAINED USING TRANSIENT POTENTIOSTATIC MEASUREMENTS (Nickel and Cobalt Electrodes in Low-Btu Fuel)

These simultaneous linear equations were solved on a programmable calculator, with the result —

$k = 2.02$
$a = 0.258$
$b = 0.275$
$c = 0.178$

Thus, Equation 34 can be written as —

$$i_o = 104.7\ [H_2]^{0.258}[CO_2]^{0.275}[H_2O]^{0.178} \qquad (37)$$

We can see that the reaction orders, with respect to H_2, CO_2, and H_2O, are close to 0.25.

We considered several reaction mechanisms for fuel oxidation that might give the i_o dependency shown in Equation 37 of possible reaction mechanisms for hydrogen oxidation and oxygen reduction in the molten-carbonate fuel cell.

The following hydrogen oxidation reaction mechanisms have been analyzed:

Model I	$H_2 + 2M \rightarrow 2\ MH$	Step (1)
	$MH + CO_3^= \rightarrow OH^- + CO_2 + M + e^-$	Step (2)
	$MH + OH \rightarrow H_2O + M + e$	Step (3)
Model II	$H_2 + CO_3^= + M \rightarrow OH^- + CO_2 + MH + e^-$	Step (1)
	$MH + OH^- \rightarrow M + H_2O + e^-$	Step (2)
Model III	$H_2 + 2M \rightarrow 2\ MH$	Step (1)
	$2(MH + OH^- \rightarrow H_2O + M + e^-$	Step (2)
	$H_2O + CO_3^- \rightarrow 2\ OH^- + CO_2$	Step (3)
Model IV	$H_2 + M + CO_3^= \rightarrow OH^- + CO_2 + MH + e$	Step (1)
	$MH + CO_3^= \rightarrow CO_2^- + OH^- + M$	Step (2)
	$CO_2^- \rightarrow CO_2 + e^-$	Step (3)
	$2OH^- + CO_2 \rightarrow CO_3^= + H_2O$	Step (4)
Model V	$H_2 + 2M \rightarrow 2\ MH$	Step (1)
	$MH + CO_3^= \rightarrow CO_2^- + OH^- + M$	Step (2)
	$MH + OH^- \rightarrow H_2O + M + e^-$	Step (3)
	$CO_2^- \rightarrow CO_2 + e^-$	Step (4)

Model VI $H_2 + 2M \rightarrow 2\,MH$ Step (1)
$2\,MH + CO_3^{=} \rightarrow CO_2^{=} + H_2O$ Step (2)
$CO_2^{=} \rightarrow CO_2^{-} + e^{-}$ Step (3)
$CO_2^{-} \rightarrow CO_2 + e^{-}$ Step (4)

From each of these reaction mechanisms, the α_a and α_c and reaction orders can be predicted for the rate-determining steps identified in Table 2.11, using different assumed electrode coverages.

The electrode kinetic data generated during this work predicts reaction orders according to Equation 37, and indicated that Model I, with step 2 as the rate-determining step, may be the actual reaction mechanism for fuel oxidation. Further examination of this reaction mechanism revealed —

$$H_2 + 2M \underset{k_{1C}}{\overset{k_{1A}}{\rightleftarrows}} 2MH \tag{38}$$

$$MH + CO_3^{=} \underset{k_{2C}}{\overset{k_{2A}}{\rightleftarrows}} OH^{-} + CO_2 + M + e^{-} \tag{39}$$

and
$$MH + OH^{-} \underset{k_{3C}}{\overset{k_{3A}}{\rightleftarrows}} H_2O + M + e^{-} \tag{40}$$

This mechanism assumes that —

a. Equation 39 is the rate-determining step.
b. Langmuir adsorption is isothermal.
c. There is low coverage, Θ, of MH.

The net current from Equation 38 is given by —

$$i_1 = F[k_{1A}\, C_{H_2}\, (1 - \Theta)^2 - k_{1C}\Theta^2] \tag{41}$$

At equilibrium, when $i_1 = 0$,

$$\frac{\Theta}{1 - \Theta} = \left(\frac{k_{1A}}{k_{1C}}\, C_{H_2}\right)^{1/2} = K_1^{1/2}\, C_{H_2}^{1/2} \tag{42}$$

Table 2.11. CALCULATED α_a, α_c, AND REACTION ORDERS FOR H_2, H_2O, AND CO_2 FOR REACTION MECHANISMS I THROUGH VI

Rate Determining Step	Type of Coverage	α_a	α_c	Reaction Orders (H_2)	(H_2O)	(CO_2)
Model I						
1	Temkin	1.0	1.0	0.5	0	0
1	Langmuir	*	2.0	1.0	0	0
2	Temkin	0.5	1.5	−0.25	0.5	0.5
2	Langmuir	0.5	1.5	0.25	0.25	0.25
3	Temkin	1.5	0.5	0	0	0
3	Langmuir	1.5	0.5	−0.25	0.75	0.25
Model II						
1	Temkin	0.5	1.5	0.75	0.25	0.25 **
1	Langmuir	0.5	1.5	0.75	0.25	0.25
2	Temkin	1.5	0.5	0.25	0.75	−0.25 **
2	Langmuir	1.5	0.5	0.25	0.75	−0.25
Model III						
1	Temkin	1.0	1.0	0.5	0	0
1	Langmuir	*	2.0	1.0	0	0
2	Temkin	0.5	0.5	0	0.75	−0.25 **
2	Langmuir	0.5	0.5	0.25	0.75	0.25
3	Temkin	*	2.0	0	1.0	0
3	Langmuir	*	2.0	0	1.0	0
Model IV						
1	Temkin	1.0	1.0	0.5	0.25	0.25
1	Langmuir	0.5	1.5	0.75	0.25	0.25
2	Temkin	0.5	1.5	0.25	0	0
2	Langmuir	1.0	1.0	0.5	0	0
3	Temkin	1.5	0.5	0.25	−0.25	0.75
3	Langmuir	1.5	0.5	0.25	−0.25	0.75
4	Temkin	2.0	0	0	1.0	0
4	Langmuir	2.0	0	0	1.0	0
Model V						
1	Temkin	1.0	1.0	0.5	0	0
1	Langmuir					
2	Temkin	*				
2	Langmuir					
3	Temkin	1.5	0.5	0	+0.75	−0.25
3	Langmuir					
4	Temkin					
4	Langmuir	1.5	0.5	+0.25	−0.25	0.75
Model VI						
1	Temkin	1.0	1.0	0.5	0	0
2	Temkin	*		0.5		
3	Temkin	0.5	1.5	0.75	−0.75	0.25

* No potential dependence.

** $e^{\gamma r \Theta}$ (in cathodic and anodic terms) cancels.

The net current from Equation 40 is —

$$i_3 = F\ \ k_{3A}\ \ \Theta\ C_{OH^-}\ e^{\beta_3 FV/RT} - k_{3_C}\ C_{H_2O}\ (1 - \Theta)e^{-(1 - \beta_3)FV/RT} \tag{43}$$

V is the potential difference between the electrode and the electrolyte. At equilibrium, when $i_3 = 0$,

$$C_{OH^-} = \frac{k_{3C}}{k_{3A}}\ CH_2O\ \frac{1}{(K_1\ C_{H_2})^{1/2}}\ e^{-FV/RT} \tag{44}$$

For Equation 39 the net current is —

$$i_2 = F\ \ k_{2A}\ \Theta\ C_{CO_3^=}\ \ e^{\beta_2 FV/RT} - k_{2C}C_{OH^-}C_{CO_2}\ \ (1 - \Theta)e^{-(1-\beta_2)FV/RT} \tag{45}$$

Upon substitution for C_{OH^-} from Equation 44 into Equation 45 for the equilibrium potential, V_o, we can write,

$$e^{FV_0/RT} = \frac{k_{2C}}{k_{2A}}\ \frac{k_{3C}}{k_{3A}}\ \frac{1}{k_1 C_{H_2}}\ {\frac{C_{H_2O}\ C_{CO_2}}{C_{CO_3^=}}}^{1/2} \tag{46}$$

Replacing V for Vo + η in Equation 45, where η is the overpotential, we obtain,

$$i_2 = F\ \ k_{2A}\ \ \Theta\ C_{CO_3^=}\ e^{\beta_2 F\eta/RT}\ \frac{k_{2C}}{k_{2A}}\ \frac{k_{3C}}{k_{3A}}\ \frac{1}{K_1 C_{H_2}}\ {\frac{C_{H_2O}\ C_{CO_2}}{C_{CO_3^=}}}^{\beta_2/2}$$

$$- k_{2C}\ \frac{k_{3C}}{k_{3A}}\ \frac{C_{H_2O}}{(K_1 C_{H_2})^{1/2}}C_{CO_2}(1 - \Theta)_{e}{}^{(-\ 2\ +\ \beta_2)F\eta/RT}\ \frac{k_{2C}}{k_{2A}}\ \frac{k_{3C}}{k_{3A}}\ \frac{1}{K_1 C_{H_2}}$$

$$\frac{C_{H_1}O\ \ C_{CO_2}}{C_{CO_3^=}}^{\frac{-\ 2\ +\ \beta_2}{2}} \tag{47}$$

From Equation 42 for low coverage we have $\Theta = K_1^{1/2}\ CH_2^{1/2}$ and $1 - \Theta = 1$. Thus, Equation 47 becomes —

$$i_2 = F\ k_2\ K_1^{1/2}\ C_{H_2}^{1/2}\ C_{CO_3^=}\ \frac{k_{2C}}{k_{2A}}\ \frac{k_{3C}}{k_{3A}}\ \frac{1}{K_1 C_{H_2}}\ {\frac{C_{H_2O}\ C_{CO_2}}{C_{CO_3^=}}}^{\beta_2/2} e^{\beta_2 F\eta/RT}$$

$$- k_{2C}\ \frac{k_{3C}}{k_{3A}}\ \frac{C_{H_2O}}{(K_1 C_{H_2})^{1/2}}\ C_{CO_2}\ \frac{k_{2C}}{k_{2A}}\ \frac{k_{3C}}{k_{3A}}\ \frac{1}{K_1 C_{H_2}}\ {\frac{C_{H_2}\ C_{CO_2}}{C_{CO_3^=}}}^{\frac{-2+\beta_2}{2}} e^{(-2+\beta_2)F\eta/RT} \qquad (48)$$

Comparing this with the general relationship for activation polarization,

$$i = i_o\ (e^{\alpha_A F\eta/RT} - e^{-\alpha_C F\eta/RT}) \qquad (49)$$

we obtain —

$\alpha_A = \beta_2 = 0.5$

$\alpha_C = 2-\beta_2 = 1.5$ for $\beta_2 = 0.5$

The dependency of i_o on the gases (for $\beta_2 = 0.5$) is —

$$i_0 \sim [C_{H_2}]^{0.25}[C_{CO_2}]^{0.25}[C_{H_2O}]^{0.25} \qquad (50)$$

The theoretical value of $\alpha_A = 0.5$ compares reasonably well with our experimentally determined α_A of 0.7 for nickel and cobalt and 0.5 for gold. Table 2.12 compares experimentally determined i_o values at 650°C with calculated values, assuming reaction orders of 0.25 for H_2, CO_2, and H_2O on a nickel anode in three different melts and with four gases. Similar data for cobalt are shown in Table 2.13.

The highest exchange current densities were measured on nickel and cobalt in the Li/Na/K ternary melt with all fuel compositions used. In these tables, we can see that good agreement exists between experimental and calculated i_o values.

We have seen in Figures 2.41 and 2.42 that currents were dependent upon the rate of fuel bubbling through the melt. The current increased further when the nickel wire was partially submerged. This suggests that in this system, the current is limited by the rate of fuel gas delivery through the melt into the electrode. However, in the porous electrode of an actual

Table 2.12. EXCHANGE CURRENT DENSITIES, i_o, FOR NICKEL IN DIFFERENT MELTS AND USING VARIOUS GASES AT 650°C

	Measured	Calculated
	mA/cm²	
Li/K		$k^* = 110$
High Btu	35.0	34.70
Medium Btu	42.0	42.17
Low Btu	21.0	19.84
Very Low Btu	16.0	14.37
Li/Na/K		$k^* = 229.09$
High Btu	57.0	55.34
Medium Btu	78.0	66.80
Low Btu	30.0	31.44
Very Low Btu	22.0	22.78
Li/Na		$k^* = 135$
High Btu	44.0	41.70
Medium Btu	54.0	50.70
Low Btu	23.0	23.85
Very Low Btu	--	17.30

Table 2.13. EXCHANGE CURRENT DENSITIES, i_o, FOR COBALT IN DIFFERENT MELTS AND USING VARIOUS GASES AT 650°C

	Measured	Calculated
	mA/cm²	
Li/K		$k^* = 45$
High Btu	12.5	14.20
Medium Btu	17.0	17.18
Low Btu	10.7	8.08
Very Low Btu	6.5	5.90
Li/Na/K		$k^* = 71.59$
High Btu	30.0	22.60
Medium Btu	26.0	27.50
Low Btu	17.4	13.00
Very Low Btu	10.5	9.40
Li/Na		$k^* = 55.2$
High Btu	15.0	17.46
Medium Btu	11.0	21.00
Low Btu	8.0	9.90
Very Low Btu	6.7	7.20

fuel cell, the situation is rather different. Fuel gas is delivered directly at the electrode from the rear side while the front side is facing the electrolyte tile. Thus, the gas can reach electroactive sites directly, or through a layer of melt, or by diffusion through the metal. Diffusion of hydrogen through nickel may be quite significant.[31] Thus, there may be a very high local concentration of hydrogen in the porous electrode. The solubility of hydrogen in nickel at 650°C has been shown to be around 2.5×10^{-5} g mol/cc atm,[32] and its diffusivity to be 3×10^{-5} cm^2/s.[33]

We have seen from Equation 37 that the exchange current density does not depend only on hydrogen concentration, but also on the other fuel components. In particular, the significance of water present in the melt appears to play an important role in the overall reaction rate.

Some preliminary work was performed on the temperature dependency of the exchange current density on nickel and cobalt electrodes in the Li/Na/K melt over a temperature range of 550° to 700°C. No correction for changes in hydrogen concentrations caused by the temperature dependence of Equation 33 was made. However, the calculated changes over this temperature range were below 10%. Figure 2.55 shows plots of log i_o versus 1/T for nickel and cobalt using low-Btu fuel.

The activation energy (E) was calculated from the relationship,

$$\Delta E = \frac{R}{0.434} \frac{d\ (\log i_o)}{d\ (1/T)} \tag{51}$$

Here we get activation energies of 6.65 kcal/mol and 7.31 kcal/mol for nickel and cobalt, respectively.

Throughout this study, we obtained reproducible current/voltage cathodic plots in fuel-gas saturated electrolytes. In general, this would suggest a well-defined cathodic reaction occurring at these potentials. However we have no evidence that the reverse of hydrogen oxidation, specifically,

$$CO_2 + H_2O + 2e \longrightarrow H_2 + CO_3^{2-}$$

occurs at these potentials. Further work is needed to identify the stoichiometric reaction and the mechanism of the electrochemical reaction.

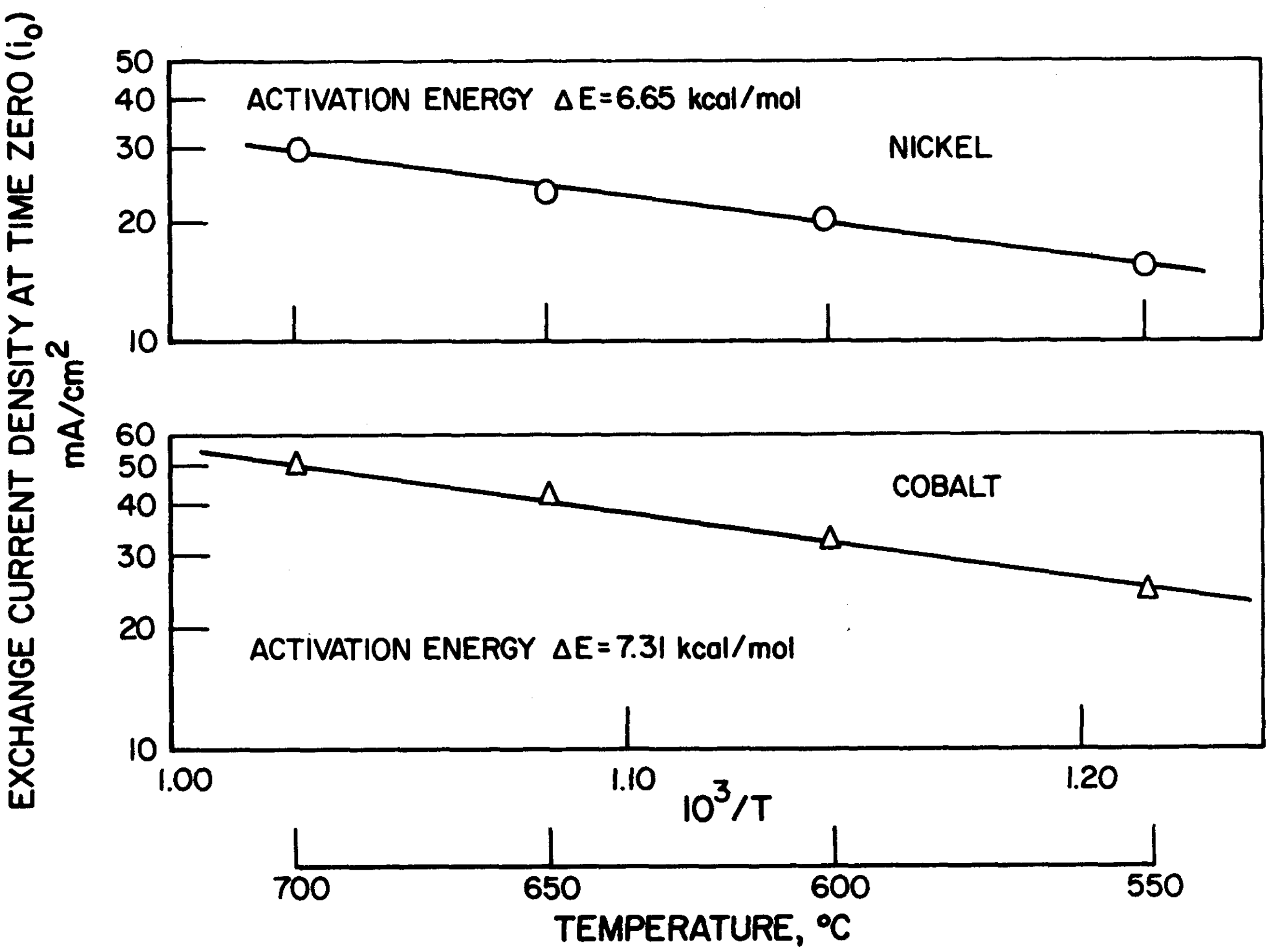

A79020478

Figure 2.55. PLOT OF LOG i_o VERSUS 1/T FOR NICKEL AND COBALT USING LOW-Btu FUEL

2.3.5. Kinetics of Oxygen Reduction

In molten-carbonate fuel cells, the cathode is initially a porous nickel sinter that, under the oxidant conditions present, will oxidize to NiO. The more fundamental nature of the electrochemical measurements required in this task has, however, required that the working electrode be of a known surface area. This has introduced the problem of how to generate in situ a stable, dense NiO electrode on the nickel surface or throughout the whole of what is initially a nickel wire. The formation of a homogeneous nickel oxide phase throughout the porous electrode sinter used in fuel cells will occur at a faster rate than if the nickel were nonporous. This reflects the large surface area available in the porous electrode for this oxidative process. In the case of the nickel wire used during these experiments, a stable, reproducible nickel oxide electrode was not obtained. Several approaches were used in an attempt to form stable NiO electrodes, including chemical, electrochemical, and sinter press techniques. However, no NiO surface was found from which reliable electrode kinetic data could be obtained. The nickel oxide electrode usually became very brittle, coarse, and fragile. The open circuit potential was initially unstable and usually settled at above 800 mV versus the standard Au/O_2-CO_2 reference electrode. Increasing the flow rate of the oxidant (70% air, 30% CO_2) did not bring the electrode potential toward the oxygen potential region. Because of the difficulty encountered with the nickel oxide, we have made an attempt to study the kinetics of oxygen reduction using a gold electrode.

The mechanism of oxygen reduction in alkali carbonate melts has been examined in detail by Appleby and Nicholson.[27,28] Their results were based on data from steady-state polarization and potential sweep experiments on a gold electrode. Our approach here is to obtain kinetic information using the transient potentiostatic technique. Compared with the potential sweep technique, the transient potentiostatic technique gives more direct information on exchange current density values and charge transfer coefficients. The experiments were performed in the electrochemical half-cell using a gold wire in 62 mole percent Li_2CO_3/38 mole percent K_2CO_3. The melt was equilibrated with oxygen by bubbling a mixture of 70% air and 30% CO_2 in the melt. The gas composition thus obtained was 30% CO_2, 15% O_2, and 55% N_2. Cathodic and anodic pulses were applied to the gold electrode. The kinetic current, i(0), was obtained by extrapolating currents between 0.3 and 0.5 ms to time zero. A plot of i(0) versus the applied pulses at different temperatures is shown in Figure 2.56. Larger currents were obtained at higher temperatures. From the slope of the curves in the low overpotential region, we could calculate the exchange current density: The values were 4, 5.2, and 6.5 mA/cm^2 at 600°, 650°, and 700°C, respectively. These values are approximately one order of magnitude larger than the exchange current densities reported by Appleby and Nicholson. A plot of log i_o versus 1/T yields an activation energy of about 7.86 kcal/mole (Figure 2.57). Allen-Hickling plots of the data are shown in Figure 2.58. The slope gives a cathodic charge transfer coefficient (α_c) of 0.62 at 650°C and 0.54 at 600°C in the cathodic region. In the anodic region, α_A is close to 1 for all temperatures. Data for 700°C are not plotted here because they are very close to the data points for the experiments conducted at 650°C. Values of the exchange current density can be read directly from the intercept of the lines. These were 4.5, 6.2, and 7 mA/cm^2 at temperatures of 600°, 650°C, and 700°C, respectively, and are close to those obtained earlier. Our results indicate that the reduction of oxygen on gold proceeds with a high, exchange current density (on the order of 1 mA/cm^2) and with a cathodic charge transfer coefficient (α_c) of about 0.5. An α value of 0.5 has been used by Appleby and Nicholson in their calculations. We have also performed a steady-state polarization measurement on gold in 650°C Li/K melt under continuous bubbling of a mixture of 70% air and 30% CO . The result, which agrees well with the data of Appleby and Nicholson, is shown in Figure 2.59.

Although we were unable to obtain i_o values experimentally for nickel oxide on the basis of the electrode modeling study (Section 2.2), we believe that the reduction of oxygen on nickel oxide may proceed with an exchange current density that is close to or even larger than the i_o of gold.

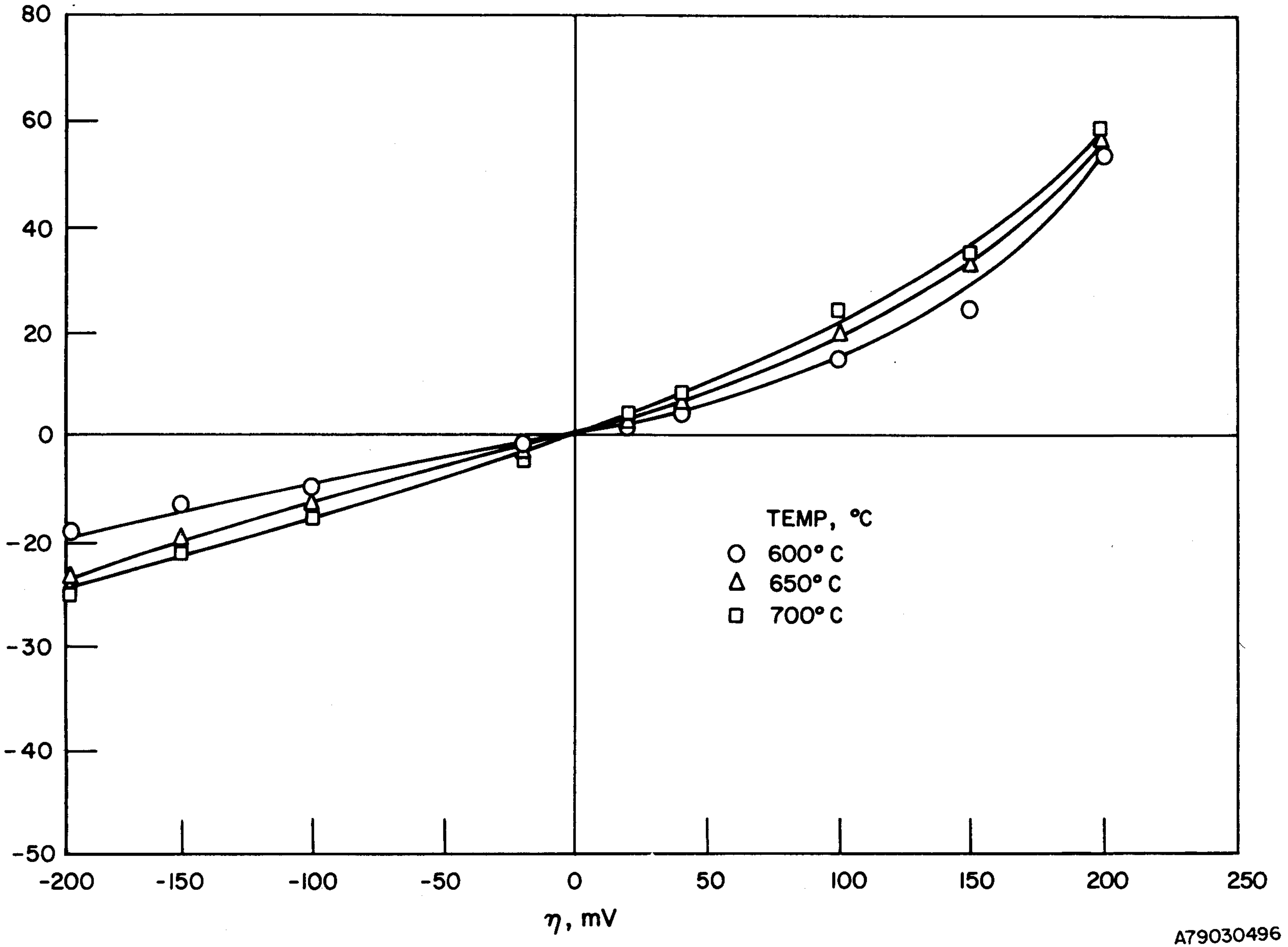

A79030496

Figure 2.56. CURRENT-VOLTAGE CHARACTERISTICS FROM TRANSIENT POTENTIOSTATIC EXPERIMENTS ON GOLD IN Li/K MELT WITH 70% AIR-30% CO_2 AT 600°, 650°, and 700° C

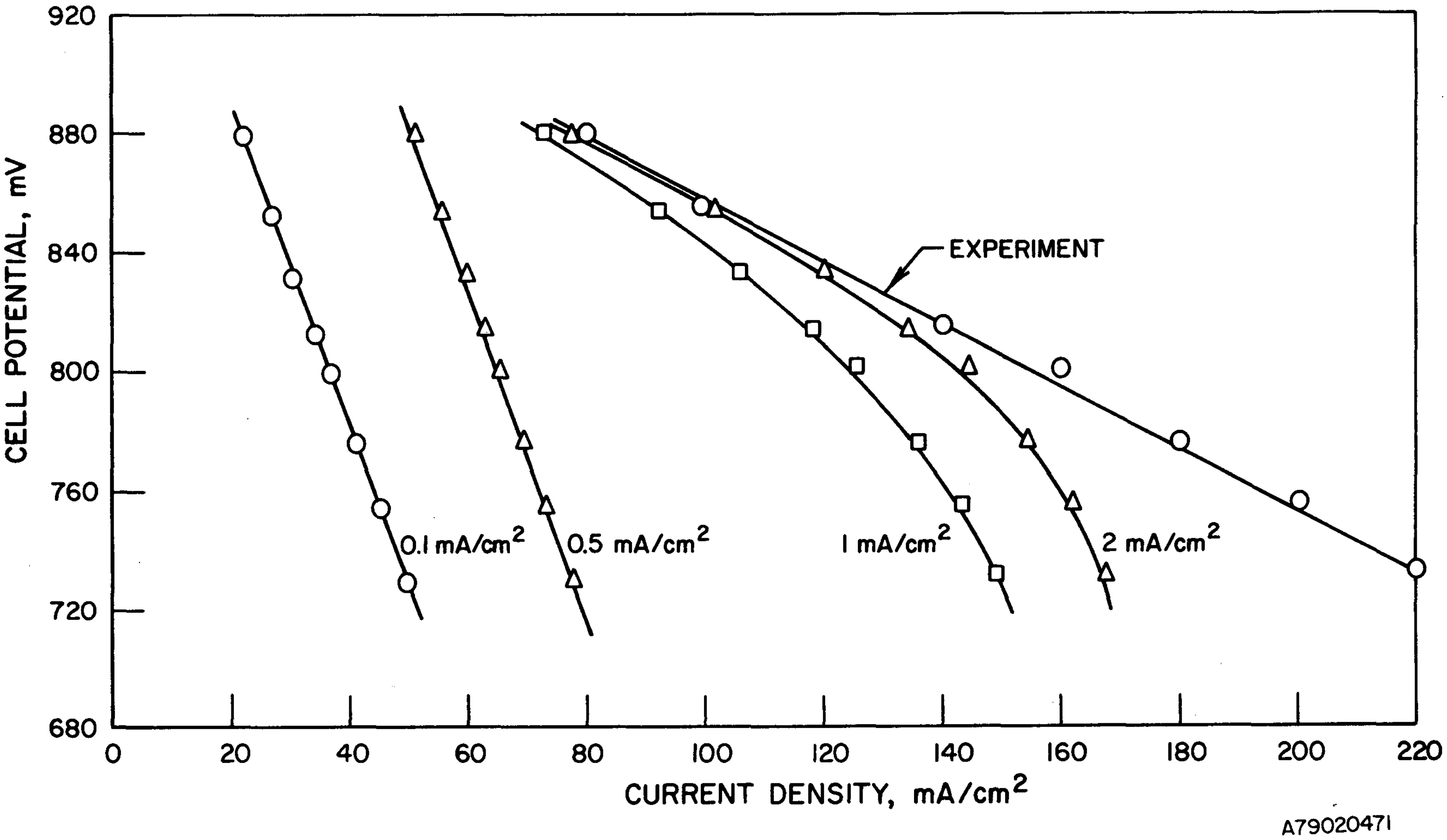

Figure 2.57. DEPENDENCY ON TEMPERATURE OF i_o VALUES USING TRANSIENT POTENTIOSTATIC MEASUREMENTS ON GOLD ELECTRODE (Li/K Melt, 75% Air-30% CO_2)

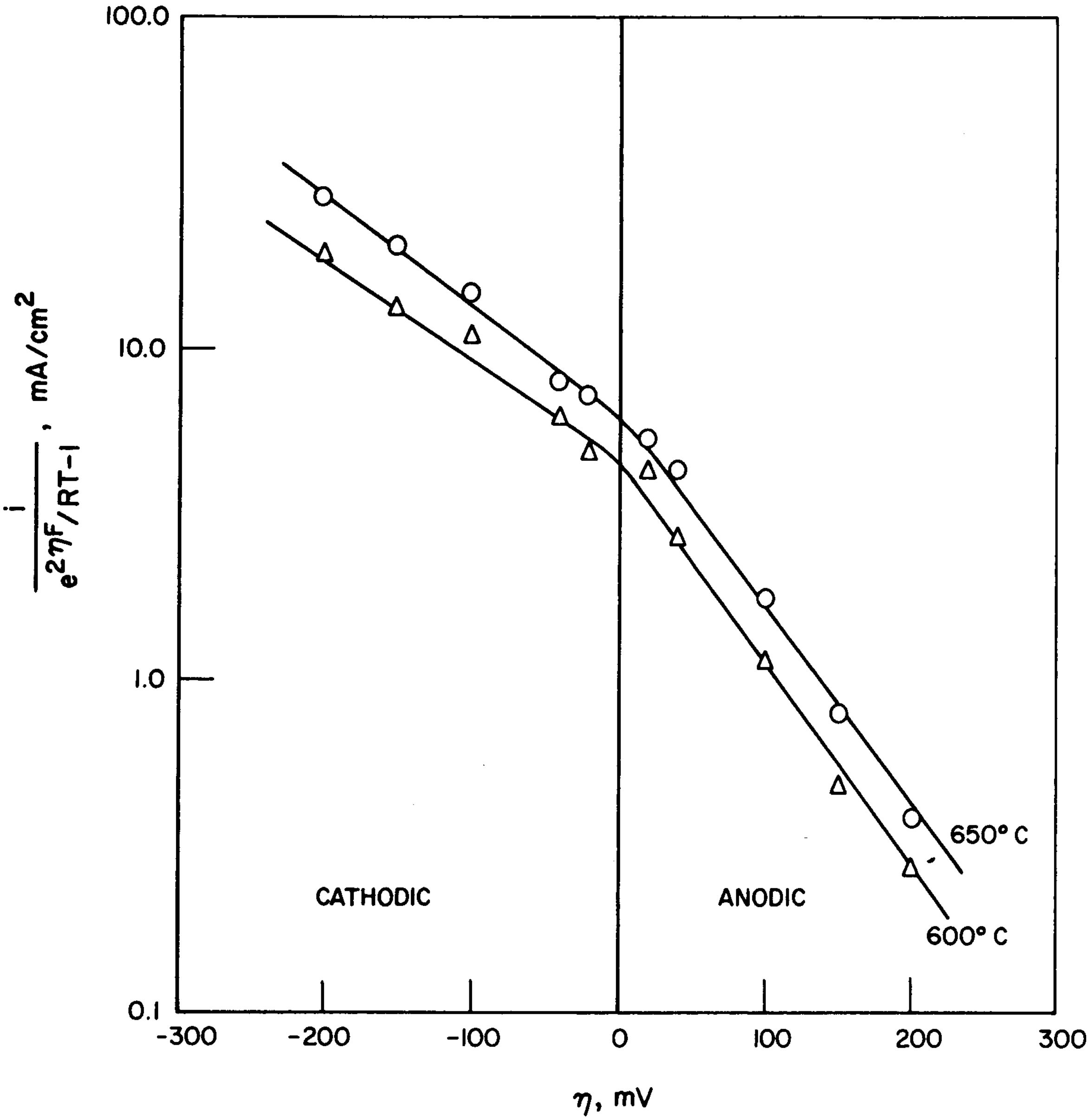

A79030493

Figure 2.58. ALLEN-HICKLING POLARIZATION CURVE FROM POTENTIAL STEP DATA (Gold Electrode, Li/K Melt, 70% Air-30% CO_2, 600° and 650°C)

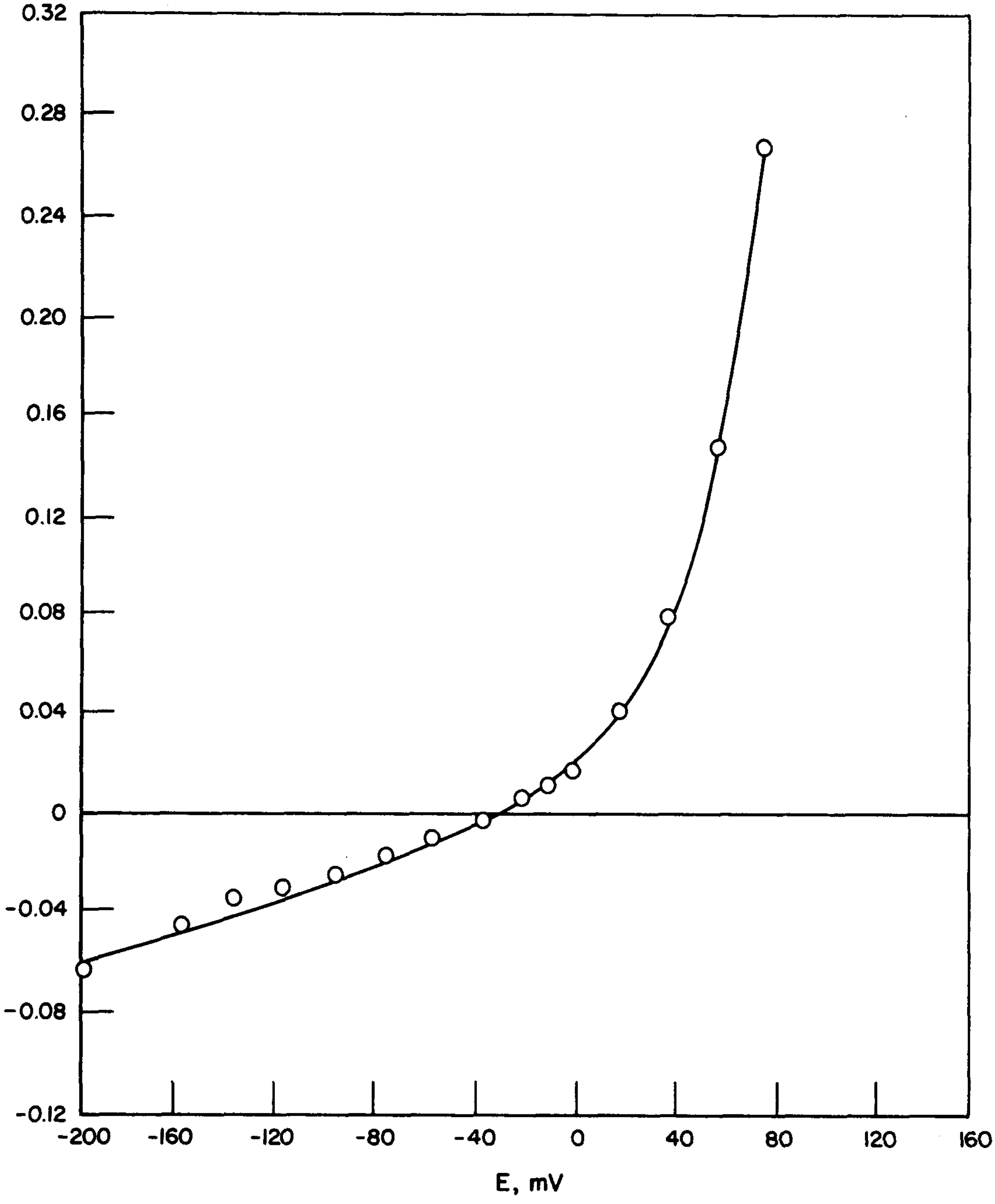

A79020479

Figure 2.59. STEADY-STATE POLARIZATION CURVE FOR GOLD IN 650°C Li/K CARBONATE MELT CONTINUOUSLY BUBBLED WITH 70% Air-30% CO_2

REFERENCES CITED

1. Rosenqvist, T., "A Thermodynamic Study of the Iron, Cobalt, and Nickel Sulfides," J. Iron Steel Inst. London 176, 37 (1954).
2. Rostrup-Nielsen, J. R., "Chemisorption of Hydrogen Sulfide on a Supported Nickel Catalyst," J. Catal. 11, 220 (1968).
3. Pannell, R. B., Chung, K. S. and Bartholomew, C. H., "The Stoichiometry and Poisoning by Sulfur of Hydrogen, Oxygen, and Carbon Monoxide Chemisorption on Unsupported Nickel," J. Catal. 46, 340 (1977).
4. Johnson, D. L., "Influence of Dispersed Refractory Oxides in Retarding Catalyst Sintering," EPRI EM-624, Research Project 371-1 Interim Report (March 1978).
5. Kinoshita, K., Argonne National Laboratory, communication of April 1977.
6. Ackerman, J. et al., "Advanced Fuel Cell Development Progress Report for April-June 1977," ANL-77-56. Argonne, Ill.: Argonne National Laboratory.
7. Lileev, I. S., Sachenko-Sakun, L. K. and Guseva, I. V., "Reaction of Hydrated Lithium Dialuminate With Sodium Hydroxide Solutions," Russ. J. Inorg. Chem. 13, 213 (1968).
8. Lejus, Rev. Hautes Temp. Refract., 1, 53-94 (1964).
9. Chang, C. H. and Margrave, J. L., "High Pressure-High Temperature Synthesis; III · Direct Synthesis of New High-Pressure Forms of $LiAlO_2$ and $LiGaO_2$ and Polymorphism in $LiMO_2$ Compounds (M = B, Al, Ga)," J. Am. Chem. Soc., 90, 2020 (1968).
10. Institute of Gas Technology, "Fuel Cell Research on Molten Carbonate Systems," Project 8984 Final Report, July 1976-September 1977.
11. Wasan, D.T., Schmidt, T.E. and Baker, B.S., "Mass Transfer in Fuel Cells: Part 1. Models for Porous Electrodes," Chem. Eng. Prog. Symp. Ser. 63 (77), 16-25 (1966).
12. Tantram, A.D.S., Tseung, A.C.C. and Harris, B.S., "Some Aspects of Molten Carbonate Fuel Cells," in Baker, B.S., Ed., Hydrocarbon Fuel Cell Technology, 187-212. New York: Academic Press, 1965.
13. Speiser, R., "The Thermodynamics of Metal-Hydrogen Systems," in Mueller, W.M., et.al., Eds., Metal Hydrides, 87 (1968).
14. Völkl, J. and Alefeld, G., "Hydrogen Diffusion in Metals," in Nowick, A.S. and Burton, J.J., Eds. Diffusion in Solids, 231 (1975).
15. Appleby, A.J. and Nicholson, S., "The Reduction of Oxygen in Molten Lithium Carbonate," J. Electroanal. Chem. Interfacial Electrochem. 53, 105-119 (1974).

TASK 3. CELL OPERATION AT HIGH PRESSURE

3.1. Introduction

The original objective of Task 3 was to test cell components developed in FY 1978 at pressures of 5 and 10 atm after they had met a performance goal of 740 mV at 160 mA/cm^2* at atmospheric pressure. The purpose of the elevated pressure-testing was to verify the performance gains obtained during the FY 1977 program and to identify the endurance characteristics of pressurized cell operation. During the interim period when the cell components were being developed, the test stands were used in a parallel EPRI program. The operating problems which prevented long-term endurance testing during the FY 1977 program continued and became more acute as testing continued during this interim period. As more operating experience was gained, a clearer understanding of the problems was obtained. Therefore, a work statement modification was submitted to DOE, and approval to continue test stand and control modifications necessary to achieve long-term pressurized-cell operation was obtained.

The major problems identified included the following:

1. Undue transient differential pressures: Increasing or decreasing total system pressure caused higher differential pressures between the anode, cathode, and vessel than those tolerable by the cell assembly.
2. Undue steady-state differential pressures: At steady-state operation (constant system pressure), differential pressures often developed between the anode, cathode, and vessel that were higher than those tolerable by the cell assembly.
3. Condensation in the anode and cathode effluent lines, which inhibited the proper functioning of the control valves.
4. Constant C_v control valves that did not allow flow rate changes above or below those of the narrow valve range.

---

* 75% H_2 conversion using low-Btu and 50% CO_2 conversion using 70% air and 30% CO_2.

The minor problems identified were —

1. High pressure vessel leakage through the flange along the bolt diameter resulting from corrosion and warping at the vessel seal area attributable to usage and thermal cycling.
2. Fluctuations in the air delivery pressure to the vessels, which caused constant adjusting responses of the control valves.
3. The system's dead volume.

The recommended solutions were —

1. Changing the differential pressure control system from the original design, Figure 3.1, to either the modified design shown in Figure 3.2 or to another that will reduce or eliminate the undue transient or steady-state differential pressures.
2. Ensuring that the effluent temperatures upstream from the control valves remain above the condensation point by heating the outlet lines.
3. Replacing the constant C_v control valves with variable C_v valves.
4. Reducing the system's dead volume by changing the tubing to 1/4-inch diameter or less.
5. Stabilizing air-delivery pressure by incorporating precision, forward-pressure regulators in series along the line.
6. Improving vessel sealing characteristics.

The improvements were completed, except Item No. 3 (variable C_v control valves are on order), and the operation of the testing facilities were successfully tested. The details are discussed below.

3.2. Results and Discussion

3.2.1. Pressure Control Design

The success of the cell operation at pressure depends on the proper pressure controls between the anode, cathode, and vessel. The objective is to control the differential pressures between the anode, cathode, and vessel to within a few inches of water (~3 inches) to protect the wet-seal and to prevent crossover.

The original control design (Figure 3.1) employed the vessel pressure as a basis for controlling the anode-vessel and the cathode-vessel pressure

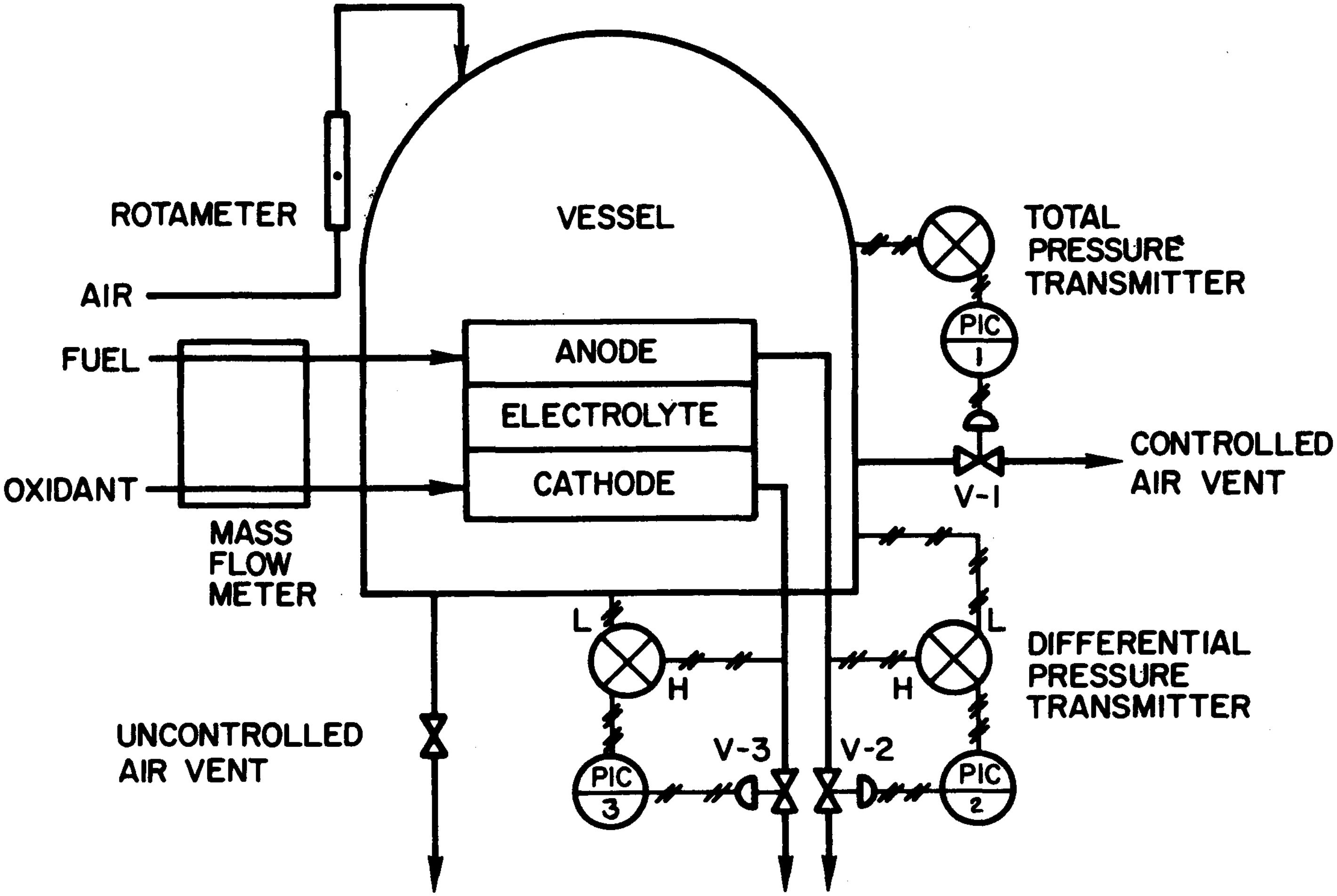

Figure 3.1. ORIGINAL PRESSURE CONTROL DESIGN

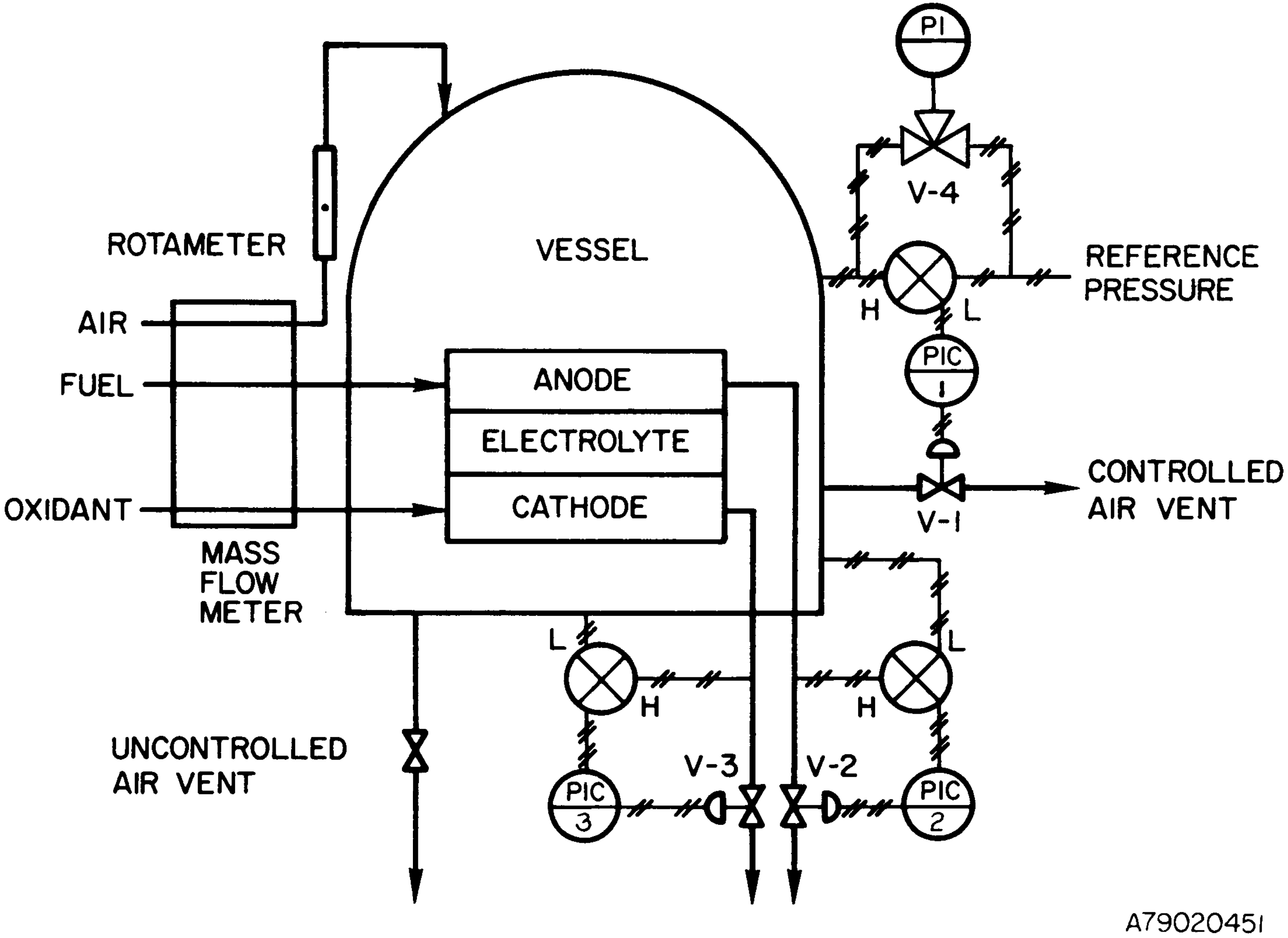

Figure 3.2. MODIFIED PRESSURE CONTROL DESIGN

differences. Air from a compressor was supplied to the vessel, and the flow rate was adjusted by a rotameter to control the rate of pressure increase. The vessel pressure was then transmitted to a panel-mounted, pressure-indicator controller, PIC-1, which actuated the vent control valve, V-1.

Fuel supplied to the anode compartment was measured using a mass flowmeter. The differential pressure between the anode outlet gas and the vessel was transmitted to PIC-2 with a differential-pressure transmitter. When this signal was higher than the setting on the PIC-2, the vent control valve, V-2, opened until the anode pressure became stable. The pressure control system for the oxidant was the same as that for the fuel.

The original design of the vessel pressure control used a pressure-indicator controller, PIC-1 (Figure 3.1), with a 0 to 300 psi range on a 5-inch scale. Because of the sensitivity of this controller, however, the vessel pressure could change ± 6 psi before the controller would actuate. This fluctuation in the vessel pressure caused fluctuations in the differential pressure across the wet-seal and the tile because of the differences in the response time of the anode, cathode, and vessel pressures. As a consequence, crossover and wet-seal leakage occurred.

This problem was corrected by using a differential-pressure transmitter with a constant reference pressure source, as shown in Figure 3.2. The constant-reference pressure was provided from a high-pressure nitrogen gas cylinder with a precision regulator that was connected to the low-pressure side of the differential-pressure transmitter. The use of a panel-mounted precision pressure gauge and a regulator allowed the reference pressure to be set at a desired vessel pressure within 0.5 psi. The differential-pressure signal was pneumatically transmitted to PIC-1, which has a range of 5 inches of water column.

Because the reference pressure remained constant, the vessel pressure also became constant at a set differential pressure above the reference pressure. The vessel and the reference pressures could be read with the pressure gauge, PI, by using a 3-way valve, V-4.

Figure 3.3 presents the test results of the modified pressure control design on a working cell at 650°C.

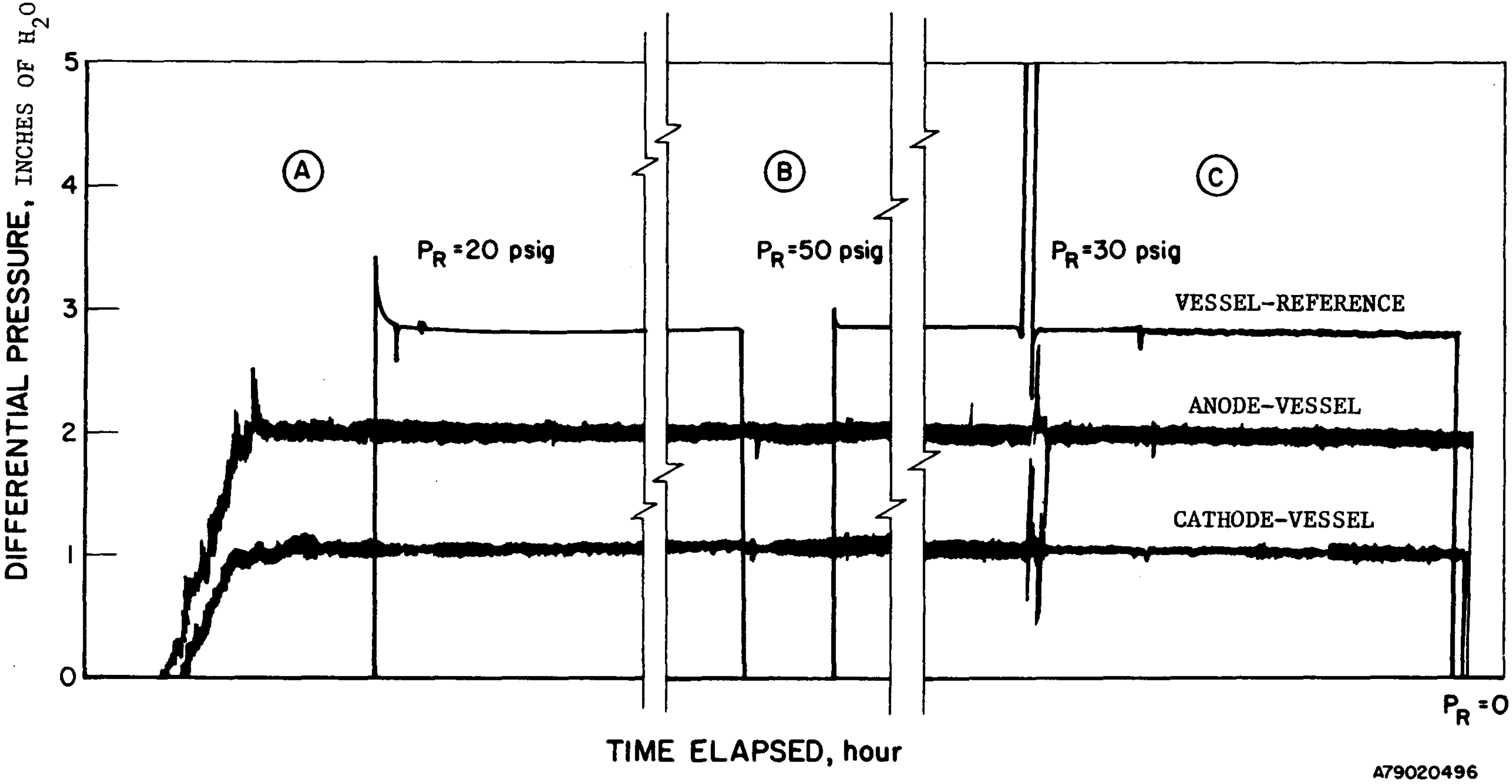

Figure 3.3. DIFFERENTIAL PRESSURES OF A WORKING CELL

In the beginning of the test, anode and cathode pressures were slowly increased until they reached a steady state at differential-pressure settings above atmospheric, as shown in Figure 3.3 (Section A). Then the reference pressure was adjusted to a desired vessel pressure (20 psig in this test), and the vessel-reference differential pressure (2.85 inches of water) was set on PIC-1. The vessel air supply from the compressor was passed through two precision forward-pressure regulators in series, and its flow rate was adjusted such that the anode and cathode systems could be pressurized within the limit of the set points. (It should be pointed out that the vessel pressure was not registered on the indicator until the vessel pressure was higher than the reference pressure.)

Therefore, at steady state, the vessel pressure, P_V, is —

$$P_V = P_R + \Delta P_{V-R} \tag{52}$$

where P_R is the reference pressure, and ΔP_{V-R} is the differential pressure between the vessel and the reference.

Similarly, the anode and the cathode pressures are expressed as —

$$P_A = P_V + \Delta P_{A-V} \tag{53}$$

and

$$P_C = P_V + \Delta P_{C-V} \tag{54}$$

where ΔP_{A-V} and ΔP_{C-V} are the differential pressures of the anode-vessel and the cathode-vessel, respectively. In Figure 3.3, the differential pressure settings were —

ΔP_{V-R} = 2.85 inches of water

and ΔP_{A-V} = 2 inches of water

ΔP_{C-V} = 1 inch of water.

When a higher vessel pressure was required, the reference pressure was simply increased to a desirable vessel pressure (50 psig in this test). Because the reference pressure became much higher than the vessel pressure, the pressure indicator of the PIC-1 returned to zero (meaning out of range). The control valve, V-1, was closed and the vessel was pressurized until it reached another steady state. During this pressurizing period, however, the differential pressures at the anode-vessel and the cathode-vessel remained constant at the previous setting points [Figure 3.3 (Section B)] indicating a steady pressure increase with the increase in vessel pressure.

When the lower vessel pressure was required, the reference pressure was decreased to the desired value (30 psig). At this point, the control valve, V-1, was wide open and the vessel was depressurized. The anode and cathode control valves, V-2 and V-3, were also opened and their pressures were reduced. However, the rate of vessel depressurization was much faster than those of the anode and cathode. The temporary fluctuations in the differential pressure are indicated in Figure 3.3 (Section C). Therefore, we decided to replace the constant C_V valves with variable C_V valves. These valves are on order at this time.

3.2.2. Vessel Air Leakage

The original vessel system used a 20-inch-ID "Flexitallic Blue Spiral-Wound Flanged Joint-type Gasket" (Flexitallic Gasket Company, Camden, N.J.), made of 304-stainless steel with asbestos filler. "Permatex" was applied on both sides of the gasket to improve the sealing characteristics, and then the flange was tightened with up to 100 ft-lb torque. Nevertheless, the vessel air was leaking through the flange along the bolt diameter, as a result of flange corrosion and warping at the vessel seal area attributable to usage and thermal cycling. In an effort to find a solution and to determine the effect of vessel leakage on the control of the system differential pressure, the following three tests were conducted:

- Test 1. Two layers of thin rubber gaskets.

  Since the vessel flange was suspected of being warped, two layers of rubber gaskets, each 1/32-inch-thick, were used to increase the compressible gaps between the flanges and the gaskets. This test was conducted at room temperature. The clamping bolts were tightened to 100 ft-lb torque as before. When the vessel was pressurized to 80 psig, the rubber gaskets failed and blew out. Upon examining the gaskets, it was concluded that the bolt tightening was not sufficient and the contact between the gaskets and the flanges was poor. The latter seemed to be attributed to dried, residual "Permatex" on the flange surfaces. As a result, the flange surfaces were rough and uneven. It was also concluded that the rubber gaskets tested lacked the rigidity to withstand the high vessel pressure.

- Test 2. Two rubber gaskets bonded with "Permatex" on both sides of the Stainless Steel Ring Gasket.

  This combined gasket design provided more rigidity than the previous design as well as the compressible gaps of the regular stainless steel ring gasket. Both flange surfaces were thoroughly polished and free of foreign materials. The clamping torque was increased to 300 ft-lb, since the first test indicated that 100 ft-lb was not sufficient to seal the gasket effectively. This test was also conducted at room temperature.

  The vessel was then pressurized up to 150 psig without any significant leakage through the flanges. With these corrections, the vessel pressure held constant and the vessel air consumption was reduced (on the order of a few cc/min).

- Test 3. Regular Stainless Steel Gasket with "Permatex" on both sides.

  This test was conducted to determine if the flange sealing characteristics of Test 2 were attributable to the use of rubber in the combined gasket or to the flange-surface polishing. Again, the flange surfaces were polished and 300 ft-lb of clamping torque was used. With this arrangement, the vessel was pressurized up to 150 psig at 650°C. The vessel pressure held constant, as in Test 2, with only a very small supply of air to the vessel.

Therefore, we conclude that the vessel air leakage was due to the uneven flange surfaces caused by corrosion and warping.

3.2.3. Slow Response of the Anode and Cathode Systems

The gas flow rates of the fuel and oxidant are relatively small, while the volumes of their system (tubing, valves, humidifier, cell, etc.) are large. This caused a slow response of each system during transient conditions. Some of the dead volume was decreased by shortening the tubing and decreasing tube diameters.

3.2.4. Water Condensation

Water condensation in the anode and cathode effluent lines was controlled by applying heating tapes to ensure that the effluent temperatures upstream from the control valves remained above the condensation point.

Water condensation also occurred in the plastic tubing to the differential-pressure transmitter, causing an electrical short circuit between the cell and ground. A longer plastic tubing was used, and the transmitter was reinstalled at a higher position. The condensed water in the plastic tubing had to be drained occasionally, which caused sudden pressure changes in the cell. The incorporation of an automatic water trap is envisioned.

3.3. Conclusions

From the test results and the experience gained during modification, we concluded that —

a. By changing the pressure control design to incorporate a differential-pressure transmitter and a reference-pressure source, the control of the vessel pressure and differential pressures was simplified and accuracy was improved.

b. Vessel air leakage was caused by uneven flange surfaces and insufficient clamping.

c. The slow response of the anode and cathode systems was improved by decreasing the dead volume of the system.

d. Variable C_v control valves will be installed as soon as received to maintain differential pressure accuracy independent of flow rates.

APPENDIX A. Electrolyte Preparation by the Original Aqueous Slurry Process

Electrolyte AD55-1A was prepared from Degussa "C" alumina following the ANL method of electrolyte preparation, which involves the following steps:

1. Prepare a slurry by mixing 56.7 grams of Degussa γ-Al_2O_3 (Degussa "C") with 300 mℓ H_2O in a 1-liter Teflon^R beaker (18.9 g Al_2O_3/100 mℓ).
2. Dissolve $LiOH \cdot H_2O$ + KOH in 500 ml H_2O using 88.71 grams $LiOH \cdot H_2O$ (17.7 g/100 ml) and 36.24 grams KOH (7.3 g/100 ml).
3. Slowly add hydroxide solution to Al_2O_3 slurry while stirring and heating at about 80°C.
4. Pour slurry into Teflon-coated baking pan and dry at 110°C in an air oven for at least 20 hours.
5. After drying, grind the powder to −325 mesh, place it in a Teflon beaker, and pass CO_2 over the powder at room temperature for 8 to 10 hours. Insert a thermocouple, and check the temperature of the powder. Obtain powder weight before and after the CO_2 treatment.
6. Regrind powder to −325 mesh, place in an Al_2O_3 crucible that has been preexposed to the molten carbonate mixture, heat at 600°C, and pass CO_2 over the powder for 22 hours. Obtain powder weight before and after firing.

With the proper assay correction for the various starting materials, this procedure is designed to produce an electrolyte of 45 weight percent $LiAlO_2$ and 55 weight percent lithium-rich carbonate eutectic (62 mole percent Li_2CO_3/38 mole percent K_2CO_3).

Our understanding of the process is summarized in Table A.1. Conversion of Al_2O_3 to $LiAlO_2$ begins when the hydroxide is mixed into the Al_2O_3 slurry (step 3), and is usually complete after the carbonation process (step 5). The high-temperature firing (step 6) completes any unfinished reaction to give the final electrolyte consisting of $LiAlO_2$, Li_2CO_3, and K_2CO_3. To understand the detailed reactions involved in each step, we prepared Electrolyte AD55-1A following the procedure described above exactly and analyzed the products obtained after each step. We recorded processing temperatures and weight changes of powders, and analyzed the electrolytes by X-ray diffraction, chemical analysis, SEM, and surface area and thermal expansion measurements. Based on these results, presented in Table A.2, the following observations were made regarding the ANL method:

- Conversion of the Degussa Al_2O_3 to $LiAlO_2$ was completed during the slurry stage (steps 3 and 4). No trace of Al_2O_3 was detected by either X-ray diffraction or SEM of the $LiAlO_2$ washed from a dried slurry. The X-ray diffraction pattern consisted of β-$LiAlO_2$, as determined by Chang and Margrave, plus several additional lines identified as $Al(OH)(CH_3COO)_2$.

Table A.1. POSSIBLE REACTIONS AND ACTUAL OBSERVATIONS DURING EACH STEP OF THE ANL ELECTROLYTE PREPARATION PROCESS (Based on Electrolyte AD55-1A)

Step	Purpose	Chemical Analysis of Products	X-ray Diffraction Pattern	Estimated Weight Change (Dry Starting Material Basis)	Observed Weight Change (Dry Starting Material Basis)
3 & 4	Initiate conversion of Al_2O_3 to $LiAlO_2$ by the reaction $Al_2O_3 + 2LiOH \rightleftarrows 2LiAlO_2 + H_2O$	None available	β-$LiAlO_2$*	0%-6.7% loss depending on degree of conversion	No data
5	Continue conversion of Al_2O_3 as in preceding steps. Convert hydroxide to carbonate by the reactions — $2LiOH + CO_2 \rightleftarrows Li_2CO_3 + H_2O$ $2KOH + CO_2 \rightleftarrows K_2CO_3 + H_2O$	Li_2CO_3 26.7% K_2CO_3 23.9% $LiAlO_2$ 30.0% Al_2O_3 2.3% Balance 17.1% Total 100.0%	β-$LiAlO_2$*	12%-19% gain depending on degree of conversion in Steps 3 & 4	24.8% Gained
6	Complete conversion of Al_2O_3 to $LiAlO_2$ and hydroxides to carbonates	Li_2CO_3 27.5% K_2CO_3 28.7% $LiAlO_2$ 38.8% Al_2O_3 0.2% Balance 4.8% Total 100.0%	β-$LiAlO_2$	1% Loss	18.7% Lost

* Plus several additional lines identified as $Al(OH)(CH_3COO)_2$, apparently formed during the washing procedure.

Table A.2. CHARACTERIZATION OF THE $LiAlO_2$ OBTAINED FROM DIFFERENT TYPES OF Al_2O_3 BY THE ANL METHOD OF ELECTROLYTE PREPARATION

	Electrolyte		
	AD55-1A	AC55-1A	AR55-1A
Starting Al_2O_3			
Commercial Name	Degussa "C"	Catapal SB	Reynolds RH-33
Chemical Formula	γ-Al_2O_3	$AlO(OH)$	$Al(OH)_3$
X-ray Diffraction of $LiAlO_2$ from Dried Slurry (Step 4)	β-$LiAlO_2$	β-$LiAlO_2$	β-$LiAlO_2$
X-ray Diffraction of $LiAlO_2$ from Carbonated Slurry (Step 5)	β-$LiAlO_2$	Not available	Not available
X-ray Diffraction of $LiAlO_2$ after the 600°C Firing (Step 6)	β-$LiAlO_2$	β-$LiAlO_2$	Not available
Li/Al Mole Ratio	0.992	0.950	Not available
Surface Area, m^2/g	7.5	11.1	Not available
Thermal Expansion	Slumped upon melting	Slumped upon melting	Slumped upon melting

A78030781

This aluminum acetate hydroxide phase apparently formed as a result of the washing procedure, which was in a preliminary stage of development at the time and used too low a concentration of acetic acid anhydride (<30%) in the glacial acetic acid. The morphology of the β-$LiAlO_2$ particles was revealed by SEM to be rod-like.

- During the carbonation process (step 5), the electrolyte seemed to retain most of the water of reaction, as indicated by a substantially greater powder weight gain than expected on the basis of the hydroxide-to-carbonate conversion. The X-ray pattern of the $LiAlO_2$ washed from Electrolyte AD55-1A after the carbonation step indicated the presence of β-$LiAlO_2$, as well as a small amount of $Al(OH)(CH_3COO)_2$ that resulted from the preliminary washing procedure. SEM again revealed the rod-like morphology of the β-$LiAlO_2$.
- During the high-temperature firing (step 6), most of the moisture was driven from the electrolyte powder, resulting in essentially stoichiometric β-$LiAlO_2$ with the desired carbonate composition. The deviation of the analyzed composition of Electrolyte AD55-1A from the theoretical value is attributed to a higher percentage of volatile matter in the starting Al_2O_3 than assumed in the calculations. An SEM micrograph of the $LiAlO_2$ particles washed from finished Electrolyte AD55-1A indicated minor changes in $LiAlO_2$ particle size occurred during the 22-hour firing at 600°C, although the rod-like morphology was retained.

Because $LiAlO_2$ particles are formed during the slurry stage and because their size is much larger than that of the starting Degussa "C" Al_2O_3, the most probable mechanism of $LiAlO_2$ formation is a dissolution-precipitation process. Alumina dissolving in the hydroxide solution reacts with lithium ions and precipitates as $LiAlO_2$.

Table A.2 presents data describing the preparation of $LiAlO_2$ from low-cost hydrated aluminas using the original process.

APPENDIX B. Characterization of Electrolyte Tile Materials

Summary of Tests

Materials characterization plays an important role in the development of the electrolyte tile. The following characterization tests are routinely performed on tile materials —

- Chemical analysis for carbonate and $LiAlO_2$ contents by acid dissolution — CO_2 evolution method
- Li/K/Al contents by atomic absorption analysis
- $LiAlO_2$ phase composition by X-ray diffraction and HCl acid dissolution
- $LiAlO_2$ surface area by nitrogen adsorption B.E.T.
- SEM of $LiAlO_2$ powders
- Tile density
- Tile thermal cycling behavior by dilatometer test.

Optional analyses include —

- Mercury porosimetry of $LiAlO_2$ powder
- $LiAlO_2$ chemical analyses
- $LiAlO_2$ thermochemical stability tests
- X-ray radiography of hot-pressed tile
- Miscroscopy of tile cross section.

Electrolyte Washing Procedure

Before the physical and chemical properties of the $LiAlO_2$ support material used in the electrolyte tiles can be determined, the carbonate must be removed. The washing procedure for this removal must not alter the $LiAlO_2$ properties or introduce artifacts. In preliminary experiments, washing the electrolyte with a dilute solution of acetic acid anhydride in glacial acetic acid resulted, in some cases, in the formation of aluminum acetate hydroxide [$Al(OH)(CH_3COO)_2$]. Therefore, subsequent washing experiments utilized a higher concentration of acetic acid anhydride (30%) in the washing solution. An excess of acetic acid anhydride will prevent formation of $Al(OH)(CH_3COO)_2$ and hydrolysis of $LiAlO_2$ by reacting with water present in the washing solution.

The following procedure was shown during the course of this work to remove the carbonate without introducing artifacts or altering the $LiAlO_2$, and was adopted as a standard procedure —

a. Weigh out approximately 3 grams of electrolyte in a beaker and add 300 ml of freshly prepared 30% acetic anhydride/70% glacial acetic acid. Stir for 1 hour using a magnetic stirrer.

b. Filter the solution through a 0.2μ filter paper.

c. Transfer the residue into a beaker, add 300 ml methanol, and stir for 1 hour. Filter through 0.2μ filter paper.

d. Dry the residue in an air oven at 120° to 140°C for at least 2 hours.

The washed $LiAlO_2$ powders thus obtained are then evaluated by SEM, B.E.T. surface area, X-ray diffraction, chemical analysis, and mercury porosimetry.

Tile Thermal Cycling Test

The screening test that is currently used to evaluate the potential of a tile for use in an operating fuel cell involves a dilatometric technique. A cylindrical disk tile specimen, about 18-mm (0.7 in.) diameter x 5-mm (0.2 in.) thick, is positioned in the dilatometer apparatus shown in Figure B.1. The axial expansion/contraction behavior of the tile is then determined under a static load corresponding to 3 psig (122 kPa total pressure) as a function of temperature between ambient and 650°C. The specimen is heated to 650°C in 5 hours and held at that temperature for 2 hours before cooling at a rate similar to the heating rate. This thermal cycle is then repeated without altering the specimen. A constant flow of oxidant gas (14% CO_2/balance air) is maintained over the specimen during the entire test.

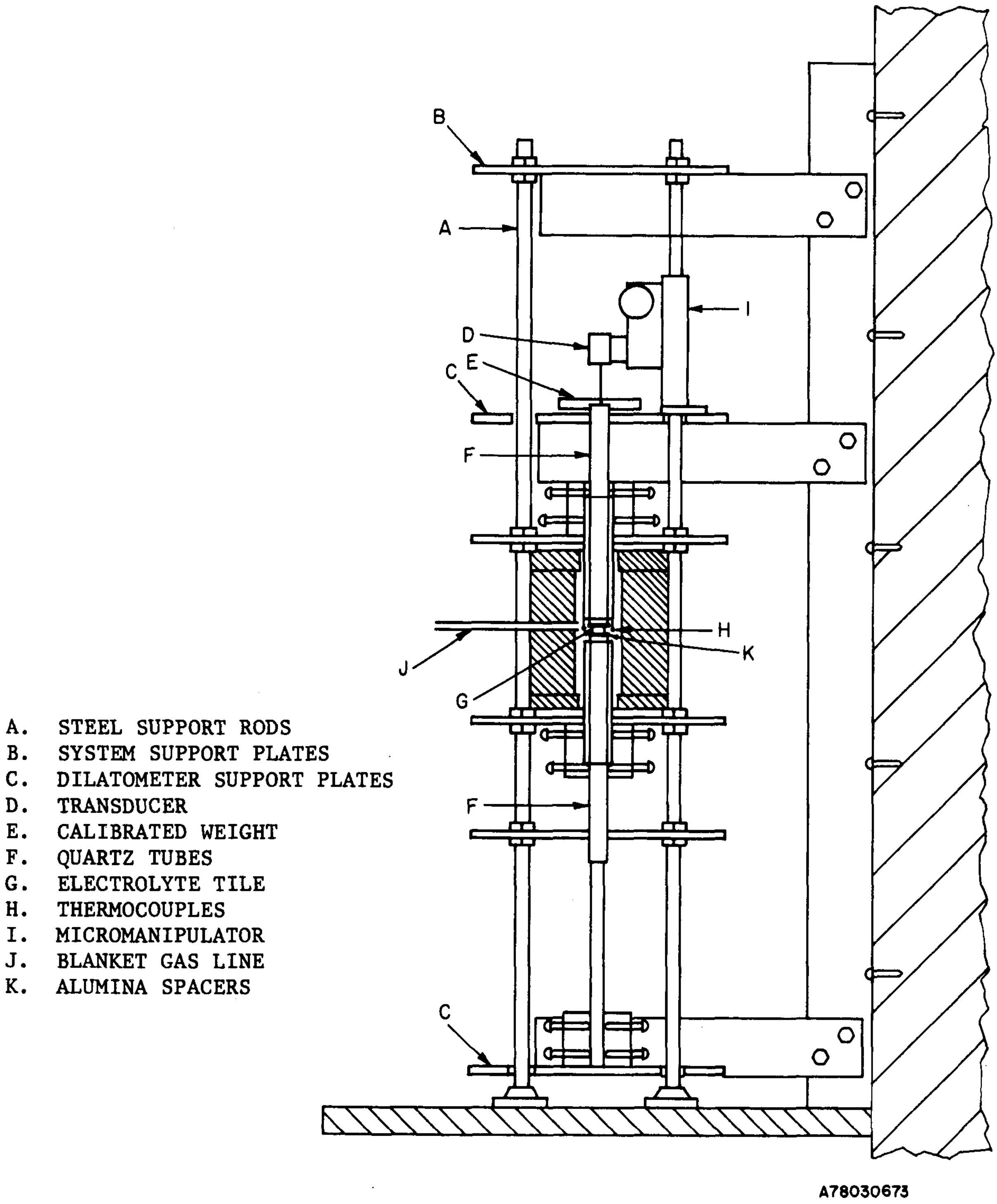

Figure B.1. APPARATUS USED FOR DILATOMETRIC SCREENING TEST

APPENDIX C. Derivation of Model Equations (Atmospheric Pressure)

Mass Balance Equations

Figure C.1 is a schematic diagram of the gas flows to the cell. It also shows how the cell is divided into sections for computation purposes. Equations C.1 through C.7 show the dependency of the fuel and oxidant gas components on the gas flow rate, length of the anode, cathode gas channels, and current density.

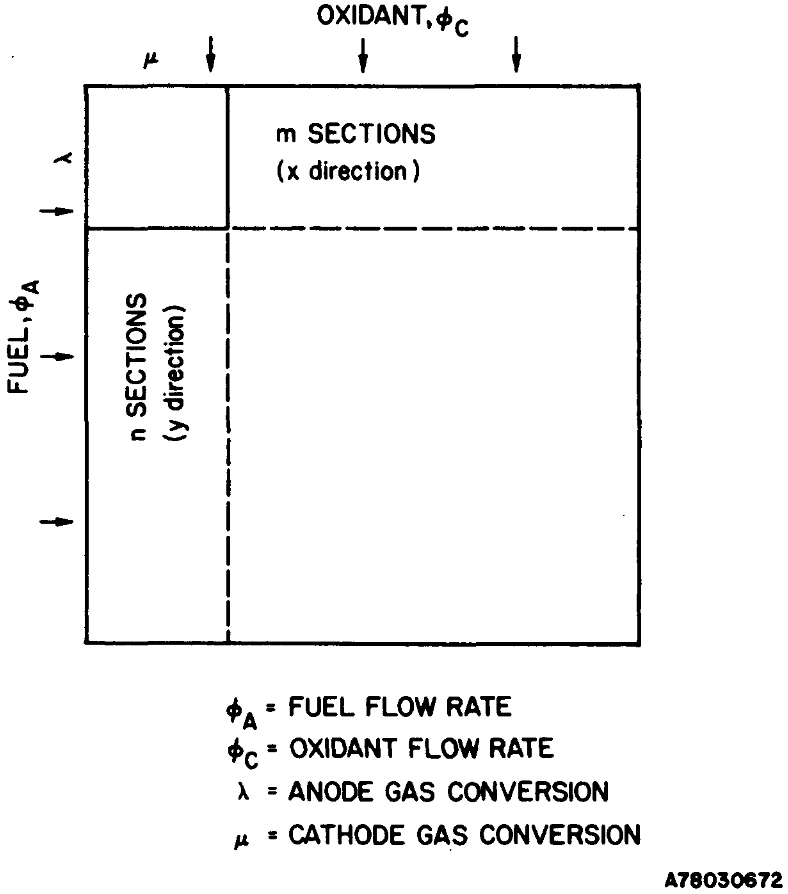

Figure C.1. SCHEMATIC DIAGRAM OF THE FUEL AND OXIDANT FLOWS TO THE CELL

Anode

$$H_2: \quad \frac{P}{RT\ L_C/n}\ \frac{d}{dx}\ \left(\frac{\Phi_A}{n}\ X_H\right) = -\frac{i_A}{2F} = -\frac{i}{2F} \qquad (C.1)$$

$$CO_2: \quad \frac{P}{RT\ L_C/n}\ \frac{d}{dx}\ \left(\frac{\Phi_A}{n}\ X_{CA}\right) = \frac{i_A}{2F} = \frac{i}{2F} \qquad (C.2)$$

$$H_2O: \quad \frac{P}{RT\ L_C/n}\ \frac{d}{dx}\ \left(\frac{\Phi_A}{n}\ X_W\right) = \frac{i_A}{2F} = \frac{i}{2F} \qquad (C.3)$$

$$CO: \quad \frac{P}{RT\ L_C/n}\ \frac{d}{dx}\ \left(\frac{\Phi_A}{n}\ X_{CO}\right) = 0 \qquad (C.4)$$

Cathode

$$CO_2: \quad \frac{P}{RT\ L_A/m}\ \frac{d}{dy}\ (\frac{\Phi_C}{m} X_{CC}) = \frac{i_C}{2F} = -\frac{i}{2F} \qquad (C.5)$$

$$O_2: \quad \frac{P}{RT\ L_A/m}\ \frac{d}{dy}\ (\frac{\Phi_C}{m} X_O) = \frac{i_C}{4F} = -\frac{i}{4F} \qquad (C.6)$$

$$N_2: \quad \frac{P}{RT\ L_A/m}\ \frac{d}{dy}\ (\frac{\Phi_C}{m} X_N) = 0 \qquad (C.7)$$

where,

Φ_A = total fuel flow rate, cm^3/s

Φ_C = total oxidant flow rate, cm^3/s

X_k = mole fraction of the gas component k

x = distance in the fuel flow direction, cm

y = distance in the oxidant flow direction, cm

i_A = anodic current density (>0), mA/cm^2

i_C = cathodic current density (<0), mA/cm^2

i = current density $[i = i_A = |i_C|]$, mA/cm^2

L_A = total length of the fuel gas channel, cm

L_C = total length of the oxidant gas channel, cm

m = number of sections in the anode flow direction

n = number of sections in the cathode flow direction

T = temperature, K

P = pressure, atm

R = gas constant, 82.06 atm-cm^3/g-mole-K

F = Faraday's constant

and the subscripts are —

A = anode

C = cathode

H = hydrogen

CA = CO_2 in anode gas

CC = CO_2 in cathode gas

W = water

CO = carbon monoxide

O = oxygen

N = nitrogen.

Conversion of H_2, λ, on the fuel side is defined as —

$$\lambda = \frac{\text{moles of } H_2 \text{ consumed}}{\text{moles of } H_2 \text{ in}} = \frac{\Phi_A^\circ X_H^\circ - \Phi_A X_H}{\Phi_A^\circ X_H^\circ} \qquad (C.8)$$

where the ° superscript refers to the initial conditions; that is,

$$\lambda = 1 - f_A \frac{X_H}{X_H^\circ} \qquad (C.9)$$

where,

$$f_A = \frac{\Phi_A}{\Phi_A^\circ}$$

Conversion of CO_2, μ, on the oxidant side is defined as —

$$\mu = \frac{\text{moles of } CO_2 \text{ consumed}}{\text{moles of } Co_2 \text{ in}} = \frac{\Phi_C^\circ X_{CC}^\circ - \Phi_C X_{CC}}{\Phi_C^\circ X_{CC}^\circ} \qquad (C.10)$$

that is,

$$\mu = 1 - f_C \frac{X_{CC}}{X_{CC}^\circ} \qquad (C.11)$$

where,

$$f_C = \frac{\Phi_C}{\Phi_C^\circ}$$

Combining Equations C.9 and C.10 for the hydrogen component of the fuel, we obtain Equation C.12. Similarly, Equations C.13 and C.14 can be derived for the CO_2 and H_2O fuel components.

$$f_A X_H = X_H^\circ - \lambda X_H^\circ \qquad (C.12)$$

$$f_A X_{CA} = X_{CA}^\circ + \lambda X_H^\circ \qquad (C.13)$$

$$f_A X_W = X_W^\circ + \lambda X_H^\circ \qquad (C.14)$$

Adding Equations C.12, C.13, and C.14, we obtain —

$$f_A = 1 + X_H^\circ. \qquad (C.15)$$

In a similar manner for the oxidant components at the cathode,

$$f_C X_{CC} = X_{CC}^{\circ} - \mu X_{CC}^{\circ} \tag{C.16}$$

$$f_C X_O = X_O^{\circ} - \frac{\mu}{2} X_{CC}^{\circ} \tag{C.17}$$

Adding Equations 20 and 21, then

$$f_C = 1 - \frac{3}{2} \mu X_{CC}^{\circ} \tag{C.18}$$

If the dimensionless distance, ξ, is defined as

$$\xi = \frac{x}{L_A/m} \tag{C.19}$$

where L_A/m is the length of one section in the x-direction, then substituting Equations C.9 and C.19 into Equations C.1 through C.3 results in Equation C.20 —

$$\frac{Pm}{RTL_C L_A} \Phi_A^{\circ} X_H^{\circ} \frac{d\lambda}{d\xi} = \frac{i}{2F} \tag{C.20}$$

The current density can be defined as —

$$J = \frac{i}{A} = \frac{im}{I_{max}} \tag{C.21}$$

where I_{max} is the current density that would result if 100% conversion of the anode gas took place and the resulting current was uniformly distributed over the entire cell. Then,

$$A = \frac{2FP\Phi_A^{\circ} X_H^{\circ} m}{RTL_C L_A} \ (A/cm^2) \tag{C.22}$$

and therefore,

$$\frac{d\lambda}{d\xi} = J \tag{C.23}$$

If the dimensionless distance η_d is defined as

$$\eta_d = \frac{y}{L_C/n} \tag{C.24}$$

where L_C/n is the length of one section in the y-direction, then substituting Equations C.11 and C.24 into Equations C.5 and C.6 results in Equation C.25 —

$$\frac{Pn}{RTL_A L_C} \Phi^\circ_C X_{CC} \frac{d\mu}{d\eta_d} = \frac{i}{2F} \qquad (C.25)$$

Let S denote the ratio of CO_2 flow rate per cathode section th the H_2 flow rate per anode section; that is,

$$S = \frac{X^\circ_{CC} \Phi^\circ_C n}{X^\circ_H \Phi^\circ_A m} \qquad (C.26)$$

Substituting Equations C.22 and C.23 into Equation C.26 we obtain —

$$\frac{d\mu}{d\eta_d} = \frac{i}{SA} + \frac{J}{S} \qquad (C.27)$$

Equations C.23 and C.27 are two mass balance equations containing three unknowns, λ, μ, and J. To solve for these unknowns, a third equation is obtained from a potential balance.

Potential Balance Equation

Figure C.2 is a schematic representation of the potential gradient in a cell for both the open-circuit condition and when under load. The cell potential is given by —

$$V = (V_{CN} - V_{AN}) - iZ_{ohm} + \eta_C - \eta_A \qquad (C.28)$$

where —

V = terminal potential

V_{CN} = equilibrium (Nernst) potential at the cathode

V_{AN} = equilibrium (Nernst) potential at the anode

i = current density, mA/cm^2

Z_{ohm} = ohmic cell resistance, ohm/cm^2

iZ_{ohm} = ohmic potential drop in cell

η_C = cathodic overpotential (<0)

η_A = anodic overpotential (>0).

The equilibrium potentials at the electrodes are —

$$V_{AN} = V^\circ_A + \frac{RT}{2F} \ln\left(\frac{X_W X_{CA}}{X_H}\right) \text{ and} \qquad (C.29)$$

$$V_{CN} = V^\circ_C + \frac{RT}{2F} \ln(X_O^{1/2} X_{CC}) \qquad (C.30)$$

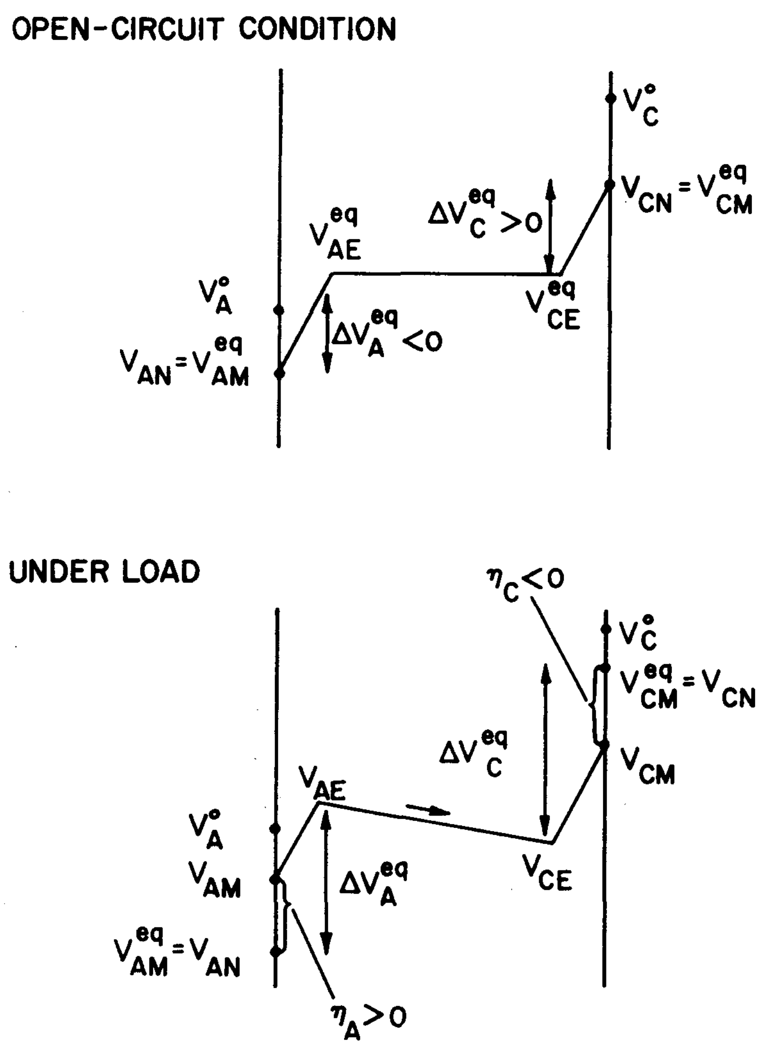
OPEN-CIRCUIT CONDITION

UNDER LOAD

V_A° = STANDARD ANODE POTENTIAL

V_C° = STANDARD CATHODE POTENTIAL

V_{AN} = ANODE NERNST POTENTIAL

V_{CN} = CATHODE NERNST POTENTIAL

V_{AM} = ANODE METAL POTENTIAL

V_{CM} = CATHODE METAL POTENTIAL

V_{AE}, V_{CE} = ELECTROLYTE POTENTIALS

$\Delta V_C^{eq} = V_{CN} - V_{CE}$

$\Delta V_A^{eq} = V_{AN} - V_{AE}$

$\eta_A = V_{AM} - V_{AM}^{eq}$

$\eta_C = V_{CM} - V_{CM}^{eq}$

SUPERSCRIPT eq INDICATES EQUILIBRIUM CONDITIONS

A78030671

Figure C.2. SCHEMATIC REPRESENTATION OF THE POTENTIAL GRADIENT IN A CELL where V°_A and V°_C are the standard anode and cathode potentials. Assuming a linear current-overpotential relationship, then —

$$n_A = i_A Z_A = iZ_A \tag{C.31}$$

$$n_C = i_C Z_C = -iZ_C \tag{C.32}$$

where Z_A and Z_C are effective electrode impedances (ohm/cm^2). Substituting Equations C.29 through C.32 into Equation C.28 we obtain —

$$V + V^\circ_A - V^\circ_C = \frac{RT}{2F} \ln (X_O^{1/2} X_{CC}) - \frac{RT}{2F} \ln \left(\frac{X_W X_{CA}}{X_H}\right) - i_A (Z_{ohm} + Z_A + Z_C) \tag{C.33}$$

Using the definition of conversions λ and μ from Equations C.9 and C.11, Equation C.33 can be written as —

$$\frac{V + V^\circ_A - V^\circ_C}{RT/2F} - \ln \left[\frac{X^\circ_{CC} (X^\circ_O{}^{1/2} X^\circ_H)}{X^\circ_W X^\circ_{CA}}\right]$$

$$= \ln \left[\frac{(1-\mu)(1 - 1/2\mu \frac{X^\circ_{CC}}{X^\circ_O})^{1/2} (1-\lambda)(1+\lambda X^\circ_H)}{(1 - 3/2\mu X^\circ_{CC})^{3/2} (1 + \lambda \frac{X^\circ_H}{X^\circ_W})(1 + \lambda \frac{X^\circ_H}{X^\circ_{CA}})}\right] - \frac{JZA}{RT/2F} \tag{C.34}$$

The first term on the right-hand side of Equation C.34 is the Nernst loss, and the second term is the overpotential term. The effective impedance, Z, is the sum of electrode impedances, Z_A and Z_C, and ohmic resistance, Z_{ohm}. Substituting Equation C.22 for A in the overpotential term, we obtain —

$$\frac{JZA}{RT/2F} = JZ \frac{P\Phi^\circ_A X^\circ_H m}{L_C L_A} \left(\frac{2F}{RT}\right)^2 \tag{C.35}$$

Rearranging Equation C.34, we then have —

$$\ln \left[\frac{(1-\mu)(1-\mu A_1)^{1/2} (1-\lambda)(1+\lambda A_2)}{(1-\lambda A_3)^{3/2} (1+\lambda A_4)(1+\lambda A_5)}\right] - U - JE = 0 \tag{C.36}$$

where —

$A_1 = 0.5\ X^\circ_{CC}/X^\circ_O$

$A_2 = X^\circ_H$

$A_3 = 1.5\ X^\circ_{CC}$

$A_4 = X^\circ_H / X^\circ_W$

$A_5 = X^\circ_H / X^\circ_{CA}$

$$U = \frac{V + V^\circ_A - V^\circ_C}{RT/2F} - \ln \left[\frac{(X^\circ_{CC})\,(X^\circ_O)^{1/2}\ (X^\circ_H)}{(X^\circ_W)\,(X^\circ{}_{CA})} \right]$$

$$\text{and } E = \frac{ZmP\Phi^\circ_A X^\circ_H}{L_C L_A} \left(\frac{2F}{RT}\right)^2$$

Equations C.23, C.27, and C.36 can be solved simultaneously to give λ, μ, and the current density at any point on the electrode surface.

APPENDIX D. Derivation of Model Equations Taking the Effect of Higher Pressure into Account

$$H_2:\quad \frac{Pn}{RTL_C}\frac{d}{dx}\left(\frac{\Phi_A X_H}{n}\right) = -\frac{d\lambda_e}{dx}\left(\frac{P}{RTL_C}\Phi^\circ_A X^\circ_H\right) + \frac{d\nu}{dx}\left(\frac{P}{RTL_C}\Phi^\circ_A X^\circ{}_{CO}\right) + 3\frac{d\pi}{dx}\left(\frac{P}{RTL_C}\Phi^\circ_A X^\circ_M\right) \tag{D.1}$$

where, by definition,

Electrochemical conversion:

$$\lambda_e = \int_o^X \frac{iRTL_C}{2F\Phi^\circ_A X^\circ_H P}\,dx \tag{D.2}$$

Conversion of CO:

$$\nu = \frac{(\Phi^\circ_A X^\circ_{CO} - \Phi_A X_{CO}) + (\Phi^\circ_A X^\circ_M - \Phi_A X_M)}{\Phi^\circ_A X^\circ_M} \tag{D.3}$$

Conversion of CH_4:

$$\pi = \frac{\Phi^\circ_A X^\circ_M - \Phi_A X_M}{\Phi^\circ_A X^\circ_M} \tag{D.4}$$

$$CC_2:\quad \frac{Pn}{RTL_C}\frac{d}{dx}\left(\frac{\Phi_A X_{CA}}{n}\right) = \frac{d\lambda_e}{dx}\left(\frac{P}{RTL_C}\Phi^\circ_A X^\circ_H\right) + \frac{Pn}{RTL_C}\frac{d\nu}{dx}\Phi^\circ_A X^\circ_{CO} \tag{D.5}$$

$$H_2O:\quad \frac{Pn}{RTL_C}\frac{d}{dx}\left(\frac{\Phi_A X_W}{n}\right) = \frac{d\lambda_e}{dx}\left(\frac{P\Phi^\circ_A X^\circ_M}{RTL_C}\right) - \frac{Pn}{RTL_C}\Phi^\circ_A X^\circ{}_{CO}\frac{d\nu}{dx} - \frac{Pn}{RTL_C}\Phi^\circ_A X^\circ_M\frac{d\pi}{dx} \tag{D.6}$$

$$CO:\quad \frac{Pn}{RTL_C}\frac{d}{dx}\left(\frac{\Phi_A X_{CO}}{n}\right) = -\Phi^\circ_A X_{CO}\frac{Pn}{RTL_C}\frac{d\nu}{dx} + \Phi^\circ_A X^\circ_M\frac{Pn}{RTL_C}\frac{d\pi}{dx} \tag{D.7}$$

$$CH_4:\quad \frac{Pn}{RTL_C}\frac{d}{dx}\left(\frac{\Phi_A X_M}{n}\right) = -\Phi^\circ_A X^\circ_M\frac{Pn}{RTL_C}\frac{d\pi}{dx} \tag{D.8}$$

Integrating species balances, we obtain —

$$X_H = \frac{X^\circ_H - X^\circ_H\lambda_e + X^\circ{}_{CO}\nu + 3X^\circ_M\pi}{1 + 2X^\circ_M\pi + X^\circ_H\lambda_e} \tag{D.9}$$

$$X_{CA} = \frac{X^\circ_{CA} + X^\circ_H\lambda_e + X^\circ_{CO}\nu}{1 + 2X^\circ_M\pi + X^\circ_H\lambda_e} \tag{D.10}$$

$$X_W = \frac{X^\circ_W + X^\circ_H\lambda_e - X^\circ_{CO}\nu - X^\circ_M\pi}{1 + 2X^\circ_M\pi + X^\circ_H\lambda_e} \tag{D.11}$$

$$X_{CO} = \frac{X^{\circ}_{CO}\ (1 - \nu) + X^{\circ}_{M}\pi}{1 + 2X^{\circ}_{M}\pi + X^{\circ}_{H}\lambda_{e}} \tag{D.12}$$

$$X_{M} = \frac{X^{\circ}_{M}\ (1 - \pi)}{1 + X^{\circ}_{H}\lambda_{e} + 2X^{\circ}_{M}\pi} \tag{D.13}$$

By substituting D.9 through D.12 in the shift reaction and methanation reaction equilibria, we obtain two equations —

$$\frac{X_{CA}X_{H}}{X_{W}X_{CO}} = K_{1} \text{ and } \frac{(X_{H})^{3}(X_{CO})}{(X_{M})(X_{W})} = \frac{K_{2}}{P^{2}} \tag{D.14}$$

The third equation is the potential balance equation given by —

$$V + \frac{V^{\circ}_{A} - V^{\circ}_{C}}{RT/2F} - \ln \frac{(X^{\circ}_{O})^{1/2} X^{\circ}_{CC} X^{\circ}_{M}}{X^{\circ}_{W} X^{\circ}_{CA}} + \frac{\text{JƵA}}{RT/2F}$$

$$= \ln \frac{\left(1 + \lambda_{e}\frac{X^{\circ}_{H}}{X^{\circ}_{W}} - \nu\frac{X^{\circ}_{CO}}{X^{\circ}_{W}} - \pi\frac{X^{\circ}_{M}}{X^{\circ}_{W}}\right)\left(1 + \lambda_{e}\frac{X^{\circ}_{H}}{X^{\circ}_{CA}} + \nu\frac{X^{\circ}_{CO}}{X^{\circ}_{CA}}\right)}{\left(1 + \lambda_{e}X^{\circ}_{H} + 2\pi X^{\circ}_{M}\right)\left(1 - \lambda_{e} + \frac{X^{\circ}_{CO}}{X^{\circ}_{H}}V + 3\frac{X^{\circ}_{M}}{X^{\circ}_{H}}\pi\right)} \tag{D.15}$$

where —

Φ_{A} = total fuel flow rate, cm^3/s

Φ_{C} = total oxidant flow rate, cm^3/s

X_{k} = mole fraction of the gas component k

x = distance in the fuel flow direction, cm

i = current density [$i = i_{A} = |i_{C}|$], mA/cm^2

L_{C} = total length of the oxidant gas channel, cm

n = number of sections in the cathode flow direction

T = temperature, K

P = pressure, atm

R = gas constant, 82.06 atm-cm^3/g-mole-K

F = Faraday's constant

and the subscripts are,

A = anode

C = cathode

H = hydrogen

CA = CO_2 in anode gas
CC = CO_2 in cathode gas
W = water
CO = carbon monoxide
O = oxygen
M = methane

The three simultaneous linear equations are solved at each mesh point of the cell, using an IGT subroutine.

☆U.S. GOVERNMENT PRINTING OFFICE:1980 -640 -258/ 1946